SENSOR BASED COMMUNICATION AWARE NAVIGATION CONTROL

BY

WAQAS AFZAL

A Dissertation Presented to the
DEANSHIP OF GRADUATE STUDIES
KING FAHD UNIVERSITY OF PETROLEUM & MINERALS
DHAHRAN, SAUDI ARABIA

In Partial Fulfillment of the
Requirements for the Degree of

DOCTOR OF PHILOSOPHY
In
ELECTRICAL ENGINEERING

FEBRUARY 2018

KING FAHD UNIVERSITY OF PETROLEUM & MINERALS
DHAHRAN 31261, SAUDI ARABIA

DEANSHIP OF GRADUATE STUDIES

This dissertation, written by **WAQAS AFZAL** under the direction of his dissertation adviser and approved by his dissertation committee, has been presented to and accepted by the Dean of Graduate Studies, in partial fulfillment of the requirements for the degree of **DOCTOR OF PHILOSOPHY IN ELECTRICAL ENGINEERING**.

Dissertation Committee

Dr. Ahmad A. Masoud (Adviser)

Dr. Salam A. Zummo (Member)

Dr. Salim Ibrir (Member)

Ashraf
Dr. Ashraf S. Hasan Mahmoud (Member)

W. Mesbah
Dr. Wessam Mesbah (Member)

Dr. Ali Ahmad Al-Shaikhi
Department Chairman

Dr. Salam A. Zummo
Dean of Graduate Studies

17/4/18
Date

Indeed, in the creation of the heavens and the earth and the alternation of the night and the day are signs for those of understanding.

The Glorious Qur'ān, *Ale-'Imrān (Family of Imran)* 3:190

To Mohammad Afzal and Ghazala, my parents who are my greatest support and greatest inspiration.
To Sidra, my wife for sacrificing all the hours I have been away.
To Qurratulein and Rumaisa, my little angels, you brought unprecedented joy in my life.
To my siblings for their tremendous encouragement.
I could not do this without all your support.

ACKNOWLEDGMENTS

First and foremost, I would like to thank the Almighty for blessing with me this opportunity. I have always found sustenance and motivation in Him even in the most difficult of times.

I would like to thank my beloved parents. I will always cherish their constant scrifice, nurturing and encouragement. No amount of gratitude is enough to encompass what they have done for me.

I would like to thank my advisor Dr. Ahmad Masoud for his unique and valuable advice and support. His guidance was invaluable in my journey in to the world of robotics. His willingness to challenge the norm was a constant source of inspiration.

I would also like to thank Dr. Salam A. Zummo, Dr. Salim Ibrir, Dr. Ashraf S. Hasan Mahmoud and Dr. Wessam Mesbah for being part of my dissertation committee. I would like to thank Dr. Abdelkader Boucherif who could not make it for my defense and Dr. Mesbah for accepting to be on my dissertation committee at such a short notice.

I would like to thank the chairman of the electrical engineering department Dr. Ali Ahmad Al-Shaikhi, for all his support.

I would also like to thank the Deanship of Graduate Studies for the stipend awarded to me during my Ph.D.

I would like to acknowledge the ICTC department at KFUPM for providing cutting edge facilities without which my research would not have been possible. The High Performance Computing provided by the ICTC matches the best in the world.

I would like to thank my wife for her patience and understanding. I would also like to acknowledge my daughters for not complaining and thoroughly enjoying whatever time I gave them.

I would like to acknowledge my colleagues who made my time at KFUPM enjoyable and whose advice and support was invaluable. I would especially like to thank Hussain Ali, Naveed Iqbal, Alamzaib, Adeel, Ali Qureshi and Asim Ghalib for the wonderful tea sessions we spent together and their kind advice.

I am also grateful to my brother Awais, for his constant encouragement. His support was indispensable during this journey.

I would also like to thank my parents-in-law for their kind advice and strong support.

Lastly, I would like to thank my dear friend and mentor Mansoor Munir Ahmad. His guidance and profound knowledge will always remain with me as a continuous source of character building.

TABLE OF CONTENTS

LIST OF TABLES

LIST OF FIGURES

NOMENCLATURE

$\mathcal{W}_a$	Admissible region of the workspace.
β	Data flow spatially assigned
σ^2	Variance of AWGN
B	Bandwidth of Communication Channel
$\mathbb{C}$	Set of complex numbers
$\mathbf{u}$	Control signal that induces motion in the agent
C	Channel Capacity
η	Channel Spectral Efficiency
$\mathcal{W}_C$	Domain of high signal strength
$\mathcal{O}_{DCZ}$	Dead communication zones
τ	Excess Time Delay: Time difference between the first and last (recobnizable) signal component.
χ	DCZ mapper
d_{pred}	Prediction band width
d_{sen}	Distance between RSS sensing antennas
ϵ_D	SNR below which communication link is lost
ϵ_G	Distance from goal point within which agent stops

ϵ_{gog}	GoG Threshold
ϵ_{gr}	Greedy DCZ update weigth
E_M	Energy consumption due to motion
ϵ_S	Radius of sphere around starting point
$\mathbf{\Upsilon}$	Functional of trajectory of an agent
$\mathbf{p}_G$	The goal position of an agent in its workspace
γ_g	Greedy MACR SNR update
$\mathcal{G}$	Sphere around goal point
δ_S	Gradient of SNR between current and previous trajectory point
$\boldsymbol{\lambda}$	local motion descriptor of agent
d_M	Total distance along trajectory
$\mathcal{I}$	The minimum invariant set
N_{sen}	Number of RSS sensing antennas
$\mathbf{\Gamma}_{\mathcal{O}}$	Boundary of all hard obstacles in Workspace
$\mathcal{O}$	Set of all points in the workspace that represent a hard obstacle or a hazardous region
$\epsilon_{OL}^{i,j}$	Update function overlap
P_M	Power consumption due to motion
$\mathbf{p}$	A point in the workspace
ϕ	Potential Field
$\mathcal{W}_\phi$	Domain in which potential filed ϕ exists

ρ	Product of gradient of PF and SNR
r_{sen}	Radius of circle of sensing antennas
γ	Represents signal to noise ratio in the workspace
$\mathcal{S}$	Sphere around starting point of trajectories
$\widehat{\gamma}$	SNR sensed at an antenna
$\mathbf{p}_S$	The starting position of an agent in its workspace
T_M	Total time taken along trajectory
$\mathcal{T}$	Set of all possible trajectories from start point to goal point for an agent
$\mathbf{p}$	The trajectory of an agent
$\mathcal{U}$	Update region
$\mathcal{U}$	SNR Update Region
θ_u	Angle of triangular update
l_u	Depth of angular update
$\mathbf{w}$	Beamforming vector
$\mathbf{\Gamma}_{\mathcal{W}}$	Boundary of workspace
$\mathbf{h}$	Wireless Communication Channel Gain
$\mathcal{W}$	Denotes workspace, the environment in which the agent exists.
$\boldsymbol{\omega}_t$	Transmit power (beamforming) vector.
$\mathbf{p}_{safe}$	Last safe point

LIST OF ABBREVIATIONS

AWGN	Additive White Gaussian Noise
BER	Bit Error Rate
bps	Bits per Second
BS	Base-Station
BVP	Boundary Value Problem
CANC	Communication Aware Navigation Control
CAT	Communication-Aware Trajectory
CBT	Communication-Blind Trajectory
CDF	Cumulative Distribution Function
CG	Conjugate Gradient
CSE	Channel Spectral Efficiency
DCZ	Dead Communication Zones
DDR	Differential Drive Robots
DFE	Data-Flow Efficiency
FDM	Finite Difference Method
FEM	Finite Element Method

FFT	Fast Fourier Transform
FIFO	First In First Out
FSR	Front Steered Robots
GHPF	Gamma-Harmonic Potential Field
GMSACR	Greedy Multiple-Sensor-Array Circular Region
GoG	Gradient of Gaussian
GPBSMR	Greedy-Prediction-Based SNR Map Reconstruction
GS	Gauss-Seidel
HO	Hard Obstacle or Hazardous Region
HPF	Harmonic Potential Field
LFC	Lyapunov Function Candidate
LHS	Left Hand Side
LoG	Laplacian of Gaussian
LoS	Line Of Signt
LS	Least Squares
LSF	Large-Scale Fading
MBCAN	Model-Based Communication-Aware Navigation
MILP	Mixed Inteer Linear Program
MMSE	Minimum Mean Square Error
MPC	Multi-Path Components
MS	Mobile Station

MSACR	Multiple-Sensor-Array Circular Region
ODE	Ordinary Differential Equation
PBSMR	Prediction-Based SNR-Map Reconstruction
PDE	Partial Differential Equation
PDF	Probability Density Function
PF	Potential Field
POI	Points of Interest
RB	Red-Black
RHS	Right Hand Side
RRT	Rapidly Exploring Random Trees
RSS	Received Signal Strength
RX	Receiver
SAR	Synthetic Aperture Radar
SBCAM	Sensor-Based Communication-Aware Navigation
SBOMR	Sensor-Based Obstacle Map Reconstruction
SBT	Sampling-Based Trajectory
SDE	Stochastic Differential Equation
SNR	Signal to Noise Ratio
SOR	Successive Over-Relaxation
SSF	Small-Scale Fading
SSG	Single Sample Greedy

TDD	Time-Division Duplex
TRX	Transceiver
TX	Transmitter
UAV	Unmanned Air Vehicles
UF	Update Function
UGV	Unmanned Ground Vehicles
USV	Unmanned Water Surface Vehicles
UUV	Unmanned Under-Water Vehicles
VVA	Virtual Velocity Attractor
WCC	Wireless Communication Channel
WCL	Wireless Communication Link
ZF	Zero-Forcing

DISSERTATION ABSTRACT

NAME: Waqas Afzal

TITLE OF STUDY: Sensor Based Communication Aware Navigation Control

MAJOR FIELD: Electrical Engineering

DATE OF DEGREE: February 6, 2018

Autonomous mission planning and execution has gained a lot of attention in recent years. Falling costs and increasing efficiency of sensors have significantly increased the interaction of agents with their environment. More data is being generated with the improvement in sensing capabilities of autonomous agents. This has created more demands on the communication capabilities of the agents. With increasingly complex missions, involving cooperation and data sharing with a command and control center or with other agents, the Wireless Communication Link (WCL) has gained more and more importance. Simplistic models of the WCL cannot be assumed in operating environments where wireless communication is difficult. The aim of this dissertation is to induce motion in agents operating in cluttered environments using techniques that integrate sensing, motion, control and communication constraints. Control signals that move the agent in a manner that enhances communication performance of the

agent based on realistic channel models that include the effects of path-loss, shadowing and multipath propagation, are studied. This is an intricate problem with multiple facets.

In this study we provide the Model-Based Communication-Aware Navigation (MBCAN) control framework, where the planner is assumed to have full Hard Obstacle or Hazardous Region (HO) and WCL knowledge. We generate mobility by integrating realistic Wireless Communication Channel (WCC) constraints with Harmonic Potential Fields (HPFs). Results show that our trajectories jointly optimize communication and energy efficiency of the agent while at the same time integrating constraints on motion due to physical obstacles. The trajectory obtained globally optimizes a joint motion and Received Signal Strength (RSS) power based functional. We provide a thorough analysis of the algorithm. Performance measures are obtained and proofs are provided for the optimality and convergence of the algorithm. Extensive simulation results for multiple scenarios are provided to verify our proposed framework. The full knowledge assumption helps to analyze the optimality properties of the framework. Later on we utlitize the properties of the MBCAN framework to generate mobility in scenarios with more realistic assumptions.

We then provide the Sensor-Based Communication-Aware Navigation (SBCAM) framework where, we assume zero Signal to Noise Ratio (SNR) and obstacle knowledge. In SBCAM, we update the WCL knowledge in the form of a SNR-map using real-time sensor data and integrate it with HPFs to generate mobility. We provide the convergence analysis. Simulation results show that updating the SNR-map locally using real-time sensor data resulted in the SBCAM matching the MBCAN for most scenarios.

We provide a local SNR-map reconstruction technique in the Single Sample Greedy (SSG) scheme, where we use a single antenna to reconstruct the SNR-map locally. The SSG scheme uses the current real-time SNR measurement along with its directional derivative to detect and reconstruct Dead Communication Zoness (DCZs). The SSG reconstruction was used with SBCAM to obtain communication-aware trajectories to goal. Convergence analysis for SSG-SBCAM is provided. Extensive simulations were done for multiple scenarios. The simulations results conformed with the theoretical expectations. Simulations results showed that goal positions inside a DCZ drastically impacted the performance of the trajectories obtained using SSG-SBCAM.

Multiple antenna SNR-map reconstruction techniques are provided in the Multiple-Sensor-Array Circular Region (MSACR) technique. We study the usage of multiple antennas to locally reconstruct the SNR-map using real-time SNR measurements. We provide analysis for the affect of the number and orientation of antennas on the SNR-map reconstruction. We also provide the conditions on the number and inter-antenna distance for convergence of MSACR-SBCAM trajectories. A greedy version of the MSACR is also provided. Simulation results for multiple scenarios are provided. Results show that large inter-antenna distance is needed for successful navigation of DCZs. It is seen that the greedy-MSACR improved performance but could lead to divergence of the SBCAM.

Finally, we provide the Prediction-Based SNR-Map Reconstruction (PBSMR) SNR-map reconstruction technique that drastically reduces the inter-antenna distance needed to reconstruct the SNR-map. Reduction in inter-antenna distance was obtained using DCZ-prediction. The prediction technique used the Laplacian of Gaussian (LoG) and Gradient of Gaussian (GoG) filters on the reconstructed SNR map to predict a DCZ in a prediction zone. Zero HO knowledge is also assumed. HO-map is reconstructed using real-time range sensor data. Simulation results showed successful navigation of DCZs with very small inter-antenna distances using PBSMR-SBCAM. The greedy version of PBSMR is provided which successfully navigated DCZs for any intern-antenna distance but could lead to the divergence of the SBCAM in some conditions.

ملخص الرسالة

الاسم: وقّاص أفضل

عنوان الدراسة: الملاحة القائمة على الاستشعار ومراقبة الإتصالات

التخصص: الهندسة الكهربائية

تاريخ الدرجة العلمية: ٦ شباط ٢٠١٨

قد اكتسبت مهمة التخطيط الذاتي والتنفيذ الكثير من الإهتمام في السنوات الأخيرة. كما أنّ انخفاض التكاليف وزيادة كفاءة أجهزة الاستشعار قد أدى إلى زيادة تفاعل الأنظمة (الروبوتات) مع بيئتها بشكل كبير. مع تحسّن قدرات الإستشعار عن بعد للأنظمة المستقلة فإنه من الممكن إنشاء المزيد من البيانات مما أدى إلى خلق المزيد من المطالب على قدرة الأنظمة للتواصل. مع تزايد المهام المعقدة والتي تشمل التعاون وتبادل البيانات مع مركز القيادة والتحكم أو مع أنظمة آخرى، اكتسبت وصلة الإتصال اللاسلكي (WCL) أهمية متزايدة. غالبا فإنه من الصعب افتراض نماذج مبسطة لـ WCL في بيئات التشغيل حيث يكون الإتصال اللاسلكي صعبًا. الهدف من هذه الرسالة هو حث الحركة في الأنظمة التي تعمل في بيئات متغيرة باستخدام تقنيات تدمج قيود الاستشعار والحركة والتحكم و الإتصال. يتم دراسة إشارات التحكم التي تحرك النظام بطريقة تحسِّن أداء الاتصال للنظام على أساس نماذج واقعية لقنوات الإتصال اللاسلكي تتضمن تأثيرات path-loss، و shadowing، و إنتشار multi-path. لذلك فإن هذه مشكلة معقدة مع جوانب متعددة.

في هذه الدراسة، نقدم إطار التحكم بالملاحة المبنية على نموذج (Model-Based Communication-Aware Navigation) أوباختصار (MBCAN)، حيث يفترض أن يكون لدى

المخطط عائق كامل أو منطقة خطرة (HO) ومعرفة WCL. نحن نقوم بتوليد الحركة من خلال دمج القيود الواقعية لقناة الاتصالات اللاسلكية (WCC) مع Harmonic Potential Fields (HPFs). HPFs تشير النتائج إلى أن مساراتنا تعمل بشكل مشترك على تحسين كفاءة الإتصالات وكفاءة استخدام الطاقة مع دمج القيود على الحركة بسبب العوائق المادية. المسار العام الذي يتم الحصول عليه يحسن الحركة المشتركة وقوة الإشارة المستقبل (RSS). نحن نقدم تحليل شامل للخوارزمية. يتم الحصول على مقاييس الأداء و توفير البراهين من أجل optimality و convergence للخوارزمية. يتم توفير نتائج المحاكاة لسيناريوهات متعددة للتحقق من عملنا المقترح. يساعد افتراض المعرفة الكاملة على تحليل خصائص optimality للإطار (framework). لاحقا، سنستخدم خصائص إطار MBCAN لتوليد الحركة في سيناريوهات مع افتراضات أكثر واقعية.

بعد ذلك، نوفر إطار التنقل والمعرفة القائم على الاستشعار (SBCAM) حيث نفترض أن نسبة الإشارة إلى الضوضاء (SNR) ومعرفة العوائق هي صفر. في SBCAM ،نقوم بتحديث المعرفة WCL في شكل خريطة-SNR باستخدام بيانات الاستشعار في الوقت الحقيقي ودمجها مع HPFs لتوليد التنقل. و يتم أيضا نقديم تحليل التقارب .(convergence) تظهر نتائج المحاكاة أن تحديث خريطة SNR محليًا باستخدام بيانات الاستشعار في الوقت الفعلي أدت إلى توافق SBCAM مع MBCAN لمعظم السيناريوهات.

يتم أيضا توفير تقنية إعادة رسم خريطة SNR محلية في مخطط Single Sample Greedy (SSG)، حيث نستخدم هوائيًا واحدًا لإعادة بناء الخريطة SNR محليًا. يستخدم مخطط SSG قياس SNR الحالي في الوقت الحقيقي إلى جانب مشتقه الاتجاهي لاكتشاف وإعادة بناء مناطق الاتصالات الميتة .(DCZs) تم استخدام SSG مع SBCAM للحصول على مسارات للهدف بحيث تضمن جودة الاتصال. يتم أيضا تحليل التقارب لـ .SSG-SBCAM تم إجراء محاكاة شاملة لسيناريوهات متعددة. نتائج المحاكاة تتوافق مع التوقعات النظرية. وأظهرت نتائج المحاكاة أن مواقع الأهداف داخل DCZ أثرت بشكل كبير على أداء المسارات التي تم الحصول عليها باستخدام SSG-SBCAM.

يتم توفير تقنيات إعادة رسم خريطة SNR متعددة الهوائي في تقنية المنطقة الدائرية متعددة

المستشعرات .(MSACR) ندرس استخدام هوائيات متعددة لإعادة بناء خريطة SNR محليًا باستخدام قياسات SNR في الوقت الفعلي. نحن نقدم تحليل لتأثير عدد وتوجيه الهوائيات على إعادة تكوين خريطة SNR. كما نقدم الشروط المتعلقة بالمسافة بين الهوائيات و أعدادها لتقارب مسارات -MSACR SBCAM يتم توفير نسخة greedy من MSACR أيضا. يتم توفير نتائج المحاكاة لعدة سيناريوهات. تُظهر النتائج أن هناك حاجة إلى مسافة كبيرة بين الهوائيات للتنقل بنجاح في مناطق DCZ. من الواضح أن استخدامgreedy-MSACR قد أدى إلى تحسن الأداء، ولكنه قد يؤدي إلى عدم استقرار SBCAM.

وأخيرًا ، فإننا نوفر تقنية (Prediction-Based SNR-Map Reconstruction (PBSMR التي تقلل المسافة اللازمة بين الهوائيات لإعادة بناء خريطة SNR. تم تقليل المسافة بين الهوائيات باستخدام التنبؤ ب DCZ. استخدمت تقنية التنبؤ مرشحات (Laplacian of Gaussian (LoG) (filter و (Gradient of Gaussian (GoG) (filter على خريطة SNR المعاد تكوينها للتنبؤ بمنطقة DCZ في منطقة التنبؤ. ويفترض أيضا عدم معرفة HO. تمت إعادة إنشاء HO-map باستخدام بيانات أجهزة الاستشعار في الوقت الفعلي. أظهرت نتائج المحاكاة نجاح الملاحة في مناطق DCZs مع مسافات بينية صغيرة جدًا للهوائيات باستخدام PBSMR-SBCAM. يتم توفير greedy-PBSMR الذي نجح في التنقل في مناطق DCZ باستخدام أي مسافة بين الهوائيات ولكنه قد يؤدي إلى عدم استقرار SBCAM في بعض الظروف.

CHAPTER 1

INTRODUCTION

> *"Even while they teach, men learn."*
>
> —Seneca the Younger.

Autonomous agents performing a multitude of tasks, in a variety of missions, while sharing information over wireless links with the central control station or cooperating with fellow agents to accomplish common goals have occupied the imagination of researchers for a long time. Recent advances in wireless communication, artificial intelligence, control and computation have opened new horizons in autonomous mission planning and execution research. A lot of interest is being generated in the use of autonomous agent(s) in areas like search and rescue, reconnaissance, surveillance, exploration (oil, minerals, land-mines) and combat. The major application is for the agents to extend the informational access of human responders, especially, in hazardous areas or regions which become inaccessible to humans (like collapsed buildings). The agents have to relay real-time data to help assess the situation at hand and effectively strategize their activities to counter the situation.

The 2005 World Disasters report [4] suggests that over 900,000 people died in urban disasters from 1999 to 2004, costing around $ 738 billion estimated damage. [5] claims that of the survivors of urban disasters, 80% are surface victims, while only 20% of the victims are from within the rubble. Moreover, the majority of the victims are located in the interior of the rubble and more critically, the mortality rate of the victims increases and peaks after 48 hrs. Thus researchers are looking at techniques to help responders explore the interiors of devastated sites. Since time is of critical importance, removing the rubble to gain access to the interior on such a large scale would require the personnel to target only those points where access to trapped victims would be enhanced. Thus researchers are looking to the use of context-sensitive, intelligent, goal-oriented agents to access the affected area and relay the data in real-time to the operator. This frees the operator from having to deal with the variables the space contains and focus on the high level aspects of the mission. This is one of the major motivation for the use of autonomous agents to help coordinate, assimilate and execute a mission plan. The agents are expected to face a variety of scenarios based on the environment and the nature of task they are assigned with. The complexity of the tasks increases with the complexity of the environment as the agent can expect to tackle a lot of unknown factors. Some of the environments the agent expect to face are:

- Natural disasters like earthquakes, tsunamis, hurricanes and typhoons, volcanoes, avalanches, landslides and floods. The affected area is very large and its architecture varies from tall mountains to deserts, the communication infrastructure is damaged. The terrain can consist of rubble, mud, fire, leaked toxic material (like the Fukushima Nuclear disaster), poisonous gases (Mine disasters), unstable rubble. The agent will be expected to traverse highly cluttered environments like rubble, which have irregular (unstructured)geometry. The terrain the agents will traverse may be unknown to the agents and might change due to the unstable nature of the structures, especially the interiors.

- Man-made disasters like vehicle crashes or hostile activity: the general communication infrastructure is intact. The map of the environment might be known as in the case of hostage situations where the map of the building is known and the agent can be used for surveillance purposes. Generally the area of consideration is small but it can be enormous in special cases like the MH370 airline disaster in March 2014.

- Reconnaissance: Exploring and mapping, for example, exploring land-mine infested areas and detecting the location of mines. The agent will have to explore a large terrain with a known map while mapping the location of mines and avoid setting them off. The environment can be unknown well in the case of scouting an enemy area to gather information. The agent will have to traverse an unknown terrain and needs to find an effective route in order to gather strategic information and relay it to the command and control center.

- Combat: Where an agent or a group of agents is mobilised in enemy territory and has to carry out a mission and return to the command and control center. This requires the agents to move in unknown hostile and environments. The agents will have to be agile and make decisions autonomously on the next course of action.

Mission planners responding to the above discussed scenarios would require the agent to perform a multitude of tasks that include, but are not limited to, the following [6],

- Search in interior of devastated structures, in caves or tunnels or wilderness without increasing risk to victims or rescuers.
- Reconnaissance and mapping: to create a reference of the destroyed environment of the large area of interest in an expeditiously at an appropriate resolution.
- Communication: Act as mobile beacon or repeater to extend wireless communication ranges, help localize personnel based on radio signal transmission and serve as landmarks for rescuers to localize themselves.
- Logistics: Automated logistic support from storage.
- Structural Inspection: Inspection of damaged interior or exterior structure to help assess the stability of the structure so as to present secondary collapses or decide whether it is safe to enter a structure.
- In situ medical assessment: Especially if the agent can use sensors to send medical conditions of trapped victims so that a proper medical diagnosis can be expedited.
- Rubble removal or using agents to drill or excavate new paths which the responders can use to reach the interiors of the affected areas.

The use of autonomous agents to accomplish their assigned tasks in an environment of complex and varying nature while satisfying multiple constraints is a multidisciplinary research problem. At the heart of successful completion of the above mentioned tasks lies an intelligent and communication constrained (communication-aware) navigation controller. To obtain a navigation system that satisfies multiple constraints in an integrated manner presents a clearly challenging research problem with many open areas. The multidisciplinary aspects that need to be integrated in the above mentioned scenarios are discussed as below [6],

1. **Mobility**: The challenge of mobility in a known, partially-known or unknown, potentially hazardous, environments is of fundamental importance to a navigator and provides the basis for a successful mission. Mobility is a multifaceted intersection of the ability of the agent to acquire information, reason and decide on the actions based on the information and realize the actuation needed for the desired action, at the same time.

   The agent might have a complete map of the environment like surveillance and monitoring in offices, public places, strategic facilities. The environment can be partially known in scenarios like fire emergencies, where the physical map of the area is available but it might be varying due to the devastation. Applications, like reconnaissance, require the agent to navigate in totally unknown environments where the agent is only aware of its immediate locality based on its sensor data. The regions within the environment, the agent needs to avoid, can be modelled as 'hard' or 'soft' obstacles. Hard obstacles are regions which will cause physical damage to the agent and lead to immediate termination of the mission. Soft obstacles, on the other hand, are undesired regions because of the soft components of the environment (like regions of low signal strength or zone of eminent detection by enemy).

Navigation is especially challenging for Unmanned Ground Vehicles (UGV). UGVs can face environments with an unpredictable combination of vertical and horizontal debris elements with unknown surface characteristics and obstacles. Moreover, the suitability of the surface for motion can vary for UGVs of different characteristics (mobility of car like agents would be difficult in loose sand). For disaster struck areas there is no characterization of rubble on which a navigation algorithm of an agent can be based (to the extent of the authors knowledge).

Unmanned Air Vehicles (UAV) need to take in to account for wind conditions near or in structures and avoid obstacles like power lines, trees and overhanging debris. Unmanned Water Surface Vehicles (USV) and Unmanned Under-Water Vehicles (UUV) face swift currents and floating or submerged debris.

Finally, a critical property of mobility is the time required to complete the mobility task. When navigating in an unknown environment, it is desired that the agent doesn't choose any time-wasting manoeuvres, rather it moves in a 'goal oriented' manner, that is, it reaches the goal without wandering in the environment (say, for exploring the environment).

2. **Communications**: For the success of missions relying on autonomous agent deployed in previously mentioned scenarios, the effectiveness of the mission relies

heavily on the real-time data being relayed back by the agent. Also, there might be other agents in the same environment and sensory data is expected to be shared with those agents in real-time so that they can update their environment knowledge-base. Apart from data transmission, the agent might be cooperating in real time with other agents in the same environment in performing the assigned task. Multiple networked agents are required to cooperate and coordinate among themselves to efficiently and expeditiously complete an assigned task like target tracking, environment mapping and so on.

The agent will be connected to the central Base-Station (BS) and other agents via a wireless communication link and sharing data like real-time video, which puts high demands on the bandwidth of the communication link and low tolerance on communication latency. The unstructured nature of the environment, especially in interiors induces a variety of phenomena on the wireless signal propagation leading to its degradation. This degradation depends on the physical position of the agent as well as on time, as the environment through which the signal is propagating might be varying with time. Thus the movement of the agent has to take in to account this degradation of the wireless communication channel in order to efficiently accomplish the assigned task. Essentially, mobility and Wireless Communication Channel (WCC) performance are dependent on one another for accomplishment of the mission (Fig. 1.1).The wireless link performance is dependent on the position of the agent relative to the BS and the mission related data (and some times mobility commands) sent and received

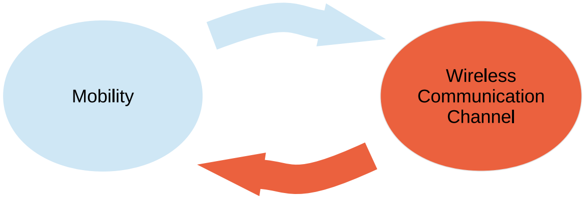

Figure 1.1: Movement as a function of Wireless Communication Channel (WCC) strength closes the loop between mobility and control

by the agent on the other hand depend on the Wireless Communication Link (WCL) quality. Thus, inducing mobility in the agent such that its motion becomes a function of the Wireless Communication Link (WCL) quality closes the loop to the mobility itself being generated due to the data obtained over the WCC.

3. **Control**: Autonomous agents obtain guidance signals based on their environment knowledge. Guidance signals are basically the behavior desired of the agent. The guidance signals are independent of the type of agent. Controllers convert the guidance signal to equivalent actuation signals and thus are a vital component of mobility. Successful control would induce behavior in the agent that closely conforms the desired reference behavior.

4. **Power**: Typically, the agents will be battery powered. Therefore it is highly desired that it performs all its navigation tasks in a energy efficient manner. The amount of energy the agent consumes, depends, among other things, on the trajectory it chooses. The smoother the trajectory, the less energy, the agent will consume. Secondly, the length of the path the agent chooses based on its environment information. The path length should be optimal (or close to

optimal) as useless lengthening of the path like wandering around for mapping purposes (say just to gather complete information of the environment) would not only waste energy but also waste time. Lastly, power consumption also depends on the wireless communication link performance. If the Wireless Communication Channel (WCC) faces severe degradation, depending on the type of degradation will be discussed in section 1.3, the agent might have to transmit at higher power to realize the desired data-rate, thus depleting the battery faster. The WCC on the other hand is again dependent on the position of the agent. Therefore, the agent has to navigate in an energy-efficient manner so as to effectively utilize the limited energy reserve provided by the battery.

The multifaceted dimensions of the problem introduced above have been investigated in a modularized manner. Recently, researchers have started looking into wholistic solutions that jointly integrate mobility, communication, control and energy constraints. Traditionally, researchers have looked at path-planning to solve navigation problems [7]. Path-planning techniques generate trajectories for the agent to navigate towards a goal while satisfying different constraints. These trajectories are a series of guidance signals, which the agent can use to navigate towards the goal. Path-planner allow integration of different constraints on the trajectories generated to guide an agent.

From [8], motion planning problem can be described as in Fig. 1.2. A higher level mission controller assigns a task to the agent. The agent equipped with a motion planner, uses its environment knowledge, to obtain a path to the goal in order to accomplish its task.

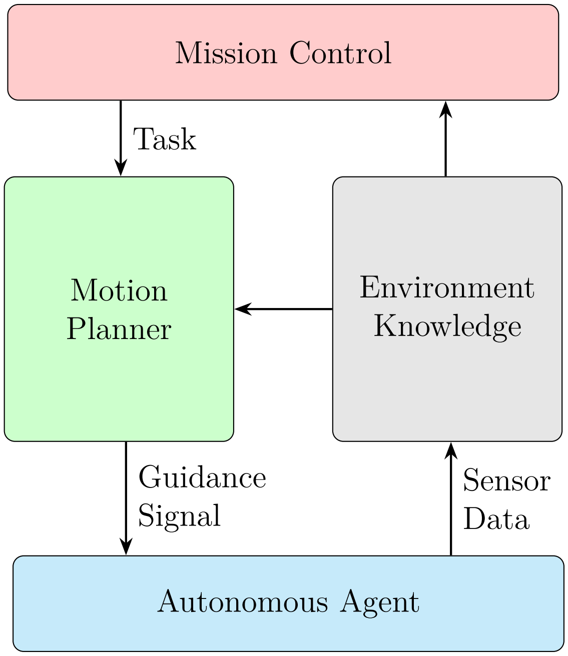

Figure 1.2: motion planning problem consists of a higher level mission controller that specifies the tasks to be achieved by the agent. The agent uses a motion planner to obtain a path to the goal using the environment information available. The environment information can be updated using sensors on the agent.

In Fig. 1.2, the motion-planner block integrates the environment information to obtain guidance signals for the agent. In this study the aim is to obtain path-planners that can integrate communication constraints along with other mission constraints while generating a realizable guidance signal that can be converted to a navigation control signal. Planners that can avoid hard obstacles have been obtained in literature but planners that maintain communication link are an open problem. In this work, the major aim is to obtain a path-planner that can use the received signal strength knowledge of the environment to obtain trajectories that are goal oriented (reach the goal, if a path to goal exists, without wandering in the first attempt) avoid obstacles, are energy efficient and can be converted to control signals for a variety of agents.

1.1 Motivation

The basic requirements for realizing a navigation controller that will operate in the aforementioned scenario can be summarized as

- Develop a plan that provides trajectories which avoids obstacles and reaches the goal.
- Trajectories to the goal are available even if the agent is bumped off path by an external force.
- The trajectories satisfy communication constraints
- The trajectories satisfy energy constraints
- The trajectories are easily converted to a control signal for agents with different dynamics.
- The navigation system is able to update its past environment knowledge with real-time data from sensors and thus be able to update its trajectory in real-time.

A diverse class of agents (UGV, UAV, USV or UUV and further variations within these categories) are expected to be employed across a range of operating conditions. Therefore, a major motivation of this thesis is to explore generic approaches that integrate sensing, communication, control and energy as part of a wholistic framework (rather than a collection of subsystems). These approaches have been studied separately for specific or highly simplified agents but not as a generic approach that assimilates the multidisciplinary aspects for a variety of agents.

The idea is to free up the command centre from the low level aspects of the agents' operation and thus effectively concentrate on high level strategy planning. This would require the agents to be able to communicate with the command centre, locally sense its environment and intelligently compute its next motion step so as to accomplish the tactical task assigned to it by the command centre as part of a global strategy.

This requires the agent to locally synthesize sensor information and use sophisticated path planning techniques to decide on its next course of action. Generally, in the available literature, researchers try to solve these problems as a graph search problem [7]. This has significant drawbacks as far as converting the obtained solution to a realizable control signal. Masoud in [9] introduced Gamma-Harmonic Potential Field (GHPF) approach to planning which could integrate real-time sensor data and generated trajectories that had favorable realizability (control) properties.

In this dissertation, we will look at integrating wireless communication constraints along with sensing constraints on agents using GHPF. The aim is to exploit favorable control properties of Harmonic Potential Field (HPF)s while at the same time integrating communication constraints in Potential Field (PF) based path plans.

In the following sections, we briefly provide a background in path-planning and the behavior of wireless communication links.

1.2 Path Planning: An Overview

Path planning can be simply defined as the generation of a feasible trajectory in an environment from a starting point to a goal such that by traversing that trajectory, the agent can avoid any obstacles or hazardous regions. More generally, path planning consists of temporal, geometrical and physical constraints that have to be satisfied during the motion of the agent, i.e., to obtain a sequence of commands (plan) such that collisions (and hazardous regions) are avoided in a known, partly known or completely unknown environment that might have dynamic (time-varying environment) or static (time-invariant environment) obstacles or having obstacles that can be moved by the agent itself. The obstacles can be of any arbitrary geometry. The agent itself can have complex geometry along with dynamics of its own [8]. In addition, motion of the agent can be constrained by differential or kinodynamic (velocity, acceleration, smoothness of the path) and integral constraints (minimum time, minimum energy, minimum fuel, shortest path).

Desirable properties of planners include a plan field that covers the complete environment so that if the agent is bumped off course, it can still navigate towards its goal (i.e., a goal seeking action instead of a trajectory tracking action). Also, the plan should make sure that while navigating around obstacles, the agent should have sufficient distance to the obstacle so that any accidental contact with the obstacles is minimized.

1.2.1 Desired Characteristics of a Motion Planner

The characteristics desired of a motion planner [8], [10], [11] are as follows:

1. **Completeness**: The property of a motion planner that it guarantees a path to the goal if there exists one is known as completeness and the path planner is

said to be complete.

2. **Optimality** Optimality of a planner is defined based on a cost or heuristic (energy, time, distance travelled etc).

3. **Computational Complexity** Computational complexity of a path planner can be divided in to two types

    - **Memory**: Typically with increase in discretization, the memory required by volumetric methods increases exponentially. On the other hand, output sensitive methods maintain a level of complexity that is commensurate with the complexity of the environment's contents.

    - **Time**: Time complexity is based on the worst case computation time of a path planner algorithm. Usually time complexity is represented using the big O notation. The big O notation gives the highest expression based on the number of input n out of the polynomial $T(n)$ which represents the upper bound on the time complexity. e.g. if $T(n) = n^3 + n + 2$, then the big O notation is $O(n^3)$. Lower bounds on time complexity can also be found [7] but are generally difficult to compute.

4. **Robustness Against a Dynamic Environment** Path planners are required to be resilient in environment where obstacles or the environment in general can change with time. A robust planner will still maintain its properties of completeness, optimality while at the same time its time complexity will not degrade. Acquiring total robustness is highly challenging but nevertheless, a certain de-

gree of robustness is desirable for any planner in uncertain environments.

1.2.2 Representation and Path-Planning

To successfully navigate towards a goal in an environment, typically, agents generate path plans based on their knowledge of the environment. The environment knowledge has to be 'represented' such that the motion planner can use it to obtain a trajectory to the goal. In [8], [10], [11] and [7], the agent obtains the representation of the environment by using its sensors to sense the environment and map the obstacles and hazardous regions.

There are two domains of representation for the environment within which the agent exists, the workspace $\mathcal{W}$ and the configuration space $\mathcal{C}$.

Workspace is the physical space in which the agent exists. It can be represented as a d-dimensional Euclidean space where, $d = 2$ or $d = 3$ and the workspace is represented as $\mathcal{W} \in \mathrm{R}^d$ and the path planning problem in the workspace is defined as follows;

Let $\mathcal{WO}_i, \quad i = 1, 2, \cdots, n_o$ represents n_o obstacles or hazardous regions in the workspace, then $\mathcal{WO} = \bigcup_{i=1}^{n_o} \mathcal{WO}_i$, is known as the obstacle region. The $\mathcal{W}_{free} = \mathcal{W} - \mathcal{WO}$ is the free space where the agent will not collide with the obstacles then the path planning problem is to find a curve starting from the starting position (x_s, y_s) to the goal position (x_g, y_g). Where, (x, y) represents the position of the agent in the two dimensional Euclidean workspace. Workspaces are mission-centered. In other words, the variables used as coordinates of space are those needed to define the mission of the agent.

Configuration space is the space consisting of all possible configurations q of an agent [7]. Configuration spaces are mobility-centered. In other words, the coordinates of the space are the variables through which energy may be injected into the agent in order to actuate motion. The dimension of the configuration space is known as the degree of freedom of the agent. Although the workspace is usually two or three dimensional, the configuration space can have much higher dimensions than the workspace. Planning in a n-dimensional configuration space, $\mathcal{C} \in \mathrm{R}^n$ with $q_s \in \mathrm{R}^n$ being the initial configuration of the agent and $q_g \in \mathrm{R}^n$ being the goal configuration of the agent can be defined by such that if, $\mathcal{CO}_i, \quad i = 1, \cdot, n_o$ represents n_o obstacles or hazardous regions in the configuration space, then $\mathcal{CO} = \bigcup_{i=1}^{n_o} \mathcal{CO}_i$, is known as the configuration obstacle space and the $\mathcal{C}_{free} = \mathcal{C} - \mathcal{CO}$ is the free configuration space consisting of all the configurations of agent where the agent will not collide with the obstacles then the path planning problem is to find a curve starting from the starting configuration q_s to the goal configuration q_g.

Khatib [12], first proposed a real-time obstacle avoidance method using potential fields (PF), thus opening the doors to using path-planners in real time. PFs don't need global knowledge of the environment to reach the goal and use local search (gradient based) on a PF representation of the environment to reach its goal. Since PFs use local search they do not guarantee global optimality. Path-planning using PFs can be summarized as follows:

1. *Attractive and Repulsive Potential*: PFs represent the robot as a point in a potential field with the goal configuration as an attractive and the obstacles as

repulsive potentials, thus the PF measured at a configuration q is given by

$$V(q) = V_{att}(q) + V_{rep}(q) \tag{1.1}$$

where V_{att} is the attractive potential towards the goal and V_{rep} is the repulsive potential from an obstacle. When the agent moves in the potential field, it computes its next direction iteratively after each step based on the potential field at its current configuration. The force induced at its current configuration due to the potential field is taken by the agent as the best direction for the next step and it is given by

$$\begin{aligned} \vec{F}(q) &= -\vec{\nabla}V(q) && (1.2) \\ &= \vec{F}_{att} + \vec{F}_{rep} && (1.3) \\ &= -\vec{\nabla}V_{att}(q) - \vec{\nabla}V_{rep}(q) && (1.4) \end{aligned}$$

Fig. 1.3 demonstrates the PF method with two circular obstacles.

2. *Local Minima*: From Eq. (1.2) we obtain the force field used to guide the agent but since it follows the gradient of the potential field, the agent can get stuck in local minima, i.e., points q^* in the potential field, which are not the goal, where $-\nabla U(q^*) = 0$ and second order derivative known as the Hessian is positive

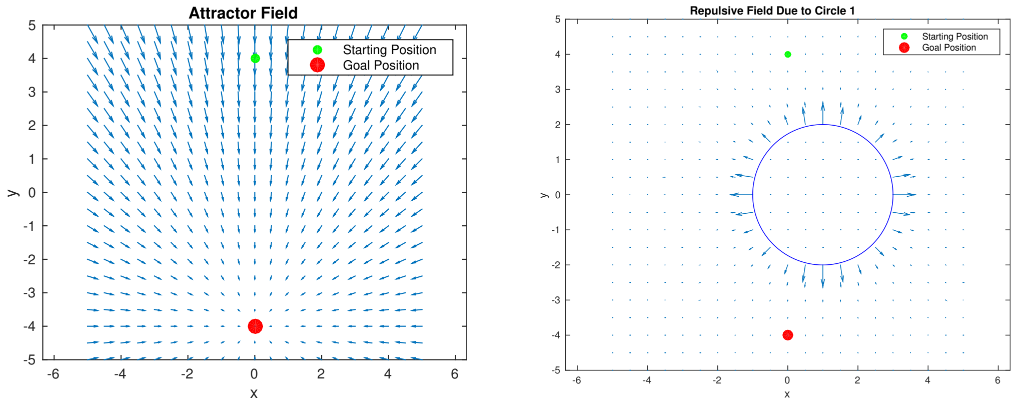

(a) Attractive potential field in a rectangular environment.

(b) Repulsive field 1

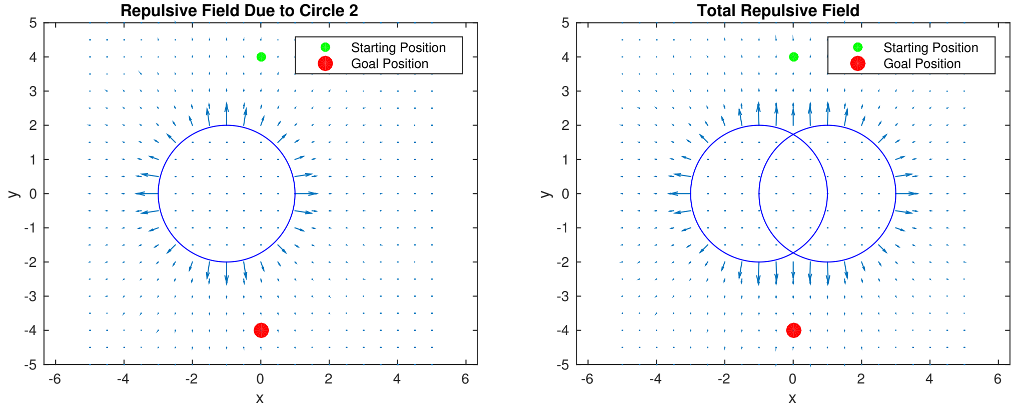

(c) Repulsive field 2

(d) Total repulsive field due to the two obstacles

Figure 1.3: Attractive and Repulsive Potential Field.

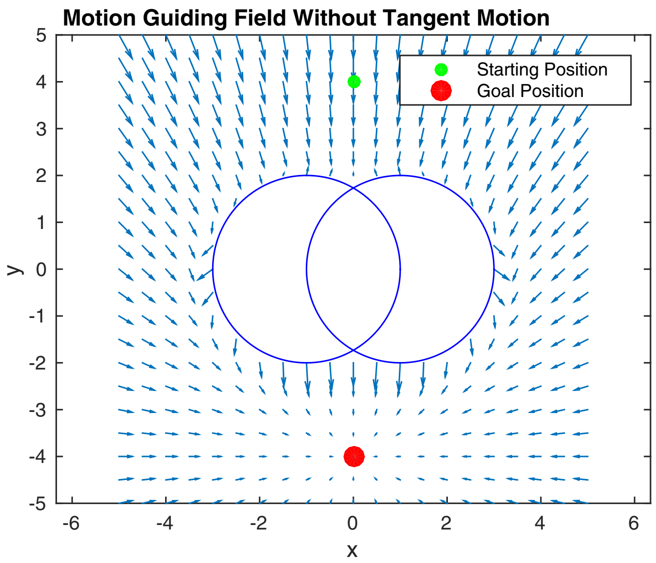

Figure 1.4: Total potential due to both the attractive and repulsive fields.

definite. The Hessian is given by

$$H(V(q^*)) = \begin{bmatrix} \frac{\partial^2 V(q^*)}{\partial q_1^2} & \cdots & \frac{\partial^2 V(q^*)}{\partial q_1 \partial q_n} \\ \vdots & \ddots & \vdots \\ \frac{\partial^2 V(q^*)}{\partial q_n \partial q_1} & \cdots & \frac{\partial^2 V(q^*)}{\partial q_n^2} \end{bmatrix}$$

Where q^* is also known as the critical point. It should be noted that a negative definite or indefinite Hessian means that the critical point is a maximum or saddle point respectively and is unstable in that if a perturbation occurs, the agent will move away from that point where as all the minima are stable.

1.2.3 Harmonic Potential Field Based Planners

Connolly [13], [14] and Sato [15] introduced the HPF based construction of potential fields and employed the HPFs in path-planning problems. Harmonic functions are obtained by solving partial differential equations which include the Laplacian [16].

$$\nabla^2 V = \sum_{i=1}^{n} \frac{\partial^2 V}{\partial q_i^2} = 0 \tag{1.5}$$

HPFs are free of local minima and hence, can be used to construct potential fields free of local minima. In fact, HPFs have only one minimum which is at the goal boundary condition. Moreover trajectories obtained from HPFs are smooth (C^∞, infinitely differentiable) which is a highly desirable property to reduce energy consumption and ensure the existence of a control sequence that can realize the path. Also, the HPF obtained covers the complete environment, therefore, it provides a plan for the complete environment so that if the agent is bumped off its original trajectory by an unexpected external force, it can still navigate towards the goal. Also planners based on HPF are goal-oriented planners, in that, they provide trajectories that do not 'wander', i.e., always moves towards the goal in a manner that is sensitive to the context in which the agent is operating. In other words, the agent's trajectories do not visit regions in the workspace for data gathering purposes only.

A number of fields like electromagnetism, fluid dynamics and heat transfer already use Partial Differential Equations (PDEs) with Laplacian terms (Laplace's Equation, Poisson's Equation, the conduction heat flow equation, Navier-Stoke's equation approximations, etc.). Harmonic functions are obtained from these PDE's by forcing boundary conditions on the boundary of the configuration space. If proper boundary conditions are used at the boundary, then the regular gradient of the Harmonic function obtained will be able to guide the agent from anywhere in $\mathcal{C}_{free}$ to the goal configuration. Typical types of boundary conditions used for navigation are the homogeneous Neumann and Dirichlet boundary conditions. The homogeneous Neumann boundary condition produces velocity vectors tangent to the boundary of the obstacles. This can lead to the agent grazing the obstacles. Dirichlet boundary conditions on the other hand, push the trajectories away from the obstacles.

In [17], Masoud introduced a setting for the HPF, in which soft obstacles (obstacles that are not physical and described using soft values representing the attribute (danger/fitness) level) can be integrated into the path-planner along with physical obstacles. It is given as,

$$
\begin{aligned}
&\text{solve} && \nabla(\sigma(\mathbf{p})\nabla V(\mathbf{p})) = 0,\ \mathbf{p} \in \mathcal{W} && \text{(1.6a)}\\
&\text{subject to} && V(\mathbf{p}_S) = 1,\ V(\mathbf{p}_G) = 0,\ \frac{\partial V}{\partial \mathbf{n}} = 0,\ \text{at } \mathbf{p} \in \Gamma && \text{(1.6b)}\\
& && \frac{\partial V}{\partial \mathbf{n}} = 0,\ \text{at } \mathbf{p} \in \Gamma_O,\ \text{Neumann Boundary} && \text{(1.6c)}\\
& && \text{OR} && \\
& && V(\mathbf{p}) = 1,\ \text{at } \mathbf{p} \in \Gamma_O,\ \text{Dirichlet Boundary} && \text{(1.6d)}
\end{aligned}
$$

where, $\mathcal{W} \in \mathbb{R}^n$, is a n-dimensional workspace with Γ representing the boundary of the workspace, $\mathbf{p} = (x_1, x_2, \cdots, x_n) \in \mathcal{W}$. is a point in the workspace. $\sigma(\mathbf{p}) \in \mathbb{R}_0^+$ is the soft descriptor at a given point in the workspace which represents the suitability of a point to support motion. $\mathbf{p}_G = (x_{G_1}, x_{G_2}, \cdots, x_{G_n}) \in \mathcal{W}$ is the target or goal point in the workspace and $\mathbf{p}_S = (x_{S_1}, x_{S_2}, \cdots, x_{S_n}) \in \mathcal{W}$ is the starting point of the agent in the workspace. The setting can have either Neumann or Dirichlet boundary setting at the boundary of the physical obstacles. Γ_O represents the boundary of the obstacles in the workspace. Letting $\mathcal{O} \subseteq \mathcal{W}$, represent the forbidden regions (physical obstacles) in the workspace and $P(t) \in \mathcal{W}$ be the trajectory to the goal $\mathbf{p}_G$ from the current position $\mathbf{p}_S$. The trajectory can be obtained using the potential field found by solving Eq. (1.6) using the following gradient dynamical system.

$$\dot{\mathbf{p}} = -\nabla V(\mathbf{p}),\ \mathbf{p}(0) = \mathbf{p}_S \tag{1.7}$$

The trajectory obtained using Eq. (1.7) has the following properties

$$\lim_{t\to\infty} \mathbf{p}(t) \to \mathbf{p}_G \tag{1.8a}$$

$$\mathbf{p}(t) \in \mathcal{W},\ \forall\ t \tag{1.8b}$$

$$\mathbf{p}(t) \notin \mathcal{O},\ \forall\ t \tag{1.8c}$$

$$\mathbf{p}(t) \notin \mathcal{O}_{\mathcal{S}} = \left\{\mathbf{p}|\sigma(\mathbf{p}) \equiv 0\right\},\ \forall\ t. \tag{1.8d}$$

Where $\mathcal{O}_{\mathcal{S}} \in \mathcal{W}$ is the soft obstacle region, i.e., the region in which the soft descriptor in Eq. (1.6) is nearly equal to zero ($\sigma(\mathbf{p} \equiv 0)$). Fig. 1.5 shows an example environment along with the Harmonic potential field, path plan and trajectory for an agent within that environment.

1.2.4 Guidance and Control

Typically, trajectories obtained using path-planners need to be converted to an appropriate control signal, $\mathbf{u}(t)$, for the agent under consideration. A multitude of agents with different structures, dynamics and control dimensions might be used to realize the trajectory obtained by the planner. Developing a generic controller, therefore, is very difficult to achieve. Moreover, the trajectory obtained using a path-planner might not be realizable (control cannot be generated), like, requiring car like agents to move sideways. Typically, designers obtain path plans using simplified models for their agents and try to translate the obtained guidance signal to a corresponding control signal. A common method is to develop a pool of discretized control signals for each agent and choose the control signal 'closest' to achieve the desired motion.

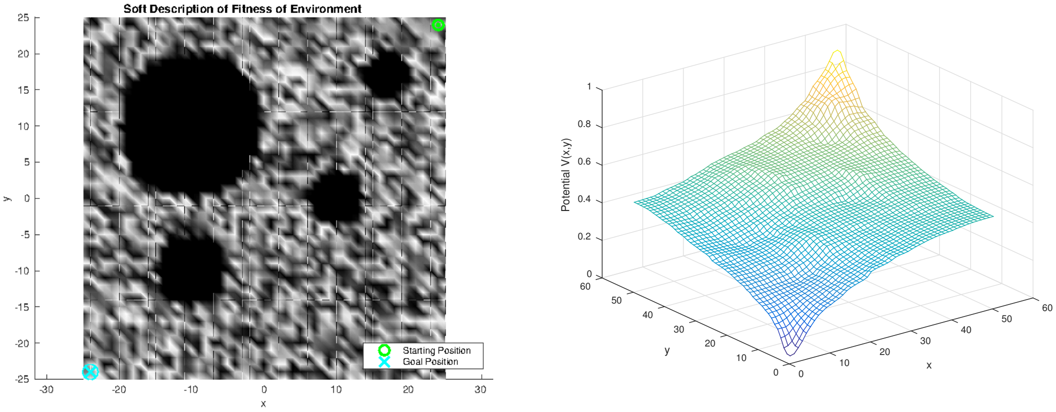

(b) HPF for the environment

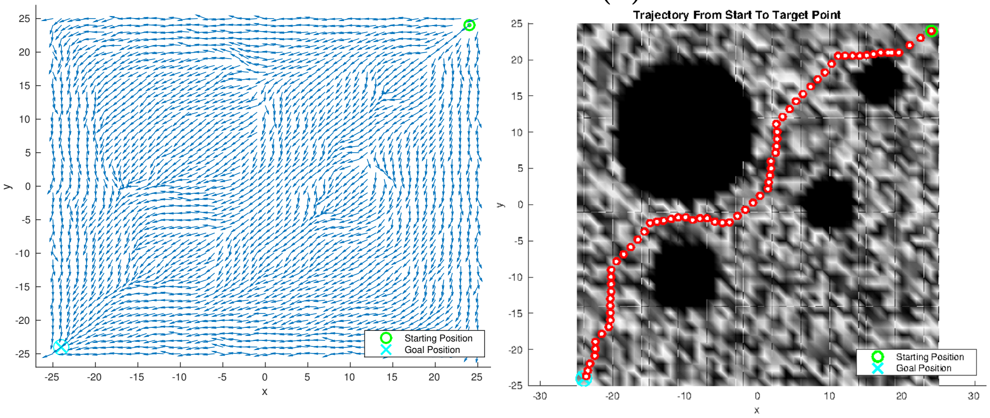

(c) Path Plan **(d)** Trajectory to goal

Figure 1.5: Path planning using Harmonic Potential Fields

Another commonly used technique is to 'condition' the reference trajectory to suit the agent like smoothing techniques to smooth the reference trajectories obtained using graph searches [8], [10], [11], [18], [19], [7].

A fundamental drawback with the above mentioned techniques is that they can lead to the realized trajectory violating constraints that were imposed on the reference trajectory by the planner. Therefore, additional separate agent-specific constraints have to be integrated in the planner to obtain trajectories that can be realized by the controller providing the actuating signal. This, would require different path-planners for different agents. Therefore a planner that can provide reference trajectories which can be realized by a sufficiently broad class of agents is highly desired.

The reference trajectory obtained using the gradient dynamical system Eq. (1.7) based on the HPFs are known to produce trajectories that are C^{∞} (infinitely differentiable) smooth. Campion [20] showed that if a trajectory is at least C^2, it guarantees realizability for a wide variety of mobile agents. Masoud [21], in 2009, introduced a two-stage model that can be used to realize the trajectories obtained using HPFs. A significant variety of agents, including UAVs, UGVs, UUVs and spherical robots [22], [23] can be modelled using the two-stage model. The two-stage model is given by

$$\begin{aligned} \dot{\mathbf{p}} &= G(\boldsymbol{\lambda}) \\ \dot{\boldsymbol{\lambda}} &= F(\boldsymbol{\lambda}, \mathbf{u}) \end{aligned} \tag{1.9}$$

where $\mathbf{p}_a(t)$ is the position of the agent in the world coordinates, $\boldsymbol{\lambda}(t)$ is the corresponding local motion descriptor and $\mathbf{u}(t)$ is the control signal that realizes the

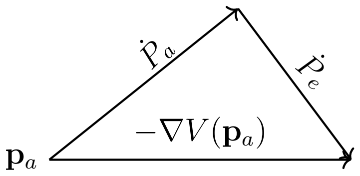

Figure 1.6: Virtual Velocity Attractor Paradigm

trajectory based on the reference trajectory obtained using HPF.

As in Eq. (1.7), by following the gradient of the HPF at each point, a reference velocity instruction can be attained which guides the motion of the agent to accomplish the mission. A massless, single integrator, holonomic system, follows this process in a provably correct manner. Moreover, [24] introduced the Virtual Velocity Attractor (VVA) approach to formulating control instructions which allow nonholonomic, highly nonlinear, higher order systems to realize the HPF trajectories as well in a provably correct manner. The VVA approach works by driving the velocity $\dot{\mathbf{p}}_a$ of the agent at its current position $\mathbf{p}_a(t)$ to coincide with the reference velocity, $-\nabla V(\mathbf{p}_a(t))$, obtained using HPF Eq. (1.7) by constructing an artificial force $\mathbf{F}_p$ proportional to the difference between the reference and the agent velocity (Fig. 1.6), so that both $-\nabla V(\mathbf{p}_a(t))$ and $\dot{\mathbf{p}}_a$ are aligned. $\mathbf{F}_p$ can be obtained by

$$\mathbf{F}_P = \mathbf{K}_P \cdot (-\nabla V(\mathbf{p}_a(t)) - \dot{\mathbf{p}}_a) \tag{1.10}$$

Where $\mathbf{K}_P$ is a positive constant. From Eq. (1.9) the local motion effects the the agents velocity in world coordinates, and the corresponding artificial attractor force

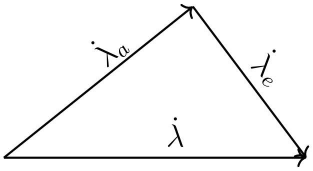

Figure 1.7: Virtual Velocity Attractor Local Coordinates

in the local coordinates $\mathbf{F}_\lambda$ is given by

$$\mathbf{F}_\lambda = \mathbf{J}_\lambda^T \mathbf{F}_p, \ \mathbf{J}_\lambda = \frac{\partial G(\lambda)}{\partial \lambda} \tag{1.11}$$

The fictitious force $\mathbf{F}_\lambda$ then gives the reference velocity, λ_r, in the local coordinates of the system. The reference velocity in the local coordinates can then be used to obtain an artificial attractive force to attract the local velocity to the reference velocity based on their difference (Fig. 1.7) as follows

$$\mathbf{F}_u = \mathbf{K}_u \cdot (\dot{\lambda} - \dot{\lambda}_a) \tag{1.12}$$

Where $\mathbf{K}_u$ is a positive constant. The artificial force in the local coordinates need to be converted to their equivalent variables in the control coordinates. The control coordinate force, $\mathbf{F}_u$, effects the change in the control signal, given by:

$$\dot{\mathbf{u}} = \mathbf{K}_u \cdot \mathbf{J}_u^T \cdot (\dot{\lambda} - \dot{\lambda}_a), \ \mathbf{J}_u = \frac{\partial F(\lambda, \mathbf{u})}{\partial \mathbf{u}} \tag{1.13}$$

using Eq. (1.9), Eq. (1.10), Eq. (1.11) and Eq. (1.12) in Eq. (1.13), it can be shown

$$\dot{\mathbf{u}} = \mathbf{K}_u \mathbf{J}_u^T \left[\mathbf{K}_\lambda \mathbf{J}_\lambda^T \left(-\nabla V(\mathbf{p}_a) - G(\boldsymbol{\lambda}) \right) - F(\boldsymbol{\lambda}, glsu) \right] = Q(\mathbf{p}_a, \boldsymbol{\lambda}, \mathbf{u}) \tag{1.14}$$

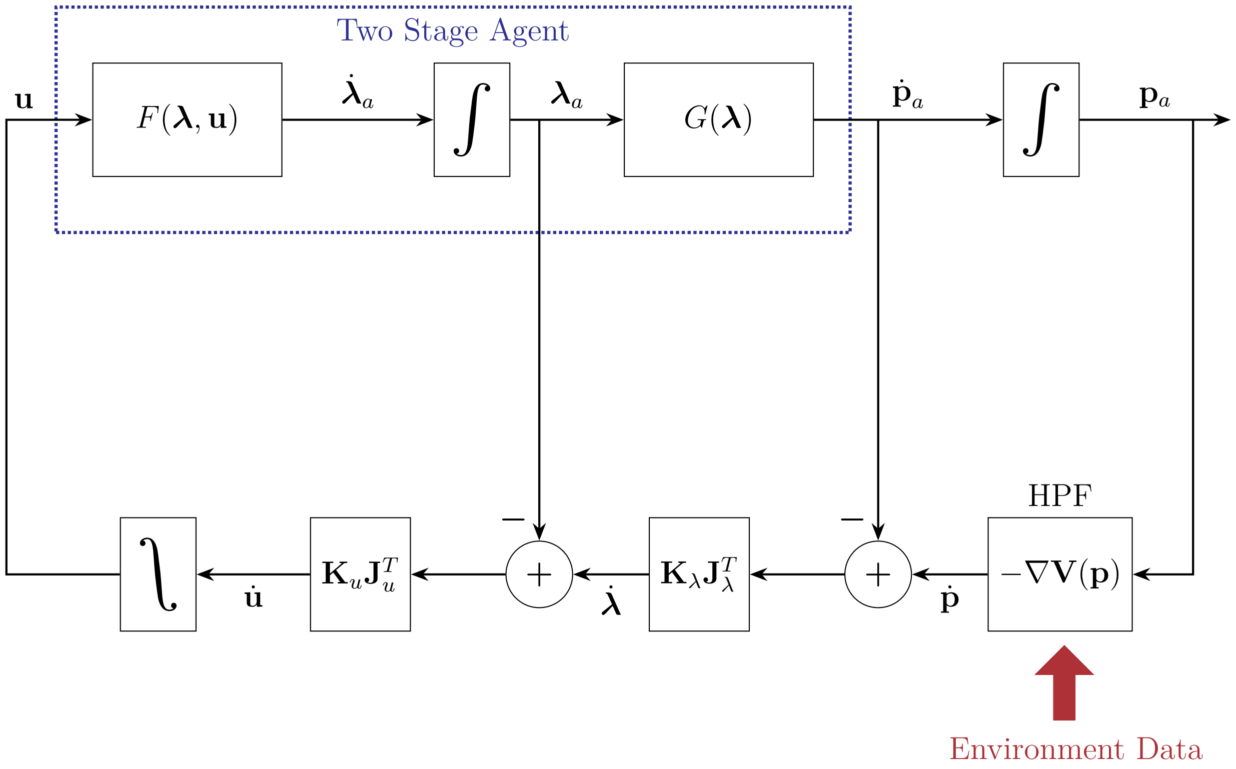

Figure 1.8: Two Stage Navigation Control System

$$\mathbf{u}(t) = \int_0^t \dot{\mathbf{u}}(t)dt$$

The overall navigation control [23] system is given in Fig. 1.8. An example of the VVA approach applied to a UAV is given in Eq. (1.15). The VVA was applied to a highly nonlinear system given in Eq. (1.15) and the guidance field was obtained using

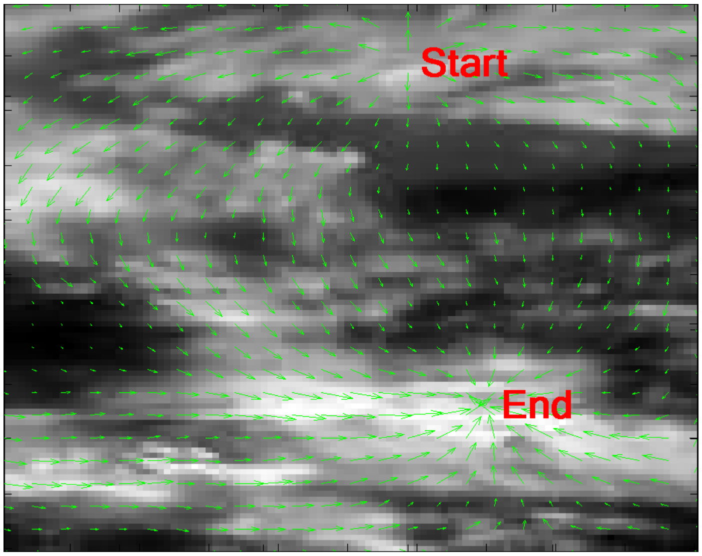

Figure 1.9: Guidance Field for the System Given in Eq. (1.15)

sensory data (Fig. 1.9).

$$\begin{aligned}
\dot{\mathbf{p}} &= \mathbf{v} \cdot \cos(\phi)\cos(\theta) \\
\dot{\mathbf{y}} &= \mathbf{v} \cdot \sin(\phi)\sin(\theta) \\
\dot{\mathbf{z}} &= \mathbf{v} \cdot \cos(\theta) \\
\dot{\mathbf{v}} &= \mathbf{u}_1 + \mathbf{u}_4 \qquad (1.15) \\
\dot{\theta} &= \cos(\mathbf{u}_2) + \mathbf{u}_3^2 + \mathbf{u}_5 \\
\dot{\phi} &= \cos(\mathbf{u}_2)\sin(\mathbf{u}_4) + \mathbf{u}_6
\end{aligned}$$

Fig. 1.11 shows the 3D-trajectory, dynamic path and the control signals obtained using the VVA approach for the system and guidance filed given above.

The environment data in Fig. 1.8 is given in the form of the soft descriptor in the HPF setup given in Eq. (1.6). The soft descriptor can be updated in real-time, which allows data from sensors to be integrated in to the HPF. Exploiting this setting of the

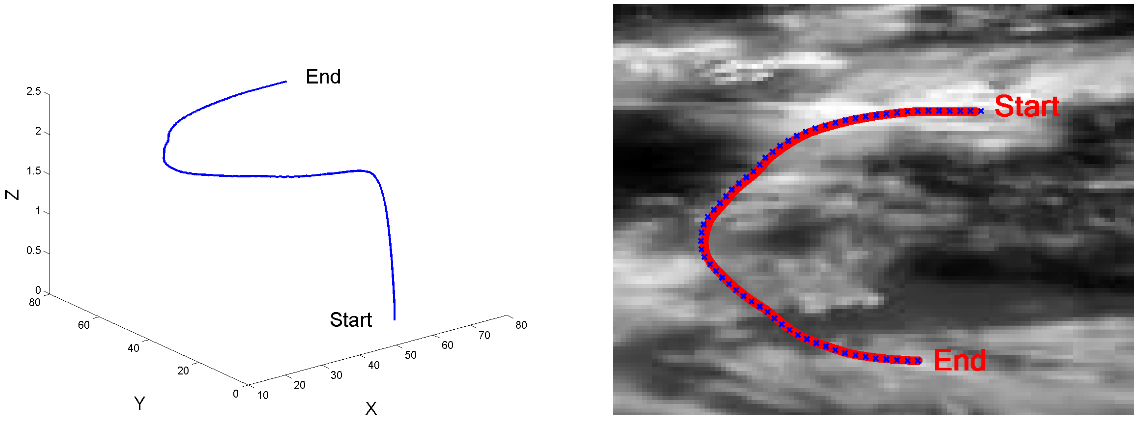

(a) 3-D trajectory of the UAV

(b) x-y Kinematic (dotted) and Dynamic (solid) trajectory

Figure 1.10: Trajectory of the UAV

HPF, the descriptor could be used to integrate quality of the wireless communication signal being received by the agent and thus, allow the agent to find a path coupled with the quality of the the wireless communication link. In the next chapter, a wireless communication signal is introduced and a model is obtained which can be used to introduce the wireless communication signal quality data in to the HPF.

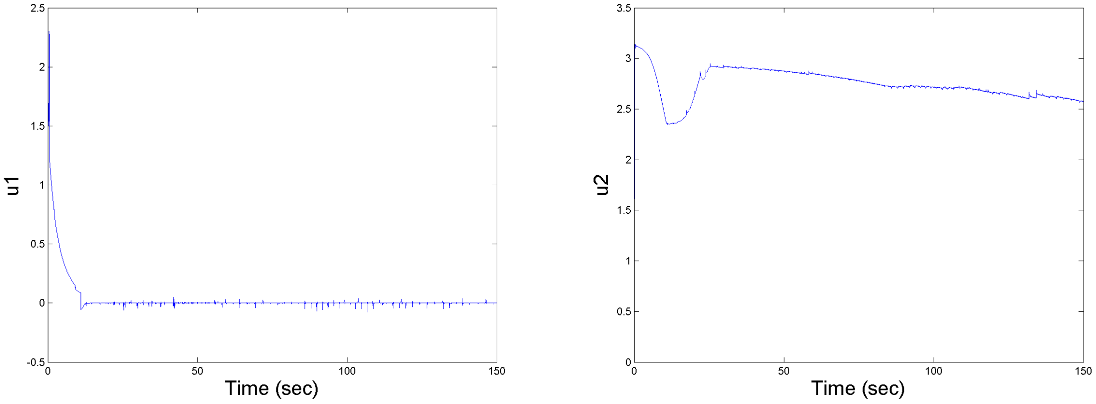

(a) Control signal $glsu_1$ **(b)** Control signal $glsu_2$

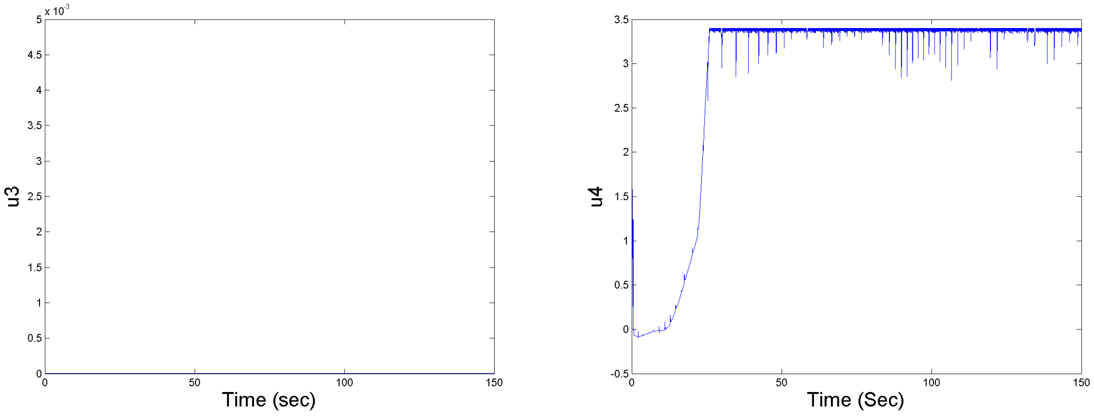

(c) Control signal $glsu_3$ **(d)** Control signal $glsu_4$

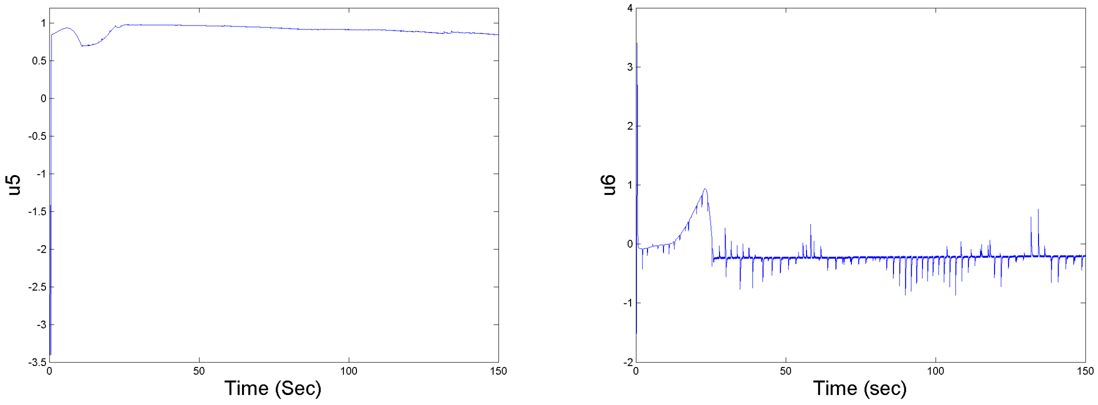

(e) Control signal $glsu_5$ **(f)** Control signal $glsu_6$

Figure 1.11: VVA applied to UAV

1.3 Wireless Communication

A Wireless Communication Link (WCL) basically acts as the connection through which an autonomous agent can relay data and receive mission information. Typically, the quality of the WCL is dependent on the Received Signal Strength (RSS) at the receiver of the agent. The RSS on the other hand is dependent on the so called wireless communication channel between the agent and the transmitter. A Wireless Communication Channel (WCC) is the medium between the transmitter and receiver through which the electromagnetic waves carrying information travel. The characteristics of the WCC determine the RSS level and therefore the quality of the WCL. In its simplest form it can be modeled as a gain (attenuation) applied to the transmitted signal, but in order to be able maximise the RSS a more detailed description of the WCC and its behavior is needed.

Practical wireless communication systems have limited resources available, i.e., limited spectrum allocation and limits imposed on the maximum power transmission due to both energy consumption of the battery as well as regulatory authorities. Within this spectrum-limited and energy-limited scenario, it is desired to increase the performance of the communication link so that it approaches its information-theoretic limit (capacity). Generally in communication systems it is desired that the signal received at the receiver is 'distinguishable' from the noise added to the signal at the receiver. The RSS should be above a certain level of the noise power level. This is usually quantified using the so called signal-to-noise ratio (SNR).

The SNR is a critical factor in defining (in band and power limited scenarios) the limit of the communication channel based on Shannon's theorem [25].

$$C = B \log_2 \left(1 + \frac{S}{N}\right) \tag{1.16}$$

where C is the data rate in bits per second, S is the received signal power and N is the total noise power. Based on Shannon's theorem, C is the maximum data rate possible for reliable transmission.

The performance of a WCC can also be limited by interference from other transmitters working at the same frequency. If the strength of the interfering signal dominates the noise strength, the performance is interference limited and is given by

$$C = B \log_2 \left(1 + \frac{S}{I + N}\right) \tag{1.17}$$

where I is the strength of the interfering signal and the ratio is known as signal to interference plus noise ratio (SINR).

As well as noise and interference, the power transmitted by the transmitter is also affected by the wireless channels through which the electromagnetic wave travels. The degradation in WCC is known as fading and can be divided into two types; Small-Scale Fading (SSF) and Large-Scale Fading (LSF).

1.3.1 Large Scale Fading (LSF)

LSF is the attenuation of the signal due to movement of the Mobile Station (MS) over large distances. It manifests itself in two major forms;

1. Path loss or signal attenuation with increasing distance between the Transmitter (TX) and Receiver (RX).

2. Shadowing Effect, when a receiver enters a 'Radio shadow', it experiences a dip in RSS. This happens when prominent terrains contours like hills, forests, high rise buildings, billboards, etc., come in between the TX and RX.

1.3.2 Small Scale Fading (SSF)

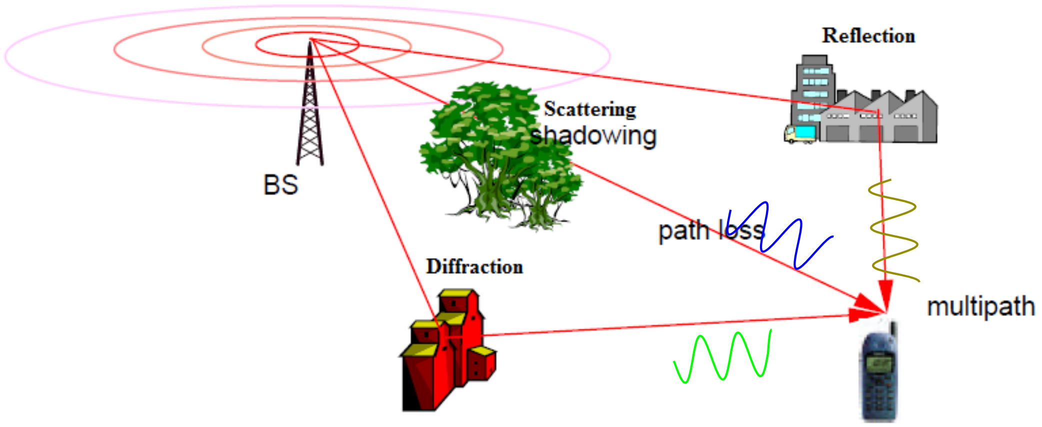

Figure 1.12: Multi Path Propagation

The signal received at the receiver, unlike wired communications, can have multiple components due to the physical phenomena like reflection, diffraction and scattering affecting the electromagnetic wave. This results in the signal being dispersed into multiple components with each component taking a different path as well as itself being further reflected, diffracted or scattered until it reaches the receiver as shown in the Fig. 1.12. The components are known as the Multi-Path Components (MPC) and they add up at the receiver. Depending on the total length of the path each

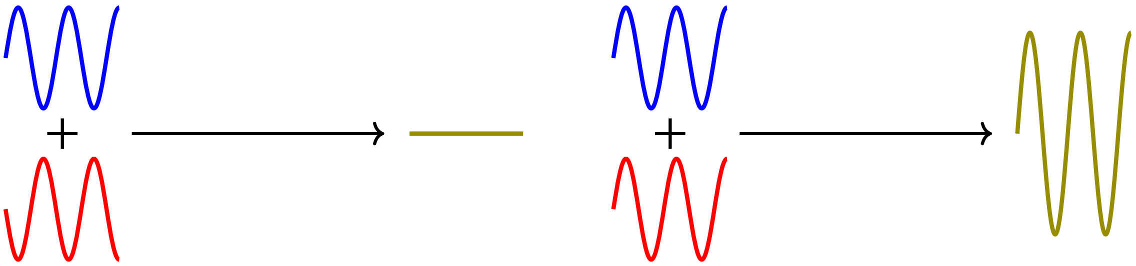

(a) Destructive Addition of MPC **(b)** Constructive Addition of MPC

Figure 1.13: MPC Interaction

component has traveled, the RSS can be adversely or favorably affected. This is due to the change in phase of the MPCs, with the worst case where the MPCs can be 180^o out of phase and their addition will lead to a complete loss of the signal as shown in Fig. 1.13a. On the other hand in-phase MPCs combine to enhance the signal strength (Fig. 1.13b). The RSS is a superposition of the LSF and SSF as shown in Fig. 1.14.

Small scale fading can be divided in to two categories:

1. **Time variation of the channel due to motion**. This is due to the mobility of either the TX or RX or the obstacles or all of them. The effects of time varying channels are more pronounced in signals with narrow bandwidth.

   Degradations in the received signal due to the the time invariance of the channels manifest themselves in two forms:

   (a) **Slow Fading**: If the channel fading rate is slower than the symbol transmission rate then it is known as slow fading.

   (b) **Fast Fading**: If the channel fading rate is faster than the symbol transmission rate, then it is known as fast fading.

2. **Time spreading of the signal due to multipath**. This is due to the delay

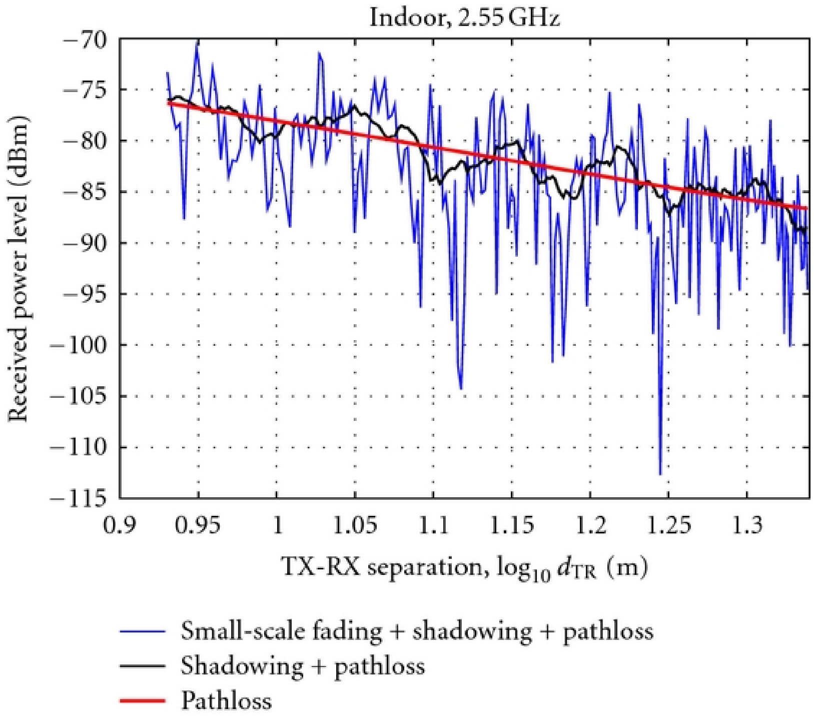

Figure 1.14: Signal at the receiver affected by fading

in the transmitted signal arriving at the RX which could lead to inter-symbol interference, where a new symbol reaches the RX before all the components of the previously transmitted symbol have reached the RX.

Degradations due to the time-spreading of a signal can categorized in to two types

(a) **Frequency Selective Fading**: If the symbol transmission time, T_s is less than the maximum access delay of the channel, then the received MPC extend beyond the symbol transmission time and the baseband signal gets degraded as an overlap between the reception times of symbols occur. This effect is known as channel-induced inter symbol interference (ISI) and results in frequency selective fading.

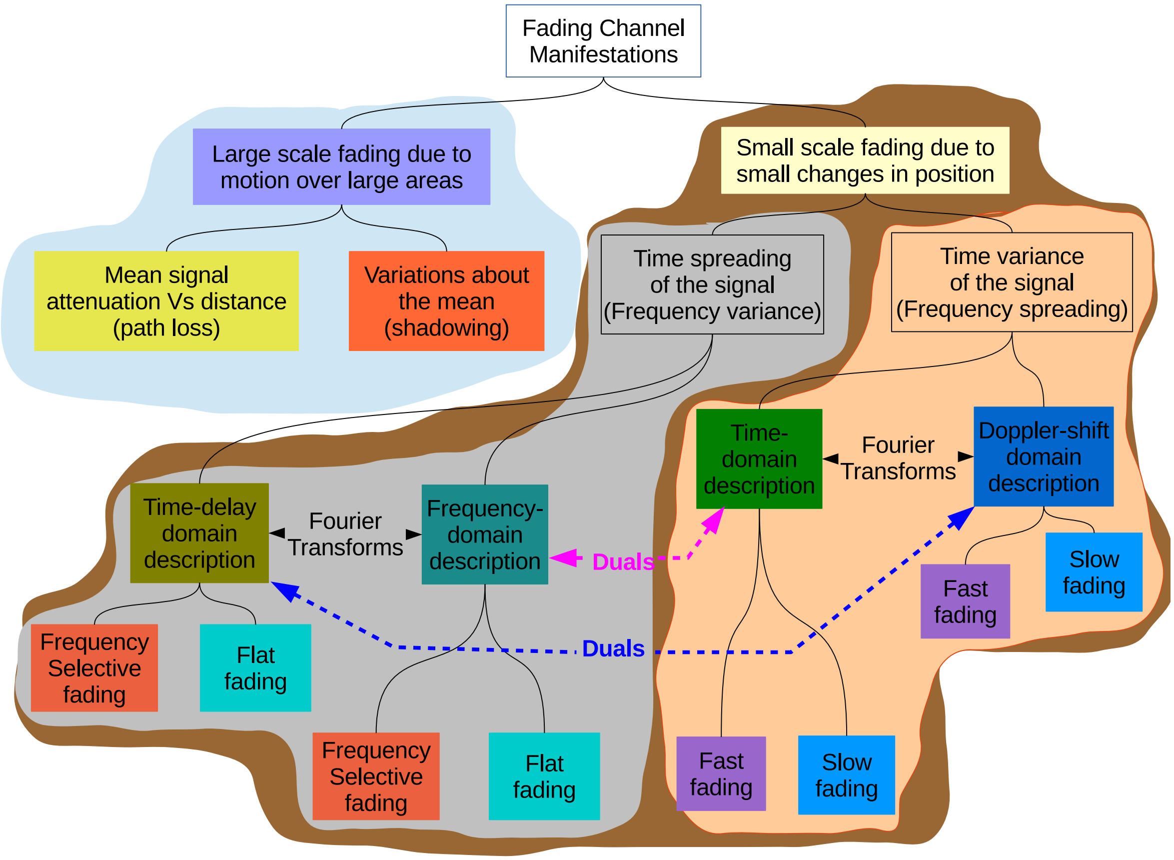

Figure 1.15: Categories of Fading [3]

(b) **Frequency Flat or Frequency Non-Selective Fading**: A channel is said to induce frequency flat fading if the symbol duration is less than the maximum access delay of the channel.

The different categories of fading are presented in Fig. 1.15.

1.3.3 Characteristics of WCC in Destroyed Environments

The characteristics of the WCC in scenarios, related to our work, discussed in chapter 1, are different from normal wireless communication channels. The agent will be traversing in, at best, a partially known environment, probably indoors, on irregular terrains and confined spaces. This will lead to the agent having a channel that is Non

Line of Sight (NLOS), with many reflections, time-varying (due to the environment being dynamic) and in some cases frequency selective. [26] Conducted tests in underground mines and road tunnels, where it was shown that high signal attenuation and intense fluctuation occur in the near region, whereas, in the far region the attenuation becomes gradual. Near and far region were defined based on the operating frequency, tunnel size and transmitter position. In a room and pillar environment, it was found that the signal experiences fluctuations in both near and far regions. [27] found that the most influential factor in degrading wireless communication links was interference from external sources or other agents working in the same area. [28] performed RSS tests in tunnels and found frequency dependent variations in the signal.

Overall there is no formal categorization for variations of WCC in scenarios like search and rescue. Therefore, the agent will have to adapt and estimate the channel characteristics online, using real-time measured data, in order to be able to maintain an acceptable quality of the wireless communication link.

This poses the question of computing a metric to determine the quality of a WCC. Typically, quality of a WCC is quantified using its information theoretic limits. The maximum data-rate (capacity) that can be transmitted reliably over a communication link as given in Eq. (1.17) can be rewritten as

$$R = B \log_2 \left(1 + \frac{\omega_t^H h_{i,t} h_{i,t}^H \omega_t}{\sum_{j \neq t} \omega_j^H h_{i,j} h_{i,j}^H \omega_j + \sigma^2} \right) \tag{1.18}$$

where B is the bandwidth of the communication signal, $\omega_t \in \mathbb{C}^{n_t \times 1}$ is the beamforming vector at the transmitter (base-station), equipped with n_t spatially correlated antennas linearly spaced $\frac{\lambda}{2}$ apart. The power transmitted at a base-station t, is $\omega_t^H \omega_t = P_t$, σ^2 is the power of the random noise affecting the signal at the receiver (section 1.3). Finally, $h_{i,t} \in \mathbb{C}^{n_t \times 1}$ is a vector whose elements represent the channel gain from each antenna at the base-station t to a user i discussed in detail in section 1.3.

In Eq. (1.18), the argument of the logarithm contains the signal to interference and noise ratio (SINR)

$$SINR = \frac{\omega_t^H h_{i,t} h_{i,t}^H \omega_t}{\sum\limits_{j \neq t} \omega_j^H h_{i,j} h_{i,j}^H \omega_j + \sigma^2} \tag{1.19}$$

where ω_j is the beamforming at other base-stations that can interfere with the signal at the receiver.

In the previous section it was shown that the WCC is dependent on the position and speed of the TX, RX and the obstacles present in the WCC or the relative position and speed of the agent to the TX and obstacles in the environment. It was shown for SSF that the time-variance of the channel depends on the relative speed of the agent and the time spreading of the transmitted signal depends on the relative position of the agent with respect to the transmitter and obstacles present in the channel. More over, the time variance of the channel sets an upper limit on the relative speed of the agent to avoid fast fading (for a fixed signalling rate). Similarly, the LSF, like shadowing and pathloss are directly dependent on the relative position of the agent.

In Eq. (1.18), the interference experienced by the agent is also dependent on the WCC from the interfering TX to the agent. The interfering channel on the other hand is also dependent on the position and speed of the agent. Therefore, interference at the agent can be decreased by degrading the interfering WCC at the agent from the interfering transmitter by choosing positions of the agent where the WCC from the interferer is weak. Thus the the trajectory an agent takes towards its goal will have a big impact on its wireless communication performance.

To navigate in an environment while maintaining its communication-link, along with other constraints on energy and obstacle avoidance, the above mentioned spacial constraints that a wireless link imposes on the mobile agent need to be integrated in to a path-planner (section 1.2). Since, the agent will be moving in an unknown (or partially known) environment, the path-planner will need to generate trajectories in real time, thus motivating the use of PF based planners. HPF planners as introduced in section 1.2, are a type of PF based planners that give trajectories that are goal driven, energy efficient, can be converted to control signals for a wide class of agents and are available for the complete environment. The aim of this work is to further integrate communication constraints with HPFs to obtain trajectories to the goal. It has to be noted that the agent should still be able to successfully navigate towards its goal, even if the communication link knowledge is absent. However, maintaining the communication link is critical for data transfer, information sharing and other cooperative mission objectives.

1.4 Dissertation Structure

The remaining dissertation is organized as follows.

Chapter 2 introduces the state of the art in communication-aware mobility. It then highlights our contributions compared to other work done in the field of communication-aware mobility.

Chapter 3 introduces our first contribution which is Model-Based Communication-Aware Navigation (MBCAN) where the agent has complete knowledge of the environment and received signal strength. It provides the problem formulation and detailed analysis of the technique. At the end it provides detailed simulation results and our conclusions.

Chapter 4 lays the foundation of Sensor-Based Communication-Aware Navigation (SBCAM), where the agent has no knowledge or partial knowledge of the received signal strength. It provides the formulation and analysis of the problem. We provide simulation results and our conclusions at the end.

Chapter 5 provides a single measurement sample based greedy Signal to Noise Ratio (SNR)-map reconstruction technique. A joint mobility and SNR-map reconstruction framework is developed. The convergence analysis of the joint motion and SNR-map reconstruction using Single Sample Greedy (SSG) is done and extensive simulation results are provided.

Chapter 6 describes different multi-sensing-antenna SNR-map reconstruction techniques. We discuss the kernel used to weight the SNR measured at different antennas. Hard Obstacle or Hazardous Region (HO) extension due to the size of an agent is also discussed. Convergence analysis due to different kernel parameters is done and we provide simulation results for a variety of environments and sensing antennas configurations.

In chapter 7 a joint motion, Hard Obstacle or Hazardous Region (HO)-map and prediction based SNR-map reconstruction using real-time sensor data framework is presented. HO-map reconstruction for different agent sizes using range sensors is discussed. Extensive simulation results and analysis of the different reconstruction techniques is provided.

Finally, chapter 8 provides conclusions and possible future directions with potential contributions.

CHAPTER 2

STATE OF THE ART

"Life must be understood backward. But it must be lived forward."

—Søren Kierkegaard.

The recent past seen a surge in interest in communication-aware path planning techniques. Researchers have looked in to jointly optimizing sensing and communication performance, [29], [30], [31], [32], [33], [34], [35], where agents find a position that enhances both sensor resolution and communication. Moving in a formation among obstacles with Line Of Signt (LoS) constraint was presented in [36], while [37] introduced an indoor search while maintaining a communication link with an external BS. All these techniques use simplistic representations of theWireless Communication Channel (WCC), assuming signal quality to be dependent on distance or based on line of sight. Multiple strategies were proposed to maintain or enhance wireless connectivity. [38] proposes restricting motion to preserve communication connectivity. [39], [40], [41] use mobile relaying agents to strengthen a weak communication link. [42] introduces the use of mobile agents to bridge disconnected groups of mobile sensors.Another approach is to define the communication link in binary terms [43], where communication is possible within a certain region but not outside it. In practical applications, especially, in highly populated areas, or indoors, using these simplified models, ignores the physical phenomena that occur from electromagnetic radiation (section 1.3). Moreover, they are incapable of trackling the situation where only one agent is present in the environment. The impact of the multiple phenomena that affect Received Signal Strength (RSS) can be mitigated using diversity techniques, array processing and frequency spreading. Multiple antenna at the receiver requires certain dimensions of the agent and thus might not be suitable for platforms of smaller size. It was also shown that frequency spreading techniques are not always effective [44]. An open area of research that has recently attracted attention is to exploit the 'converse' of spatial diversity, i.e., change the spatial position of the Receiver (RX) so as to improve the RSS characteristics of the RX.

Typically, autonomous agents compute the so called path-plans, which are trajectories an agent intends to follow while accomplishing an assigned mission. Thus, researchers started exploring techniques to integrate constraints on these trajectories such that the agent improves its RSS characteristics using knowledge of its wireless communication channel. Lindhé et al. [45] first studied the improvement that can be gained by taking in to account the effect of Multi-Path Components (MPC) on the transmitted signal. A probabilistic framework was developed to find the number of spatial sampling points, by deviating from the original trajectory, required to find the point where the agent will obtain the desired gain with a certain probability. Sampling in a circular and hexagonal lattice pattern were studied. It was shown that a gain of up to $5dB$ could be obtained with these strategies. Only Differential Drive

Robots (DDR) and Front Steered Robots (FSR) type agents were studied. In [46] Lindhé proposed a controlled stopping policy for a DDR. The agent tracks a reference trajectory in a stop and go manner. Motion is based on the incoming data in to its First In First Out (FIFO) buffer from its sensors and average capacity along the predetermined trajectory the agent is tracking. If the incoming rate becomes higher than the average capacity, the agent stops at a point whose link capacity is higher than the incoming data and thus prevents its buffer from overflowing. The strategy tries to exploit the fact that the MPC constructively add within a few cm (function of wavelength). After stopping to empty the buffer it increases its speed to converge to the reference speed. The problem is formulated as a relaxed dynamic programming problem. [47] builds on the the controlled stopping policy by exploring strategies that do not depend on the link capacity for stopping. Instead a periodic stopping scheme is used where the agent stops after a predefined time interval, measures the Signal to Noise Ratio (SNR) and then decides the length of the stopping interval based on the SNR quality. Two schemes where explored, the first one uses a stopping interval directly proportional to the SNR magnitude and the other stops the agent only if the SNR exceeds a threshold and the stopping interval is fixed. The stop go strategies so far only try to exploit the Small-Scale Fading (SSF) and assume that the Large-Scale Fading (LSF) remains constant over the distance the agent moves. In [48] a stop go policy based on an estimate of the average SNR (shadowing) along the trajectory is used. The stop time and the threshold are obtained based on the estimate of the average SNR. Although stop and go policies help increase the amount of data that can be transferred via a wireless link, they tend to increase the time of the mission.

Thus, they become ineffective in time-critical missions. Moreover, frequent stopping and accelerations increases energy usage which deplete the battery energy reserve. [49] presents a multi-robot path following framework with constraints on line of sight communication. Each robot's position is considered to be a dimension of configuration space with obstacles that can obstruct the line of sight communication signal. Each agent is assigned a reference path such that its path doesn't intersect with the path of the other agents. Finally the Rapidly Exploring Random Trees (RRT) algorithm was deployed to find a path from the starting configuration to the goal configuration while avoiding the LoS obstructing obstacles and thus probabilistically guaranteeing a line of sight link for all the agents.

[47], [45], [46], [48] focused on exploiting the SSF using stop-go strategies, Mostofi in [50], [51] introduced strategies to adapt the motion of a group of Unmanned Air Vehicless (UAVs), cooperatively tracking a target with linear dynamics. The agents share their sensing information via wireless communication link and the proposed work uses on-line SNR and correlation information of the Wireless Communication Link (WCL) to help predict its information gain via communication and assess its overall information gain and decide on its next action. It also shows the effects of LSF fading on the performance of the group. Finally it shows that uncorrelated fading due to its natural randomization helps agents avoid deep fades. This is because correlated fading can lead to the agent being in a deep fade for a long time and an adaptive step size manipulation (increasing step size in deep fades) can help the agent leave deep fades. The control signal was taken as a set of motion vectors with equal magnitude but different phase. The approach also does not take in to account physical obstacles

in the path-plan and assumes that the environment is stationary (the communication signal only changes as a function of the agent position).

[52] proposes a compressive sensing based estimation of the wireless channel variations (sparse in the Fourier domain) and advocates its usage in robotic networks. [53] proposes a probabilistic model based representation of the wireless communication channel and its utility in predicting the WCC using a small number of measurements. It is shown that for the most part, the compressive sensing based estimation outperforms the model based approach for a small number of samples.

‘ [54] introduces a communication-aware target sensing problem, where a group of autonomous agents locally sense the presence of static targets and relay the sensed data to a Base-Station (BS) via a WCL. The BS then fuses the information to reduce the probability of error detection. The WCL was modelled as a random variable described probabilistically using underlying parameters that can be estimated based on previous observations. Based on the multi-scale WCC model, the next control command for the agent was computed by jointly maximizing the connectivity with the BS and probability of detection at the BS. First order dynamics were assumed for the agent and the trajectory was computed based on a set of admissible control commands. The connectivity was quantified by estimating the SNR at the next state of the agent based on previous measurements. [55], [56] extended the surveillance of targets to scenarios where the states of the target can vary with time. It introduced periodic trajectories for multiple agents such that sensing of the target state and connectivity with a base station were optimized. The optimization aims to make the sensing uncertainty of the targets bounded. The problem of finding a periodic trajectory was formulated as a mixed integer programming problem (MIP) on a graph and the transmitted power was optimized using nonlinear programming (NLP) so as to maximize connectivity and reduce transmitted power wastage. The agents were considered as point, massless and holonomic robots, thus their dynamics were ignored. The velocities of the agents were considered to be uniform along the trajectory.

Ghaffarkhah and Mostofi in [57] developed a modified version of the so called navigation (potential) function [58] to obtain path plans for tracking a mobile target (only tracking from a safe distance and not capture) while avoiding obstacles and transmitting their estimated data (own location and location of target) to a BS and obtaining control signal from the BS. The BS computes and transmits the control command based on the potential function developed using the received information from the agents. A holonomic agent was assumed and the dynamics of the target were assumed to be linear. The agent receives its next control command via a WCL. If it gets disconnected from the BS, the agent moves in random direction until it gets connected again. The connectivity was defined by comparing the SNR of the agent to a threshold and the regions where the SNR was less than the threshold were modelled as obstacles and thus were integrated along with other physical obstacles (other agents also considered as obstacles) in to the navigation function. The navigation function approach restricts the workspace, the agents and obstacles to a sphere. The authors use diffeomorphism to transform workspaces of different topologies to a sphere or conservatively model the workspace as a sphere. It was assumed that the starting point and the target never enters the disconnected region of the workspace. [59] extends the use of the navigation function to the decentralized case where each agent computes its own control signal while maintaining a WCL with the BS. In the decentralized case inter-agent communication is vital to avoid inter-agent collisions. It was also shown that errors in SNR estimation can lead to degradation in the performance of the centralized case. However the decentralized planner is more robust to errors in the SNR estimation.

[60] builds on the work on estimation of the SNR field by estimating the underlying parameters of a multiscale (path loss, shadow fading and multipath fading) probabilistic model of the SNR. A communication aware plan for a holonomic agent was proposed based on minimizing the error in prediction of the SNR field. The approach seeks to find the next control command based such that the error in the prediction of the SNR at the next spatial point is minimized (a more strict objective of minimizing the average error of prediction). A gradient based controller was developed in [61] to explore and estimate a field (a signal other than the RSS) using mobile sensing agents while maintaining connectivity. The BS fuses the sensing data using a Bayesian filter and the error in the estimation depends on the communication signal. A holonomic agent and a packet dropping receiver BS (which drops a packet if the SNR is below a threshold) were assumed. The workspace was divided into connected and disconnected regions based on a SNR threshold. The strategy used to generate the control signal is to explore regions where the error in the estimation (of the field) is large so as to sense the region and fuse the sensed data at the BS. This reduces the error (in the field estimation) but on the other hand transmission of the sensed data is dependent on the connectivity. Thus, while sensing the region, if an agent

enters a disconnected zone, a control signal that moves the agent with a high enough speed to the nearest connected region is applied. Ghaffarkhah and Motofi in [62] proposes a communication-aware approach for multi-agent target tracking. The authors first introduce a framework to estimate the underlying parameters for a multiscale wireless communication channel model such that the error in the mean squared error in channel assessment is minimized at the next step. The results were shown when the agent already had some measurements available but the technique is purported to work without any initial measurements availability. The planning problem was then introduced for holonomic agents with linear dynamics such that each agent decides on its next action based on its local optimization of its channel assessment and target tracking objective assuming the other agents as obstacles and assuming physical obstacles as circular. The work showed that their channel assessment was most sensitive to the estimation of the pathloss parameters and thus the communication-aware framework was developed based on predicting the pathloss parameters only.

[63] extends the work in [55] to account for variations in velocity along trajectories and energy expended due to motion and communication. A Mixed Inteer Linear Program (MILP) was developed to obtain an optimal policy for periodic sensing of multiple point of interests in an obstacle free environment while minimizing communication and motion energies at the the agent. [64] builds on the work presented in [54] introducing communication aware area exploration techniques. It assumes holonomic agents and decentralized control such that each agent computes its next step based on an optimization objective. A communication-aware scheme is proposed where the detection probability of a static target at the BS is maximized taking in to account

the connectivity of the agent. A switching technique is proposed in case an agent enters a zone with no connectivity, such that it moves in an sensing-aware (exploring unexplored area with higher probability) until it reconnects with the BS. Another so called Hybrid switching scheme was proposed where the agent first explores the area in a given time for sensing and makes sure it only moves in an unexplored area. The strategy aims to maximize connectivity at the end of a surveillance session such that it collects data during the surveillance session and then at the end of the session the agent seeks a position with high connectivity chances and transmits its data to the BS. In the case of multi-path fading which was not taken care of in the study, if an agent loses connection in a region with high chances of connectivity based on shadow fading, then the agent makes a jittery movement (stopping at different points on a circle about its position) until it connects to the BS. Robustness techniques againt SSF like increasing SNR threshold or adapting power transmission at the agent to the quality of the channel at the agent like water-filling (transmitting at a higher power at points with good channel characteristics and vice versa) can be also used.

Yuan et al. in [65], [66] examined the problem of maximizing the amount of information sent to a BS while moving on a fixed trajectory within a fixed time. The aim is to modulate the speed of the agent during its motion along the trajectory to minimize the energy consumed. The fixed trajectory was divided into a number of subtrajectories. The agent predicts the SNR along the trajectory based on estimating the pathloss and shadowing parameters of the underlying wireless channel model using a few available measurements. The strategy adapts to the WCC by moving at a constant speed along trajectories with poor channel characteristics. The agent moves with a slower speed along the sub-trajectory with best channel characteristics and increases its spectral efficiency (by transmitting at maximum power when the channel characteristics are best (water-filling)). A holonomic agent is considered and mutipath fading is not estimated. [67] proposes a router formation framework where, robots fitted with relays move to form formations to minimize Bit Error Rate (BER) at the RX. [68] proposes a periodic trajectory to sense multiple points of interests and then transmitting the sensed data to a BS at a point most suited for wireless communication. The periodic trajectory is optimized to reduce energy consumption due to motion (shortest possible path) while maintaining good communication characteristics.

Yan and Mostofi in [69] present a way-point navigation framework where the agent visits many Points of Interests (POIs) to gather data before reaching the goal in a fading environment. It proposes a communication and motion energy co-optimization technique based on real-time prediction of the received signal strength. The problem is posed as a MILP. Motion energy is assumed to be dependent on velocity which gives a good approximate of the energy consumed by slow moving agents. The 'dilemma' of should the agent incur motion energy to to improve communication or transmit at a higher power at current location is tackled. Conditions resulting in minimized path length and agent moving to regions with very high connectivity were derived. Also conditions in which agent can incur motion energy to improve communication along with conditions relating co-optimized motion and communication energy were obtained. A point agent is assumed and the environment is assumed to have no obstacles. The trajectories obtained are not smooth.

Ali et al. in [70] provide a motion and communication co-optimization framework for the case where an agent is moving along a fixed path in a fading environment. The agent is tasked with transmitting a fixed number of bits in a fixed time interval by choosing a transmission spectral efficiency (transmission power) from a discrete set of transmission spectral efficiencies. The problem was formulated in continuous domain. The motion energy consumption was approximated based on acceleration of the agent. The problem was posed an optimal control problem with the communication energy constraint introduced as a dynamic constraint. A Hamiltonian based algorithm was obtained as part of the solution. The approach was integrated with on-line prediction of received signal strength. The environment was assumed to have no obstacles and an agent with double integrator dynamics (unit mass) was assumed.

[71] introduced a directionality of signal strength based approach for a team of robots where a subset of the robots act as routers. It explores router formation to expand coverage of other robots using directionality of received signal strength. The approach exploits both the euclidean disk coverage model and sampling based approach for modeling received signal strength. Position controller developed to find positions for routers and clients to exploit spatial directionality of received signal strength. Synthetic Aperture Radar (SAR) techniques used (to avoid bulky directional antennas) to construct signal strength profile at different angles. Gradient based approaches employed on signal strength profile map to find positions with highest received signal strength. The approach assumes obstacles in environment and the consequent attenuation of signal components passing through the obstacles. A point agent was assumed. The approach on finds positions as opposed to complete trajectories from

on point to another.

[72] builds on the work of [70]. It presents an optimal control based motion and communication energy co-optimization approach where the agent has to obtain its path to goal while minimizing motion and communication energy. The agent needs to send a fixed amount of bits in a fixed time interval. A Hamiltonian based algorithm was developed. The agent needs to choose an acceleration, direction and transmission spectral efficiency (from a discrete set) as part of the solution. Results for both offline model-based and online prediction based received signal strength were provided. No obstacles were assumed and an agent with double integrator dynamics (unit mass) was assumed.

Muralidharan et al. in [73] present a so called 'First Passage Distance' finding problem for mobile robots to ensure connectivity. It attempts to obtain the distance needed to traverse by an agent before it gets connectivity. The problem was tackled by finding the Probability Density Function (PDF) of the traveled distance with respect to the underlying parameters governing the wireless communication channel. A point agent was assumed. It was also assumed that no obstacles exist in the environment. The received power was modeled as a Gauss-Markov stochastic process. The PDF was obtained for the case with no multi-path fading using the Stochastic Differential Equation (SDE) literature. A more generic approach including multi-path fading was solved using stochastic dynamic programming.

A distributed transmit beamforming framework was proposed in [74]. The problem of a network of nodes (agents) tasked with transmitting the same data is presented. The single antenna equipped nodes emulate beam-forming using multiple antennas, where the the same signal is transmitted at each antenna such that it adds constructively at the receiver. The agents perform distributed beamforming by choosing position in space such that the signal adds constructively at the receiver. The problem is formulated as a motion and communication energy co-optimization problem such that the probability of outage is kept below a threshold. The agents need to find a position within a constrained region. An ϵ-optimal solution was found by posing the problem as a family of multiple choice knapsack problems when perfect channel knowledge is considered. The problem was subsequently solved as an optimization problem for the case where the agents have only 5% channel knowledge and predict the channel online in real-time.

A graph-theoretic path-planning approach was developed in [75]. The path an agent needs to obtain connectivity was found using realistic channel models. Connectivity was defined as when the received power goes above a certain threshold. It was required to minimize the energy consumption in the sense of total distance traveled. The problem was formulated as a stochastic short path problem. It was solved using stochastic dynamic programming tools. No obstacles were assumed to be present in the environment and a point agent was assumed. The resulting trajectories were non-smooth.

Most of the work found in the literature focuses on subproblems of Communication Aware Navigation Control. Aspects of wireless communication affecting robotic motion are studied by some researchers. However highly simplified motion models of the agents are assumed. This simplification can lead to the dynamics of the agent being ignored. This can result in the actual results significantly (sometime destructively)

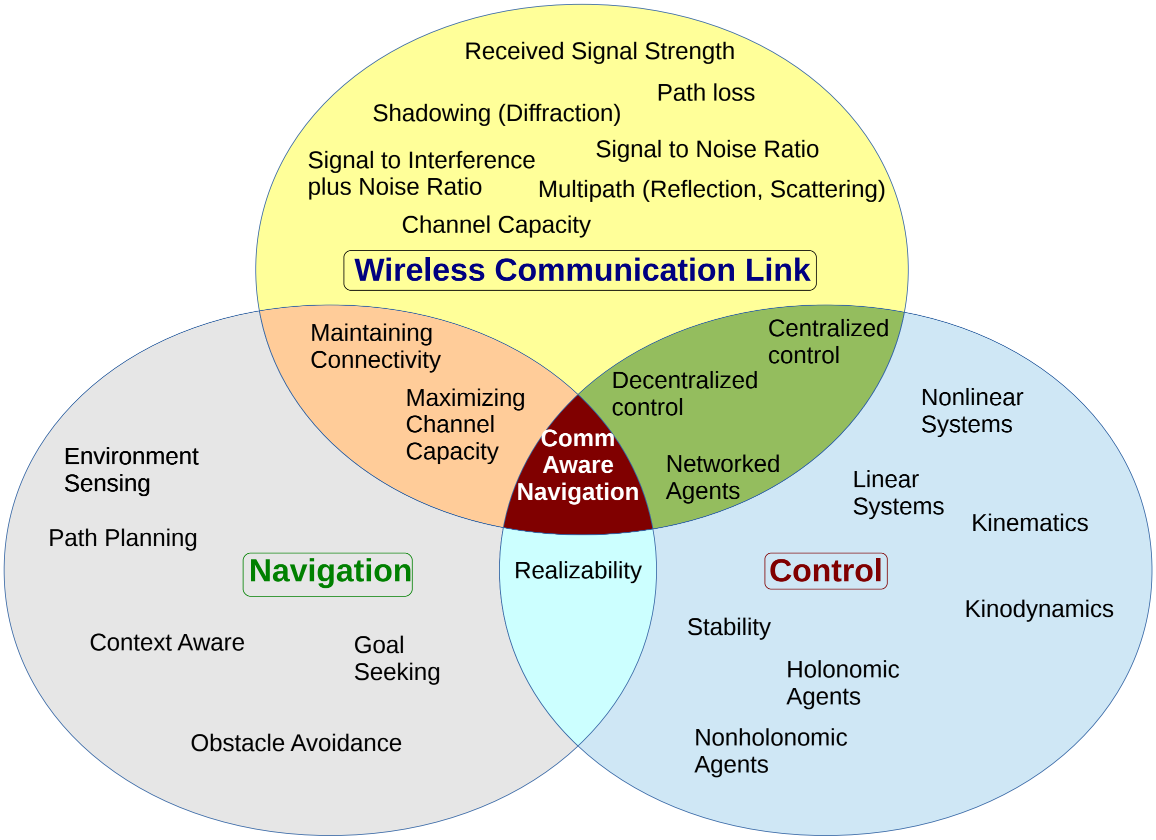

Figure 2.1: State of the art in Communication Aware Navigation Control

deviating from the produced results. On the other hand if realistic models of the agent are assumed then either a very simplistic communication model (disk model) is used or only a specific aspect of communication is tackled. Most of the work in literature also lacks stability analysis of the developed control system. It is assumed the the obtained control will be immediately realizable by the agent. Our work focuses on the intersection of the three most important aspects of Communication Aware Navigation Control (CANC) as shown in Fig. 2.1. Our focus is on developing a framework that is able to fuse together, in a provably-correct manner, the three critical aspects, wireless communication, path planning and control of an agent. Ignoring either of these aspects can lead to results (although impressive) impossible to realize. At the heart of our work is the integration of wireless communication constraints with Harmonic Potential Field (HPF)s to obtain goal seeking fields, which as shown in section 1.2 have highly favorable realizability properties.

CHAPTER 3

MODEL-BASED COMMUNICATION-AWARE MOBILITY

”Whether you think you can or you think you can’t, you’re right.”

—Henry Ford.

In Model-Based Communication-Aware Navigation (MBCAN), the agent is assumed to have complete knowledge of the wireless Received Signal Strength (RSS) in its environment. Thus, the agent is able to build a soft representation (using measured values unlike binary representations that represent an environment as accessible or inaccessible) of the RSS for the complete environment. We assume in indoor environment. It is also assumed that the agent has the complete Hard Obstacle or Hazardous Region (HO) knowledge and therefore has the complete hard representation of the environment. Fig. 3.1 shows an example representation of the Signal to Noise Ratio (SNR) and HO knowledge (in blue color) for a complete rectangular environment. By assuming full knowledge of the RSS, we can obtain performance benchmarks for more realistic operation conditions where full knowledge of the RSS is not available to the agent.

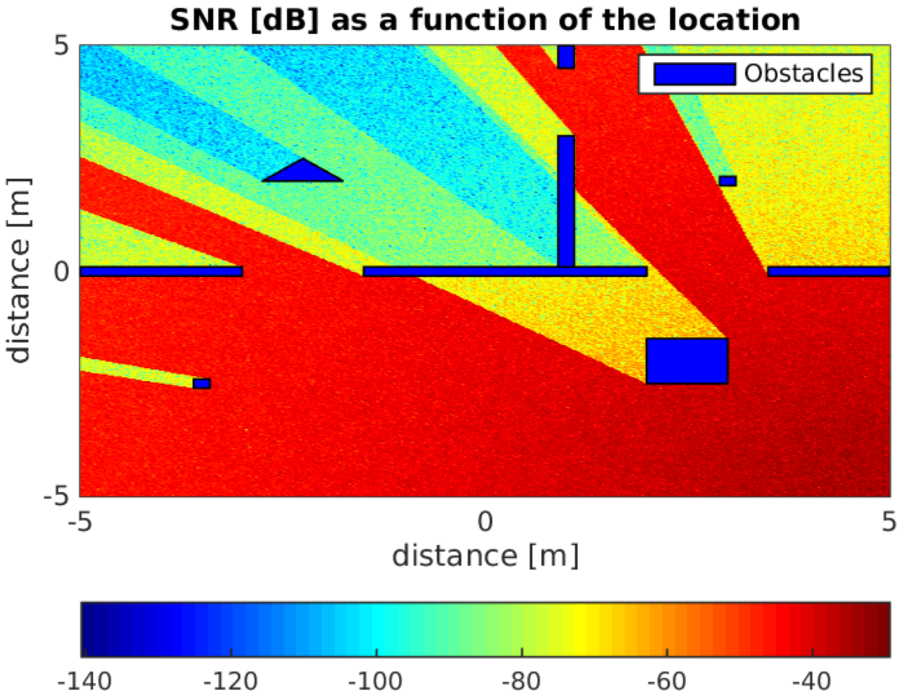

Figure 3.1: Representation of the Soft SNR Knowledge and HO of a Complete Environment

The environment data has to be processed in a manner that enables the agent to move towards a known goal position while avoiding the HO (or hazardous regions) and maintaining its Wireless Communication Link (WCL) at an acceptable quality. The soft representation of the RSS allows the agent to choose trajectories based on quality of the WCL. The agent's environment might have the so called Dead Communication Zones (DCZ) (Formally defined in Def. 3.3). DCZ are zones where the quality of the WCL goes below a certain threshold (RSS becomes difficult to distinguish from noise) thus leading to a break down in the wireless communication link. The agent

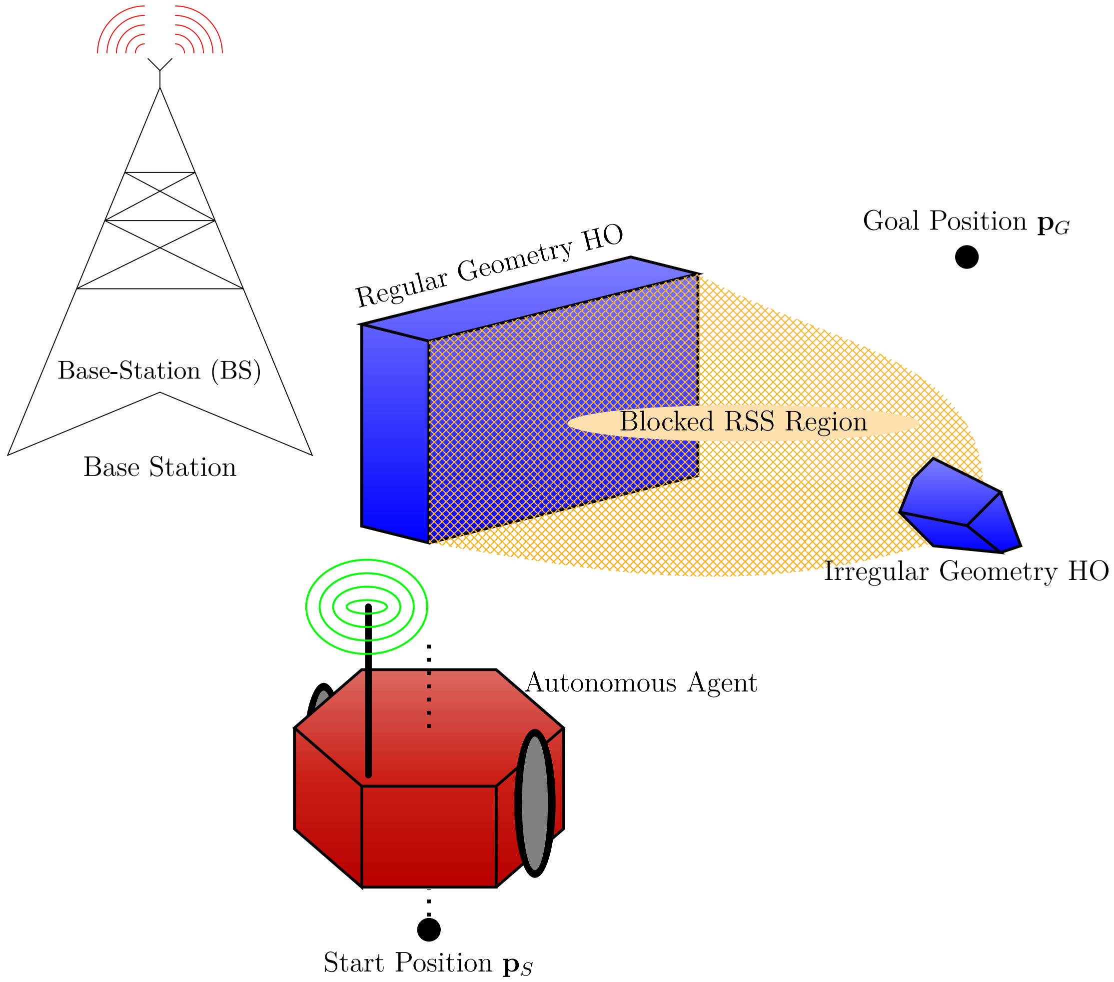

Figure 3.2: Autonomous agent with a WCL to a BS moving in a cluttered environment

is expected to avoid the DCZ while proceeding towards the goal. Let an autonomous agent be moving in a n-dimensional workspace $\mathcal{W}$ ($\mathcal{W} \in \mathbb{R}^n$). Let $\mathbf{p}$ ($\mathbf{p} \in \mathcal{W}$) be a point in the workspace. The HO (regions in the environment where the agent can get damaged) in the workspace are denoted by $\mathcal{O}$, ($\mathcal{O} \subset \mathcal{W}, \mathcal{O} = \bigcup\limits_{i=1}^{N_O} o_i$). N_O is the number of HO in the environment and $o_i, i = 1, \cdots, N_O$, is the i^{th} HO, in the environment. The HO can be convex or non-convex, i.e., the region (set) describing the HOs can be a convex or non-convex. The HOs can be disjoint or overlapping. Let $\mathcal{W}_a = \mathcal{W} - \mathcal{O}$ be the admissible workspace. The agent's starting point is $\mathbf{p}_S$ ($\mathbf{p}_S \in \mathcal{W}_a$). The agent is required to reach a goal position $\mathbf{p}_G$ ($\mathbf{p}_G \in \mathcal{W}_a$).

The scalar SNR at a point $\mathbf{p}$ in the workspace is denoted by $\gamma(\mathbf{p}) \in \mathbb{R}$. The DCZs are denoted by $\mathcal{O}_{DCZ}, (\mathcal{O}_{DCZ} \subset \mathcal{W}, \mathcal{O}_{DCZ} = \bigcup_{i=1}^{N_{O_c}} o_{c_i})$, where N_{O_c} is the number of DCZs in the workspace. The trajectory of the agent is denoted by $\mathbf{p}(t), (\mathbf{p}(0) = \mathbf{p}_S)$.

In the rest of the chapter it is assumed that both the BS and agent are equipped with single antenna transceivers. We assume a single BS and a single agent as it represents the worst case scenario in case of an emergency. In this scenario, the agent has no other agent or BS to fall back on. Thus the WCL between the BS ang the agent is highly critical for the success of the mission. It is also assumed that there is no external interference at the receiver (agent). Moreover, It is assumed that complete SNR and HO knowledge of the workspace is available to the agent.

3.1 Performance Measures

Typically, the quality of a WCL in a single transmitter and single receiver scenario with no external interference is characterized using the SNR (Eq. (1.19)) of the WCL. SNR is the ratio of the RSS to noise-power at the receiver. The higher the value of the SNR, the better the quality of the WCL. The communication capability of a WCL referred to as the channel capacity is directly dependent on the SNR of the WCL. The channel capacity is the maximum possible rate at which data can be reliably communicated over a communication link as given in its generalized form in Eq. (1.18). In this scenario with no external interference at the agent's receiver and single transmit and receive antenna, it reduces to the following form

$$C = B\log_2\left(1 + \frac{S}{N}\right) \tag{3.1}$$

where C is the channel capacity in Bits per Second (bps), B is the bandwidth of the WCL, S is the received signal power and N is the noise power at the receiver. We assume zero-mean Additive White Gaussian Noise (AWGN) at the receiver with unit variance, $\mathcal{N}(0, \sigma^2 = 1)$. Assuming unit transmit power (${\boldsymbol{\omega}_t}^H \boldsymbol{\omega}_t = 1$), the SNR (reduces to the channel to noise ratio) in Eq. (3.1) can be written as

$$\gamma = \frac{S}{N} = \frac{\mathbf{h}\mathbf{h}^H}{\sigma^2} \tag{3.2}$$

where $\mathbf{h} \in \mathbb{C}$ is the complex channel gain from a single antenna Transceiver (TRX) at the BS to a single-antenna TRX at the agent. The Wireless Communication Channel (WCC) is assumed to be reciprocal and Time-Division Duplex (TDD) communication link is assumed. Since a single antenna is assumed at both the BS and Mobile Station (MS) (agent), $\boldsymbol{\omega}_t$ and $\mathbf{h}$ will be complex scalars. As explained in section 1.3, γ is dependent on time t, position $\mathbf{p}$ and excess time delay $\tau(\mathbf{h}(\mathbf{p}, t, \tau))$. Its dependence on time is due to the spatial and geometrical changes in the reflectors, scatterers, refractors and diffractors in the environment. Its dependence on τ is due to the spreading effect on the signal by the environment. The spatial position of the agent affects the path loss suffered by the transmitted signal.We assume a narrow band channel and therefore, the effect of the excess time delay can be ignored [76]. Thus the

SNR and consequently the channel capacity depend on the time and spatial position of the receiver (the agent).

Realistic wireless communication is power limited and band limited. Therefore, the channel capacity can only be improved by improving the WCC. Thus assuming fixed transmitted power (unit transmit power assumption Eq. (3.2) ($\boldsymbol{\omega}_t{}^H\boldsymbol{\omega}_t = 1$)) and normalizing the channel capacity in Eq. (3.1) by the bandwidth B, we can define the Channel Spectral Efficiency (CSE), η, [77], [76], [78] as

$$\eta(\mathbf{h}) = \frac{C}{B} = \log_2\left(1 + \gamma(\mathbf{h})\right)\left(\frac{bits/Hz}{sec}\right) \tag{3.3}$$

The CSE is dependent on the SNR. The assumption that there is no external interference at the receiver makes the SNR at the receiver dependent only on the WCC. Assuming the environment to be stationary and the channel to be narrow band, the WCC will only depend on the position of the agent. Narrow band channels have a symbol time greater than the max excess delay (flat fading) (section 1.3). Therefore, the WCC and the channel capacity of the WCC becomes a function of space only.

The channel capacity (Bits per Second (bps)) is the maximum possible rate at which data (bits) can be reliably transmitted over a communication channel. The total data that can be reliably transmitted at a particular location depends on the time spent by the agent at that location. The time an agent spends at a location along its trajectory is the inverse of the magnitude of the velocity at that location . This leads us to the following definition.

DEFINITION 3.1 *Let β be a function that maps each point in the workspace to a scalar positive real number equal to the maximum possible data that can be reliably transmitted at that point*

$$\beta : \mathcal{W} \rightarrow \mathbb{R}_+$$

Then, let β be defined as the Data-Flow Efficiency (DFE) of a point in the workspace and $\beta(\mathbf{p})$ is a scalar field defined by,

$$\beta(\mathbf{p}) = \frac{\eta}{|\dot{\mathbf{p}}|} \quad \left(\frac{bits/Hz}{m}\right) \tag{3.4}$$

Def. 3.1 is important in the sense that it gives a measure of the communication performance based on the kinematic properties of the agent. It should also be noted that the DFE can easily be generalized for broad band channels and time varying environments.

The agent's trajectory to the goal should be such that the SNR at each point in the trajectory allows the sensor data to be reliably transmitted. As well as wireless communication, the trajectory should be safe, energy-efficient, as short as possible, does not include loops (i.e.,the agent should not wander aimlessly or just for exploratory/mapping purposes) and should be realizable [7] by a well-behaved control signal.

Energy-efficiency requires the chosen trajectory to be smooth. Smoothness is determined by the degree of differentiability of the trajectory. Length of the trajectory is determined by the "goal-orientedness" of the agent, i.e. it should always be moving towards the goal and does not take any unnecessary steps whose aim is not to bring the agent closer to its target. Therefore, the performance of the mobility generator can be measured by quantifying the smoothness, realizability, goal-orientedness and WCC along the trajectory obtained by the generator. For this purpose a functional that measures the quality of the agent's trajectory as it relates to communication-aware mobility needs to be obtained. The functional must integrate both the SNR and motion characteristics of the agent. This functional can then be used to jointly optimize both the path properties and WCC during the motion of the agent.

In the following, the measure defined in Def. 3.1(defined only for a spatial point) is tied to the integral properties of the agent's motion in the workspace. Let the trajectory, $\mathbf{p}(t)$ be divided into $N_{\mathbf{p}}$ segments of equal time intervals Δt. Let the DFE at the i^{th} segment of the trajectory be $\beta_i = \beta(\mathbf{p}(i\Delta t)), i = 1, 2, \cdots, N_{\mathbf{p}}$. The total (accumulated) DFE over the i^{th} segment, D_i, will then be given by,

$$D_i = \beta_i \Delta t$$

and total data-flow over the trajectory $D_{\mathbf{p}}$ is given by

$$D_{\mathbf{p}} = \sum_{i=1}^{N_{\mathbf{p}}} D_i = \sum_{i=1}^{N_{\mathbf{p}}} \beta_i \Delta t \tag{3.5}$$

Let $N_{\mathbf{p}} \to \infty$ and $\Delta t \to 0$, then Eq. (3.5) becomes an integral over the trajectory of the agent accumulating the DFE.

$$\lim_{\Delta t \to 0} D_{\mathbf{p}} = \int_0^\infty \beta(\mathbf{p}(t))dt = \mathbf{\Pi}(\mathbf{p}) \tag{3.6}$$

This leads us to definition 3.2, which ties the communication performance to a continuum of points (trajectory).

DEFINITION 3.2 *Let* $\mathbf{\Pi}(\mathbf{p})$ *be a functional that maps a trajectory of an agent in a workspace to a real positive scalar*

$$\mathbf{\Pi}(\mathbf{p}(t)): \ \mathbf{p} \rightarrow \mathbb{R}_+$$

Then, $\mathbf{\Pi}(\mathbf{p})$*, is defined as*

$$\mathbf{\Pi}(\mathbf{p}) = \int_0^\infty \beta(\mathbf{p}(t))dt \tag{3.7}$$

$$\textbf{\textit{Subject to:}} \ \mathbf{p}(0) = \mathbf{p}_G$$

$$\mathbf{p}(\infty) = \mathbf{p}_S$$

$$|\dot{\mathbf{p}}| > 0$$

where Eq. (3.7) *is an integral over the trajectory of the agent and gives the DFE accumulated over the trajectory.*

We can see from the differential properties of Eq. (3.4) that the amount of data transmitted at a point along the agents trajectory can be controlled by modulating the magnitude of the velocity of the agent at that point. By reducing the velocity magnitude an agent can spend more time at a location to transmit more data while higher velocities will allow less data to be transmitted at a location. Thus it ties the kinematics of the trajectory to the communication performance at each point. Also, it can be noticed that this measure can act as generalized form of measures previously used in communication-aware motion planning. As an example it can be seen that as

$$|\dot{\mathbf{p}}| \to 0$$

then

$$\beta \to \infty$$

which is a strategy used by Lindhé et al. in devising communication aware stop go strategies to increase data throughput along an agent's trajectory. The functional in Eq. (3.7) introduces the WCC as a degree of freedom in designing trajectories for an agent in a workspace. It ties the WCC to the kinematics (position and velocity) of the trajectory and not just a single spacial point. Finally, it can be noted that the SNR (Eq. (3.2)) and CSE (Eq. (3.3)) are monotonically related. Therefore, we will use γ and η interchangeably in this thesis.

The RSS at the antenna of an agent is affected by the environment between the BS and agent. Thus, based on the position of an agent in the environment, its RSS could be severely degraded due the different phenomena (section 1.3) that can affect electromagnetic signals. This could lead to regions in the environment where communication between the agent and the BS is practically impossible. Fig. 3.3 depicts a scenario where shadowing of the RSS caused by an obstacle leads to a region in the environment with very low SNR. We define regions where communication can get cut off as Dead Communication Zones (DCZ).

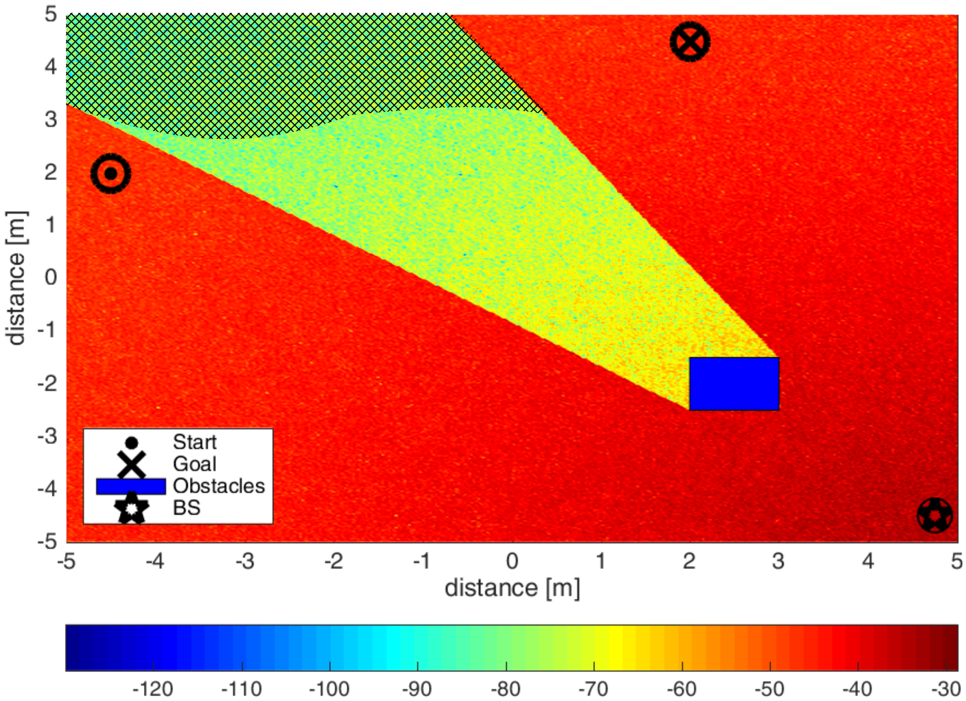

Figure 3.3: A possible DCZ (shaded region)

DEFINITION 3.3 *A DCZ is defined as the region where the data-rate of a WCL becomes prohibitively low. Let* $\mathcal{O}_{DCZ} \subseteq \mathcal{W}$ *represent a region that is a DCZ, then it can be defined as follows*

$$\mathcal{O}_{DCZ} = \{\mathbf{p} \in \mathcal{W} | \gamma(\mathbf{p}) \leq \epsilon_D, \epsilon_D \to 0\}, \epsilon_D \in \mathbb{R} \tag{3.8}$$

As the SNR goes to zero, the maximum possible data-rate, η, also goes to zero. Thus severe degradation of the RSS can result in DCZ in a region.

At the end, we introduce the following definition

DEFINITION 3.4 *Let* $\mathcal{T}$ *be a set of unique trajectories that cover the workspace of an agent. Each trajectory emanates from a single starting point,* $\mathbf{p}_S$*, and ends at a single target or goal point,* $\mathbf{p}_G$*. As shown in Fig. 3.4, the set of trajectories* $\mathcal{T}$ *can be*

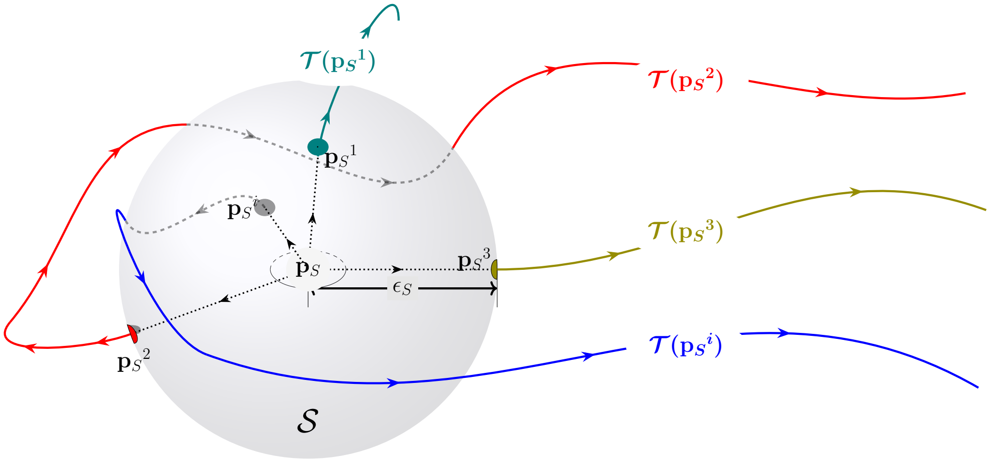

Figure 3.4: Trajectories emanate from the starting point $\mathbf{p}_S$ uniquely parameterized by points $\mathbf{p}_S{}^i$

parameterized using points, $\mathbf{p}_S{}^i, i = 1, 2, 3, \cdots, \infty$*, on a sphere* $\mathcal{S}$ *of radius* ϵ_S *(where* $\epsilon_S \to 0$*) around the starting point* $\mathbf{p}_S$*. The set of trajectories* $\mathcal{T}$ *can be defined as follow.*

$$\mathcal{T} = \left\{\mathcal{T}(\mathbf{p}_S{}^1), \mathcal{T}(\mathbf{p}_S{}^2), \mathcal{T}(\mathbf{p}_S{}^3), \cdots, \mathcal{T}(\mathbf{p}_S{}^\infty)\right\} \tag{3.9}$$

Where,

$$\left\{\mathbf{p}_S{}^1, \mathbf{p}_S{}^2, \mathbf{p}_S{}^3, \cdots, \mathbf{p}_S{}^\infty\right\} \in \mathcal{S} \tag{3.10}$$

And

$$\mathcal{S} = \left\{\mathbf{p} \in \mathcal{W} \;\middle|\; |\mathbf{p} - \mathbf{p}_S| = \epsilon_S\right\}, 0 < \epsilon_S \ll 1. \tag{3.11}$$

Finally, let each trajectory in $\mathcal{T}$ be denoted by $\mathbf{q}_i(t)$ such that

$$\mathbf{q}_i(t) = \mathcal{T}(\mathbf{p}_S{}^i) \tag{3.12}$$

where each trajectory is parameterized by time.

3.2 Problem Formulation

The MBCAN problem can be formulated as finding the control signal as a function of the SNR, which will realize the required motion in an agent from the start position, $\mathbf{p}_S$, to the goal position, $\mathbf{p}_G$ and avoid the hard obstacles, $\mathcal{O}$.

for

$$\dot{\mathbf{p}} = \mathbf{u} \tag{3.13a}$$

find

$$\mathbf{u}(\mathbf{p}, \mathbf{p}_G, \mathbf{p}_S, \gamma, \mathcal{O}) \tag{3.13b}$$

Such that,

$$\lim_{t \to \infty} \mathbf{p}(t) \to \mathbf{p}_G \tag{3.13c}$$

$$\mathbf{p}(t) \bigcap \mathcal{O}_{DCZ} \equiv \phi, \ \forall t \tag{3.13d}$$

$$\mathbf{p}(t) \bigcap \mathcal{O} = \phi, \ \forall t \tag{3.13e}$$

$$\mathbf{p}(t) \in \mathcal{T} \mid \mathbf{\Upsilon}(\mathbf{p}(t)) \leq \mathbf{\Upsilon}(\mathbf{q}_i(t)), \mathbf{q}_i(t) \in \mathcal{T}, \ \forall i = 1, 2, \cdots, \infty \tag{3.13f}$$

Where $\mathbf{\Upsilon}$ is the functional that should be minimized and $\mathcal{T}$ is the set of all possible trajectories as defined in Def. 3.4 and $\mathbf{q}_i(t) \in \mathcal{T}(\mathbf{p}_S{}^i)$, is a time-parameterized trajectory uniquely identified by point $\mathbf{p}_S{}^i$ belonging to a sphere about the starting position as defined in Eq. (3.11).

3.3 Communication-Aware Mobility Generation

Mobility generation is the most basic and core component of autonomous operation of any agent. In MBCAN, the agent has complete SNR and HO knowledge. The mobility generator at the agent needs to assimilate this information and generate actuation that is in accordance with a given mission. The actuation should result in the generation of a path towards the goal that exhibits communication and mobility constraints. In this work we modify the Gamma-Harmonic Potential Field (GHPF) based path planner (section 1.2.3) to generate the desired communication-aware motion.

We assume a two dimensional workspace without loss of generality. Thus all trajectories will be restricted to a plane. The sphere $\mathcal{S}$ defined in Eq. (3.11) will be reduced to a circle. Let $\chi : \mathbb{R}^2 \rightarrow \mathbb{R}^2$ be a function that maps a two-dimensional SNR-map of the workspace, $\gamma(\mathbf{p})$ to a 2-D scalar field where the regions with SNR less than ϵ_D (Def. 3.3) to a constant value. χ maps DCZ regions to ϵ_D (Def. 3.3) in the workspace.

$$\chi(\gamma(\mathbf{p})) = \begin{cases} \epsilon_D, & \gamma(\mathbf{p}) \leq \epsilon_D \\ \gamma(\mathbf{p}), & \text{elsewhere.} \end{cases} \tag{3.14}$$

Let $\mathbf{\Gamma}_{\mathcal{W}}$ represent the boundary of the workspace and $\mathbf{\Gamma}_{\mathcal{O}}$ be the boundary of all the HO in the workspace. Finally, let $\phi(\mathbf{p})$ be a scalar potential field defined at each point in the workspace.

The communication-aware path to the goal position can be obtained by first solving the following configuration of the GHPF system

$$
\begin{aligned}
&\text{solve} && \nabla \cdot (\chi(\gamma(\mathbf{p}))\nabla\phi(\mathbf{p})) = 0,\ \mathbf{p} \in \mathcal{W} && \text{(3.15a)}\\
&\text{subject to} && \phi(\mathbf{p}_S) = 1,\ \phi(\mathbf{p}_G) = 0,\ \frac{\partial \phi}{\partial \mathbf{n}} = 0,\ \text{at } \mathbf{p} \in \mathbf{\Gamma}_{\mathcal{W}} && \text{(3.15b)}\\
& && \frac{\partial \phi}{\partial \mathbf{n}} = 0,\ \text{at } \mathbf{p} \in \mathbf{\Gamma}_{\mathcal{O}},\ \text{Neumann Boundary} && \text{(3.15c)}
\end{aligned}
$$

Before proceeding further, we introduce the following definition.

DEFINITION 3.5 *Let $\rho(\mathbf{p})$, be defined as follows,*

$$\rho(\mathbf{p}) = -\nabla\phi(\mathbf{p})\chi(\gamma(\mathbf{p})) \tag{3.16}$$

ρ represents the volumetric flow density directed by the gradient of the potential field. ρ is similar to the definition of electric current density in volumetric flow of electrons in a conductor [79]. It can be noted from the definition of ρ in Eq. (3.16) *that it is a vector.*

Then a sphere $\mathcal{S}$ (circle in 2-D) of arbitrarily small radius $0 < \epsilon_S << 1$ (Eq. (3.11)) is taken around $\mathbf{p}_S$ as shown in Fig. 3.5

$$\mathcal{S} = \left\{ \mathbf{p} \in \mathcal{W} \;\middle|\; |\mathbf{p} - \mathbf{p}_S| = \epsilon_S \right\}, 0 < \epsilon_S \ll 1 \tag{3.17}$$

A point $\mathbf{p}_S{}' \in \mathcal{S}$ is selected such that

$$|\rho(\mathbf{p}_S{}')| \geq \left|\rho(\mathbf{p}_S{}^i)\right| \tag{3.18}$$

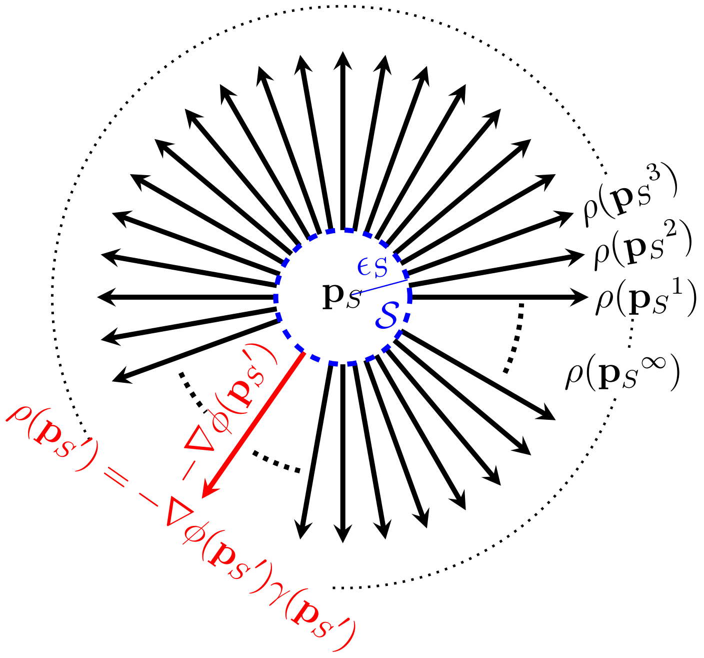

Figure 3.5: Different values of ρ at different points on $\mathcal{S}$ which is a circle in a 2D workspace

or

$$\mathbf{p}_S{}' = \underset{i}{\operatorname{argmax}} \ \left|\rho(\mathbf{p}_S{}^i)\right| \tag{3.19}$$

where, $\mathbf{p}_S{}^i \in \mathcal{S}, i = 1, 2, \cdots, \infty$ and ρ is given by Eq. (3.16). Finally, the path is generated using the following gradient dynamical system.

$$\dot{\mathbf{p}} = -\nabla\phi(\mathbf{p}),\ \mathbf{p}(0) = \mathbf{p}_S \tag{3.20}$$

The motion is stopped when the path reaches inside a sphere $\mathcal{G}$ of radius ϵ_G around $\mathbf{p}_G$.

$$\mathcal{G} = \left\{\mathbf{p} \in \mathcal{W} \,\middle|\, |\mathbf{p} - \mathbf{p}_S| \leq \epsilon_G\right\}, 0 < \epsilon_G \ll 1 \tag{3.21}$$

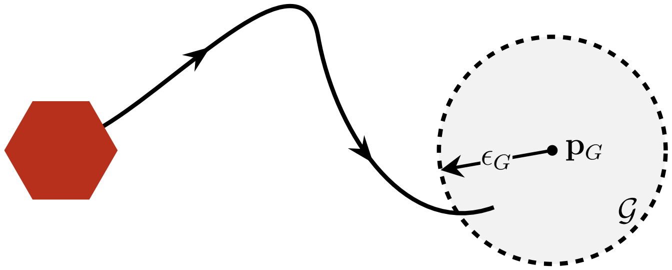

Figure 3.6: Motion stops when trajectory comes to within ϵ_G of $\mathbf{p}_G$

Fig. 3.7 gives the MBCAN algorithm flow. The trajectory obtained using MBCAN can be exactly realized by a single integrator system

$$\dot{\mathbf{p}} = \mathbf{u} \tag{3.22}$$

where $\mathbf{u}(t) = -\nabla\phi(\mathbf{p}(t))$. In the remainder of this section we assume a single integrator system. We will show later on that a large class of agents can realize the trajectory obtained by MBCAN.

An intuition on how the GHPF based planner works can be developed by rewriting Eq. (3.15) as

$$\nabla \cdot (\chi\,(\gamma(\mathbf{p}))\,\nabla\phi(\mathbf{p})) = \chi\,(\gamma)\,\nabla^2\phi + \nabla\chi\,(\gamma)\cdot\nabla\phi = 0 \tag{3.23}$$

$$\Rightarrow \nabla^2\phi = -\frac{1}{\chi\,(\gamma)}((-\nabla\chi\,(\gamma))\cdot(-\nabla\phi)) \tag{3.24}$$

Where $-\nabla\chi\,(\gamma)$ points in the direction of decreasing communication performance (decreasing Signal to Noise Ratio (SNR)) and $-\nabla\phi$ points in the direction the agent's motion will take at that point to reach the goal. Looking at the Left Hand Side

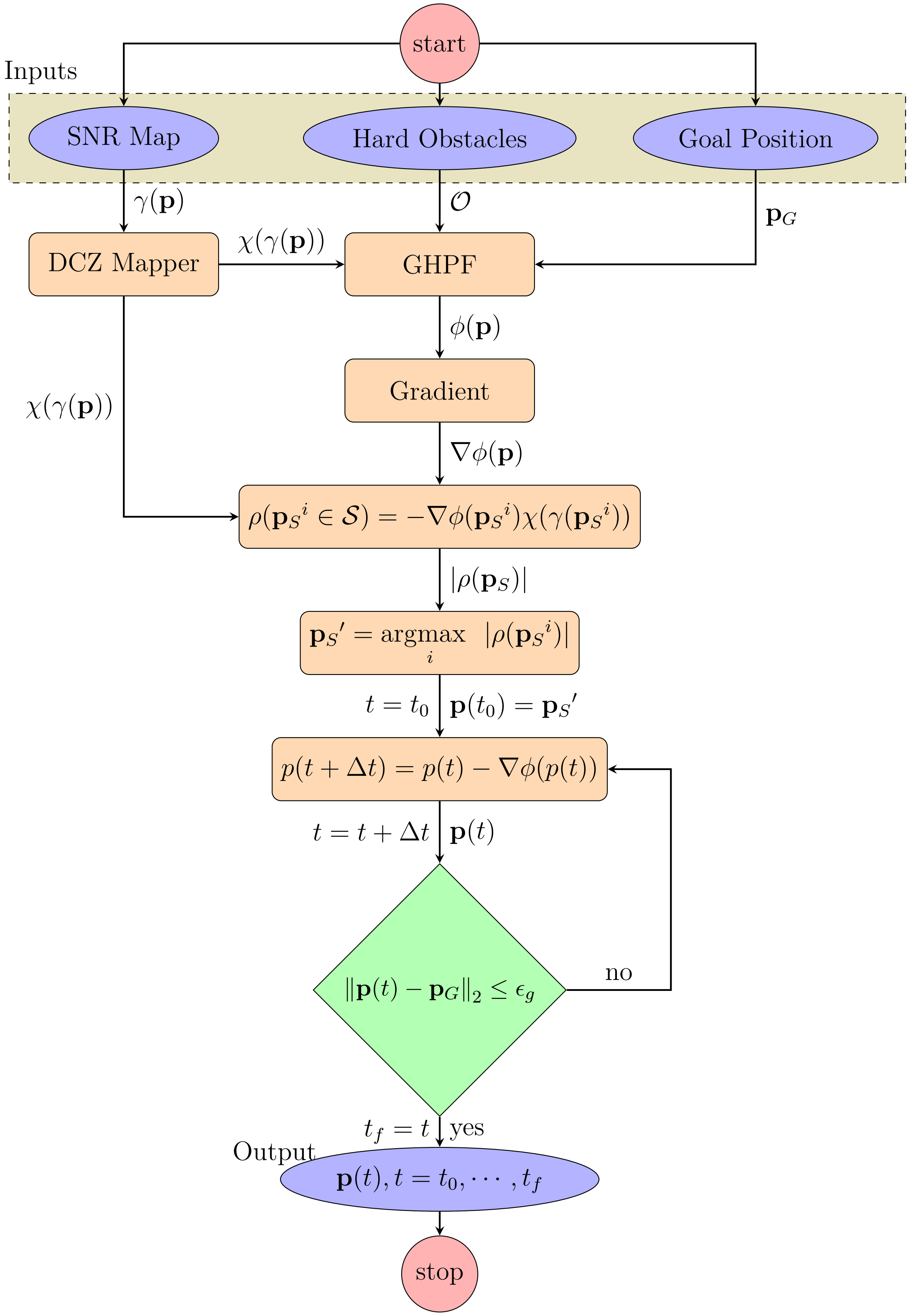

Figure 3.7: MBCAN flow

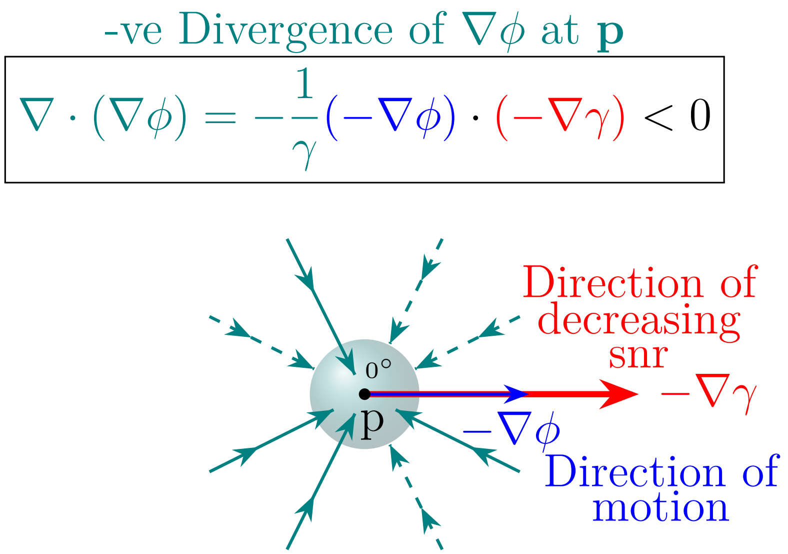

Figure 3.8: -ve divergence of $\nabla\phi$

(LHS) of Eq. (3.24), it is nothing but the divergence of the gradient of a potential field. It describes the flow of the potential field (flux) through a differential volume in the space. If the divergence is positive then that differential volume is a source of potential flow, as shown in Fig. 3.9, and would repel the flow of the gradient radially away from that point. On the other hand if the divergence is negative, then that differential volume acts as a sink, as shown in Fig. 3.8, and would attract the flow of the potential radially.

The Right Hand Side (RHS) is a dot product of two vectors, the negative gradient of the SNR, $-\nabla\chi\left(\gamma\right)$, which points in the direction of decreasing communication performance and negative gradient of the potential field, $-\nabla\phi$, which points in the direction of motion, scaled by $-\frac{1}{\chi\left(\gamma\right)}$. Also, the DCZ-mapped SNR, $\chi\left(\gamma\right)$, by definition (Eq. (3.14)) is either zero or postive (i.e. $\chi\left(\gamma\right) \geq 0$). If at a point $\mathbf{p}$ the dot product, $(-\nabla\phi(\mathbf{p})) \cdot (-\nabla\chi\left(\gamma\right)(\mathbf{p}))$, is positive, i.e., motion is directed towards the direction of decreasing communication performance then the divergence of $\nabla\phi$,

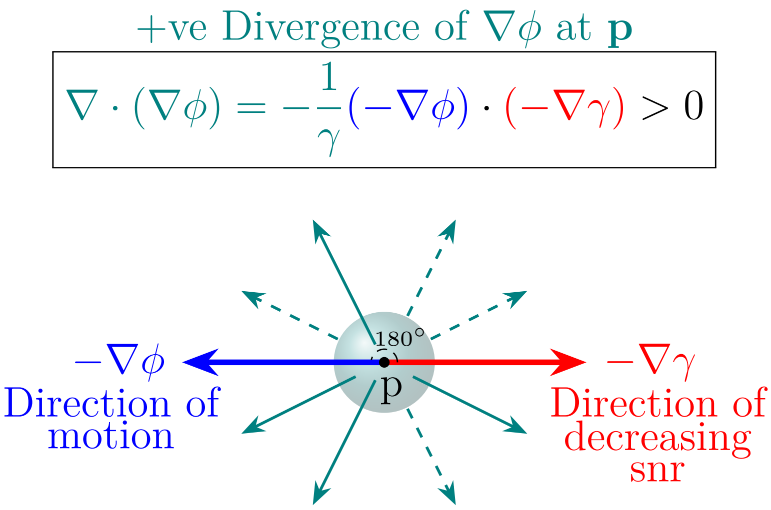

Figure 3.9: +ve divergence of $\nabla\phi$

$\nabla \cdot (\nabla\phi)) = -\dfrac{1}{\chi(\gamma)}(-\nabla\phi) \cdot (-\nabla\chi(\gamma))$, at that point is negative. It acts as a sink attracts the potential flow $(-\nabla\phi)$ in its vicinity. Since motion is guided by $-\nabla\phi$, the divergence attracts the motion radially inwards towards the point $\mathbf{p}$ and thus discourages motion towards the region of decreasing SNR.

In a similar manner if the direction of motion at a point $\mathbf{p}$ is antipodal to the direction of decreasing SNR, then the dot product $(-\nabla\phi(\mathbf{p})) \cdot (-\nabla\chi(\gamma)(\mathbf{p}))$, at that point is negative, i.e., direction of motion is diametrically opposite to the direction of decreasing communication performance. Therefore, the divergence of $\nabla\phi$ at that point is positive and $\mathbf{p}$ acts as a source. The positive divergence repels the potential flow $(-\nabla\phi)$ radially away from the point $\mathbf{p}$. Therefore, it encourages motion in the current direction.

The strength of this sink or source (strength of attraction or repulsion due to positive or negative divergence) at a point in the workspace is directly dependent on

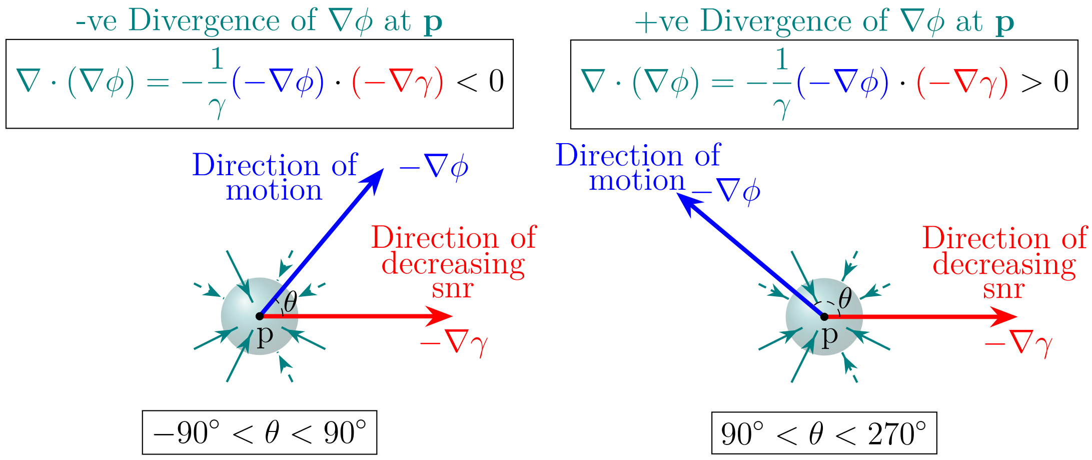

Figure 3.10: Strength of divergence depends on the orientation of $-\nabla\phi$ with respect to $-\nabla\chi\left(\gamma\right)$

the magnitude of $-\frac{1}{\chi\left(\gamma\right)}\left(-\nabla\phi\right)\cdot\left(-\nabla\chi\left(\gamma\right)\right)$ which can be written as

$$\left|-\frac{1}{\chi\left(\gamma\right)}\left(-\nabla\chi\left(\gamma\right)\right)\cdot\left(-\nabla\phi\right)\right| \tag{3.25}$$

$$= \left|-\frac{1}{\chi\left(\gamma\right)}\left\|-\nabla\chi\left(\gamma\right)\right\|_2\right|\left\|-\nabla\phi\right\|_2\cos\theta \tag{3.26}$$

Where θ is the angle between the direction of decreasing communication performance $-\nabla\chi\left(\gamma\right)$ and direction of motion $-\nabla\phi$ as shown in Fig. 3.10. $\chi\left(\gamma\right)$ at a point is constant with respect to time (as environment is assumed constant in this scenario) therefore, $\left\|-\nabla\chi\left(\gamma\right)\right\|$ is also constant with respect to time at each point in the workspace. Similarly, $\left\|-\nabla\phi\right\|$ and ϕ do not vary with time and are constant at a point in the workspace. Therefore, the magnitude in Eq. (3.26) will only vary with θ (the orientation of $-\nabla\phi$ with respect to $-\nabla\chi\left(\gamma\right)$).

Figures 3.8 and 3.9 depict extreme cases where the vectors $-\nabla\phi$ and $-\nabla\chi\left(\gamma\right)$ are perfectly aligned ($\theta = 0°$) or diametrically opposite ($\theta = 180°$) respectively (i.e.

there is no component of $-\nabla\phi$ in any other direction). Generally, if any component of $-\nabla\phi$ is aligned with $-\nabla\chi\left(\gamma\right)$ at a point, the divergence of $\nabla\phi$ at that point will be negative and that point acts as a sink. Its strength depends on the orientation, θ, of $-\nabla\chi\left(\gamma\right)$ with respect to $-\nabla\chi\left(\gamma\right)$. Similarly, if any component of $-\nabla\phi$ is antipodal to $-\nabla\chi\left(\gamma\right)$ then the divergence of $\nabla\phi$ at that point is positive and the point acts as a source with its strength modulated by θ. Finally, it can be noted from Eq. (3.26) that when the vectors $-\nabla\phi$ and $-\nabla\chi\left(\gamma\right)$ are orthogonal (there is no component of $-\nabla\phi$ parallel to $-\nabla\chi\left(\gamma\right)$) then the divergence at that point is zero. The right hand side of Eq. (3.24) reduces to zero and motion is guided by the simple Laplace equation [13], [15] such that energy due to motion is minimized and communication performance is ignored.

The MBCAN procedure is given in algorithm 1.

Algorithm 1 Model-Based Communication-Aware Navigation (MBCAN)

```
Get Workspace $\mathcal{W}$.
Get SNR representation $\gamma(\mathbf{p})$ for $\mathcal{W}$.
Get HO representation $\mathcal{O}(\mathbf{p})$ for $\mathcal{W}$.
Get start position $\mathbf{p}_S$ of agent.
GHPF($\mathcal{W}$,$\chi\left(\gamma\right)$,$\mathcal{O}$,$\mathbf{p}_S$,$\mathbf{p}_G$).          ▷ Calling function GHPF
Find $\mathbf{p}_S{}'$ using Eq. (3.18)
Solve $\dot{\mathbf{p}} = \int_0^\infty -\nabla\phi dt,\ \mathbf{p}(0) = \mathbf{p}_S{}'$ for $\mathbf{p}(t)$.
function GHPF($\mathcal{W}$,$\chi\left(\gamma\right)$,$\mathcal{O}$,$\mathbf{p}_S$,$\mathbf{p}_G$)
    Set $\frac{\partial\phi}{\partial n} = 0$ at $\mathbf{\Gamma}_{\mathcal{W}}$.
    Set $\frac{\partial\phi}{\partial n} = 0$ at $\mathbf{\Gamma}_{\mathcal{O}}$.
    Set $\phi(\mathbf{p}_S) = 1$.
    Set $\phi(\mathbf{p}_G) = 0$.
    Solve $\nabla\cdot\left(\chi\left(\gamma\right)\nabla\phi\right) = 0$ for $\phi$.
    return $\phi$.
end function
```

3.3.1 Communication-Blind Model-Based Navigation

In the case, the agent is oblivious to its communication performance, its path to the goal is computed using the same strategy as detailed in the MBCAN algorithm but with the SNR field in Eq. (3.15) equal to a finite constant, γ_{const}. This reduces Eq. (3.15) to the simple Laplace equation as shown in the following.

$$\begin{aligned} &\text{solve} && \nabla \cdot (\gamma_{const} \nabla \phi(\mathbf{p})) = 0,\ \mathbf{p} \in \mathcal{W} && \text{(3.27a)} \\ &\text{subject to} && \phi(\mathbf{p}_S) = 1,\ \phi(\mathbf{p}_G) = 0,\ \frac{\partial \phi}{\partial \mathbf{n}} = 0,\ \text{at } \mathbf{p} \in \mathbf{\Gamma}_{\mathcal{W}} && \text{(3.27b)} \\ & && \frac{\partial \phi}{\partial \mathbf{n}} = 0,\ \text{at } \mathbf{p} \in \mathbf{\Gamma}_{\mathcal{O}},\ \text{Neumann Boundary} && \text{(3.27c)} \end{aligned}$$

3.4 Analysis

In this section, a series of propositions and their proofs are presented regarding the characteristics of the MBCAN procedure provided in section 3.3.

PROPOSITION 3.1 *The trajectory generated by the gradient dynamical system in Eq.* (3.20) *will always avoid the HO*

$$\mathbf{p}(t) \bigcap \mathcal{O} = \varnothing,\ \forall t \tag{3.28}$$

Proof. The proof follows from the fact that the homogeneous Neumann boundary conditions at the HO boundary $\mathbf{\Gamma}_{\mathcal{O}}$ forces the motion to be tangent to the HO boundary. Thus the trajectory cannot cross the HO boundary and will always remain in

$\mathcal{W}_\phi$. $\mathcal{W}_\phi$ is defined as follows

$$\mathcal{W}_\phi = \mathcal{W} - \mathcal{O} \tag{3.29}$$

where $\mathcal{W}_\phi$ is the domain (a connected open subset) in which ϕ exists. ▌

PROPOSITION 3.2 *If the starting position of the agent lies outside the Dead Communication Zones (DCZ) (Def. 3.3),*

$$\mathbf{p}_S \bigcap \mathcal{O}_{DCZ} \equiv 0 \tag{3.30}$$

and the domain (a connected open subset) of acceptable communication performance, $\mathcal{W}_C$, is given by

$$\mathcal{W}_C = \mathcal{W}_\phi - \mathcal{O}_{DCZ} \tag{3.31}$$

Assuming no external force is acting on the agent, then the trajectory obtained by solving the gradient dynamical system in Eq. (3.20) *will always avoid DCZ.*

$$\mathbf{p} \in \mathcal{W}_C \subseteq \mathcal{W} \tag{3.32}$$

Proof. Similar to [9], rewriting Eq. (3.24), we get

$$\left(\left(-\nabla\chi\left(\gamma\right)\right) \cdot \left(-\nabla\phi\right)\right) = -\chi\left(\gamma\right)\left(\nabla^2\phi\right) \tag{3.33}$$

Since at the boundary of a DCZ, $\mathbf{\Gamma}_{\mathcal{O}_C}$,

$$\chi\left(\gamma(\mathbf{p})\right) \to 0 \tag{3.34}$$

then

$$(-\nabla\chi\left(\gamma\right))\cdot(-\nabla\phi)\to 0,\ \mathbf{p}\in\mathbf{\Gamma}_{\mathcal{O}_C} \tag{3.35}$$

$$\left\|-\nabla\chi\left(\gamma\right)\right\|_2\left\|-\nabla\phi\right\|_2\cos\theta\to 0,\ \mathbf{p}\in\mathbf{\Gamma}_{\mathcal{O}_C} \tag{3.36}$$

This implies that if the mapped-SNR at a point $\mathbf{p}$, $\chi\left(\gamma(\mathbf{p})\right)$, goes to zero then the dot product $(-\nabla\chi\left(\gamma(\mathbf{p})\right))\cdot(-\nabla\phi(\mathbf{p}))$ also goes to zero in order to satisfy Eq. (3.15). At a point on the boundary of a DCZ, the mapped-SNR goes from high to low, therefore,

$$\left\|-\nabla\chi\left(\gamma(\mathbf{p})\right)\right\|>0 \tag{3.37}$$

and since there are no local or global extrema within the domain of ϕ, $\mathcal{W}_\phi$ (see proposition 3.4),

$$\left\|-\nabla\phi(\mathbf{p})\right\|>0 \tag{3.38}$$

Therefore, for the dot product in Eq. (3.35) to go to zero,

$$\cos\theta\to 0 \tag{3.39}$$

$$\Rightarrow\theta\to 90^\circ, 270^\circ \tag{3.40}$$

Thus forcing the motion of the agent $-\nabla\phi$ to be tangent to the boundary of the DCZ $\mathbf{\Gamma}_{\mathcal{O}_C}$ and orthogonal to the direction of highest decrease in communication performance, $-\nabla\chi\left(\gamma(\mathbf{p})\right)$ as shown in Fig. 3.11. Therefore $\mathcal{O}_{DCZ}$ will always be avoided. ∎

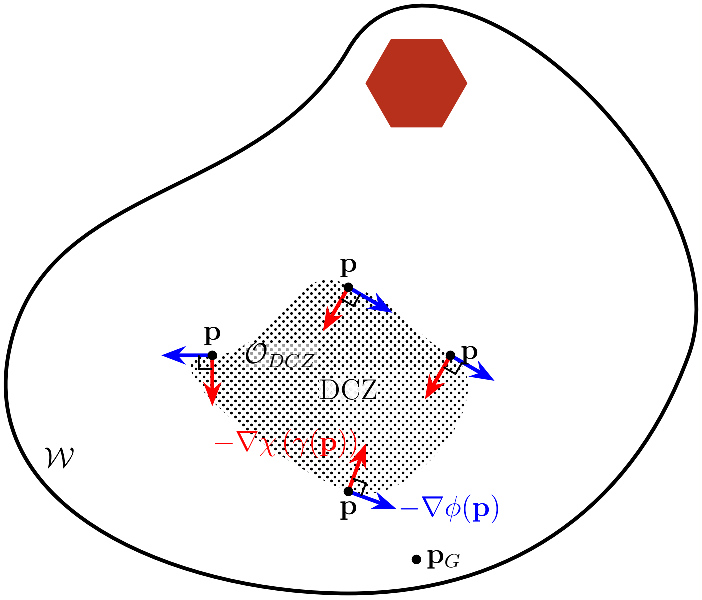

Figure 3.11: Motion at the boundary of DCZs is forced orthogonal to $-\nabla\chi\left(\gamma(\mathbf{p})\right)$ to satisfy Eq. (3.15)

This is an important implication in tackling DCZ. It implies that when an agent reaches the boundary of DCZs the potential flow, $-\nabla\phi(\mathbf{p})$ and consequently the motion of the agent at that point is forced orthogonal to the direction of decreasing communication performance, $-\nabla\chi\left(\gamma(\mathbf{p})\right)$. Thus motion is directed tangentially at the boundary of the DCZ. It acts as a boundary that cannot be breached much like the homogeneous Neumann boundary condition.

PROPOSITION 3.3 *If the starting position of an agent lies in a DCZ, $\mathbf{p}_S \in \mathcal{O}_{DCZ}$, or an agent is pushed in to a DCZ due to an external force, its motion will be governed by the Harmonic Potential Field (HPF). i.e., motion will be directed along the least energy path to the goal until the trajectory leaves the DCZ or reaches the goal.*

Proof. By definition of DCZ (Eq. (3.8))

$$\chi\left(\gamma(\mathbf{p})\right) = \epsilon_D, \forall \mathbf{p} \in \mathcal{O}_{DCZ} \tag{3.41}$$

Using Eq. (3.41) in Eq. (3.24), we get

$$\nabla^2\phi(\mathbf{p}) = -\frac{1}{\epsilon_D}\left(\left(-\nabla\chi\left(\gamma(\mathbf{p})\right)\right)\cdot\left(-\nabla\phi(\mathbf{p})\right)\right),\ \mathbf{p} \in \mathcal{O}_{DCZ} \tag{3.42}$$

Since, $\chi(\gamma) = \epsilon_D$ (Eq. (3.14)) is constant inside a DCZ (Def. 3.3), therefore, the gradient $-\nabla\chi\left(\gamma(\mathbf{p})\right)$ vanishes inside a DCZ.

$$-\nabla\chi\left(\gamma(\mathbf{p})\right) = 0,\ \forall \mathbf{p} \in \mathcal{O}_{DCZ} \tag{3.43}$$

Using Eq. (3.43) in Eq. (3.42), we get

$$\nabla^2\phi(\mathbf{p}) = 0, \forall \mathbf{p} \in \mathcal{O}_{DCZ} \tag{3.44}$$

Which is the simple Laplace equation and motion generated using Eq. (3.20) in a DCZ would be independent of the WCL performance of the agent as shown in Fig. 3.12. Motion generated using the HPF obtained using the simple Laplace equation makes the agent move so as to minimize the energy consumption due to motion (Section 1.2.3). ▮

Therefore motion within a DCZ would be decoupled from the WCL performance. This is a useful property for tackling DCZs since, if an agent starts inside or is bumped

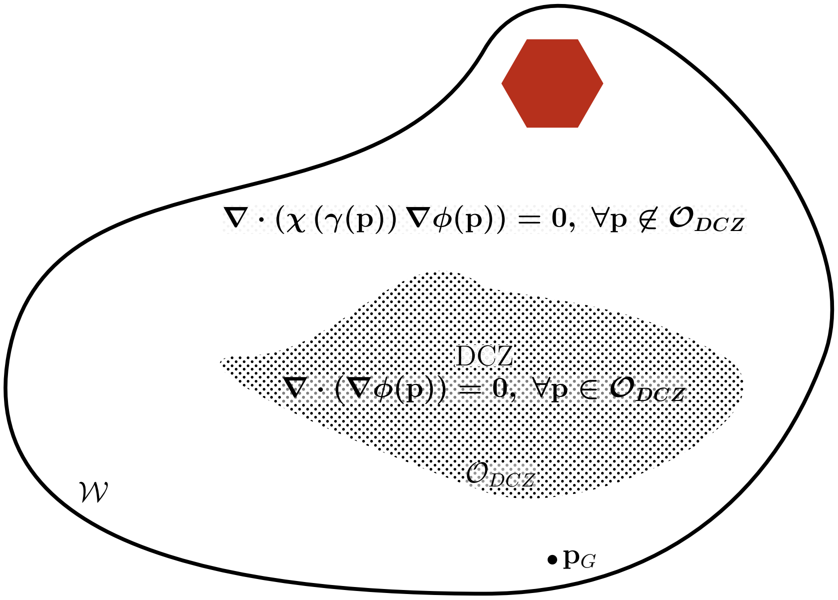

Figure 3.12: Motion inside a DCZ is governed by the simple Laplace equation independent of WCL performance.

into a DCZ due to some external force, motion would still be guaranteed towards the goal. This is a highly desirable property as it ensures motion even in the absence of a reliable WCL.

PROPOSITION 3.4 *By solving the Boundary Value Problem (BVP) in Eq.* (3.15)*, the potential field* ϕ *obtained will not have global or local extrema in its domain* $\mathcal{W}_\phi$

$$\mathcal{W}_\phi = \mathcal{W} - \mathcal{O} \tag{3.45}$$

Proof. Using proposition 3.2 and noting that

$$\nabla\phi(\mathbf{p}_j^C \in \mathcal{W}_\phi) = 0, j = 1, 2, \cdots, N_{CP} \tag{3.46}$$

where $\mathbf{p}_i^C \in \mathcal{W}_\phi$ are critical points, and N_{CP} is the total number of critical points in $\mathcal{W}_\phi$, Eq. (3.33) reduces to

$$\nabla \cdot (\gamma(\mathbf{p}_j^C)\nabla\phi(\mathbf{p}_j^C)) = \gamma(\mathbf{p}_j^C)\nabla^2\phi(\mathbf{p}_j^C) = \gamma(\mathbf{p}_j^C)\sum_{i=1}^{n}\frac{\partial^2\phi(\mathbf{p}_j^C)}{\partial x_i^2} = 0 \tag{3.47}$$

Assuming one of the critical points $\mathbf{p}_{min}^C \in \{\mathbf{p}_1^C, \mathbf{p}_2^C, \cdots, \mathbf{p}_{N_{CP}}^C\}$ is a minimum of ϕ, the second derivative for $\mathbf{p}_{min}^C$ will be positive for all x_is. Since $\gamma(\mathbf{p}) > 0, \forall \mathbf{p} \in \mathcal{W}_\phi$, this would violate Eq. (3.47).

If the agent starts from a DCZ or is pushed in to a DCZ because of an external force; Using the definition of DCZ (Eq. (3.8)) and proposition 3.3, Eq. (3.33) reduces to

$$\nabla^2\phi(\mathbf{p}_j^C) = \sum_{i=1}^{n}\frac{\partial^2\phi(\mathbf{p}_j^C)}{\partial x_i^2} = 0,\ \mathbf{p}_j^C \in \mathcal{O}_{DCZ} \tag{3.48}$$

Using the same argument as above, it can be shown that if a minimum of ϕ exists in the DCZ, it would violate the relationship Eq. (3.48).

The same line of argumentation holds if a maximum is assumed in $\mathcal{W}_\phi$. Thus, no extrema of ϕ can occur in $\mathcal{W}_\phi$. ▌

PROPOSITION 3.5 *$\phi(\mathbf{p}), \forall \mathbf{p} \in \mathcal{W}_\phi$, where $\mathcal{W}_\phi$ is of finite size, is a Lyapunov Function Candidate (LFC).*

Proof. Following the same argumentation as in [9], a LFC defined on a finite space must satisfy the following three conditions:

1. it should be at least continuous (belongs to $\mathcal{C}^0$).
2. it must be positive in $\mathcal{W}_\phi$, $\phi(\mathbf{p}) > 0, p \in \mathcal{W}_\phi$.

3. it should equal zero at the goal point $\mathbf{p}_G$, i.e., $\phi(\mathbf{p}_G) = 0$

Since ϕ is obtained as a solution of Eq. (3.15), it satisfies the first condition directly. Since the global maximum is at the starting point ($\phi(\mathbf{p}_S) = 1$) and the global minimum at the goal point ($\phi(\mathbf{p}_G) = 0$), therefore

$$1 < \phi(\mathbf{p}) < 0, \mathbf{p} \in \mathcal{W}_\phi \tag{3.49}$$

it should be noted that the boundary points are excluded from $\mathcal{W}_\phi$. Therefore, conditions two and three are also satisfied. Thus ϕ is a LFC. ▌

PROPOSITION 3.6 *If* $\phi(\mathbf{p})$ *is constant for any subset of* $\mathcal{W}_\phi$*, it is constant for all* $\mathcal{W}_\phi$

Proof. Following the same line of argumentation as in [9]. Let

$$\mathcal{A} \subset \mathcal{W}_\phi \tag{3.50}$$

and assume $\phi(\mathbf{p}) = a$, where a is constant. Let $\mathcal{A}'$ be an infinitesimal region surrounding $\mathcal{A}$ and $\mathbf{p}_o$ is a point that lies on the boundary $\partial\mathcal{A}$ of $\mathcal{A}$ and $\mathbf{p}_o^+$ lies on $\partial\mathcal{A}'$. The potential at $\mathbf{p}_o^+$ would then be given by

$$\phi(\mathbf{p}_o^+) = \phi(\mathbf{p}_o) + dr \cdot (-\nabla\phi(\mathbf{p}_o)^T n) \tag{3.51}$$

dr is a differential element and n is a unit vector normal to $\partial\mathcal{A}$. But, ϕ is constant in $\mathcal{A}$ which leads to the gradient degenerate to zero in $\mathcal{A}$. Since the governing relation

Eq. (3.15) imposes the continuity condition on ϕ, it is enforced on both $\mathcal{A}$ and $\mathcal{A}'$. Thus Eq. (3.51) reduces to

$$\phi(\mathbf{p}_o^+) = \phi(\mathbf{p}_o) = a \tag{3.52}$$

The above procedure can be expanded recursively, the subregion $\mathcal{A}$ can be shown to span the complete domain $\mathcal{W}_\phi$, implying that if ϕ is constant on any subset of $\mathcal{W}_\phi$, it would be constant for all $\mathcal{W}_\phi$. ∎

DEFINITION 3.6 *Let a function ϕ map a n-dimensional real space to real scalar*

$$\phi : \mathbb{R}^n \to \mathbb{R} \tag{3.53}$$

Let ϕ be twice differentiable, then a point $\mathbf{p}_c$ is called a critical point of ϕ if

$$\nabla\phi(\mathbf{p}_c) = 0 \tag{3.54}$$

A critical point is Morse if its Hessian matrix is nonsingular and a Morse function V is one in which all critical points are Morse [80]. Kodidchek in [81] propounded that for generating a provably correct navigation policy, the Potential Field (PF) should be Morse. Morse critical points are saddle points which do not trap motion and thus prevent the agent from reaching its target.

PROPOSITION 3.7 *Let $\phi(\mathbf{p})$ be a function defined in an n-dimensional space ($\mathbf{p} \in \mathbb{R}^n$) on an open set $\mathcal{W}_\phi$ and satisfies Eq. (3.15), then ϕ is Morse (Hessian matrix at all the critical points of ϕ are nonsingular).*

Proof. The proof can be established as in [9]. The following two properties of ϕ are the basis of the proof.

1. From proposition 3.4, $\phi(\mathbf{p}), \mathbf{p} \in \mathcal{W}_\phi$ has no maxima or minima in $\mathcal{W}_\phi$. An extrema of $\phi(\mathbf{p})$ can only occur at the boundary of $\mathcal{W}_\phi$, $\partial\mathcal{W}_\phi$.
2. From proposition 3.6, ϕ is constant in any open subset of $\mathcal{W}_\phi$, then it is constant for all $\mathcal{W}_\phi$.

Let $\mathbf{p}_c \in \mathcal{W}_\phi$ be a critical point of ϕ then $\mathbf{p}_o$ is a saddle point as no extrema of ϕ exists in $\mathcal{W}_\phi$. Expanding $\phi(\mathbf{p})$ in the neighborhood of $\mathbf{p}_c$ using a second order Taylor series

$$\phi(\mathbf{p}) = \phi(\mathbf{p}_c) + \nabla\phi(\mathbf{p}_o)^T + \frac{1}{2}(\mathbf{p} - \mathbf{p}_c)^T H(\mathbf{p}_c)(\mathbf{p} - \mathbf{p}_c), |\mathbf{p} - \mathbf{p}_c| \ll 1. \tag{3.55}$$

At the critical point $\mathbf{p}_c$ the gradient of ϕ vanishes, reducing Eq. (3.55) to

$$\phi' = \phi(\mathbf{p}) - \phi(\mathbf{p}_c) = \frac{1}{2}(\mathbf{p} - \mathbf{p}_c)^T H(\mathbf{p}_c)(\mathbf{p} - \mathbf{p}_c), |\mathbf{p} - \mathbf{p}_c| \ll 1. \tag{3.56}$$

Adding or subtracting a constant to ϕ gives another potential field ϕ' which satisfies Eq. (3.15). Applying eigenvalue decomposition to Λ in Eq. (3.56), we get

$$\phi' = \frac{1}{2}(\mathbf{p} - \mathbf{p}_c)^T U^T \begin{bmatrix} \lambda_1 & 0 & \cdots & 0 \\ 0 & \lambda_2 & \cdots & 0 \\ & \vdots & & \\ 0 & 0 & \cdots & \lambda_n \end{bmatrix} U(\mathbf{p} - \mathbf{p}_c) \tag{3.57}$$

$$= \frac{1}{2}\boldsymbol{\zeta}^T \begin{bmatrix} \lambda_1 & 0 & \cdots & 0 \\ 0 & \lambda_2 & \cdots & 0 \\ & \vdots & & \\ 0 & 0 & \cdots & \lambda_n \end{bmatrix} \boldsymbol{\zeta} \tag{3.58}$$

$$= \frac{1}{2}\sum_{k=1}^{n} \lambda_k \zeta_k^2. \tag{3.59}$$

U is a matrix of orthonormal eigenvectors, λ_k are the eigenvalues of $H(\mathbf{p}_c)$ and

$$\boldsymbol{\zeta} = [\zeta_1, \zeta_2, \cdots, \zeta_n]^T \tag{3.60}$$

$$= U(\mathbf{p} - \mathbf{p}_c) \tag{3.61}$$

Since ϕ' cannot be zero in any subset of $\mathcal{W}_\phi$, Eq. (3.59) will only be true if all λ_ks are non-zeros. This implies that the Hessian at critical points $\mathbf{p}_c$ of ϕ is nonsingular. Thus ϕ is a Morse function. ▮

PROPOSITION 3.8 *The trajectory of the agent*

$$\dot{\mathbf{p}} = \mathbf{u} \tag{3.62}$$

denoted by $\mathbf{p}(t)$ *from the dynamical system*

$$\dot{\mathbf{p}} = -\nabla\phi(\mathbf{p}) \tag{3.63}$$

will always (asymptotically) converge to th goal position $\mathbf{p}_G$.

$$\lim_{t\to\infty} \mathbf{p} \to \mathbf{p}_G,\ \ \mathbf{p}(0) = \mathbf{p}_S \in \mathcal{W}_\phi \tag{3.64}$$

Where $\phi(\cdot)$ *is obtained as a solution to the system given in Eq.* (3.15).

Proof. Using the same argument as in [9], from proposition 3.5, ϕ is a LFC. Let Λ represent the LFC $\phi(\mathbf{p})$, where $\mathbf{p}(t), \mathbf{p}(0) = \mathbf{p}_S$ is the trajectory of the agent.

$$\Lambda = \phi(\mathbf{p}) \tag{3.65}$$

The time derivative of Eq. (3.65) can be obtained using the chain rule.

$$\dot{\Lambda}(\mathbf{p}, \dot{\mathbf{p}}) = \nabla\phi(\mathbf{p})^T \dot{\mathbf{p}} \tag{3.66}$$

substituting Eq. (3.20) in Eq. (3.66)

$$\dot{\Lambda} = -\left\|\nabla\phi(\mathbf{p})\right\|^2 \tag{3.67}$$

$\nabla\phi$ vanishes at the goal $\mathbf{p}_G$ and might have isolated critical points $\{\mathbf{p}_{c_i}\}, i = 1, 2, 3, \cdots, n_c$ (n_c is the number of isolated critical points) in $\mathcal{W}_\phi$. This leads to

$$\dot{\Lambda} \leq 0, \forall \mathbf{p} \in \mathcal{W}_\phi \tag{3.68}$$

The LaSalle principle [82] states that any bounded solution of Eq. (3.20) will converge to the minimum invariant set

$$\mathcal{I} \subset \{\mathbf{p}_G \cup \{\mathbf{p}_{c_i}\}\}. \tag{3.69}$$

where finding $\mathcal{I}$ requires studying critical points of $\mathbf{p}$

$$\{\mathbf{p}_{c_i}\} = \{\mathbf{p} | \nabla\phi(\mathbf{p}) = 0\} \tag{3.70}$$

From proposition 3.4, $\mathbf{p}_G$ is the only minimum (a stable equilibrium point) of $\phi(\mathbf{p})$. On the other hand, $\{\mathbf{p}_{c_i}\}$ are isolated critical points where the Hessian of ϕ is nonsingular and therefore, the isolated critical points are Morse (proposition 3.7). Thus it can be concluded that $\mathcal{I}$ can only have one point to which motion can converge. ▌

PROPOSITION 3.9 *The magnitude of the product,*

$$\rho(\mathbf{p}(t)) = -\nabla\phi(\mathbf{p}(t))\gamma(\mathbf{p}(t)), \forall t, \tag{3.71}$$

defined in Eq. (3.16) *is constant along the trajectory described by Eq.* (3.20) *and is equal to* $|\rho(\mathbf{p}_S{}')|$. *Where,* ϕ *is obtained as a solution to Eq.* (3.15).

Proof. It can be noted that Eq. (3.15) implies that the divergence of the term

$$\gamma(\mathbf{p})\nabla\phi(\mathbf{p}),\ \mathbf{p} \in \mathcal{W}_\phi \tag{3.72}$$

is zero. In other words continuity of the product in Eq. (3.72) is imposed locally at each point in ϕ. But the product in Eq. (3.72) is represented by $\rho(\mathbf{p})$ as described in

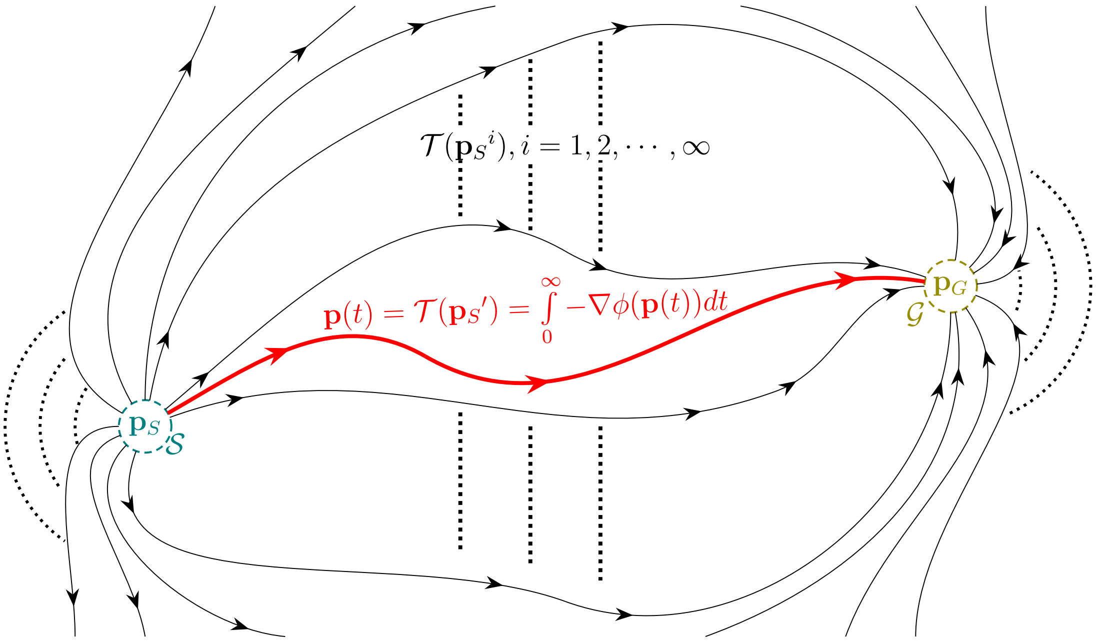

Figure 3.13: Possible trajectories from a start position to a goal position.

Eq. (3.16). Therefore, $|\rho(\mathbf{p}(t))|$ will be constant along the complete trajectory. Since at the starting point chosen on the sphere $\mathcal{S}$ (Algorithm 1), it is given by $|\rho(\mathbf{p}_S{}')|$, it can be concluded that

$$|\rho(\mathbf{p}(t))| = constant = |\rho(\mathbf{p}_S{}')| \qquad \blacksquare \tag{3.73}$$

DEFINITION 3.7 *Let $\mathcal{T}$ be a set of all possible trajectories (as defined in Def. 3.4), an agent can take from its starting position, $\mathbf{p}_S \in \mathcal{W}_\phi$, to the goal position, $\mathbf{p}_G \in \mathcal{W}_\phi$, in its workspace as shown in Fig. 3.13. A trajectory $\mathbf{q}_i \in \mathcal{T}$ can be realized by choosing a starting position, $\mathbf{p}_S{}^i$, on $\mathcal{S}$ (3.11) and then following the gradient of ϕ until the agent reaches the goal position (Eq.* (3.20)*). Since the PF obtained as a solution to*

(3.15) *is conservative [16], using the fundamental theorem of calculus [83], the line integral over any trajectory* $\mathbf{q}_i$ *over* ϕ *obtained as a solution to Eq.* (3.15) *will be given by*

$$\int_{\mathbf{p}_S=\mathbf{q}_i(0)}^{\mathbf{p}_G=\mathbf{q}_i(\infty)} -\nabla\phi(\mathbf{q}_i)\cdot d\vec{\mathbf{q}_i} = \phi(\mathbf{p}_S) - \phi(\mathbf{p}_G) = 1 \tag{3.74}$$

Using Eq. (3.16) *from definition 3.5, Eq.* (3.74) *can be written as*

$$1 = \int_{\mathbf{p}_S}^{\mathbf{p}_G} \frac{\rho(\mathbf{q}_i)}{\gamma(\mathbf{q}_i)}\cdot d\vec{\mathbf{q}_i} \tag{3.75}$$

where ρ *can be written as*

$$\rho = |\rho|\,\frac{\nabla\phi}{|\nabla\phi|} \tag{3.76}$$

Similarly $d\vec{\mathbf{q}_i}$ *can be written as*

$$d\vec{\mathbf{q}_i} = |\dot{\mathbf{q}}_i|\,\frac{\nabla\phi}{|\nabla\phi|}dt \tag{3.77}$$

Using Eq. (3.76) *and Eq.* (3.77) *in Eq.* (3.75) *we get,*

$$1 = \int_0^\infty \frac{|\rho|\,\frac{\nabla\phi}{|\nabla\phi|}}{\gamma}\cdot|\dot{\mathbf{q}}_i|\,\frac{\nabla\phi}{|\nabla\phi|}dt \tag{3.78}$$

$$= \int_0^\infty \frac{|\rho|\,|\dot{\mathbf{q}}_i|}{\gamma}dt \tag{3.79}$$

From proposition 3.9

$$|\rho(\mathbf{q}_i(t))| = constant, \forall t \tag{3.80}$$

This leads us to the definition of a functional, $\boldsymbol{\Upsilon}$, that returns a scalar for any trajectory taken by the agent

$$\boldsymbol{\Upsilon}(\mathbf{q}_i) = \frac{1}{|\rho|} = \int\limits_0^\infty \frac{|\dot{\mathbf{q}}_i|}{\gamma} dt \tag{3.81}$$

Note: It can be noted here that the relationship between γ and η is monotonic (Eq. (3.3)). Therefore, the γ in the funcational in Eq. (3.81) can be replaced by η without losing any of the properties of the presented algorithm

$$\frac{|\dot{\mathbf{q}}_i|}{\gamma} \Leftrightarrow \frac{|\dot{\mathbf{q}}_i|}{\eta} \tag{3.82}$$

Thus γ and η will be used interchangeable in the this work.

PROPOSITION 3.10 *The trajectory $\mathbf{p}(t) = \mathcal{T}(\mathbf{p}_S{}')$ obtained from the gradient dynamical system in Eq.* (3.20)*.*

$$\dot{\mathbf{p}} = -\nabla\phi(\mathbf{p}), \;\; \mathbf{p}(0) = \mathbf{p}_S{}' \in \mathcal{W}_\phi \tag{3.83}$$

where ϕ is obtained as a solution to Eq. (3.15) *minimizes the functional, $\boldsymbol{\Upsilon}$.*

$$\boldsymbol{\Upsilon}(\mathbf{p}) = \frac{1}{|\rho(\mathbf{p}(t))|} = \int\limits_0^\infty \frac{|\dot{\mathbf{p}}|}{\eta} dt \tag{3.84}$$

where the trajectory $\mathbf{p}(t)$ is parameterized by time.

Proof. In the MBCAN algorithm, the initial point, $\mathbf{p}_S{}'$, for solving the gradient dynamical system in Eq. (3.20) was chosen out of infinite points on $\mathcal{S}$ (Eq. (3.18)) such that ρ is maximum. Since $|\rho|$ is constant along a chosen trajectory (Proposition 3.9) and by definition $\boldsymbol{\Upsilon}$ (Eq. (3.81)) and $|\rho|$ are inversely related, therefore, the functional $\boldsymbol{\Upsilon}$ will be the minimum of all possible trajectories $\mathbf{q}_i = \mathcal{T}(\mathbf{p}_S{}^i)$. ▮

It can be noted that the integrand in Eq. (3.84) is the inverse of DFE as defined in Eq. (3.4). Therefore Eq. (3.84) can be rewritten as

$$\boldsymbol{\Upsilon}(\mathbf{p}) = \frac{1}{|\rho|} = \int_0^\infty \frac{1}{\beta(\mathbf{p}(t))} dt \tag{3.85}$$

PROPOSITION 3.11 *If the agent starts moving at time instant t_s and stops at time instant t_f (when it reaches within $\mathcal{G}$) using MBCAN, then the minimum β along its trajectory will be the maximum of the minimum β of all the other possible trajectories.*

$$\min_t \beta(\mathbf{p}(t)) \geq \min_t \beta(\mathbf{q}_i(t)), i = 1, 2, \cdots, \infty \tag{3.86}$$

Proof. It can be trivially shown for the reciprocal of the functional in Eq. (3.81) for starting time, t_s, and stopping time, t_f, that

$$\Xi(\mathbf{q}_i(t)) = \frac{1}{\boldsymbol{\Upsilon}(\mathbf{q}_i(t))} \leq \min_t \beta(\mathbf{q}_i(t)) \tag{3.87}$$

Since $\boldsymbol{\Upsilon}$ is minimum for $\mathbf{p}(t)$ obtained using MBCAN (proposition 3.10), then

$$\Xi(\mathbf{p}(t)) \geq \Xi(\mathbf{q}_i(t)), i = 1, 2, \cdots, \infty \tag{3.88}$$

Eq. (3.86) is a direct consequence of Eq. (3.88) ▮

PROPOSITION 3.12 *The functional in Eq.* (3.81) *is bounded.*

Proof. Eq. (3.81) can be written as

$$\frac{1}{|\rho|} = \int\limits_0^\infty \frac{|\dot{\mathbf{p}}|}{\gamma} dt \tag{3.89}$$

$$\leq \int\limits_0^\infty |\dot{\mathbf{p}}|\, dt \int\limits_0^\infty \frac{1}{\gamma} dt, \quad \because |\dot{\mathbf{p}}| > 0,\ \gamma > 0) \tag{3.90}$$

Notice that,

$$\int_0^\infty |\dot{\mathbf{p}}|\, dt = L \tag{3.91}$$

where L is the length of the path taken by the agent from start to goal position. Moreover, it can be observed that $\frac{|\dot{\mathbf{p}}|}{L}$ is a probability distribution function. Thus, the lower bound of the functional (Eq. (3.81)) can be found using the Jensen's inequality [84]. Rewriting Eq. (3.81), we get the lower bound as follows

$$L \int_0^\infty \frac{1}{\gamma} \cdot \frac{|\dot{\mathbf{p}}|}{L} dt \overset{Jensen's Inequality}{\geq} \frac{L}{\int_0^\infty \gamma \cdot \frac{|\dot{\mathbf{p}}|}{L} dt} \tag{3.92}$$

Therefore, the upper and lower bounds on the functional (Eq. (3.81)) are given as follows

$$\frac{L}{\int_0^\infty \gamma \cdot \frac{|\dot{\mathbf{p}}|}{L} dt} \leq \int\limits_0^\infty \frac{|\dot{\mathbf{p}}|}{\gamma} dt \leq \int\limits_0^\infty |\dot{\mathbf{p}}|\, dt \int\limits_0^\infty \frac{1}{\gamma} dt \qquad \blacksquare \tag{3.93}$$

PROPOSITION 3.13 *Letting* $\boldsymbol{\lambda}$ *describe the local coordinates of an agent and* $\mathbf{u}$ *be* *the control signal, then the trajectory of a system governed by the dynamic equation:*

$$\dot{\mathbf{p}} = G(\boldsymbol{\lambda}) \tag{3.94a}$$

$$\dot{\boldsymbol{\lambda}} = F(\boldsymbol{\lambda}, \mathbf{u}) \tag{3.94b}$$

and controlled by

$$\mathbf{u}(t) = \int_0^t k_1 \left(\frac{\partial F}{\partial \mathbf{u}}\right)^T \left[k_2 \left(\frac{\partial G}{\partial \boldsymbol{\lambda}}\right)^T [-\nabla\phi(\mathbf{p}) - \dot{\mathbf{p}}]\, \dot{\boldsymbol{\lambda}}\right] \tag{3.95a}$$

Such that:

$-\nabla\phi(\mathbf{p})$ *is obtained from Eq.* (3.15),

k_1, k_2 *are positive constants,*

$$\dot{\boldsymbol{\lambda}}(0) = k_2 \left(\frac{\partial G}{\partial \boldsymbol{\lambda}}\right)^T \left[-\nabla\phi(\mathbf{p}(0)) - \mathbf{p}\dot{(0)}\right] \tag{3.95b}$$

and

$$\dot{\mathbf{p}}(0) = -\nabla\phi(\mathbf{p}(0)) \tag{3.95c}$$

Satisfies

$$\lim_{t\to\infty} \mathbf{p}(t) \to \mathbf{p}_G \tag{3.96a}$$

$$\mathbf{p}(t) \bigcap \mathcal{O}_{DCZ} \equiv \phi,\ \forall t \tag{3.96b}$$

$$\mathbf{p}(t) \bigcap \mathcal{O} = \phi,\ \forall t \tag{3.96c}$$

$$\mathbf{p}(t) \in \mathcal{T} \mid \boldsymbol{\Upsilon}(\mathbf{p}(t)) \leq \boldsymbol{\Upsilon}(\mathbf{q}_i(t)), \mathbf{q}_i(t) \in \mathcal{T},\ \forall i = 1, 2, \cdots, \infty \tag{3.96d}$$

if and only if

$$\mathbf{p}_S \bigcap \mathcal{O}_{DCZ} \equiv 0. \tag{3.97}$$

Proof. A control signal of the form (Eq. (3.95)) can connect a kinematic path (single integrator system) that is generated from an underlying harmonic potential with an identical kinodynamic path for the system in Eq. (3.94). For proof see [24]. ▌

PROPOSITION 3.14 *The increase in the expected value of the SNR, $\mathbb{E}[\gamma]$, along a communication-aware path of length L_{CA} is equal to the increase of the length of the Communication-Aware Trajectory (CAT) relative to the length, L_{CB} of the Communication-Blind Trajectory (CBT).*

Proof. Using the Jensen's inequality for the communication-aware case as in Eq. (3.92), we have

$$\boldsymbol{\Upsilon}_{CA} = \int_0^\infty \frac{|\dot{\mathbf{p}}|}{\gamma} dt = L_{CA} \int_0^\infty \frac{1}{\gamma} \cdot \frac{|\dot{\mathbf{p}}|}{L_{CA}} dt \overset{Jensen'sInequality}{\geq} \frac{L_{CA}}{\displaystyle\int_0^\infty \gamma \cdot \frac{|\dot{\mathbf{p}}|}{L_{CA}} dt} = \frac{L_{CA}}{\mathbb{E}[\gamma(\dot{\mathbf{p}})]} \tag{3.98}$$

Since $\boldsymbol{\Upsilon}$ is minimized along the path, where MBCAN drives motion along,

$$\int_0^\infty \frac{|\dot{\mathbf{p}}|}{\gamma(\mathbf{p})} dt = \frac{L_{CA}}{\mathbb{E}[\gamma(\dot{\mathbf{p}})]} \tag{3.99}$$

Since for the communication blind-case (section 3.3.1), the SNR field is assumed to be equal to a constant γ_{const}. Therefore, the functional $\boldsymbol{\Upsilon}$ for the communication-blind case is given by

$$\boldsymbol{\Upsilon}_{CB} = \int_0^\infty \frac{|\dot{\mathbf{p}}|}{\gamma_{const}} dt = \frac{1}{\gamma_{const}} \int_0^\infty |\dot{\mathbf{p}}|\, dt = \frac{L_{CB}}{\gamma_{const}} \tag{3.100}$$

Taking the ratio of of Eq. (3.99) to Eq. (3.100), we get

$$\frac{\displaystyle\int_0^\infty \frac{|\dot{\mathbf{p}}|}{\gamma(\mathbf{p})} dt}{\displaystyle\frac{1}{\gamma_{const}} \int_0^\infty |\dot{\mathbf{p}}|\, dt} = \frac{\dfrac{L_{CA}}{\mathbb{E}[\gamma(\dot{\mathbf{p}})]}}{\dfrac{L_{CB}}{\gamma_{const}}} \tag{3.101}$$

$$\Rightarrow \mathbb{E}[\gamma(\dot{\mathbf{p}})] = \gamma_{const} \frac{L_{CA}}{L_{CB}} \tag{3.102}$$

Since, γ_{const} is constant, any increase in the path length of the CAT will lead to a gain in the mean SNR along the communication-aware trajectory. ▮

PROPOSITION 3.15 *MBCAN steers motion along the shortest path inside a DCZ.*

Proof. The MBCAN procedure minimizes the functional given in Eq. (3.81). For scenarios where, the agent starts in a DCZ, it can be written as

$$\boldsymbol{\Upsilon} = \boldsymbol{\Upsilon}' + \boldsymbol{\Upsilon}'' \tag{3.103}$$

where $\boldsymbol{\Upsilon}'$ is part of the integral that lies inside the DCZ and $\boldsymbol{\Upsilon}''$ is the part outside it. The component inside the DCZ can be written as

$$\boldsymbol{\Upsilon}' = \int_0^{t'} \frac{|\dot{\mathbf{q}}_i(t)|}{\gamma(\mathbf{q}_i(t))} dt \tag{3.104}$$

where $\mathbf{q}_i$ is the i$^{\text{th}}$ trajectory from $\mathbf{p}_S$ to $\mathbf{p}_G$ and t' is the time, the agent leaves the

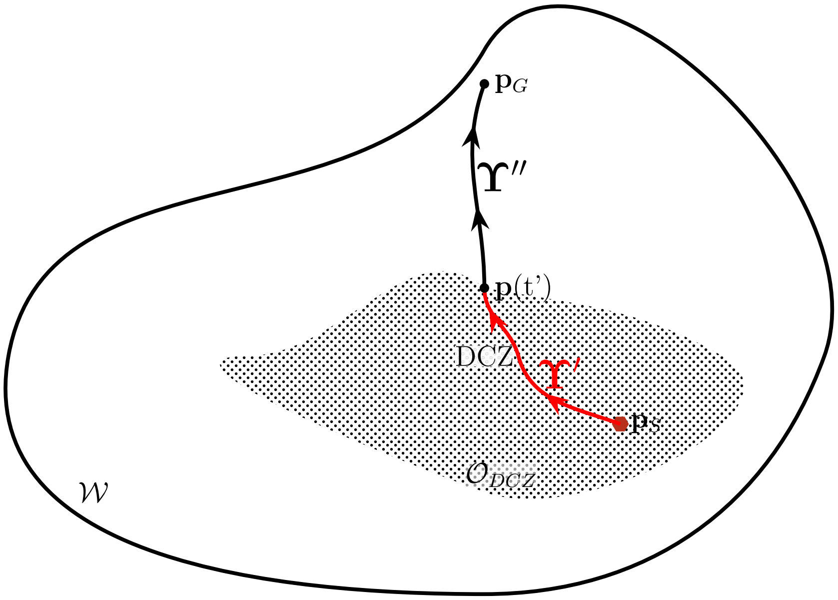

Figure 3.14: Trajectory inside a DCZ

DCZ. Since, from the definition of DCZ (def. 3.3),

$$\gamma(t) \leq \epsilon_D, 0 \leq t < t' \tag{3.105}$$

therefore, we can conservatively assume that

$$\gamma(t) = \epsilon_D, 0 \leq t < t'. \tag{3.106}$$

Substituting Eq. (3.106) in Eq. (3.104) we get,

$$\Upsilon' \simeq \int_0^{t'} \frac{|\dot{\mathbf{q}}_i(t)|}{\epsilon_D} dt \tag{3.107}$$

$$\simeq \frac{1}{\epsilon_D} \int_0^{t'} |\dot{\mathbf{q}}_i(t)| \, dt \tag{3.108}$$

$$\simeq \frac{L_{DCZ}}{\epsilon_D} \tag{3.109}$$

where L_{DCZ} is the trajectory in a DCZ. The functional $\boldsymbol{\Upsilon}$ can be rewritten as

$$\boldsymbol{\Upsilon} \simeq \frac{L_{DCZ}}{\epsilon_D} + \boldsymbol{\Upsilon}''. \tag{3.110}$$

Since from the definition of a DCZ (def. 3.3),

$$0 < \epsilon_D \lll 1 \tag{3.111}$$

therefore,

$$\boldsymbol{\Upsilon} \simeq \frac{L_{DCZ}}{\epsilon_D}. \tag{3.112}$$

Since MBCAN minimizes the functional $\boldsymbol{\Upsilon}$ and ϵ_D is constant, therefore, L_{DCZ} is minimized. ▮

From the differential properties of the trajectory obtained by Eq. (3.20), it can be seen that the magnitude of the velocity of the agent along its trajectory to goal is directly proportional to the magnitude of the gradient of ϕ at each point. A desirable property of the trajectory is that the agent spends more time in the region where it has better wireless channel characteristics. Conversely, the agent should spend less time in the region where it has poor wireless channel quality. The velocity of an agent at a point controls the time the agent spends at a position, This implies a relation between the SNR and the velocity of the agent at each point. Let the communication-aware energy be defined as the following product.

$$\gamma \left|\nabla\phi\right|^2 \tag{3.113}$$

This product is similar to the power consumption when a volumetric electric current flows through a conductor [79]. In a stationary environment, SNR at a position can be improved by increasing the transmission power but this would increase the energy consumption. Similarly, the velocity of the agent is directly proportional to $\nabla\phi$ and therefore, $|\nabla\phi|^2$ represents the actuation energy at the agent. Thus, Eq. (3.113) captures both the data-transmission and actuation energy of the agent at a point. Note that the BVP Eq. (3.15) minimizes the Dirichlet Integral [85], which has Eq. (3.113) as its integrand.

$$\int_{\mathcal{W}_\phi} \gamma \left|\nabla\phi\right|^2 d\mathcal{W}_\phi = \sum_{i=1}^{\infty} \int_{\mathbf{p}_S}^{\mathbf{p}_G} \gamma \left|\nabla\phi\right|^2 dq_i \tag{3.114}$$

The agent can choose from infinitely many trajectories, $\mathbf{q}_i, i = 1, 2, \cdots, \infty$, as shown in Fig. 3.13. Eq. (3.114) is a sum of line integrals that accumulate Eq. (3.113) over each trajectory $\mathbf{q}_i$. Any increase in path length of a trajectory will increase the line integral value. Moreover locally if the SNR is high in a region then, Eq. (3.113) can only be minimized if $|\nabla\phi|$ is minimized. Thus, minimization of Eq. (3.114) will assign the shorted possible trajectories to segments of the workspace with high γ.

The product in Eq. (3.113) can be seen as a product of transmission power and actuation power. Choosing the the trajectory that minimizes the integral in Eq. (3.114) is a variational problem. Using variational principles [86], it can be shown by perturbing ϕ and minimizing Eq. (3.114), we get the Laplace equation as the solution,

$$\nabla \cdot (\gamma\nabla\phi) = 0 \tag{3.115}$$

this is the same as the BVP Eq. (3.15). Eq. (3.115) enforces continuity on the product in Eq. (3.113). As a result, it can be seen that along a trajectory if the SNR goes low, the continuity condition will force $\nabla\phi$ to go high. Since velocity of the agent is directly proportional to $\nabla\phi$, the agent will move faster in regions with low SNR and by extension, the speed for the agent will be slow in high SNR region to maintain the continuity condition. Therefore, it can be seen that minimization of the Dirichlet integral for communication effort (Eq. (3.113)), manifests a tradeoff between energy consumption due to communication and energy consumption due to motion such that amount of data transmission over the complete trajectory is done in an energy-efficient manner. By moving fast in low SNR regions, the agent spends less time in that region and thus tries to reduce energy consumption due to data transmission and similarly, increases time spent in high SNR regions (where lesser energy is required to transmit the same amount of data) by moving slowly.

Fig. 3.15 depicts the behavior of MBCAN locally at the intersection of two different SNR regions. It shows equi-potential lines superimposed on the region. Equi-potential lines are positions where the potential is equal to some constant $c_i \in \mathbb{R}$.

$$\phi(\mathbf{p}) = c_i, i = 1, 2, \cdots, \infty \tag{3.116}$$

$$c_{i+1} > c_i \tag{3.117}$$

The potential lines are equally spaced, i.e. they have the same gradient in the region with same SNR. This gradient changes when the potential lines enter a region with different SNR. This is due to continuity (divergence of flow density vanishes) being imposed locally by Eq. (3.15). Let $\phi_1(\mathbf{p}), \forall\mathbf{p} \in \{\mathbf{p}|\gamma\mathbf{p} = \gamma_1\}$ be the potential in the

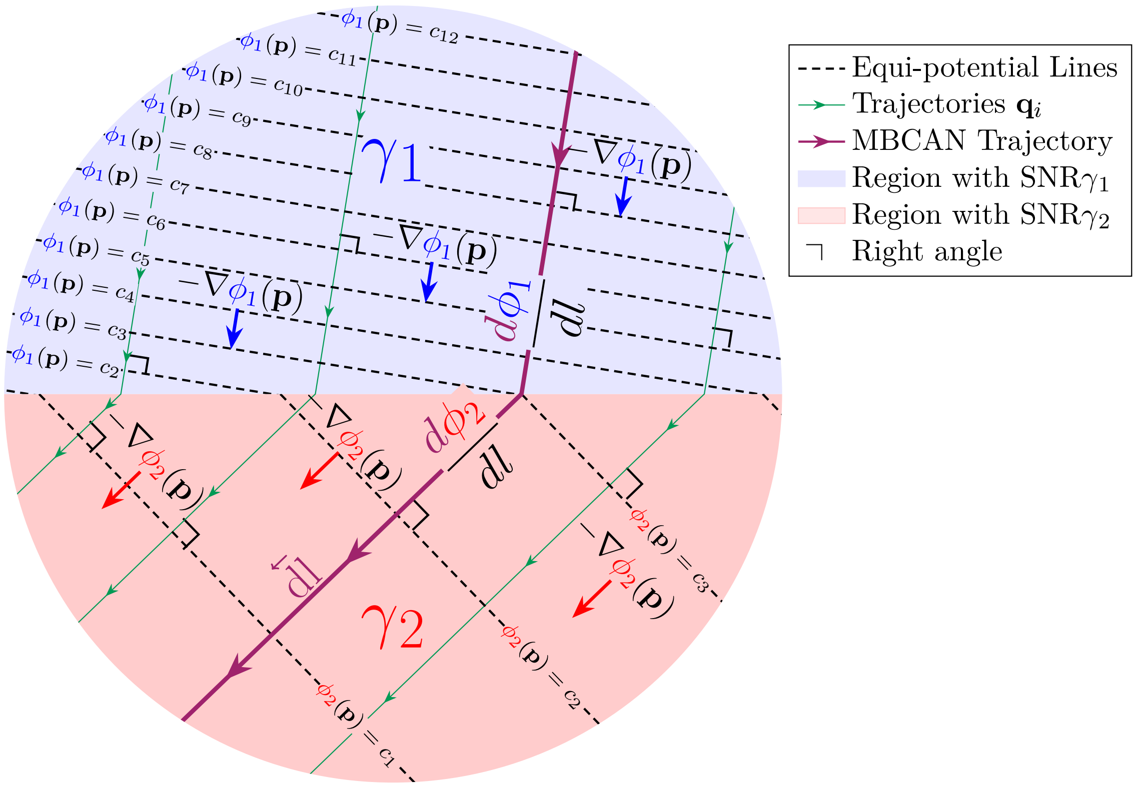

Figure 3.15: Local behavior of MBCAN when the SNR changes

region with SNR $\gamma_1(\mathbf{p})$ and $\phi_2, \forall \mathbf{p} \in \{\mathbf{p}|\gamma\mathbf{p} = \gamma_2\}$ be the potential in the region with SNR γ_2. Then as a consequence of Eq. (3.15),

$$|\gamma_1 \nabla\phi_1(\mathbf{p})| = |\gamma_2 \nabla\phi_2(\mathbf{p})| \tag{3.118}$$

From Fig. 3.15, if we observe the change in gradient along the MBCAN trajectory in the two SNR regions, then Eq. (3.118) can be rewritten as,

$$\gamma_1 \frac{d\phi_1}{dl} = \gamma_2 \frac{d\phi_2}{dl}. \tag{3.119}$$

Since

$$\gamma_1 \neq \gamma_2 \tag{3.120}$$

therefore,

$$\frac{d\phi_1}{dl} \neq \frac{d\phi_2}{dl} \tag{3.121}$$

Now, if we observe a constant change in ϕ, $d\phi$ along the MBCAN trajectory in both regions, i.e.,

$$d\phi_1 = d\phi_2 = d\phi \tag{3.122}$$

then this would lead to a different change in length, dl, to preserve the condition in Eq. (3.121).

$$\frac{d\phi_1}{dl} = \frac{d\phi}{dl_1} \neq \frac{d\phi}{dl_2} = \frac{d\phi_2}{dl}, dl_1 \neq dl_2 \tag{3.123}$$

Using Eq. (3.121) in Eq. (3.119), we get,

$$\gamma_1 \frac{d\phi}{dl_1} = \gamma_2 \frac{d\phi}{dl_2}. \tag{3.124}$$

Taking the ratio of γ_2 to γ_1 using Eq. (3.124) we get,

$$\frac{\gamma_2}{\gamma_1} = \frac{dl_2}{dl_1}. \tag{3.125}$$

Equation 3.125, gives a key relation between the trajectory length and the SNR in a region. From Eq. (3.125), if,

$$\gamma_2 > \gamma_1 \tag{3.126}$$

then

$$dl_2 > dl_1. \tag{3.127}$$

Thus, locally,the component of the trajectory which lies in a region with higher SNR is increased and vice verse. The MBCAN procedure increases the time an agent spends in a region with higher SNR whereas the time spent in regions with low SNR is reduced.

3.5 Computational Complexity

The MBCAN algorithm was given in detail in section 3.3. The steps required to obtain the MBCAN trajectory require solving the Partial Differential Equation (PDE) in Eq. (3.15) over the workspace and then iteratively obtaining each step of the trajectory (Eq. (3.20)) until the goal is reached.

Eq. (3.15) is a variable coefficient Laplace equation (elliptic PDE). It can be solved over a workspace by discretizing the workspace and solving the PDE using the boundary conditions given in Eq. (3.15). There are two predominant methods [87] used to solve PDEs,

- Finite Difference Method (FDM).
- Finite Element Method (FEM).

FDM works on a simple rectangular discretization of the workspace, where as, FEM requires more advanced meshing. However, meshing can discretize grids of any geometry. Both, the FDM and FEM methods require solving a linear system of equations.

$$\mathbf{A}\mathbf{x} = \mathbf{b} \tag{3.128}$$

This requires inversion of matrices for a direct solution [87]. However, iterative numerical method schemes can be employed which drastically lower the computational time at the cost of accuracy. Iterative solution can also have convergence issues.

Apart from computational complexity, discretization also requires storage for storing the discretized values. Thus storage complexity has to be taken in to account as well when solving a PDE over the workspace. The computational and storage complexity of different algorithms used to solve the PDE is given in table 3.1. Considerable effort has also been done in developing hardware dedicated to path-planning resulting in a large reduction in computation time. Memristors based planners chips that can generate a plan in micro-seconds [88], [89].

Algorithm	Type	Time	Storage
Inversion	Direct	$\mathcal{O}\left(n^3\right)$	$\mathcal{O}\left(n^2\right)$
LU Decomposition	Direct	$\mathcal{O}\left(n^3\right)$	$\mathcal{O}\left(n^2\right)$
Jacobi	Iterative	$\mathcal{O}\left(n^2\right)$	$\mathcal{O}\left(n\right)$
Gauss-Seidel (GS)	Iterative	$\mathcal{O}\left(n^2\right)$	$\mathcal{O}\left(n\right)$
Conjugate Gradient (CG)	Iterative	$\mathcal{O}\left(n^{\frac{3}{2}}\right)$	$\mathcal{O}\left(n\right)$
Successive Over-Relaxation (SOR)	Iterative	$\mathcal{O}\left(n^{\frac{3}{2}}\right)$	$\mathcal{O}\left(n\right)$
Fast Fourier Transform (FFT)	Direct	$\mathcal{O}\left(n \log n\right)$	$\mathcal{O}\left(n\right)$
Multigrid	Iterative	$\mathcal{O}\left(n\right)$	$\mathcal{O}\left(n\right)$
Parallel Jacobi	Iterative	$\mathcal{O}\left(\frac{n^2}{p}\right)$	$\mathcal{O}\left(n\right)$
Parallel RB GS	Iterative	$\mathcal{O}\left(\frac{n^2}{p}\right)$	$\mathcal{O}\left(n\right)$
Parallel RB SOR	Iterative	$\mathcal{O}\left(\frac{n\sqrt{n}}{p}\right)$	$\mathcal{O}\left(n\right)$

p = # of processors, RB = Red-Black (RB) method [1]

Table 3.1: Time and memory complexity of different algorithms [1], [2] for solving the PDE given in Eq. (3.15)

3.6 Results

In the following we present a series of results to demonstrate the capabilities of the MBCAN algorithm algorithm we developed in the previous sections. We consider a 10m×10m rectangular environment. The SNR at each point in the environment is generated using wireless channel gains obtained using the WINNER channel models [90] for an indoor environment. The transmission frequency is taken to be 2.54 GHz and zero mean AWGN, unit variance ($\mathcal{N}(0,1)$), Gaussian noise was assumed at the receiver. Letting the transmitted power to be 1, the SNR at any point in the environment is given by

$$\gamma = \frac{\mathbf{h}\mathbf{h}^*}{\sigma^2} \tag{3.129}$$

Where $\mathbf{h} \in \mathbb{C}$ is the complex channel gain from a single-antenna BS to a single-antenna agent. The simulation parameters are given in table 3.2.

In the following subsections, we will present different scenarios for the case where the SNR-map for the complete environment is known to the agent.

Parameter	Value
Environment Dimensions	10m×10m
Agent Type	Point Agent
Antennas at BS	1
Antennas at agent	1
Communication Scheme	TDD
Transmission Frequency	2.54 GHz
Receiver Noise	$\sim \mathcal{N}(0,1)$
ϵ_D	-70 dB

Table 3.2: Simulation Parameters

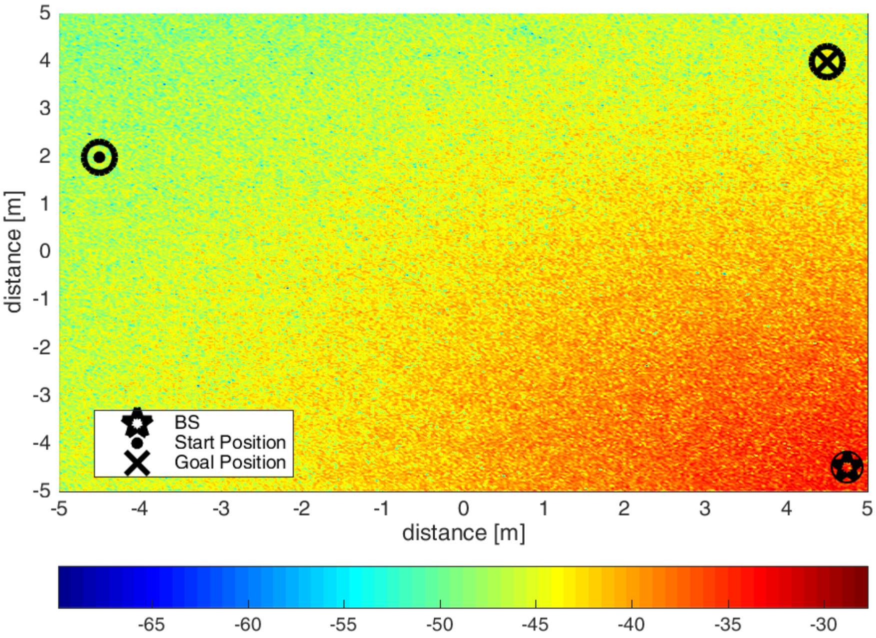

Figure 3.16: SNR map of an empty environment.

3.6.1 MBCAN: Empty Environment

Let an agent move from a start position to a goal position in the above described environment containing no physical obstacles. The SNR-map with the BS at position $(5, -5)$, is given in Fig. 3.16. Trajectories were computed using MBCAN for the scenario where the agent is aware of the SNR-map (CAT) and when its blind to it (CBT). Fig. 3.17 shows both the CAT in red color and CBT in blue dots. It can be seen that the CAT bends towards the high SNR region. This is due to the knowledge of the SNR-map. The MBCAN algorithm tries to maximize the SNR at each point along the trajectory while ensuring that the agent reaches the goal as well. In the case when the agent is blind to the SNR-map, it goes straight towards the target without wandering or other undesirable motion actions. The trajectory in the communication-aware case is longer than the unknown case. This increase in length is explained by the

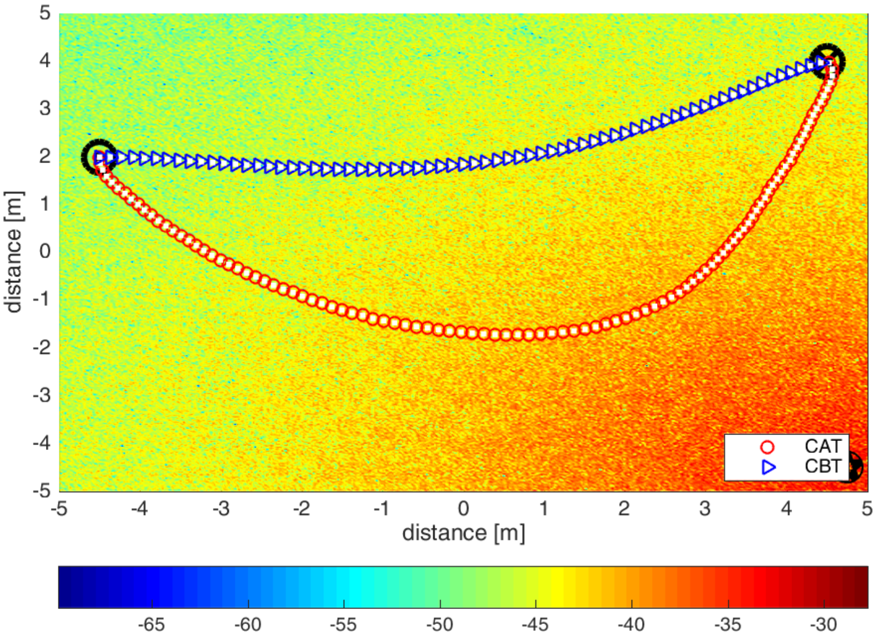

Figure 3.17: Trajectory From Start to Goal Positions

gain in WCL performance along the trajectory and will be explained later. Another important point to note, however, is that the CAT also has no loops. This is a direct consequence of the path being generated from the gradient of a HPF

The SNR at each point along both the CAT and CBT is shown in Fig. 3.18 It can be seen that both the trajectories start in the same SNR region but as they move towards the goal, the SNR along CAT increases. Finally, both the trajectories converge to the same SNR region about the goal position. The mean SNR of the CAT is greater than the mean SNR of CAT.

Fig. 3.19 shows multiple trajectories for the scenario given in Fig. 3.16 along with the CAT. The trajectories have been computed using different starting orientations other than $\mathbf{p}_S{}'$ (Eq. (3.18)) and then using the PDE-Ordinary Differential Equation (ODE) system in Eq. (3.20) using the PF obtained from Eq. (3.15)

Fig. 3.20 compares the magnitude of the product ρ (Eq. (3.16) for different starting

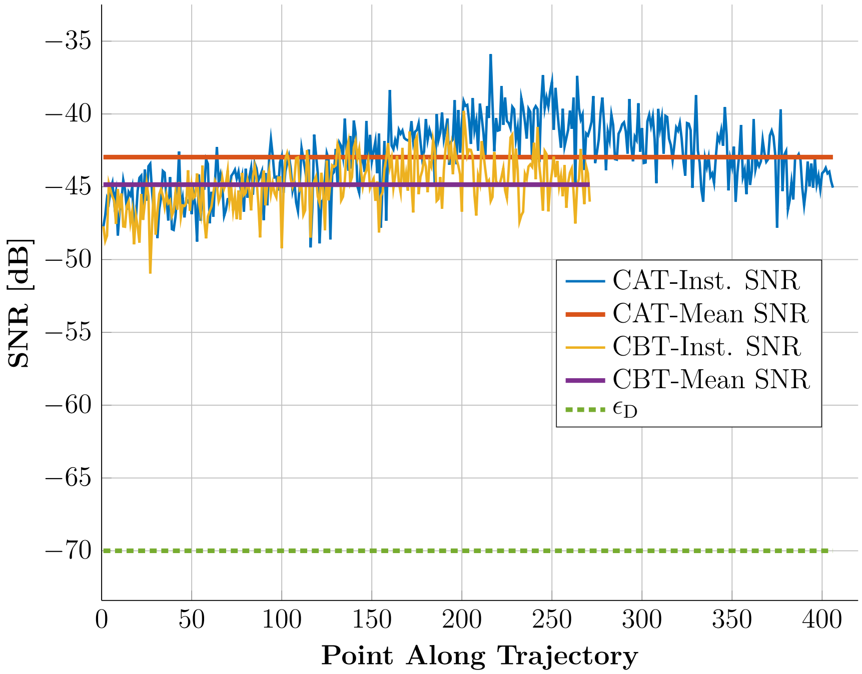

Figure 3.18: Comparison of SNR along CAT and CBT

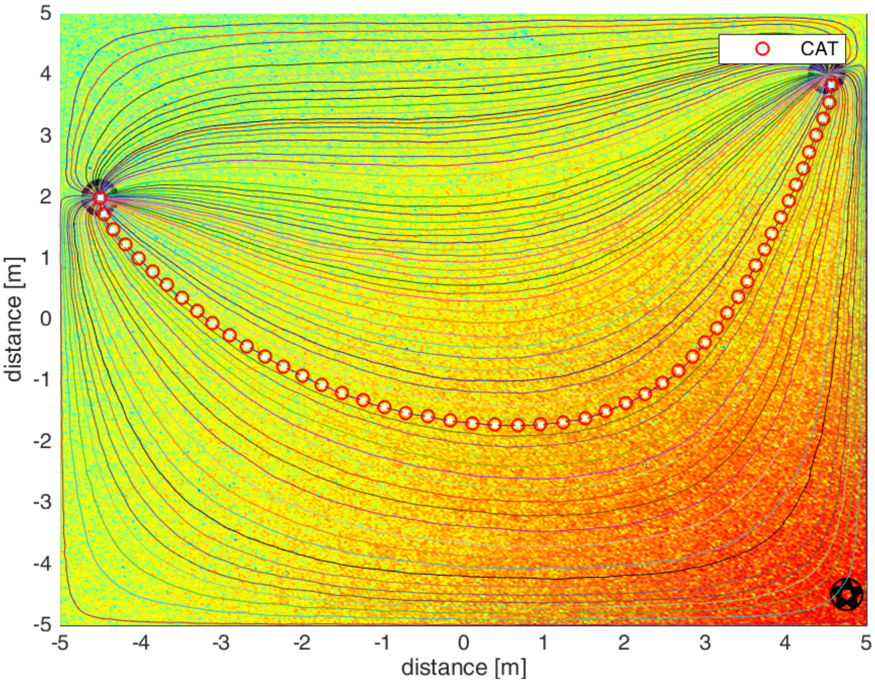

Figure 3.19: Trajectories due to Different Starting Orientations

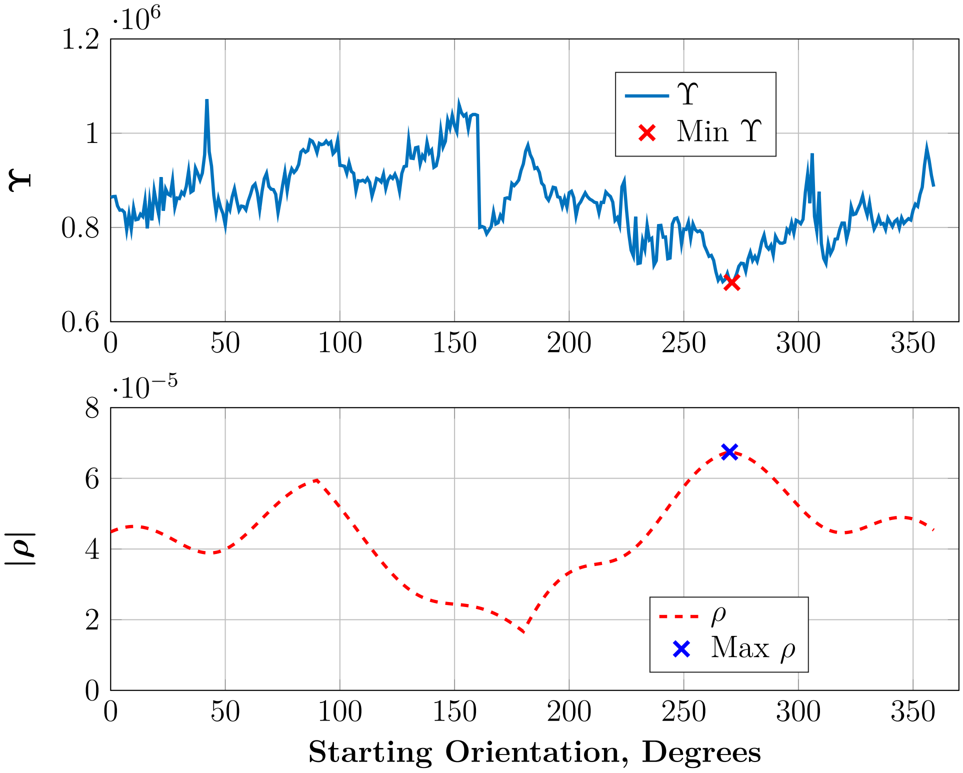

Figure 3.20: $|\rho|$ (Eq. (3.16)) and functional (Eq. (3.81)) Values for Trajectories due to Different Starting Orientations Given in Fig. 3.19

orientations of the agent with the functional magnitude $|\Upsilon|$ (Eq. (3.81)) from the resulting trajectories. It can be seen that the functional value has its minimum at the starting orientation where the magnitude of ρ is the highest.

Fig. 3.21 shows the Cumulative Distribution Function (CDF) of the instantaneous SNR along 4000 different trajectories obtained using random start and goal positions for the environment in Fig. 3.16. It can be seen that since both the CAT and CBT have a Line Of Signt (LoS) link with the BS, their CDFs nearly match. The CDF of the mean-SNR along 4000 different trajectories obtained for different random start and goal positions is given in Fig. 3.22. It can be seen that the CDF of the mean-SNR of the CATs gives an improvement of up to $1dB$ over the CBTs CDF. Therefore, there is a gain in the overall data-transmission performance for the CATs but the

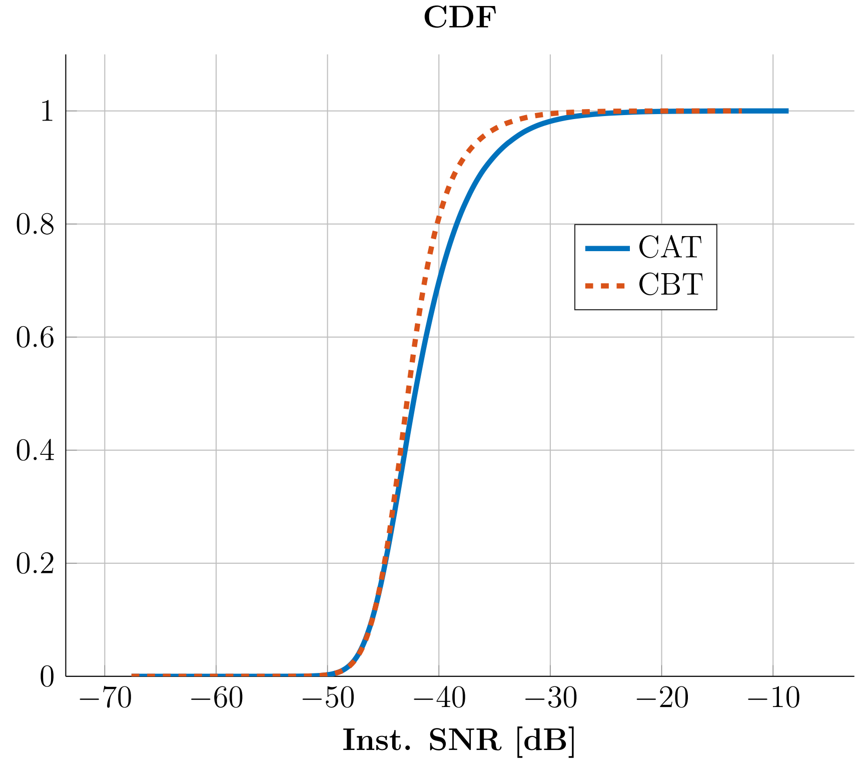

Figure 3.21: CDF of Instantaneous SNR along multiple trajectories with random start and goal positions.

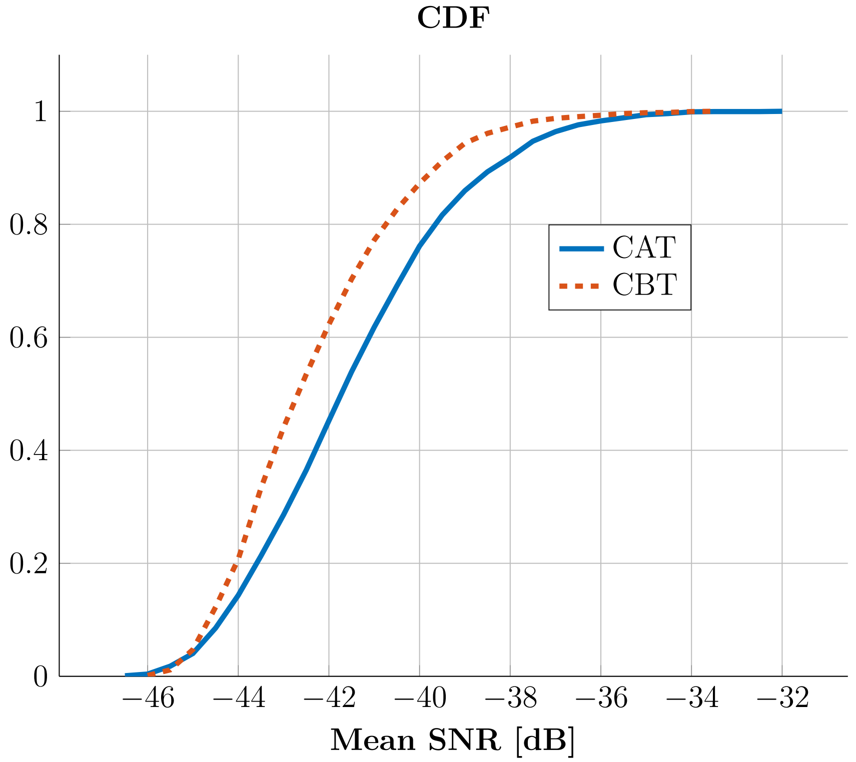

Figure 3.22: CDF of the mean-SNR along different trajectories obtained using multiple random start and goal positions.

improvement is not significant as the complete region has a LoS link to the BS.

3.6.2 MBCAN: Environment with a Single Obstacle

So far we have shown the CAT and CBT in empty environments which have no physical obstacles. Fig. 3.23 shows a scenario with one rectangular physical obstacle. The BS is located at the position $(5, -5)$. Physical obstacles not only block the path of the agent, they also present collision hazards which can render the agent nonfunctional. Moreover, physical obstacles can induce different artifact on the wireless communication signal due to electromagnetic phenomena (section 1.3). The most significant of which is the blocking or shadowing of the wireless signal. Fig. 3.23 shows the shadowed regions due a rectangular obstacle. The SNR in the shadowed region is significantly

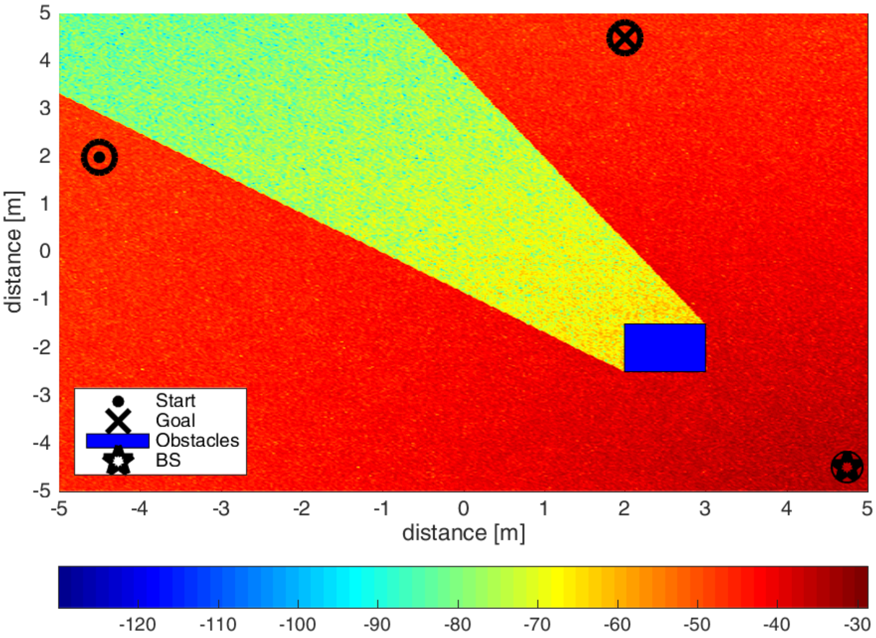

Figure 3.23: SNR Map of Environment with Obstacles

less than the region with no shadowing. The CAT and CBT generated for the single obstacle scenario is shown in Fig. 3.24. It can be seen that the CAT avoids the region of the SNR where the RSS is shadowed by the obstacle. The CBT, on the other hand, goes through the shadowed region towards the goal. Fig. 3.25 compares the SNR along the CAT and CBT. It can be seen that the CAT avoids the shadowed region and therefore has a consistently high SNR throughout its motion from the start to goal. The CBT on the other hand takes a shorter route to the goal but has an approx. $30dB$ dip in the SNR for a significant portion of the trajectory. This dip in SNR is due to the shadowing of the wireless signal caused by the obstacle and leads to an approximate difference of $20dB$ in the mean SNR along the CAT and CBT. Thus the CBT has a high chance of losing the wireless link (prohibitively low data rate) for a significant portion of the trajectory due to shadowing. In the following figure (Fig. 3.26) trajectories due to different starting orientations computed using the PDE-

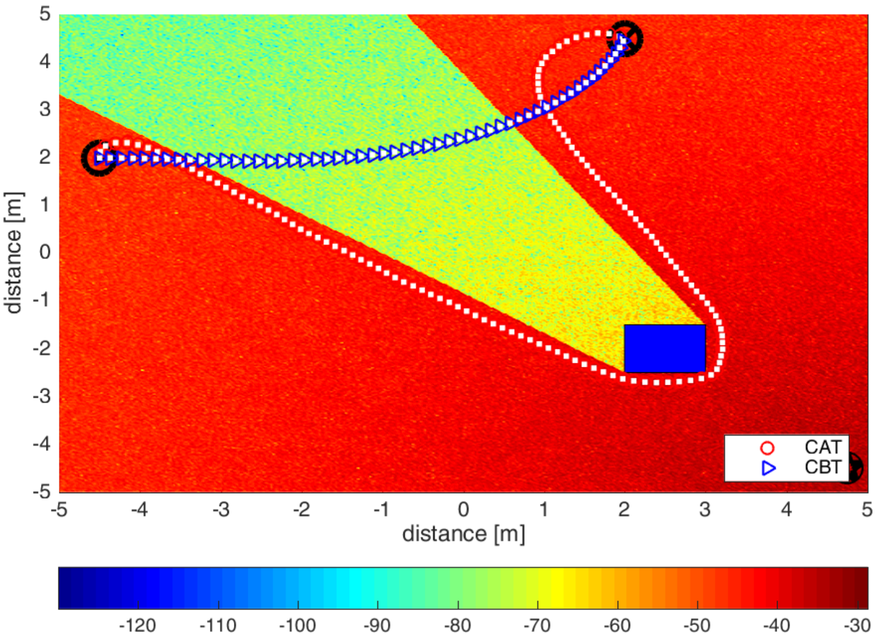

Figure 3.24: CAT and CBT in Environment with Shadowing of Wireless Signal due to Single Obstacle.

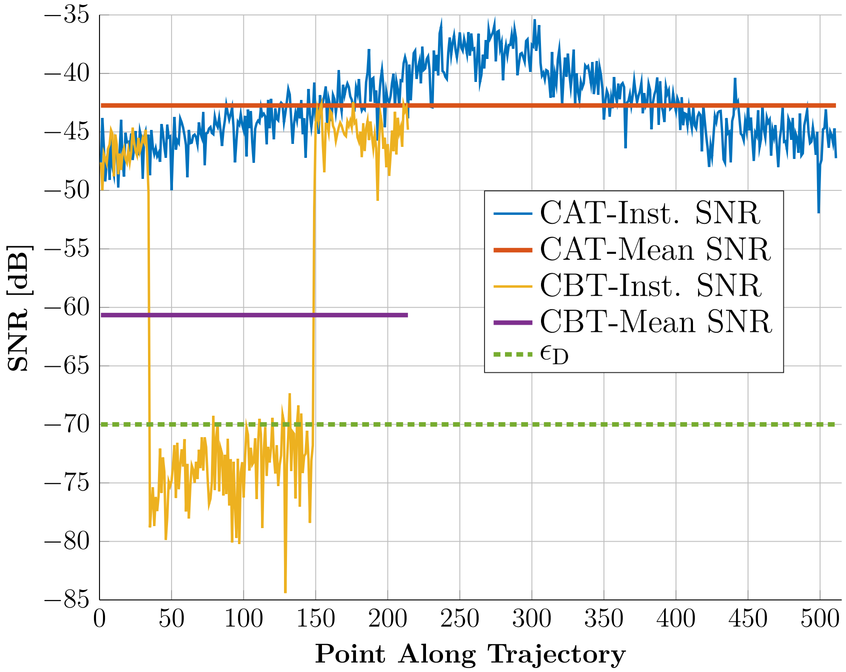

Figure 3.25: Comparison of SNR along CAT and CBT in Environment with Shadowing due to a Single Obstacle

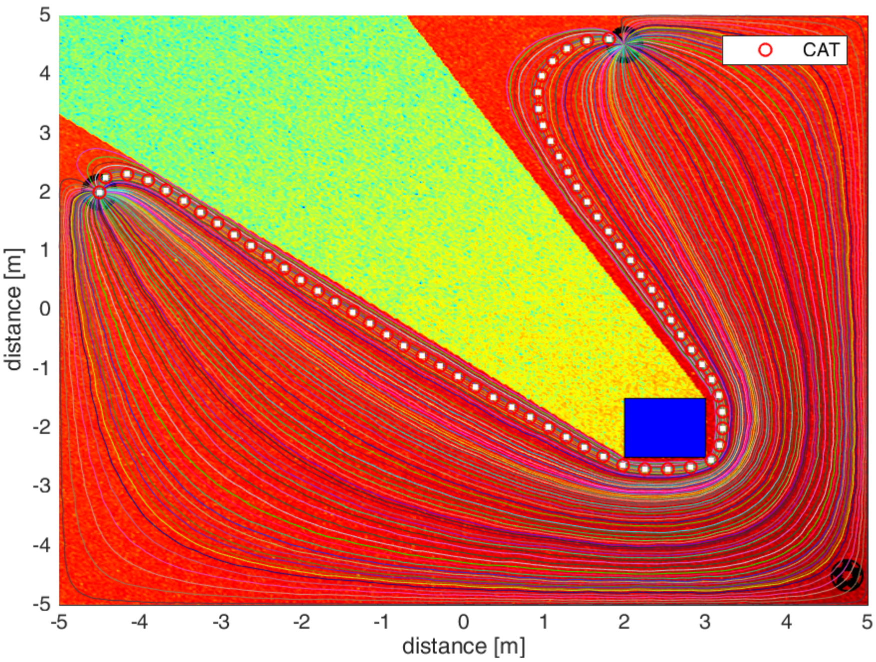

Figure 3.26: Trajectories due to Different Starting Orientations

ODE system (Eq. (3.20)) for the HPF obtained as a solution to Eq. (3.15) are shown. It can be observed that all the trajectories due to any starting orientation avoid the shadowed region as well as the physical obstacle. This demonstrates the robustness of our approach as any error in the initial orientation of the agent, would still result in the agent avoiding the shadowed region and the obstacle. Fig. 3.27 shows trajectories due to different starting orientations using the gradient dynamical system Eq. (3.20) for the HPF obtained as a solution to Eq. (3.15) when the agent has no knowledge of the SNR field. It can be seen that the navigator exhibits two important properties. Firstly, even with no SNR knowledge it guarantees convergence to the goal. With any starting orientation, the agent will reach the goal which again highlights the robustness of the approach. The second property to note here is that all the trajectories avoid the physical obstacle. Finally, another significant feature of the approach can be seen from Fig. 3.28. It shows the guidance field computed for the scenario depicted

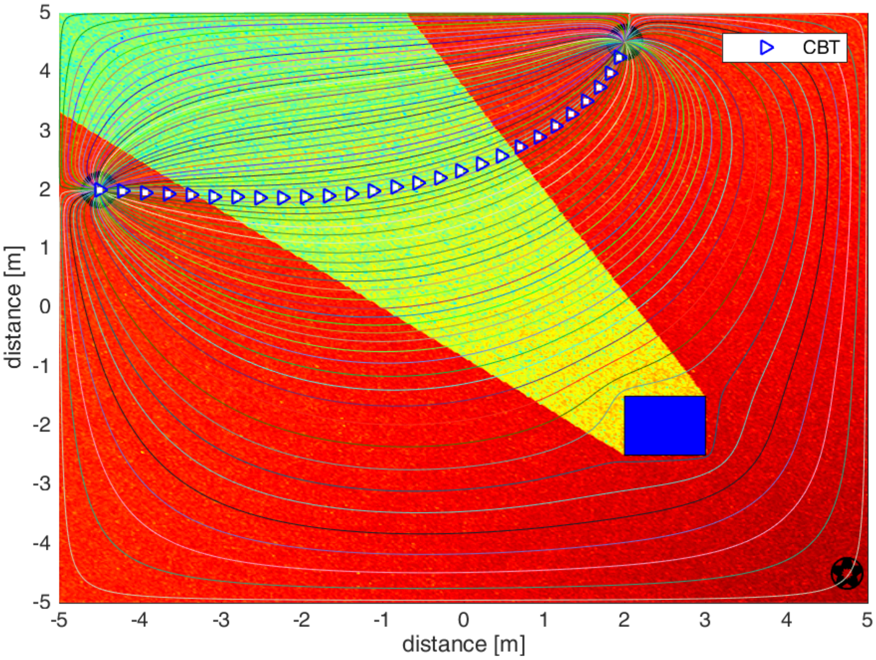

Figure 3.27: Trajectories due to Different Starting Orientations With no SNR Knowledge

in Fig. 3.23. It can be seen that a reference is available for the agent throughout the field. Thus, if the agent is bumped off course due to some unexpected external force, it would still be able to navigate its way to the goal in a communication-aware manner. Thus guaranteeing movement and convergence to goal from any point in the region.

Fig. 3.29 shows the CDF of the instantaneous SNR along 4000 different trajectories obtained using random start and goal positions for the environment in Fig. 3.23. The single rectangular obstacle in the environment cases the transmitted wireless signal to attenuate for the region where the agent does not have a LoS link with the BS due to blocking by the obstacle. It can be seen that the CATs provide a large gain in instantaneous SNR (up to 25 dB) in communication performance especially in the region where the signal is blocked. However, in regions where a LoS link is available, the gain in performance of the CATs over the CBTs is not very significant. The CDF

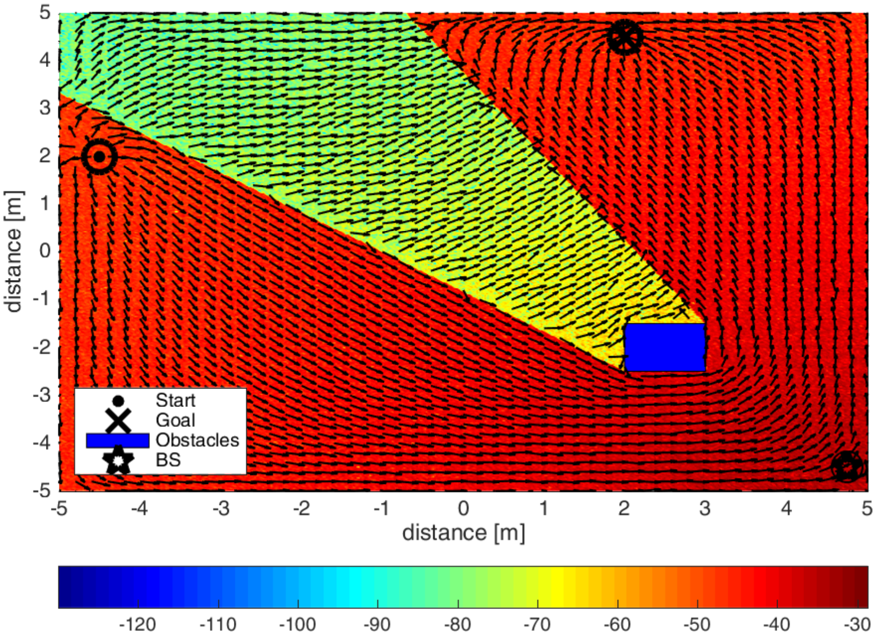

Figure 3.28: Guidance Field Obtained for The Environment Shown in Fig. 3.23

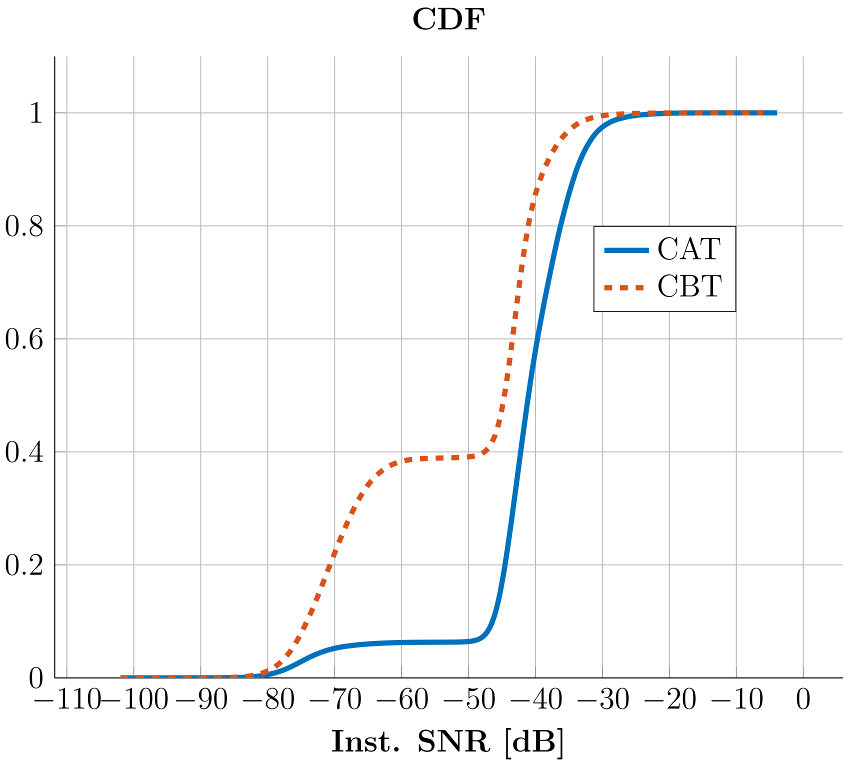

Figure 3.29: CDF of Instantaneous SNR along multiple trajectories with random start and goal positions.

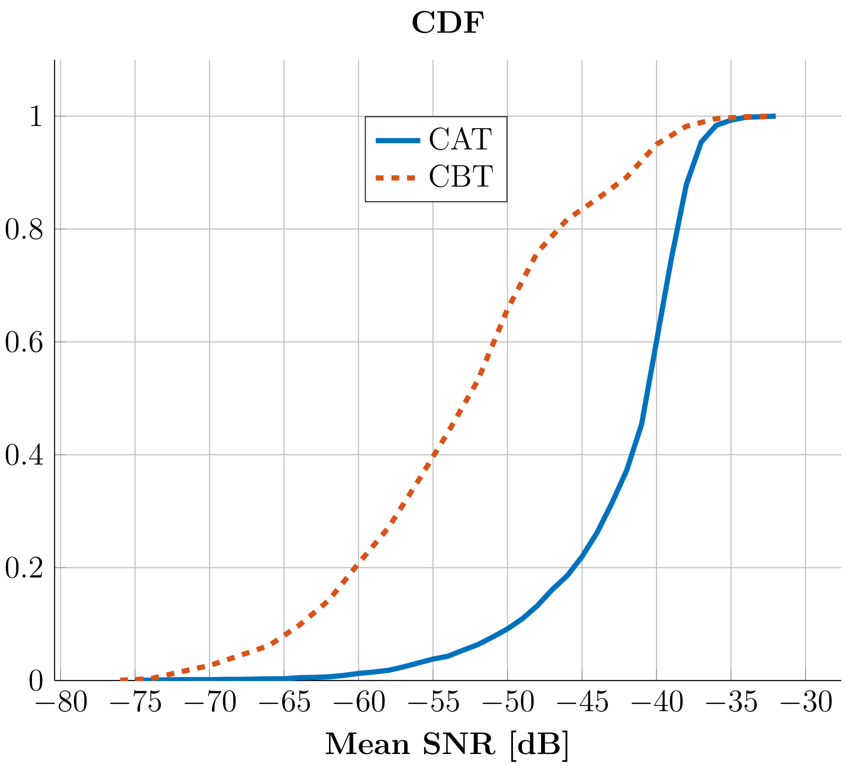

Figure 3.30: CDF of the mean-SNR along different trajectories obtained using multiple random start and goal positions.

of the mean-SNR along 4000 different trajectories obtained for different random start and goal positions in the environment given in Fig. 3.23 is given in Fig. 3.30. The mean-SNR provides an indication of the overall data-transmission performance of the CATs and CBTs. It can be seen that the CATs can have a gain of up to 15 dB in the mean-SNR along their trajectories which is a significant gain in overall communication performance along a trajectory. It can be also seen that the mean-SNR performance of the CATs and CBTs matches when the trajectories start and end in regions with high SNR.

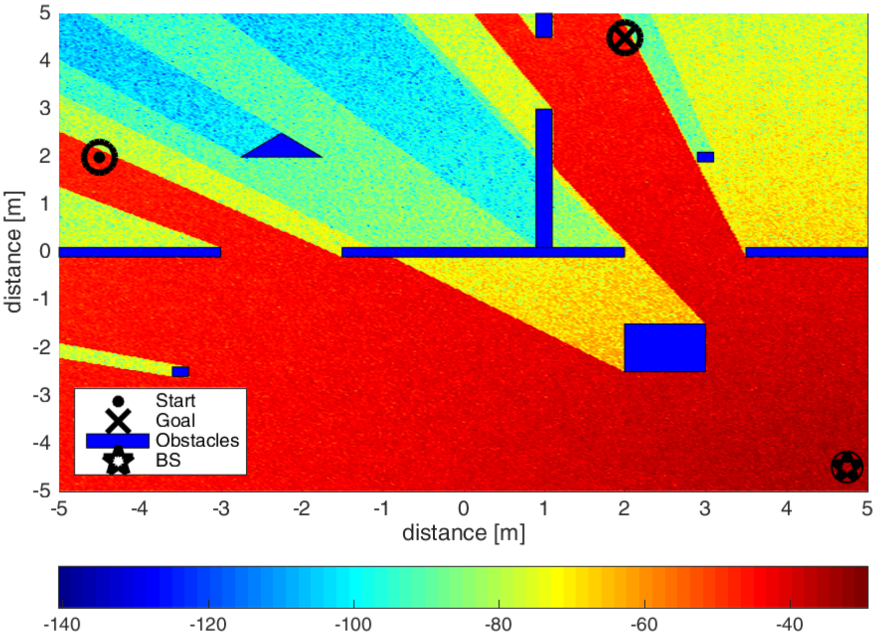

Figure 3.31: SNR Map of a Complex Environment With Many Obstacles

3.6.3 MBCAN: Cluttered Environment with Different Arbitrarily Shaped Obstacles

Typically environments in which the agent exists will have many obstacles of different geometries. In this subsection, we let the agent move in an environment with multiple obstacles of arbitrary geometry. Fig. 3.31 depicts one such environment. Along with constituting a hazard to the agent, the hard obstacle introduces multiple shadowed regions of the RSS in the environment. The CAT and CBT obtained for this environment are shown in Fig. 3.32. It can be seen that the CAT avoids the shadowing caused by the different objects as well as all the physical obstacles and reaches the goal. The CBT on the other hand is oblivious to the SNR-map but still reaches the goal goal while avoiding the physical obstacles. The comparison of mean SNR of the trajectories in the SNR- aware and unaware cases is given in Fig. 3.33. We can see that the CAT

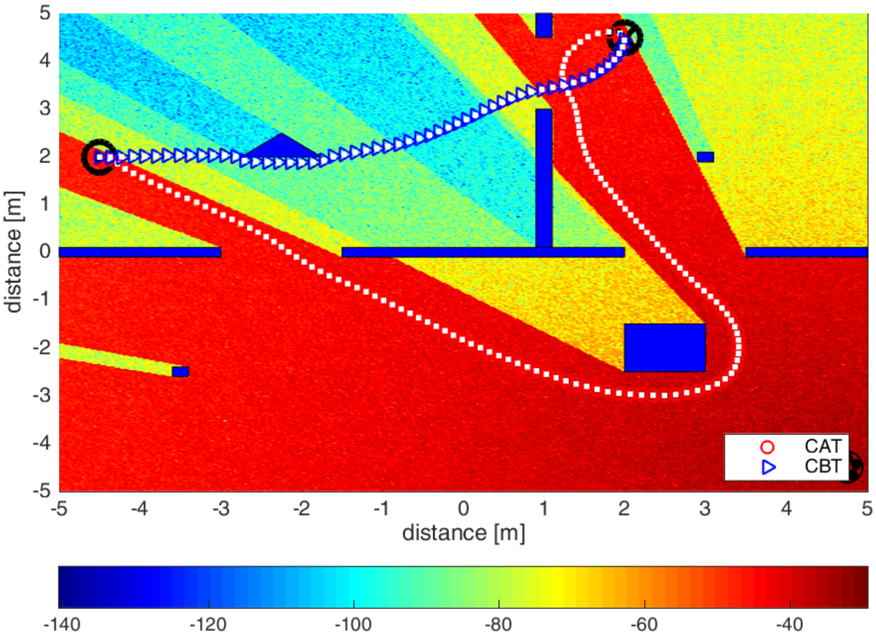

Figure 3.32: CBT and CAT in a Complex Environment

maintains a consistently hight SNR along its trajectory, whereas, the CBT sees up to a $60dB$ (approx.) drop in SNR for parts of its trajectory compared to the CAT. The mean SNR along the CAT is around $30dB$ higher than the mean SNR along the CBT. Fig. 3.34 shows the different trajectories obtained due to different starting orientations at the start position. The trajectories were obtained by choosing a starting orientation and using the PDE-ODE (Eq. (3.20)) for the HPF obtained as a solution to Eq. (3.15). It can be seen that all the trajectories avoid the shadowed regions and the obstacles and converge to the goal. Fig. 3.35 shows different trajectories from the start point to the goal due to different starting orientations at the start point. These trajectories were obtained using the PDE-ODE system Eq. (3.20) for different chosen starting orientations for the HPF obtained as a solution to Eq. (3.27). It can be seen that all the trajectories avoid the physical obstacles but since the planner has no SNR information, the trajectories pass through shadowed regions for significant durations.

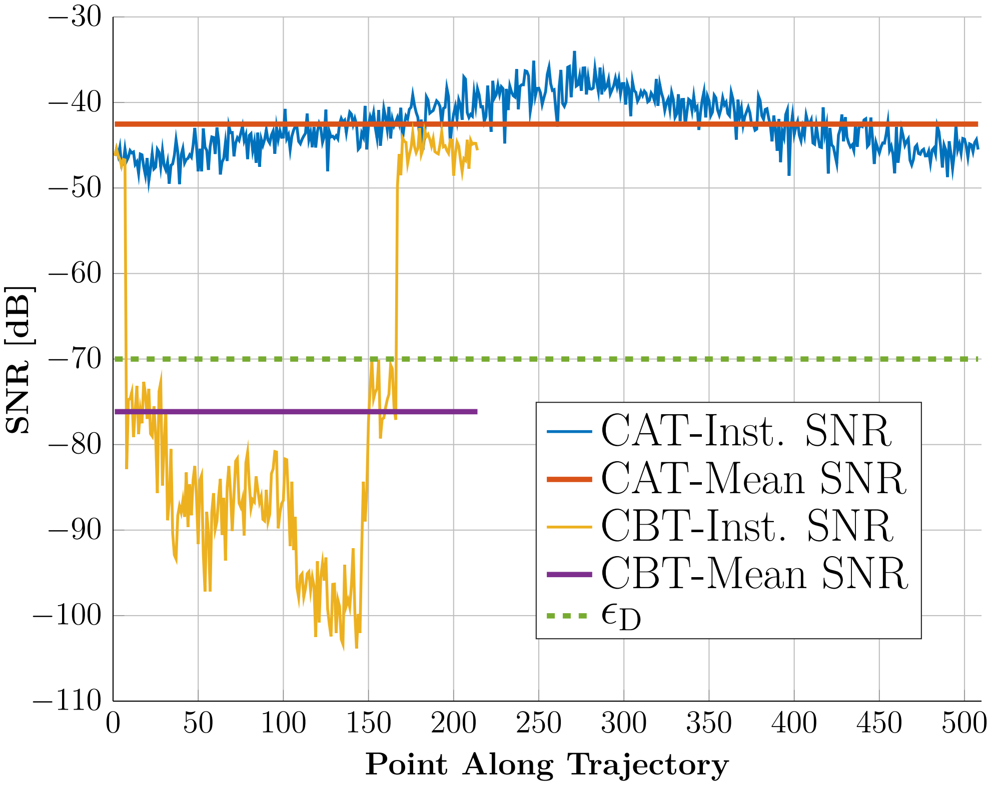

Figure 3.33: Comparison of SNR of CAT and CBT for a Complex Environment given in Fig. 3.31

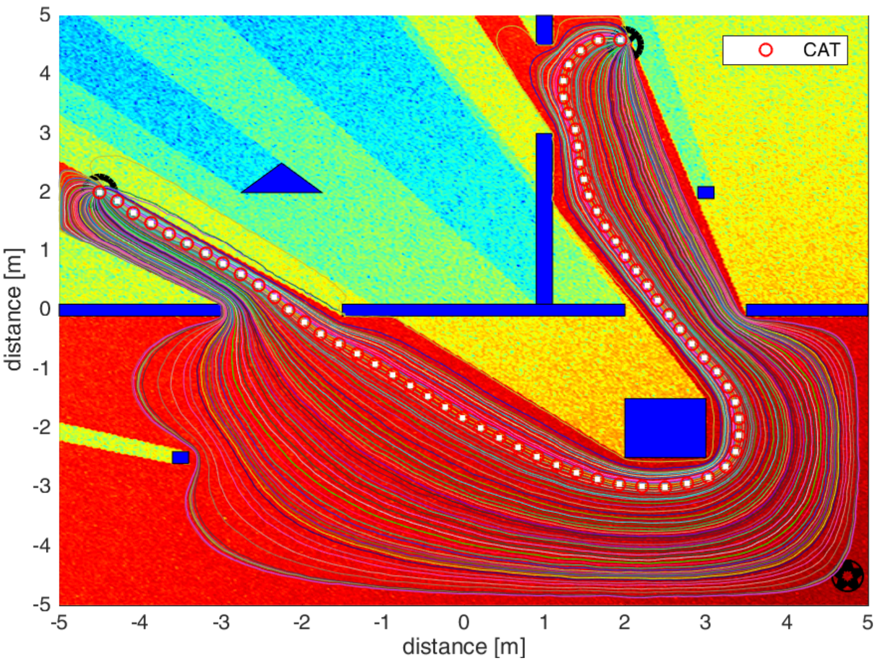

Figure 3.34: SNR-Aware Trajectories with Different Starting Orientations

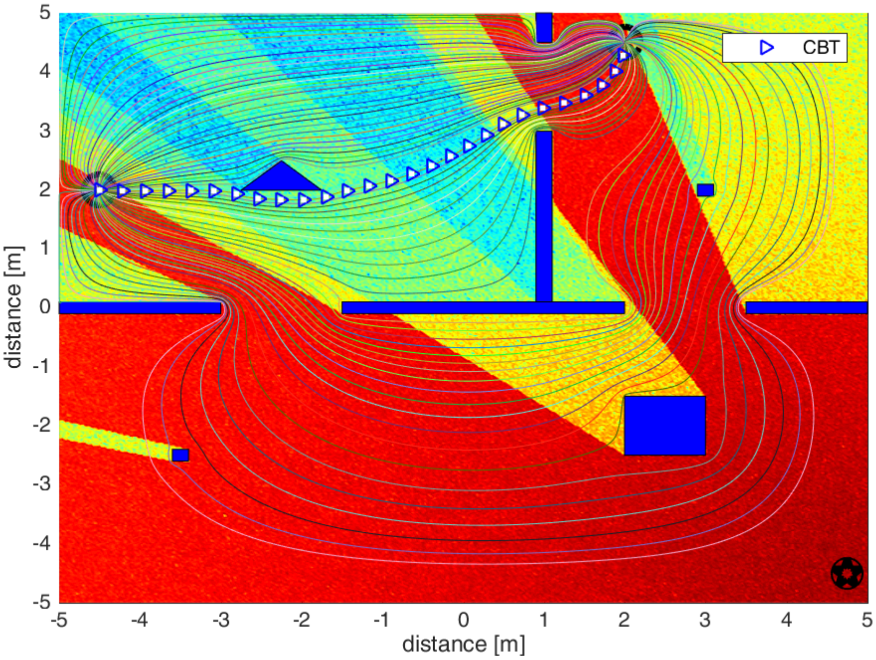

Figure 3.35: SNR-Blind Trajectories with Different Starting Orientations

Fig. 3.36 compares the Probability Density Function (PDF) of the instantaneous SNR at each instant along the trajectory of the agent to the goal. The figure compares the PDF of the CATs with the CBTs. The PDF was obtained by generating 4000 trajectories in the cluttered environment from the start position goal using MBCAN. The instantaneous SNR PDF was obtained for the SNR at each instant for each of these trajectories and plotting its probability density. It can be seen that the PDF of the CAT, has a higher concentration at higher SNRs. It can be seen that nearly 30% of the instantaneous SNR of the CBT lie in a DCZ. However, only 12% of instantaneous SNR for CAT lie in DCZs. This can be explained by the scenario when $\mathbf{p}_S$ and $\mathbf{p}_G$ lie in a DCZ and the robot has to move within the DCZ until it enters higher SNR regions. A more clear picture can be seen in Fig. 3.37, where the CDF of the instantaneous SNRs are compared. It can be seen that the communication aware trajectories can give gains of approximately 36 dB especially in poor wireless communication quality scenarios

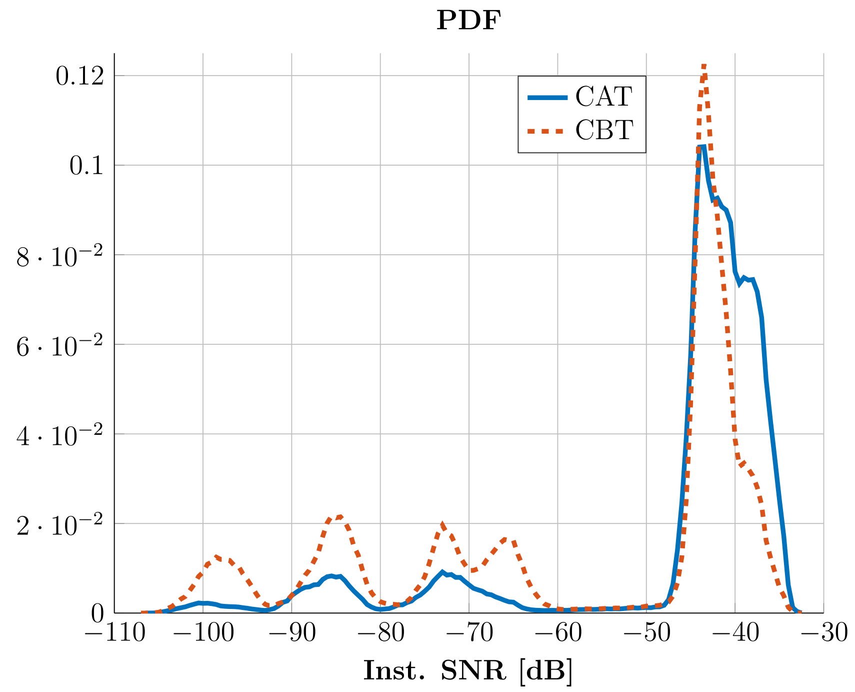

Figure 3.36: PDF of Instantaneous SNR at Each Point along the Trajectory computed using different random start and goal positions

(This is specific to the cluttered scenario considered above). The difference is very small for trajectories that are in high SNR regions compared to low SNR regions. This is mainly due to the avoidance of shadowed regions using MBCAN. At high SNRs the performance of both blind and communication aware trajectories start to converge. Fig. 3.38 compares the PDF of the mean SNR of blind and communication-aware trajectories obtained using MBCAN. It can be seen that compared to the PDF of the mean SNR of blind trajectories, the PDF of the communication-aware trajectories is highly dense at high mean SNRs. The CDF of the mean SNR of trajectories both blind and communication-aware scenarios is compared in Fig. 3.39. It can be seen the mean SNR performs consistently better than the blind trajectories throughout the SNR range before converging for trajectories in high SNR regions. As compared to the inst. SNR, the mean SNR increases for the CATs in both high and low SNR

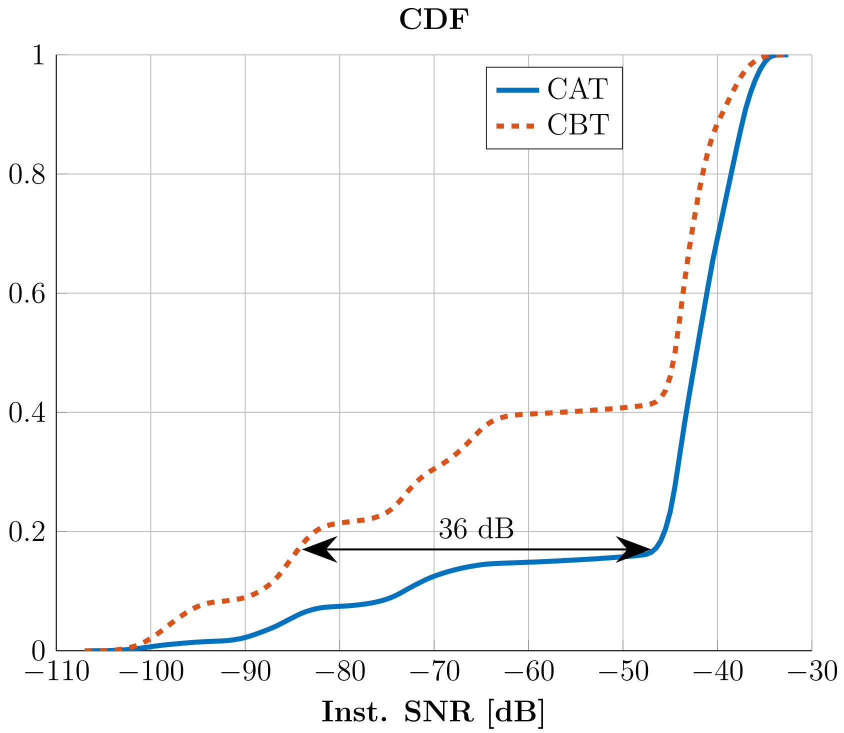

Figure 3.37: CDF of Instantaneous SNR at Each Point along the Trajectory

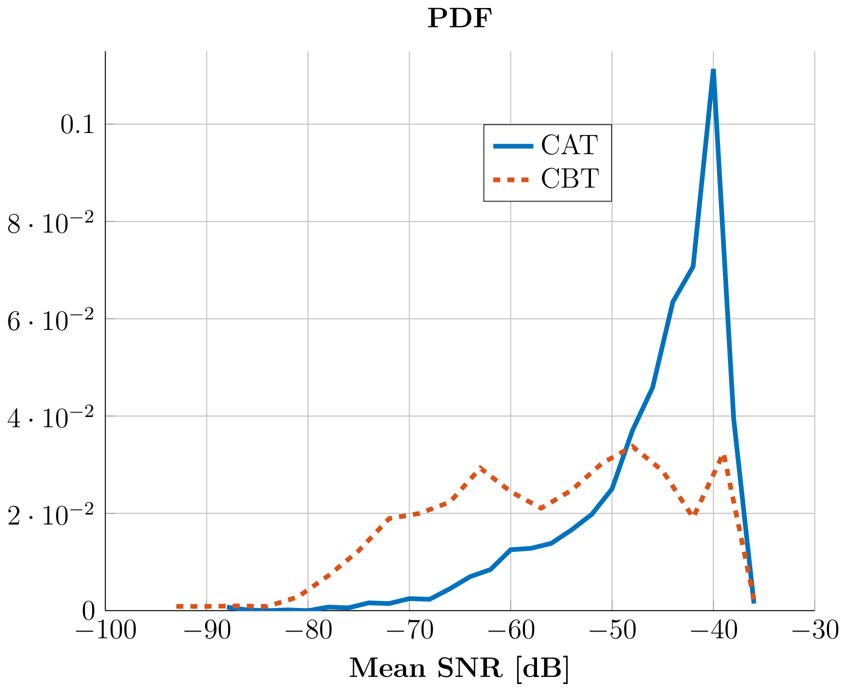

Figure 3.38: PDF of the Mean of the SNR of Each Point along the Trajectory

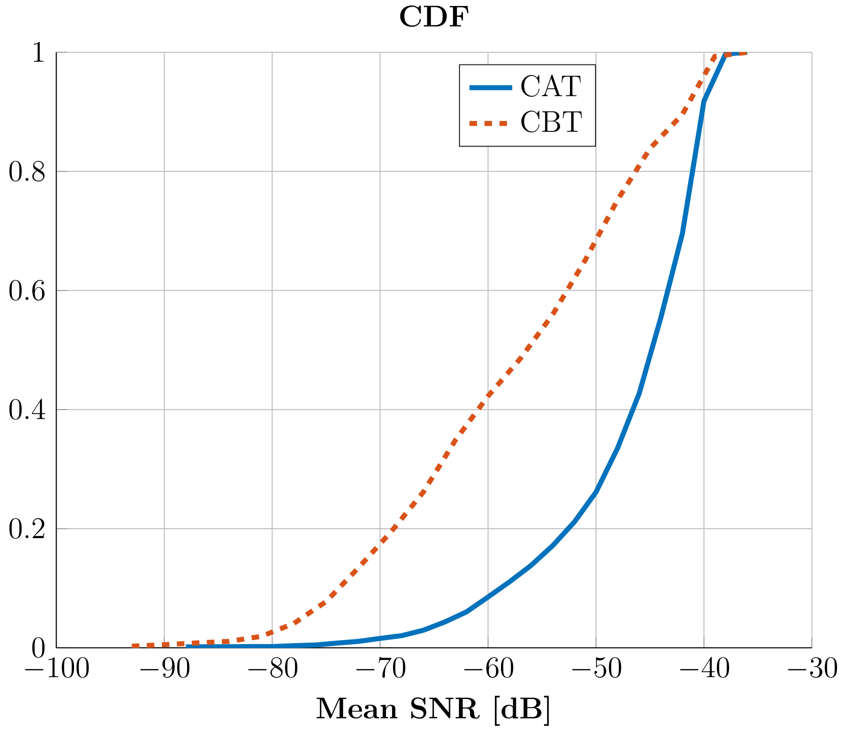

Figure 3.39: CDF of the Mean of the SNR of Each Point along the Trajectory

regions. This shows that the MBCAN gives a much more robust performance for overall communication along a complete trajectory rather than instantaneous gains. This falls directly from the integral properties of the MBCAN. The trajectories in low SNR regions gain as much as 16 *db* approximately as compared to trajectories that are blind to communication performance. More significantly, we can see nearly 90% of the CBT have mean SNR lower than ϵ_D but less than 1% of the CAT have mean SNR below ϵ_D. This highlights the overall robustness of the system in obtaining trajectories with better overall communication performance.

3.6.4 Dead Communication Zones and Trajectories

In this section, we show trajectories obtained using MBCAN with the agent's start or goal position is inside a DCZ. We also show the trajectory obtained in the case an agent is bumped in to a DCZ due to an unknown external force.

Fig. 3.40 shows the trajectory obtained using MBCAN when the starting position $\mathbf{p}_S$ is in a DCZ. It can be seen that the path moves towards the nearest zone which is not a DCZ and remains in the high SNR region until it reaches the goal. In the plot with different trajectories due to different starting orientation, some trajectories are unable to reach the high SNR zone as they are pushed in to another DCZ. These trajectories still move towards the target using a smooth path. Fig. 3.41 shows the trajectories obtained if the goal position is in a DCZ. The path goes as close as possible to the target before entering the DCZ and reaching the target. The planner keeps the path in the high SNR region for as long as possible. Fig. 3.42, shows the trajectory in the scenario where an unknown external force bumps the agent in to a DCZ Fig. 3.43 shows an important aspect of MBCAN. It shows trajectories 15cm above and below the CAT due to errors. The SNR along these trajectories is nearly the same as along the CAT. This is due to the fact that MBCAN generates a trajectory such that the region around it also has a high SNR. This is a consequence of using the highest magnitude of ρ while selecting a starting orientation (3.19). In Fig. 3.20, it can be observed that ρ values near the maximum are also high, therefore, trajectories resulting from these orientations will also have a better SNR performance comparable with CAT. We can see from the close up of the CAT (inset) in Fig. 3.43 that trajectories within an error

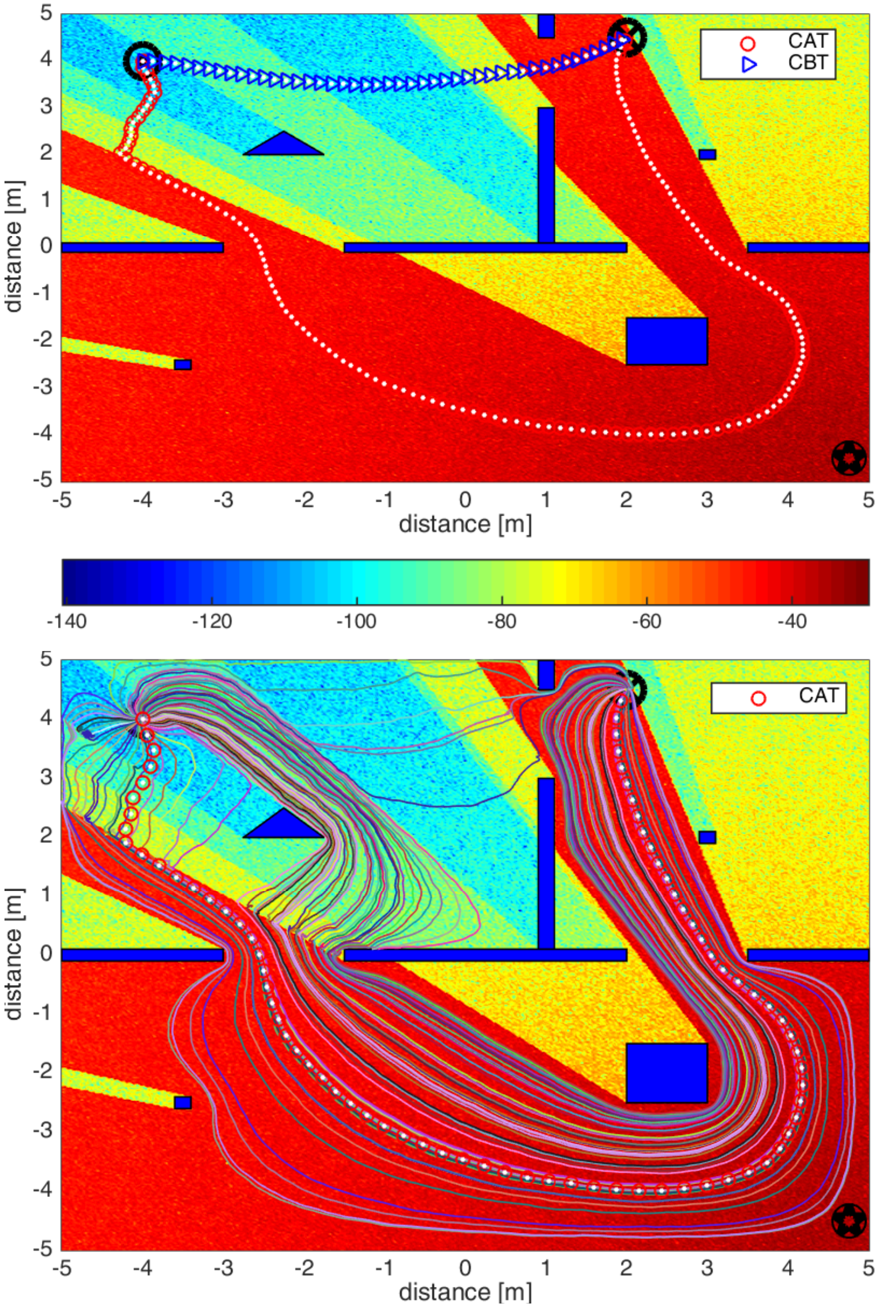

Figure 3.40: Trajectories obtained with start position in a DCZ

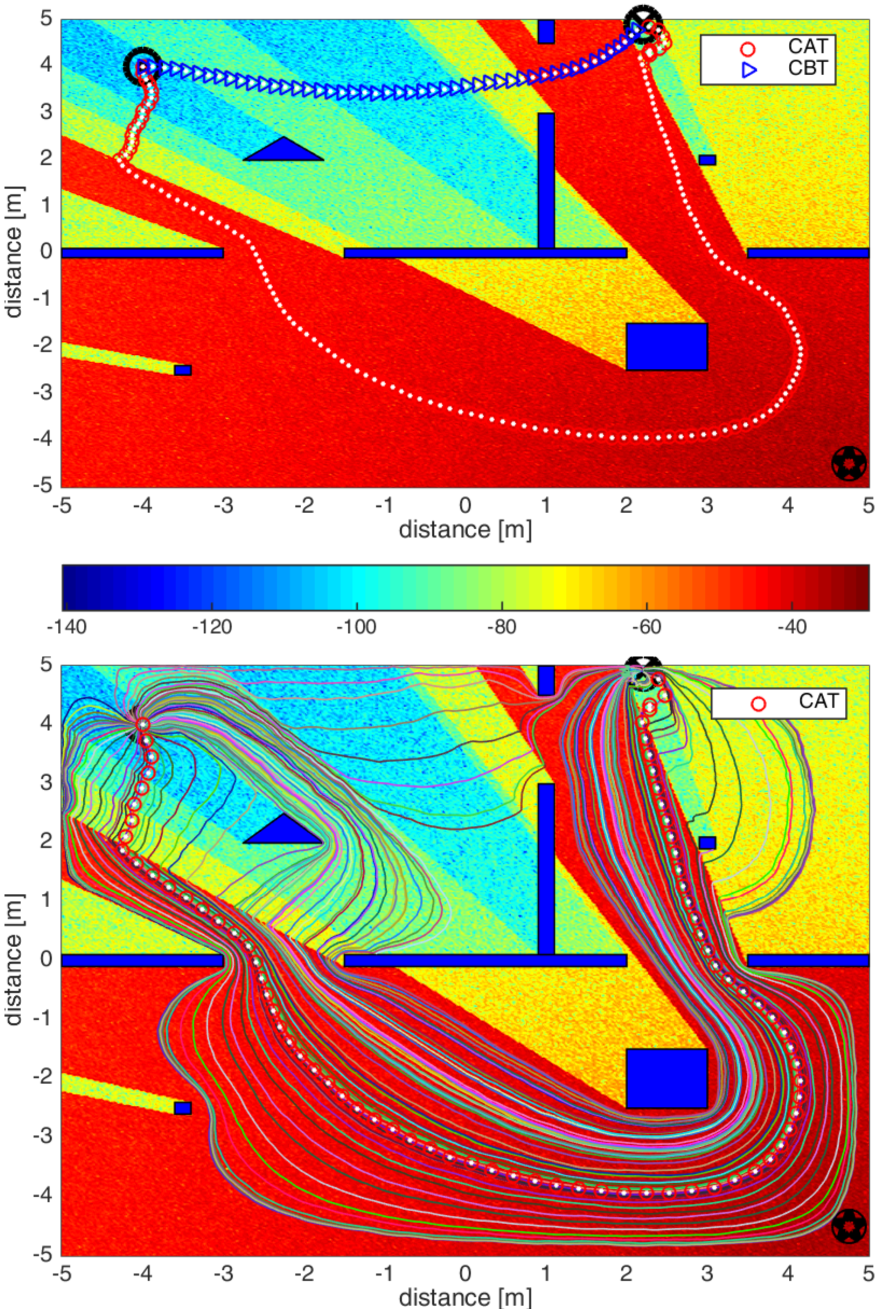

Figure 3.41: Trajectories obtained with both start and positions in a DCZ

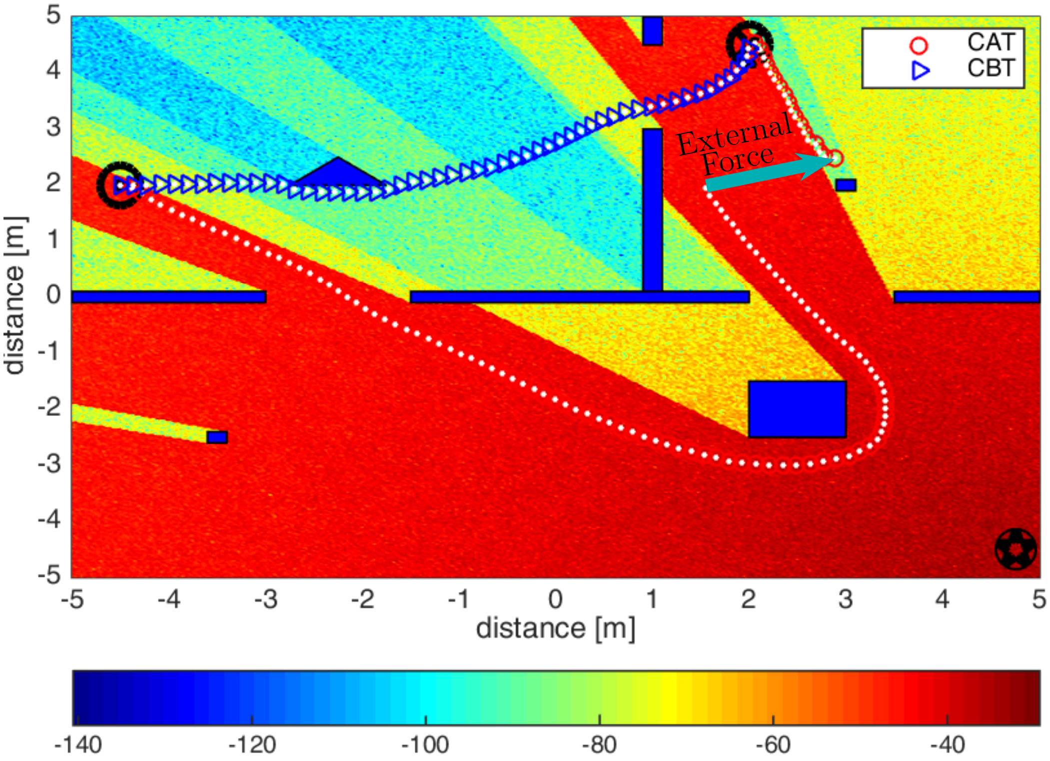

Figure 3.42: Agent bumped in to DCZ due to an external force

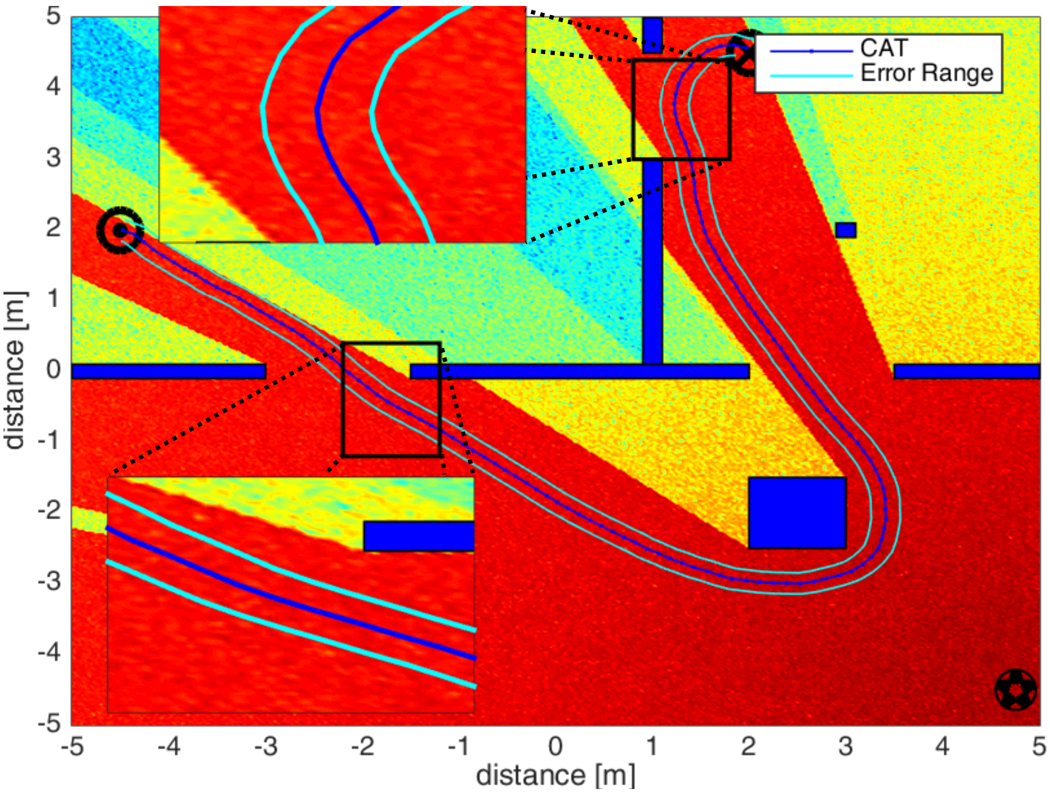

Figure 3.43: SNR in the region around the CAT.

of 15cm around the CAT are in a high SNR region. The SNR at 15cm and -15cm from the main trajectory is shown in figures 3.44 and 3.45. It can be seen that the SNR and mean-SNR (ratio of total SNR to length) is nearly the same as the CAT at these error margins.

3.6.5 MBCAN: Environment with Obstacles of Irregular Geometry

Fig. 3.46 presents an environment consisting of many obstacles that have irregular geometric shapes. The obstacles have sharp edges. These kinds of obstacles can be expected in disaster hit scenarios. The environment consists of a single-antenna BS.

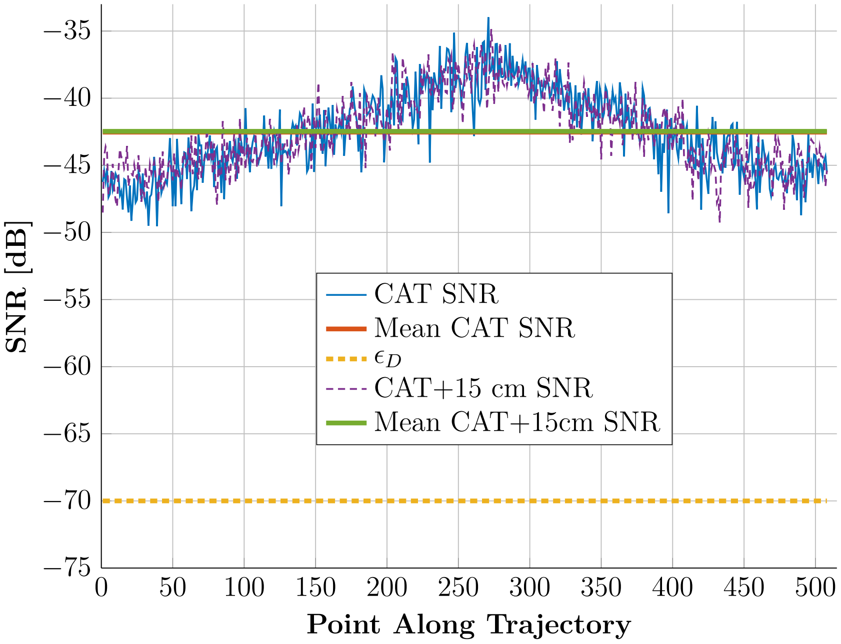

Figure 3.44: SNR comparison of the CAT and a trajectory 15cm above the CAT

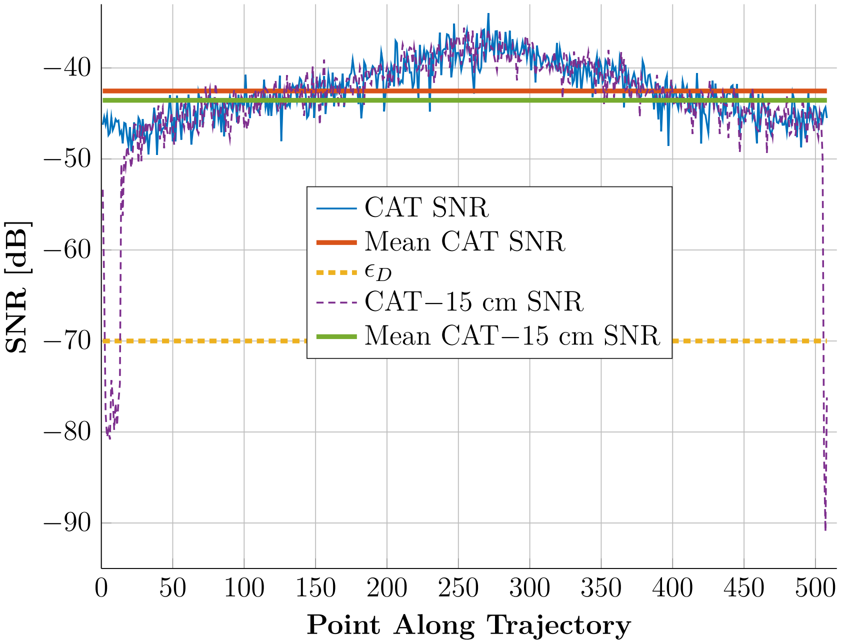

Figure 3.45: SNR comparison of the CAT and a trajectory 15cm below the CAT

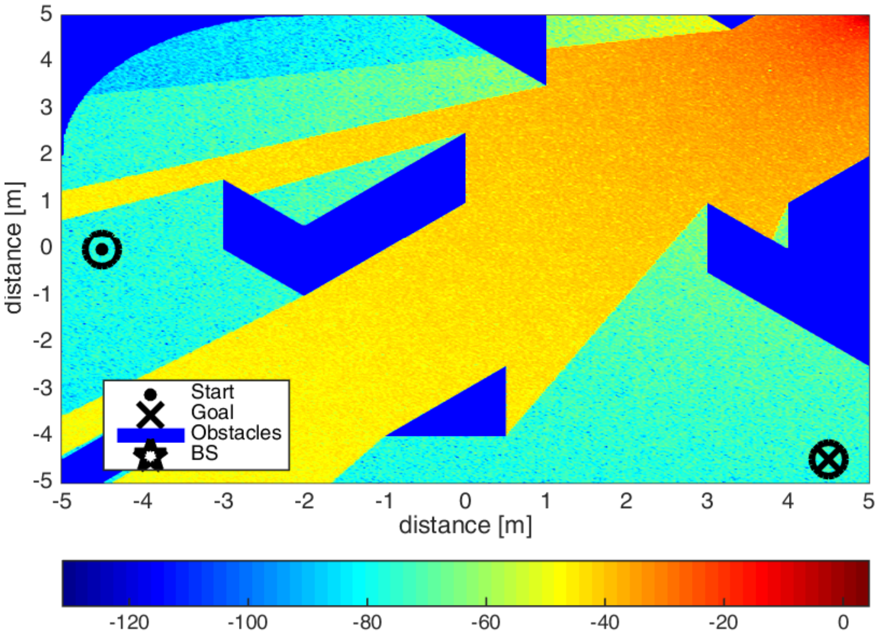

Figure 3.46: A complex environment with convex and non-convex obstacles of irregular geometry.

An agent is tasked with navigating this environment while exchanging data with the BS over a wireless link.

As can be seen in Fig. 3.46, the agent starts in a region with very low SNR (a possible DCZ) and needs to navigate to the goal position. The goal position is also located in a possible DCZ. This presents a very challenging scenario as the agent has to navigate a DCZ at start and goal positions.

Fig. 3.47 shows the CAT and CBT in the environment shown in Fig. 3.46. It can be seen that the CAT takes the shortest route out of the low SNR region around the start position. It then moves towards the goal position. While traversing towards the goal inside a low SNR region, it tries to keep as close as possible to the BS to maximize the SNR along the trajectory. This is due to the motion being attracted by the high-SNR region as explained in section 3.4. The CBT, on the other hand,

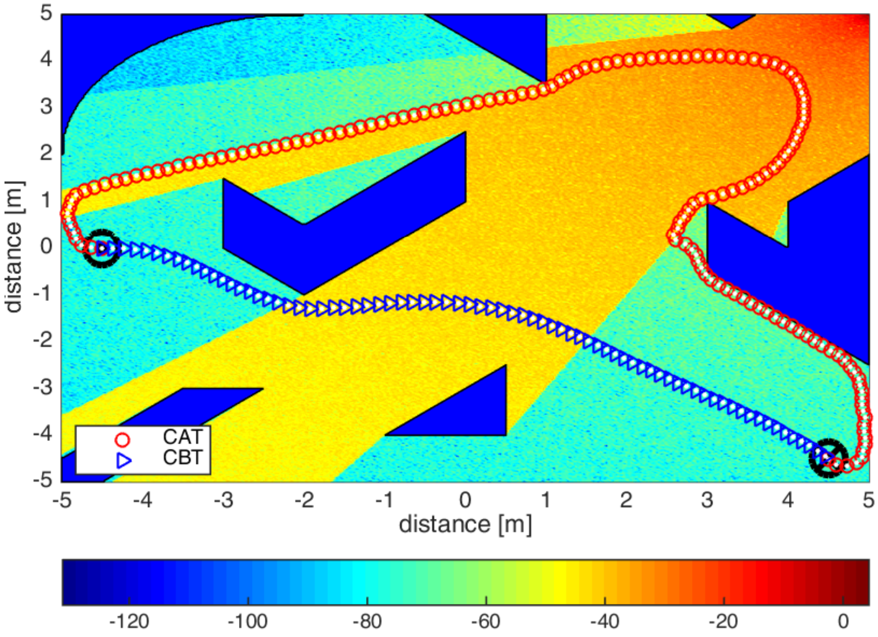

Figure 3.47: CAT and CBT in the environment given in Fig. 3.46

directly goes to the goal position while avoiding the HO in a smooth manner.

In Fig. 3.48, the instantaneous and mean SNR along the CAT and CBT is compared. It can be seen that although the start and goal positions are in low SNR regions, the mean CAT SNR is more than 12 dB higher than that of the CBT. Thus, the CAT considerably improves the overall communication performance. Fig. 3.49 shows the CDF of the instantaneous SNR along CATs and CBTs for 4000 different random start and goal positions inside the environment shown in Fig. 3.46. It can be seen that the instantaneous SNR CDF of the CATs gives a significant improvement in the SNR for regions with low SNR. The CDF of the mean-SNR along 4000 different trajectories obtained for different random start and goal positions in the environment given in Fig. 3.23 is given in Fig. 3.50. It can be seen that the CATs' CDF outperforms the CBTs' CDF for all SNR regions.

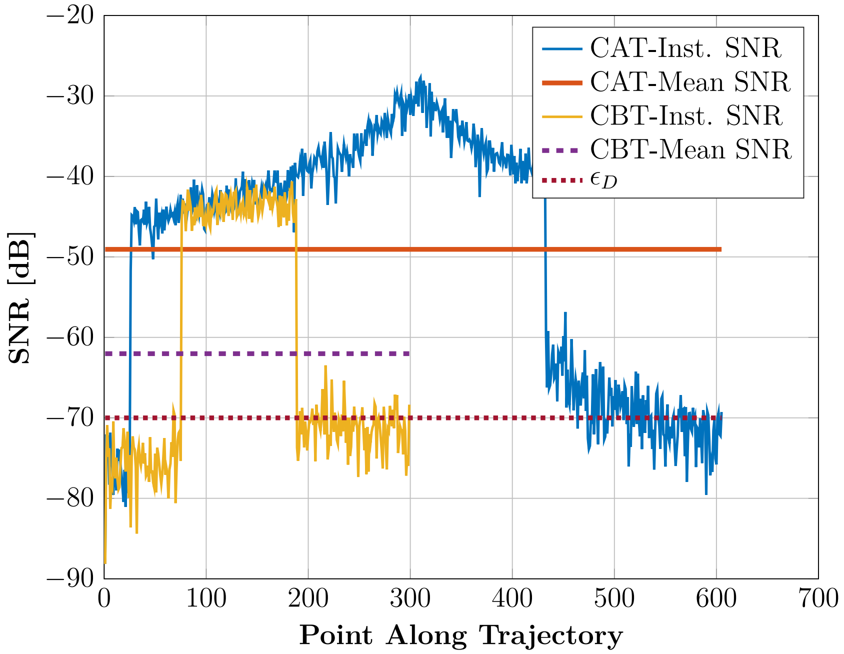

Figure 3.48: Comparison of the instantaneous SNR along the CAT and CBT

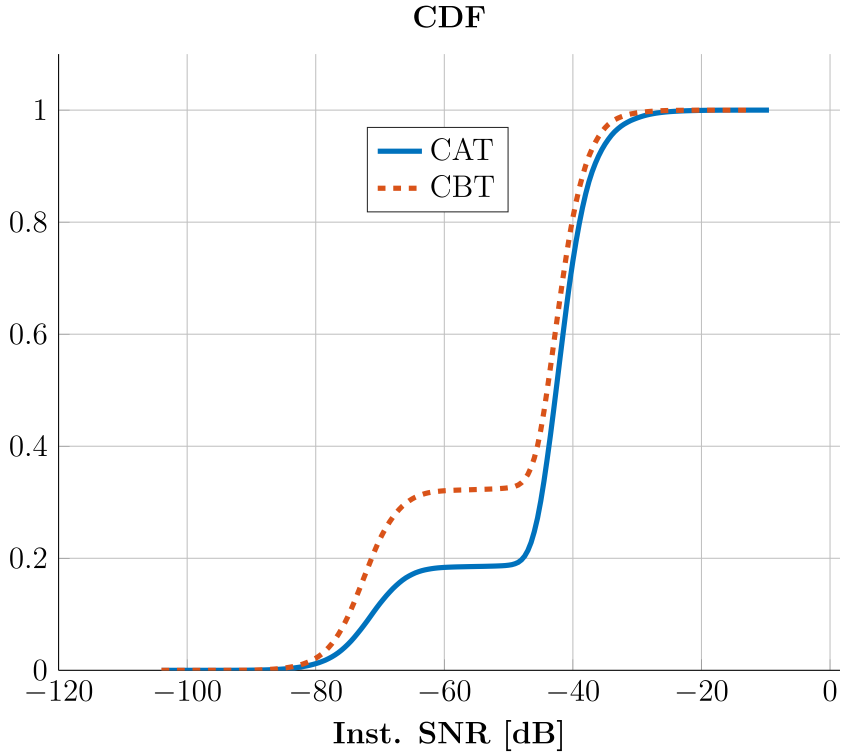

Figure 3.49: CDF of Instantaneous SNR along multiple trajectories with random start and goal positions.

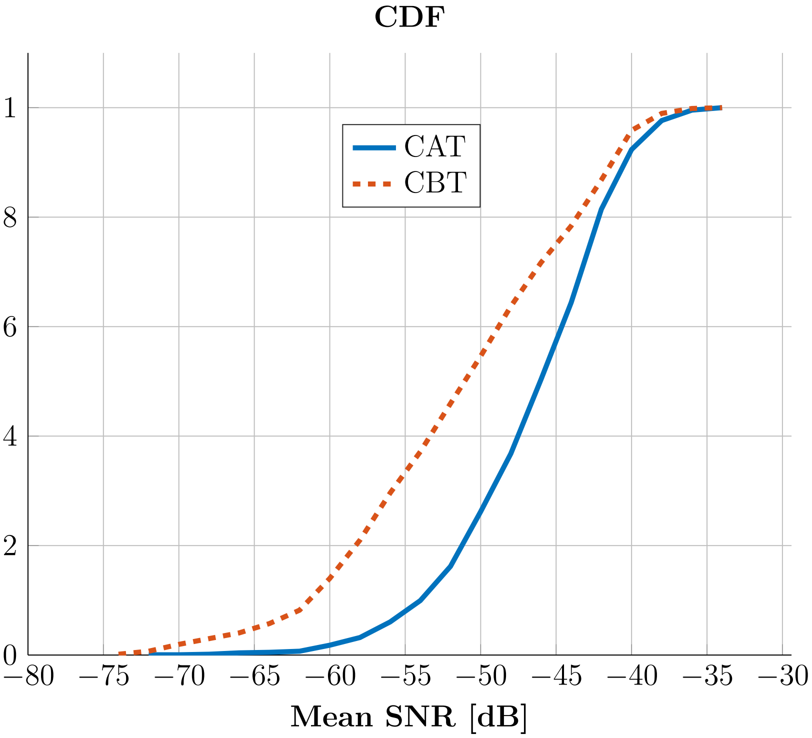

Figure 3.50: CDF of the mean-SNR along different trajectories obtained using multiple random start and goal positions.

3.6.6 Motion and Communication Energy: A Comparison

In section 3.6, it was shown that CATs obtained for different environments using MBCAN always avoided the DCZs where as the CBTs failed to avoid the DCZs. However, it can be seen that this results in a longer trajectory for the CATs.

The longer trajectories obtained using MBCAN would consume more energy as a result of traveling a longer distance. However, the longer trajectory results in better SNR for the WCL. This would result in less transmission energy required for wireless communication.

In the following we present a comparison of the total energy consumed due to motion and wireless communication by an agent as it moves towards it goal in the environments presented in section 3.6. The power cost due to motion of a robot can be approximated [91] using the following model.

$$P_M = \begin{cases} \kappa_1 v + \kappa_2 & \text{if } 0 < v \leq v_{max}, \\ \\ 0 & \text{if } v = 0. \end{cases} \tag{3.130}$$

Where, P_M is the power cost due to motion. κ_1 and κ_2 are constants and v is the speed of the agent. The total energy consumed due to motion will then be given by,

$$E_M = \kappa_1 d_M + \kappa_2 T_M. \tag{3.131}$$

Where, d_M, is the total distance the robot travels along its trajectory to the goal. T_M is the total time taken by the robot from start to goal along its trajectory.

It was shown in [91] that $\kappa_1 = 7.4$ and $\kappa_2 = 0.29$ give a good energy consumption approximate for robots moving up to speeds of 0.9 m/s.

In Fig. 3.51, the energy consumption comparison is presented for the four different scenarios given in Figs. 3.16, 3.23, 3.31 and 3.46. The stacked bars show the combined motion and communication energy for the CBT and CAT trajectories in each scenario. In the first scenario where there is no obstacle in the environment, the total energy consumption of the CAT is marginally higher than that of the CBT. However for the other scenarios where obstacles are present in the environment, the total energy consumption of the CBT is significantly higher (more than double) than that of the CAT.

Observing the bars independently, it can be seen that the energy consumption due

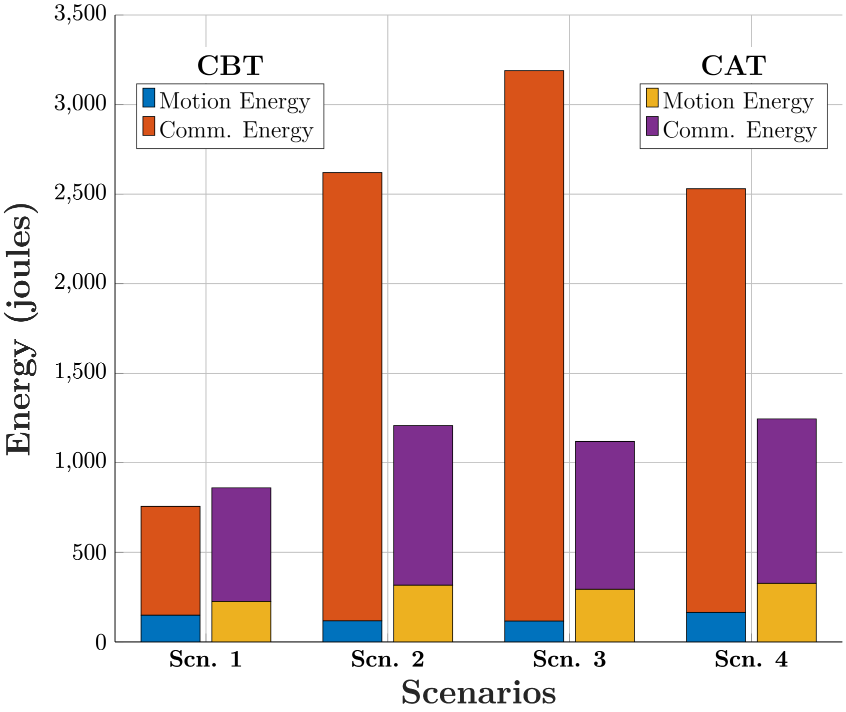

Figure 3.51: Energy consumption comparison of the CAT and CBT for different scenarios

to motion is always higher in the CATs for each scenario. For the environments with obstacles, the energy consumption due to motion for the CATs is more than double of that of the CBTs. However, the energy consumption due to data transmission is extremely high (nearly three times) for the CBTs as compared to the CATs.

3.6.7 Dynamic Trajectory of a Differential Drive Robot (DDR)

The trajectories obtained using Eq. (3.20) for a ϕ can be realized for a large class of agents using the Virtual Velocity Attractor (VVA) approach presented in [24] (prop. 3.13). The trajectory of a Differential Drive Robots (DDR) described by the following

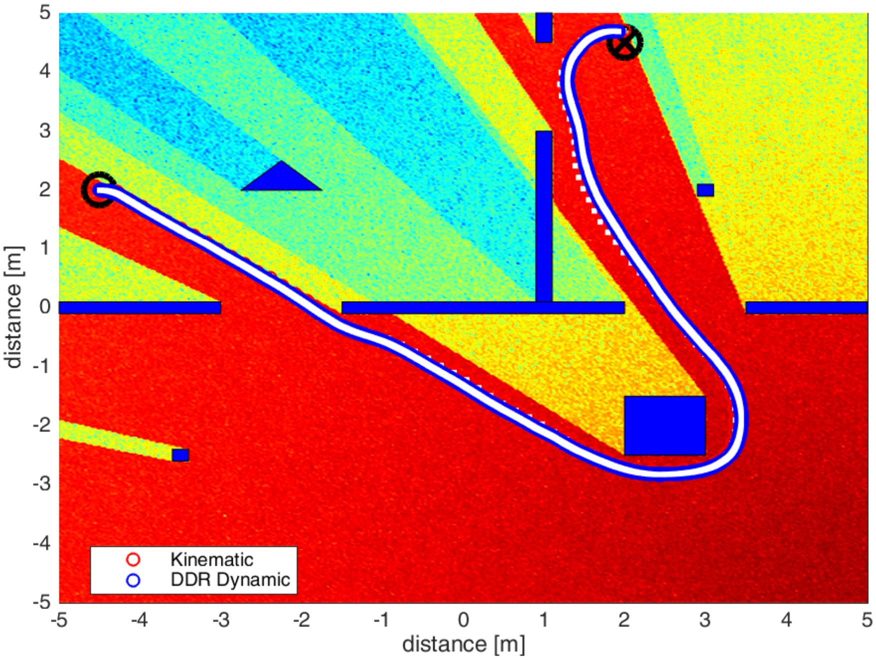

Figure 3.52: Dynamic Trajectory of a DDR

system of equations

$$
\begin{aligned}
\dot{x} &= v \cos \theta \qquad (3.132) \\
\dot{y} &= v \sin \theta \\
\dot{\theta} &= u \\
\dot{v} &= a
\end{aligned}
$$

is shown in Fig. 3.52 for the scenario given in Fig. 3.31. Fig. 3.53 shows the control signals that realized the above depicted trajectory of the DDR.

3.6.8 MBCAN & State of the Art: A Comparison

In this section, we compare our results with the communication-aware trajectories obtained in [56]. The work in [56] proposes a communication-aware mobility framework,

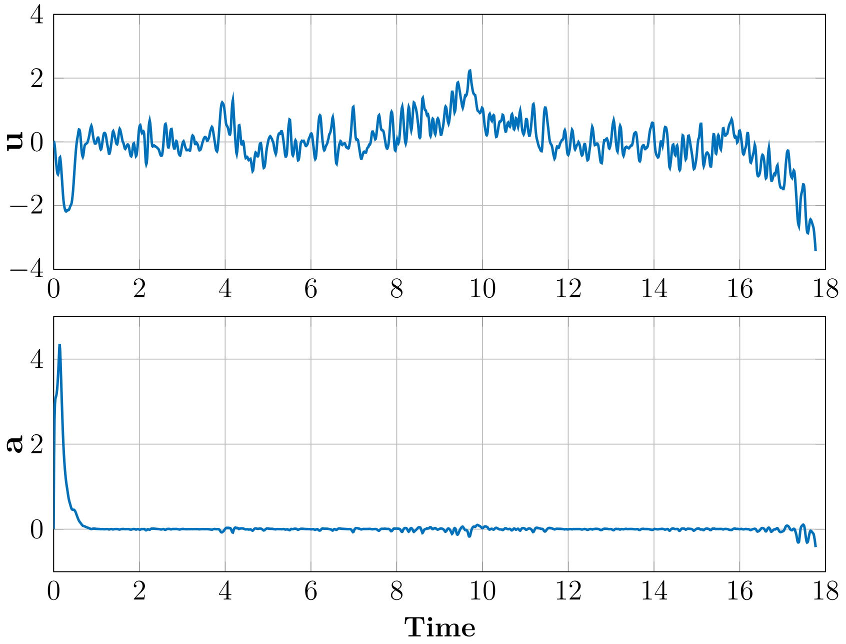

Figure 3.53: Control signals for the DDR

where an agent moves towards a target while communicating with a BS. A packet dropping wireless link is assumed. The data packet is dropped if the SNR of the WCL is below a threshold $\Upsilon_{\mathrm{dB,TH}}$ (i.e. when the agent is inside a DCZ). Motion is generated assuming a point agent (dynamics are ignored). The communication-aware mobility problem is proposed as finding the next position of the agent that maximizes a cost function and is given as follows.

$$v_t^* = \underset{v_t}{\operatorname{argmax}} \quad J_{TRACK,t}(q_{t+1}) \tag{3.133}$$

$$\text{s.t. } 1)\ q_{t+1} = q_t + v_t \tag{3.134}$$

$$2)\ v_t \in \mathcal{V} \tag{3.135}$$

$$3)\ q_{t+1} \in \mathcal{W} \setminus \mathcal{O} \tag{3.136}$$

Where $J_{TRACK,t}(q_{t+1})$ is given as follows,

$$J_{TRACK,t}(q_{t+1}) \triangleq \frac{Q\left(\left(\Upsilon_{\mathrm{dB,TH}} - \Upsilon_{\mathrm{dB},t,est}(q_{t+1})\right)/\sigma_{t,est}(q_{t+1})\right)}{g(\|q_{t+1} - \mathbf{p}_G\|)} \tag{3.137}$$

$\Upsilon_{\mathrm{dB},t,est}(q_{t+1})$ and $\sigma_{t,est}(q_{t+1})$ are the RSS estimate in dBs and its error variance estimate respectively. The Minimum Mean Square Error (MMSE) and the suboptimal Least Squares (LS) estimate of $\Upsilon_{\mathrm{dB},t,est}(q_{t+1})$ and $\sigma_{t,est}(q_{t+1})$ was discussed in detail in [92]. q_t and q_{t+1} are the current and future positions of the agent and $\mathcal{V}$ is the set of velocities the agent can assume. The Q-function is given as follows.

$$Q(a) = \left(\frac{1}{2\pi}\right) \int\limits_{a}^{\infty} \mathrm{e}^{-s^2/2}\, ds \tag{3.138}$$

and the function $g(\cdot)$ is given as follows.

$$g(r) = \bar{\omega}(r - \epsilon_G)^2 + \nu \tag{3.139}$$

Where $\bar{\omega} > 0$ and $\nu > 0$ are scaling constants and ϵ_G is region around the goal position where the agent stops moving after entering it.

It can be seen that the optimization problem in Eq. (3.137) takes a decision on the next step based on the estimated RSS in a local region around the agent and the distance to the goal. Since a data packet will be dropped, if the agent enters a region with RSS below $\Upsilon_{\mathrm{dB,TH}}$, the planner in Eq. (3.137) will always avoid regions or positions where the RSS estimate is less than $\Upsilon_{\mathrm{dB,TH}}$. The trajectories obtained using the planner given in Eq. (3.137) will be referred to as the Sampling-Based Trajectorys

(SBTs) in the following.

MBCAN VS Sampling Based Planner: Low DCZ Threshold

In this section, the RSS packet dropping threshold $\Upsilon_{\mathrm{dB,TH}}$ is taken as -70 dB (The region with RSS below -70 dB is defined as the DCZ). In the following we compare the MBCAN-based and the sampling-based trajectories when the RSS packet dropping threshold is -70 dB. Fig. 3.54a shows the CAT, CBT and SBT for the scenario given in Fig. 3.16 and the corresponding SNR along these trajectories in compared in Fig. 3.54b. It can be seen that the SBT performs similar to the CBT. However, the SBT moves in a straight line as compared to the smooth curve obtained for the CBT. The CAT performs marginally better than both CBT and SBT in overall performance. There is not a significant performance difference between the the SBT and CAT as there is no obstacle in the environment that blocks the signal between the BS and the agent. Moreover, the SBT moves directly towards the goal because the packet-dropping threshold is very low, therefore, the RSS is always above the threshold in the region between the goal and the start position. Thus the SBT just moves towards the goal and doesn't attempt to improve its communication performance. The MBCAN on the other hand always maximizes the communication performance irrespective of the threshold.

The CAT, CBT and SBT trajectories and their corresponding SNR along the trajectories, are compared in an environment with a single rectangular obstacle in Fig. 3.55. It can be seen in Fig. 3.55a that the CAT avoids the low SNR region even though the threshold is very low. The SBT initially enters the low SNR region. How-

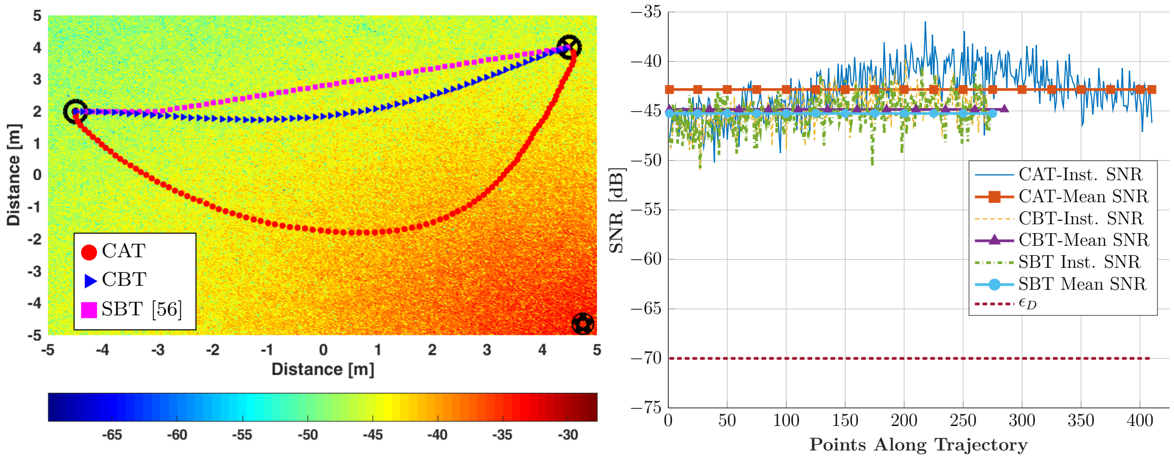

(a) Trajectories superimposed on SNR plot.

(b) SNR Comparison.

Figure 3.54: MBCAN-trajectory vs sampling based trajectory for the environment in Fig. 3.16 with $\epsilon_D = -70$ dB

ever, it then moves out of the low SNR region and moves towards the transmitter along the boundary of the low SNR region, as the high SNR region is near the transmitter. However, it then enters the low SNR region where it estimates, the SNR to be above the threshold before moving towards the goal in a straight line after exiting the low-SNR region. In the SNR comparison in Fig. 3.55b, it can be seen that the SNR along the SBT in the low SNR region is below the threshold. This is due to erroneous RSS prediction. The spatial RSS prediction in [92] assumes that the underlying channel parameters remain constant throughout the workspace. Due to the blocking of the wireless signal by the obstacle, the underlying channel parameters change in the low SNR region. Thus producing erroneous RSS predictions and consequently, the SBT entering regions with SNR less than the packet-dropping threshold. The overall communication performance of the SBT is slightly better than the CBT (mean SNR of the SBT is approximately 1.5 dB higher than that of the CBT). However, the mean SNR along the trajectory of the CAT is significantly higher ($\approx$ 18 dB). It has to be

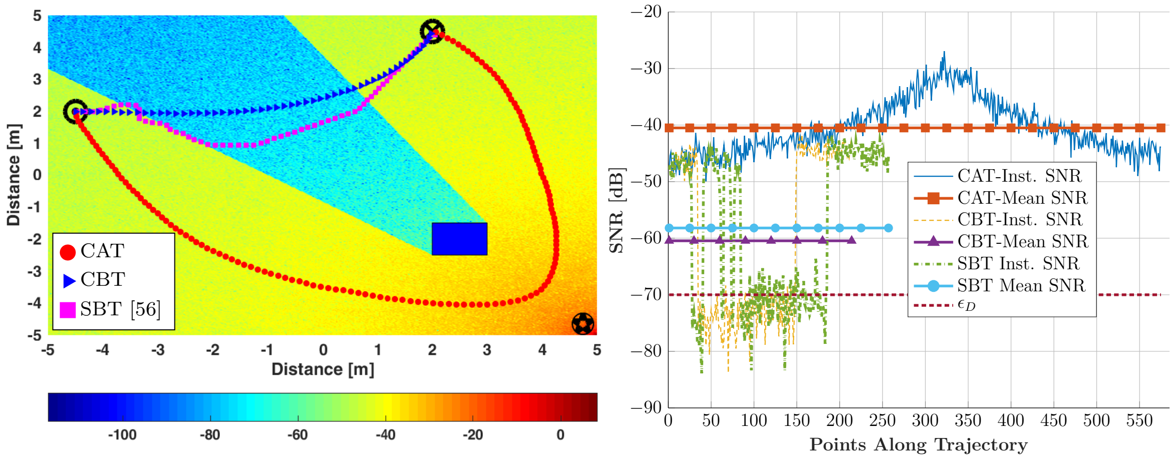

(a) Trajectories superimposed on SNR plot.

(b) SNR Comparison.

Figure 3.55: MBCAN-trajectory vs sampling based trajectory for the environment in Fig. 3.23 with $\epsilon_D = -70$ dB

noted that the SBT is obtained with complete SNR-map knowledge.

The CAT, CBT and SBT are compared in a more realistic scenario in **??**. The environment has many obstacles that induce attenuation in the wireless communication signal. Therefore, there are many regions with different underlying channel parameters. Again, it can be seen that the SBT performs marginally better than the CBT. However, the SBT still enters the region with SNR below the packet-dropping threshold. This is again due to erroneous prediction of the RSS (even with complete SNR-map knowledge). The SBT reaches the goal after it has exited the low SNR region. However, the mean SNR of the SBT is significantly lower than that of the CAT.

Fig. 3.57 presents the comparison of the CAT, CBT and the SBT for an environment with convex and non-convex obstacles with irregular geometry. Since the packet dropping threshold is very low, the SBT simply moves towards the goal in straight line. It only changes its course to avoid the obstacle in between. Comparing, the

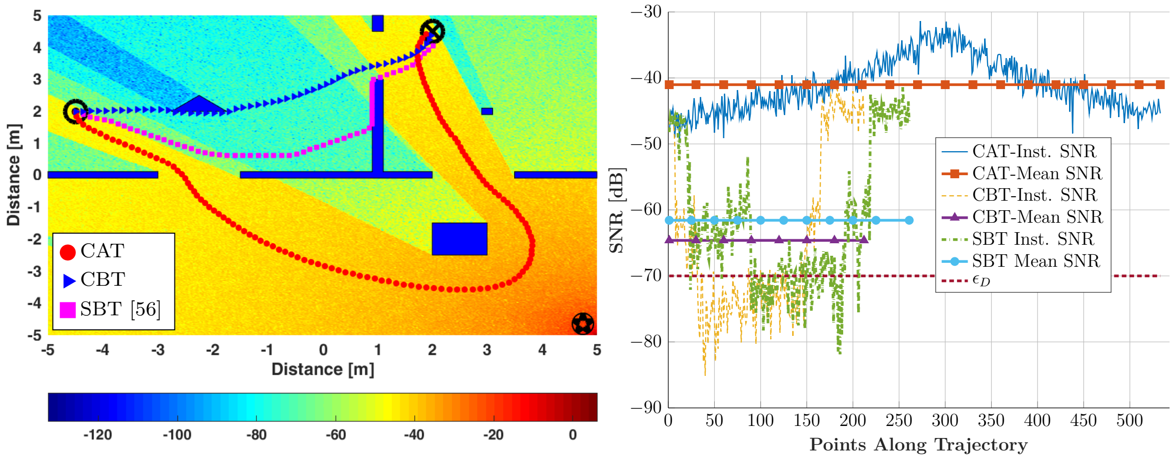

(a) Trajectories superimposed on SNR plot.

(b) SNR Comparison.

Figure 3.56: MBCAN-trajectory vs sampling based trajectory for the environment in Fig. 3.31 with $\epsilon_D = -70$ dB

communication performance, it can be seen in Fig. 3.57b that the mean-SNR of the SBT is nearly the same as that of the CBT and significantly lower ($\approx$ 8 dB) than the mean-SNR of the CAT.

It can be seen for all the scenarios in this section that for a low packet dropping RSS threshold, the SBT performs poorly as compared to the CAT in communication performance. However, the SBT tries to move in a straight line to goal. While this reduces the length of the trajectory, it tends to introduce sharp turns which are difficult to realize by a controller.

MBCAN VS Sampling Based Planner: High DCZ Threshold

In the following we compare the MBCAN algorithm the the communication-aware mobility generator given in [56]. Where it is assumed that the mobility generator in [56] also has full knowledge of the environment. We assume a high value of the packet-dropping threshold (-40 dB).

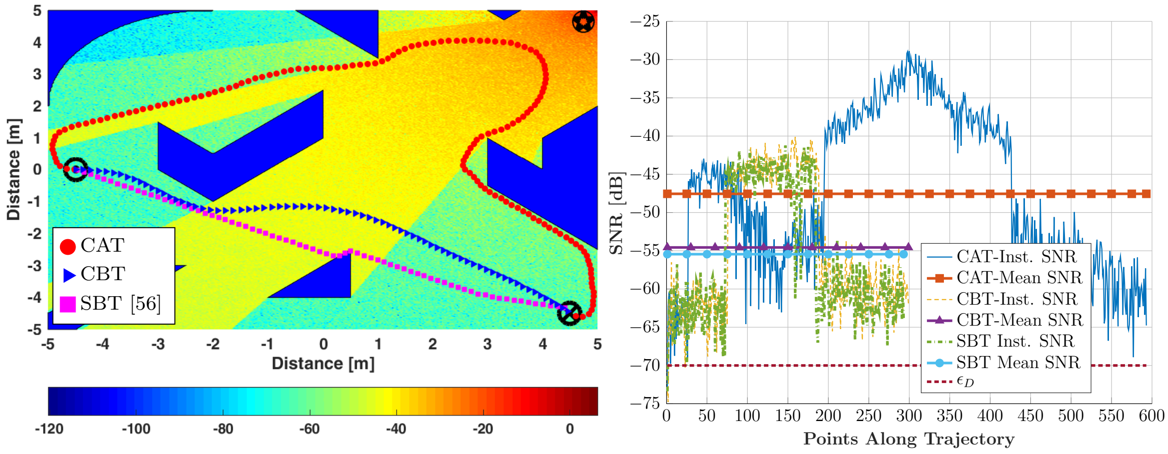

(a) Trajectories superimposed on SNR plot. **(b)** SNR Comparison.

Figure 3.57: MBCAN-trajectory vs sampling based trajectory for the environment in Fig. 3.46 with $\epsilon_D = -70$ dB

In Fig. 3.58, the CAT, CBT and SBT and their SNR is compared for the environment given in Fig. 3.16. Since there are no obstacles in the environment, the performances are similar. However, the SBT has the highest mean-SNR, which is slightly better than that of the CAT. Although, the SBT outperforms the CAT in mean-SNR, it is unable to reach the goal position and stops near the transmitter in the region where the SNR is −40 dB. Since, the planner in Eq. (3.137), chooses the next position based on both the distance from the goal and the distance of the RSS from the packet-dropping threshold, it forbids motion away from regions with SNR higher than the threshold towards regions with lower SNR. Thus, it can be seen that the SBT moves towards the region with the same SNR as the threshold and tries to move towards the goal while remaining in that region. Thus it fails to reach the goal as the region around the goal as a low SNR than the packet dropping threshold.

The comparison of the CAT, CBT and SBT for an environment with a single rectangular obstacle is given in Fig. 3.59a for a high packet dropping threshold. It can

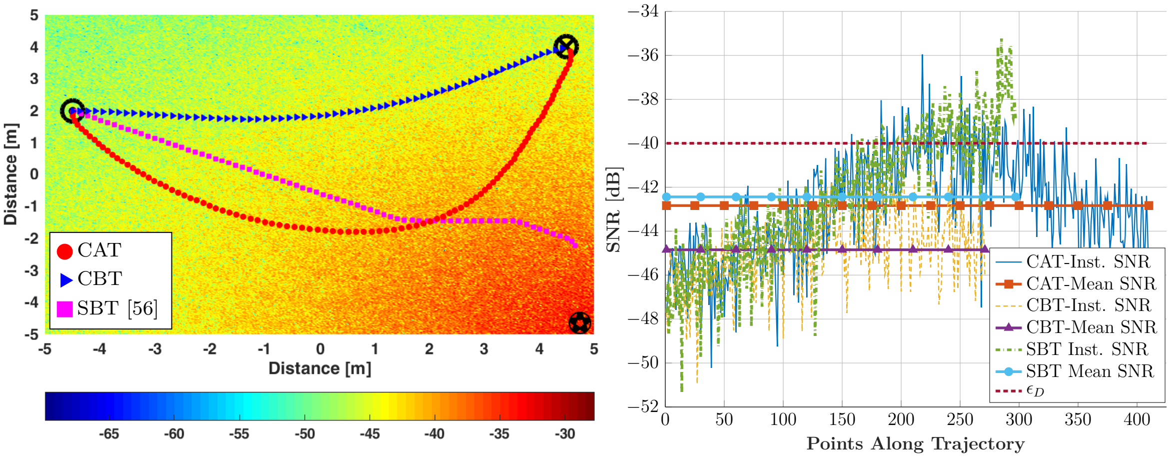

(a) Trajectories superimposed on SNR plot.

(b) SNR Comparison.

Figure 3.58: MBCAN-trajectory vs sampling based trajectory for the environment in Fig. 3.16 with $\epsilon_D = -40$ dB

be seen that the SBT matches the CAT but fails to reach the goal. This is again due to the planner in Eq. (3.137) forbidding the trajectory to move away from a region with SNR equal to the packet dropping threshold to a region with lower SNR. Hence, the SBT enters the region with SNR above or equal to the threshold and moves towards the goal but stops when it needs to move enter a region with lower SNR. This can be verified in the SNR comparison in Fig. 3.59b. It can be seen that the SBT matches the instant and mean-SNR performance of the CAT, but significantly the SBT fails to reach the goal.

Mobility in a realistic environment with multiple obstacles is compared in Fig. 3.60. Interestingly, the SBT stops after just a few steps. Therefore, the planner given in Eq. (3.137) completely fails. There are multiple reasons for this behavior. Examining the planner in Eq. (3.137), it can be seen that chooses it next step based on the estimated RSS in a local region and the distance to goal. Since, there are multiple shadowed regions with different underlying parameters, the agent needs to move away

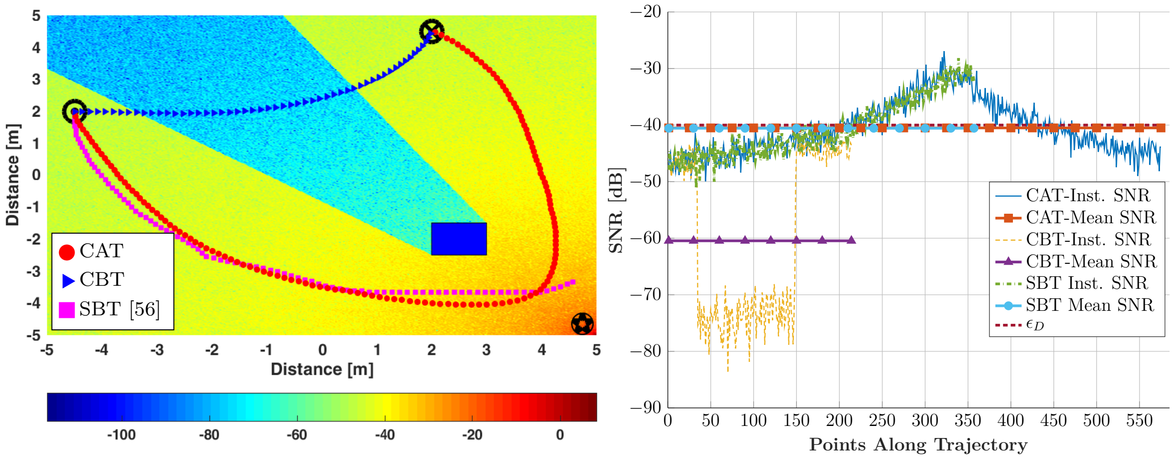

(a) Trajectories superimposed on SNR plot.

(b) SNR Comparison.

Figure 3.59: MBCAN-trajectory vs sampling based trajectory for the environment in Fig. 3.23 with $\epsilon_D = -40$ dB

from the goal to move towards the region with the RSS above the packet dropping threshold (which is very high). Moving away from the goal reduces the cost in the maximization problem in Eq. (3.137). On the other hand moving towards the goal requires the agent to move towards a region with a SNR lower than that of the packet dropping threshold. Moreover, since there are multiple shadowed regions with different underlying parameters, the spatial RSS prediction in [92] fails as it assumes the same underlying channel parameters throughout the workspace. Consequently, the agent predicts a low SNR locally even when it is surrounded by a region consisting of higher RSS values. The composition of the planner in Eq. (3.137) thus, forbids the agents motion away from the goal and from a higher to lower SNR region (based on the agent's perception). Thus results in the behavior of the SBT shown in Fig. 3.60a.

Finally, the CAT, CBT and SBT are compared in Fig. 3.61a for an environment with multiple obstacles of irregular geometry. The packet dropping threshold is −40 dB. It can be seen in the SNR comparison in Fig. 3.61b that the mean-SNR along

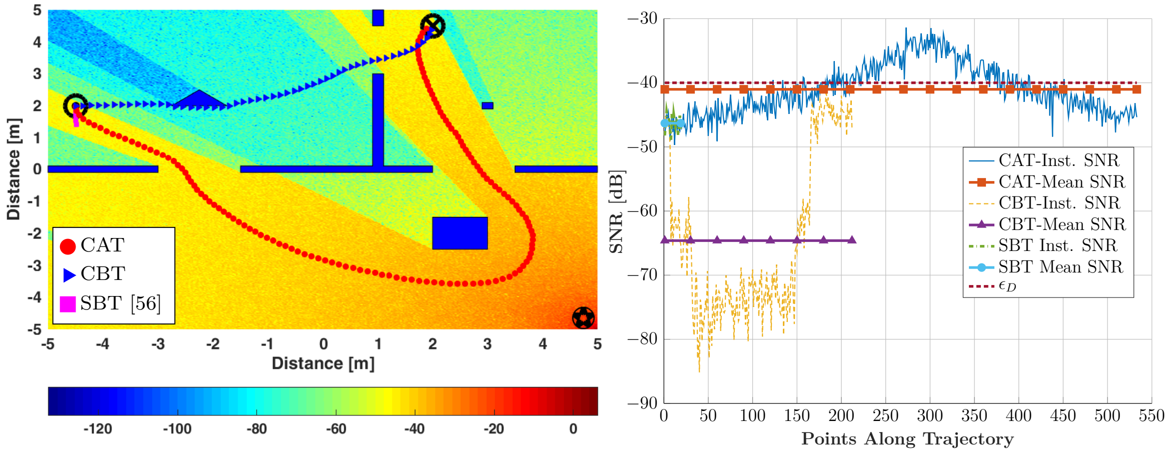

(a) Trajectories superimposed on SNR plot. **(b)** SNR Comparison.

Figure 3.60: MBCAN-trajectory vs sampling based trajectory for the environment in Fig. 3.31 with $\epsilon_D = -40$ dB

the SBT is higher than that of the CAT. However, as seen in Figs. 3.58a and 3.59a, the SBT fails to reach the goal position. Rather it moves towards the transmitter as the SNR increases as the agent gets closer to the BS. After entering the region with SNR higher than the packet dropping threshold, the planner in Eq. (3.137) discourages motion from regions with higher SNR towards a region with lower SNR. Thus the SBT stops motion at the boundary of the region with SNR greater or equal to the packet dropping threshold such that it is as close as possible to the goal. It has to be noted that the multiple wireless signal shadowed regions induce errors in the spatial RSS prediction ([92]) employed by the planner in Eq. (3.137), thus the agent erroneously predicts lower SNR for regions with high SNR.

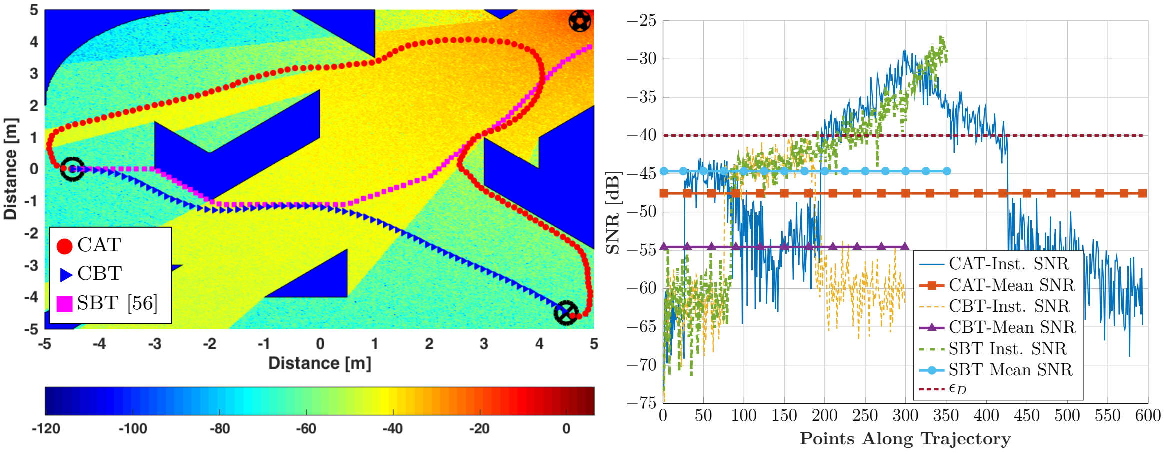

(a) Trajectories superimposed on SNR plot. **(b)** SNR Comparison.

Figure 3.61: MBCAN-trajectory vs sampling based trajectory for the environment in Fig. 3.46 with $\epsilon_D = -40$ dB

3.7 Joint Motion and Beamforming

Typically, in the wireless communication literature, the user (robot in our case) is considered to have a fixed position while beamforming is applied at the BS [93]. This is valid for slow moving robots but for high speed agents, this could lead to the beam being formed for positions that are no longer occupied by the robot. Also, the future spatial positions of the user are not known in traditional beamforming problems. Using the MBCAN, the robot computes its position as a continuous trajectory, $\mathbf{p}(t)$, to the goal. This spatial information of the robot can be used to predict the WCC, $\mathbf{h}(t)$ along the trajectory [56]. Thus, a complex vector trajectory $\mathbf{w}(t)$ can then be simultaneously computed to improve the SNR along the trajectory of the agent.

Zero-Forcing (ZF) beamforming is known to give near system capacity performance if the WCC is known [94]. Based on the predicted WCC, $\mathbf{h}(t)$, for the robot path,

$\mathbf{p}(t)$, we propose a ZF beamforming frame work as follows

$$\mathbf{w}(t) = \frac{\mathbf{h}(t)(\mathbf{h}(t)^H\mathbf{h}(t))^{-1}}{\|\mathbf{h}(t)(\mathbf{h}(t)^H\mathbf{h}(t))^{-1}\|_2} \tag{3.140}$$

where $\|\mathbf{w}(t) \in \mathbb{C}^{n_T \times 1}\|_2 = 1, \forall t$. The agent is equipped with a single antenna and beamforming is only employed at the BS. This is due to the reason that adding multiple antennas requires an increase in the agent size. It also increases energy consumption. Since we assume reciprocity in the WCC in uplink and downlink, techniques like maximal ratio combining can be used to obtain a similar gain at the BS for data transmitted by the single antenna agent to the BS.

Fig. 3.62 compares the PDF and CDF of the instantaneous SNR and ZF beamforming at each instant along the trajectory of the CATs with trajectories that have no SNR knowledge. The PDF was obtained by generating 4000 trajectories in the cluttered environment (Fig. 3.31), using random start and goal position for each trajectory sample. It can also be seen that with joint simultaneous ZF beamforming and MBCAN, there is a further gain in the the instantaneous SNR of the CAT in the whole SNR range. Finally, it can be seen that nearly 9% of the instantaneous SNR of the joint ZF and MBCAN trajectories lie in a DCZ. As a consequence of a gain in the inst. SNR over all the trajectories, the mean SNR was also higher for the joint ZF and MBCAN trajectories with Less than 0.5% of the trajectories having mean SNR below ϵ_D as shown in Fig. 3.63.

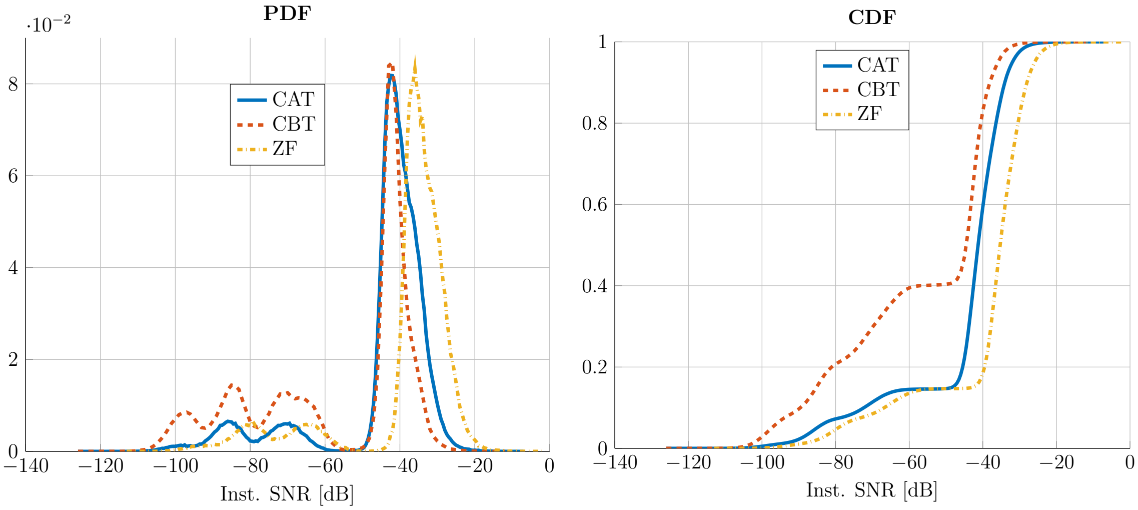

Figure 3.62: PDF and CDF of instantaneous SNR at each point along trajectories computed using MBCAN with ZF beamforming.

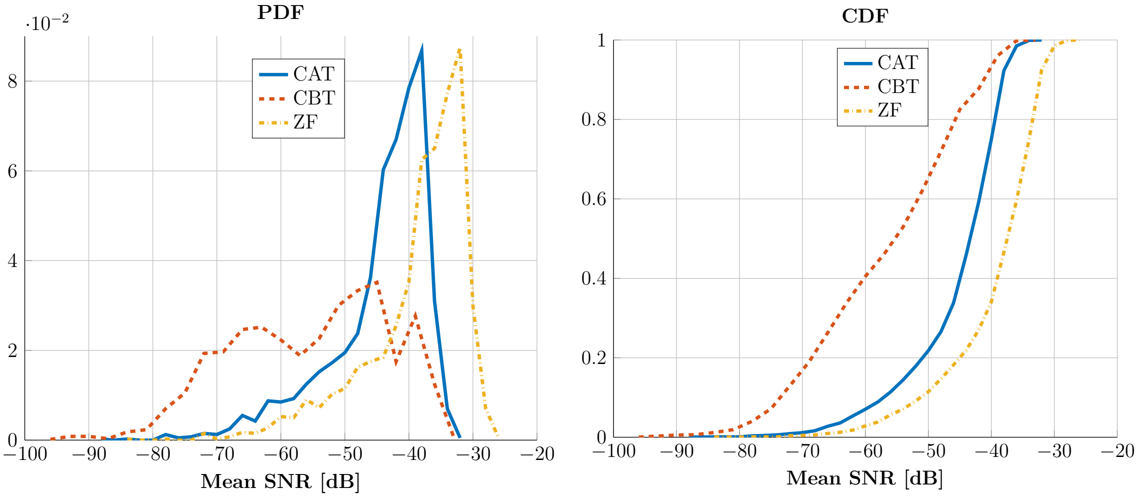

Figure 3.63: PDF and CDF of mean SNR of a trajectories computed using MBCAN with ZF beamforming.

3.8 Conclusions

In this chapter, we introduced a HPF-based navigation algorithm that integrates wireless communication performance constraints in autonomous agent mobility. We assume full knowledge of the RSS. A representation of the WCC is obtained in the form of an SNR map. WCC gains were obtained using the WINNER II [90] channel models for indoor environments.

We found that our method MBCAN is able to generate spatially well-behaved trajectories that had significantly better SNR performance than regular HPF based trajectories that were blind to the WCL. Moreover, we are able to guarantee no channel outage if the agent is initially connected to the base-station and the good SNR (SNR above a threshold) region is connected, i.e., a path with good SNR exists to the target.

Extensive simulation of the suggested approach demonstrated that the actuation and communication properties of the MBCAN procedure persisted irrespective of the geometric complexity of the environment. Also, simulation results supported their theoretical counterparts regarding the fact that the increase int he length of the communication-aware trajectory relative to the communication-blind one is equal to the gain in the expected signal strength.

While MBCAN jointly treats Dead Communication Zones (DCZ)s and Hard Obstacle or Hazardous Region (HO)s as undesirable regions of the workspace which motion should be steered away from, it observes the difference in their physical nature. In a region occupied by a HO, the gradient field degenerates and MBCAN looses its ability to steer motion. This is understandable, since by moving into a region marked as a hard obstacle, the agent gets damaged and it no longer matters whether it receives guidance or not. On the other hand, if accidentally, the agent enters a DCZ and communication with the Base-Station (BS) is lost, MBCAN does provide guidance that enables the agent to exit the DCZ as fast as possible and restore the communication link.

The performance of MBCAN is optimal in the sense of minimizing a utility functional that is jointly designed to suit both the actuation and communication requirements of the agent. Although, this functional is neither convex nor continuous for that matter, MBCAN can actuate the agent and drive it along a trajectory which is the global minimizer of the functional.

The statistical properties of the single transmitter WCL, MBCAN can provide to the agent are explored experimentally by constructing the SNR and mean-SNR PDFs and CDFs of an ensemble of trajectories covering the whole workspace. It is shown that MBCAN can significantly improve the instantaneous SNR along the trajectory in the low SNR region compared to the trajectories computed with no SNR knowledge. In the high SNR region, the trajectories computed using MBCAN and no SNR knowledge behave similarly. This demonstrates the on-demand nature of MBCAN where it influences the agent's mobility when its needed. For the mean SNR, it is shown that MBCAN gives an approximately consistent significant improvement throughout the environment except at extremely high SNR. In extremely high SNR regions, the mean SNR performance converges to the SNR performance for trajectories that are blind to the WCL.

A review of the computational complexity for the MBCAN is provided. The total energy consumption (communication and motion energy) due to the CAT and CBT is provided. It was seen that the energy consumption due to CAT is much lower than that of the CBT for most of the scenarios. However, for the scenario without any obstacles, the energy of the CBT is marginally less than that of the CAT.

We compared our proposed approach with the SBT in [56]. It is seen that our approach outperforms the SBT for the different scenarios for different packet-dropping thresholds. Especially for high packet dropping threshold, the SBT fails to reach the goal in all the scenarios.

In the following chapters, a sensor-based algorithm for communication-awar mobility is developed so as to improve the WCL performance along a trajectory to the goal, when signal strength is measured on-line. The results obtained using MBCAN will be used as a benchmark for the sensor-based case.

CHAPTER 4

SENSOR-BASED COMMUNICATION-AWARE MOBILITY (SBCAN)

"The greatest danger for most of us is not that our aim is too high and we miss it, but that is is too low and we reach it."

—MICHELANGELO.

In this chapter, we develop real-time sensor-based algorithms that avoid Dead Communication Zones (DCZ)s while navigating an environment with no a priori known Received Signal Strength (RSS). We assume that the Hard Obstacle or Hazardous Region (HO) information is completely available. However, the scenario that no Hard Obstacle or Hazardous Region (HO) information is available initially can also be tackled by our planner as HO information can be obtained using range sensors like ultrasonic sensors. The variations in spatial RSS on the other hand is extremely difficult to obtain. A reasonable estimate of the RSS in a region can only be obtained

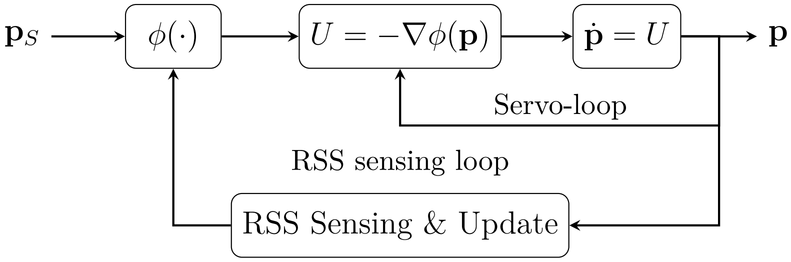

Figure 4.1: Sensor-Based Mobility Controller

by visiting locations in that region or locations in its neighborhood.

The Signal to Noise Ratio (SNR) information, therefore, has to be constantly updated as the agent moves in order to obtain plans that can avoid regions with poor wireless connectivity. The mobility controller in this case has two loops (Fig. 4.1) of different natures: a servo loop that has a continuous nature (the output of this loop is always available) and the RSS sensing loop which measures and updates the SNR-map at discrete locations along the agent's trajectory. Since, the agent has no initial SNR-map, it will not know the DCZ in the environment. Therefore, the agent cannot compute a plan to the goal that avoids the DCZs. However, as the agent moves in the environment, it can sense the RSS and update its SNR-map. This requires, the agent to constantly update its path-plan to accommodate the new RSS information. Also, since DCZs are caused by obstacles blocking the RSS to the agent, predicting the location of a DCZ is very challenging due to the random locations and geometric shapes of the obstacles. If the agent doesn't know the location of a DCZ, it could enter the DCZ and lose communication. Thus, the agent needs to have the RSS information in order to compute a plan that avoids DCZs.

On the other hand, since the agent has no RSS information initially, it can only obtain the DCZ information on time by moving in the environment and sensing the

RSS. This results in a cyclical problem where both mobility and RSS information are dependent on each other.

In [92] a framework was provided to predict the RSS in a region. However, it assumes that the underlying parameters that govern the RSS variations remain constant. In scenarios, like search and rescue, the environment changes very fast. Therefore, the parameters, that govern the variations in RSS over space will also change. Therefore, the prediction of RSS over space is valid in a localized region. The underlying parameters that govern the RSS in a DCZ are different than the parameters in a region where RSS is not blocked.

In this chapter, we build on the Harmonic Potential Field (HPF)-based planner used in Model-Based Communication-Aware Navigation (MBCAN). However, no knowledge of the RSS map is assumed before motion starts. The SNR-map has to be updated as the agent moves in the environment. As the agent starts moving in the environment, it updates its SNR map by measuring the RSS at each spatial position it visits as shown in Fig. 4.2. After each RSS update, the motion policy is recomputed. Therefore, the Partial Differential Equation (PDE) given in eq. 3.15 has to be solved after each update of the SNR map. The Potential Field (PF) obtained as a result will change at each step based on the SNR update.

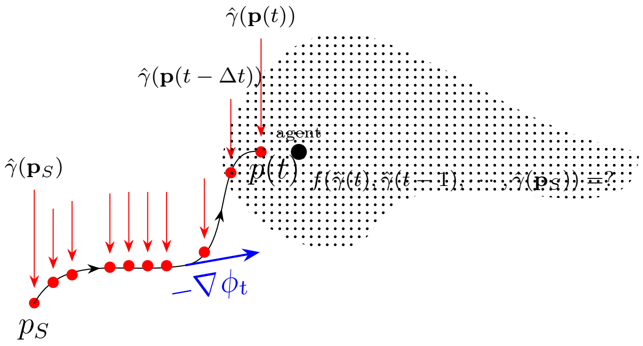

Figure 4.2: SNR measurement and prediction updates

4.1 Sensor-Based Updates & Mobility

As mentioned in the previous section, the agent has to move to unexplored locations to sense and update its SNR-map and consequently avoid low-SNR regions.The agent starts will a initial guess, γ_S of the SNR-map, $\gamma(\mathbf{p})\ \ \forall \mathbf{p} \in \mathcal{W}$, of the environment and then updates this map with the sensed SNR, $\widehat{\gamma}(\mathbf{p}(\tau)),\ 0 \leq \tau \leq t,\ \mathbf{p}(0) = \mathbf{p}_S$, as it moves. The SNR-map is updated based on the sensed SNR using an update function, $f(\widehat{\gamma}(\mathbf{p}(\tau))),\ 0 \leq \tau \leq t,\ \mathbf{p}(0) = \mathbf{p}_S$. The SNR-map update is given as follows

$$\gamma(\mathbf{p}, t) = \begin{cases} f(\widehat{\gamma}(\mathbf{p}(\tau))), & \mathbf{p} \in \mathcal{U}, \mathcal{U} \subseteq \mathcal{W} \\ \text{Don't Update}, & \mathbf{p} \in \mathcal{U}' \end{cases} \tag{4.1}$$

Where, $\mathcal{U}$, is the region where the SNR is updated in the SNR-map. It could be the complete region [92] or a localized region $\mathcal{U}$ around the current position, $\mathbf{p}(t)$, of the agent.

Also, notice that the global SNR-map is a function of time as it is updated by agent after each measurement. Since the SNR-map is updated with time, the PF, which guides the motion of the agent has to be updated with each SNR update. Therefore, the updated PF at a time instant t is generated by solving the following Boundary Value Problem (BVP).

$$\text{solve at each } t \quad \nabla \cdot (\gamma(\mathbf{p}, t)\nabla\phi(\mathbf{p})) = 0,\ \mathbf{p} \in \mathcal{W} \tag{4.2a}$$

$$\text{subject to} \quad \phi(\mathbf{p}_S) = 1,\ \phi_t(\mathbf{p}_G) = 0,\ \frac{\partial\phi}{\partial\mathbf{n}} = 0,\ \text{at } \mathbf{p} \in \mathbf{\Gamma}_{\mathcal{W}} \tag{4.2b}$$

$$\frac{\partial\phi}{\partial\mathbf{n}} = 0,\ \text{at } \mathbf{p} \in \mathbf{\Gamma}_{\mathcal{O}},\ \text{Neumann Boundary} \tag{4.2c}$$

Comparing the BVP in Eq. (4.2) with Eq. (3.15) of the model-based case, it can be seen that the BVP Eq. (4.2) has to be solved continuously with time, since, the SNR-map is continuously being updated. Where as, in the MBCAN the SNR-map is fully known and therefore remains unchanged throughout the motion of the agent. Hence the Harmonic Potential Field (HPF) obtained as a solution to Eq. (4.2), $\phi(\mathbf{p}, \gamma(\mathbf{p}, t))$, is dependent on a time-dependent SNR map. In the following, we let

$$\phi_t(\mathbf{p}) = \phi(\mathbf{p}, \gamma(\mathbf{p}, t)) \tag{4.3}$$

The trajectory of the agent is then obtained by following the gradient of the updated ϕ_t after each measurement.

$$\dot{\mathbf{p}} = -\nabla\phi_t(\mathbf{p}),\ \mathbf{p}(0) = \mathbf{p}_S \tag{4.4}$$

The update $f(\cdot)$ is critical in determining the performance of the planner as the future positions of the agent depend on the the HPF obtained after the SNR update. Any errors in the update could lead to the agent entering a DCZ. The Sensor-Based Communication-Aware Navigation (SBCAM) algorithm for single integrator system

$$\dot{\mathbf{p}} = u \tag{4.5}$$

is given in algorithm 2 and the corresponding SBCAM flow is given in Fig. 4.3.

Algorithm 2 SBCAM

```
1: Get Workspace $\mathcal{W}$.
2: Get HO representation $\mathcal{O}(\mathbf{p})$ for $\mathcal{W}$.
3: Initialize SNR representation $\gamma(\mathbf{p})$ for $\mathcal{W}$.
4: Get start position $\mathbf{p}_S$ of agent.
5: GAMMA-HARMONIC POTENTIAL FIELD (GHPF)($\mathcal{W}$,$\gamma$,$\mathcal{O}$,$\mathbf{p}_S$,$\mathbf{p}_G$).    ▷ Calling function GHPF
6: Find ${\mathbf{p}_S}'$ using eq. 3.18
7: Solve $\dot{\mathbf{p}} = \int_t^{\Delta t} -\nabla\phi dt,\ \mathbf{p}(0) = {\mathbf{p}_S}'$ for next trajectory step $\mathbf{p}(t+\Delta t)$.
8: if $\|\mathbf{p}(t) - \mathbf{p}_G\| \leq \epsilon_G$ then
9:     Stop algorithm.
10: else
11:     Update SNR-map $\gamma$ using SNR measurement at $\widehat{\gamma}\left(\mathbf{p}(t+\Delta t)\right)$.
12:     GHPF($\mathcal{W}$,$\gamma$,$\mathcal{O}$,$\mathbf{p}_S$,$\mathbf{p}_G$).
13:     Go to operation 7.
14: end if
15: function GHPF($\mathcal{W}$,$\gamma$,$\mathcal{O}$,$\mathbf{p}_S$,$\mathbf{p}_G$)
16:     Set $\frac{\partial\phi}{\partial n} = 0$ at $\mathbf{\Gamma}_{\mathcal{W}}$.
17:     Set $\frac{\partial\phi}{\partial n} = 0$ at $\mathbf{\Gamma}_{\mathcal{O}}$.
18:     Set $\phi(\mathbf{p}_S) = 1$.
19:     Set $\phi(\mathbf{p}_G) = 0$.
20:     Solve $\nabla \cdot \left(\chi\left(\gamma\right)\nabla\phi\right) = 0$ for $\phi$.
21:     return $\phi$.
22: end function
```

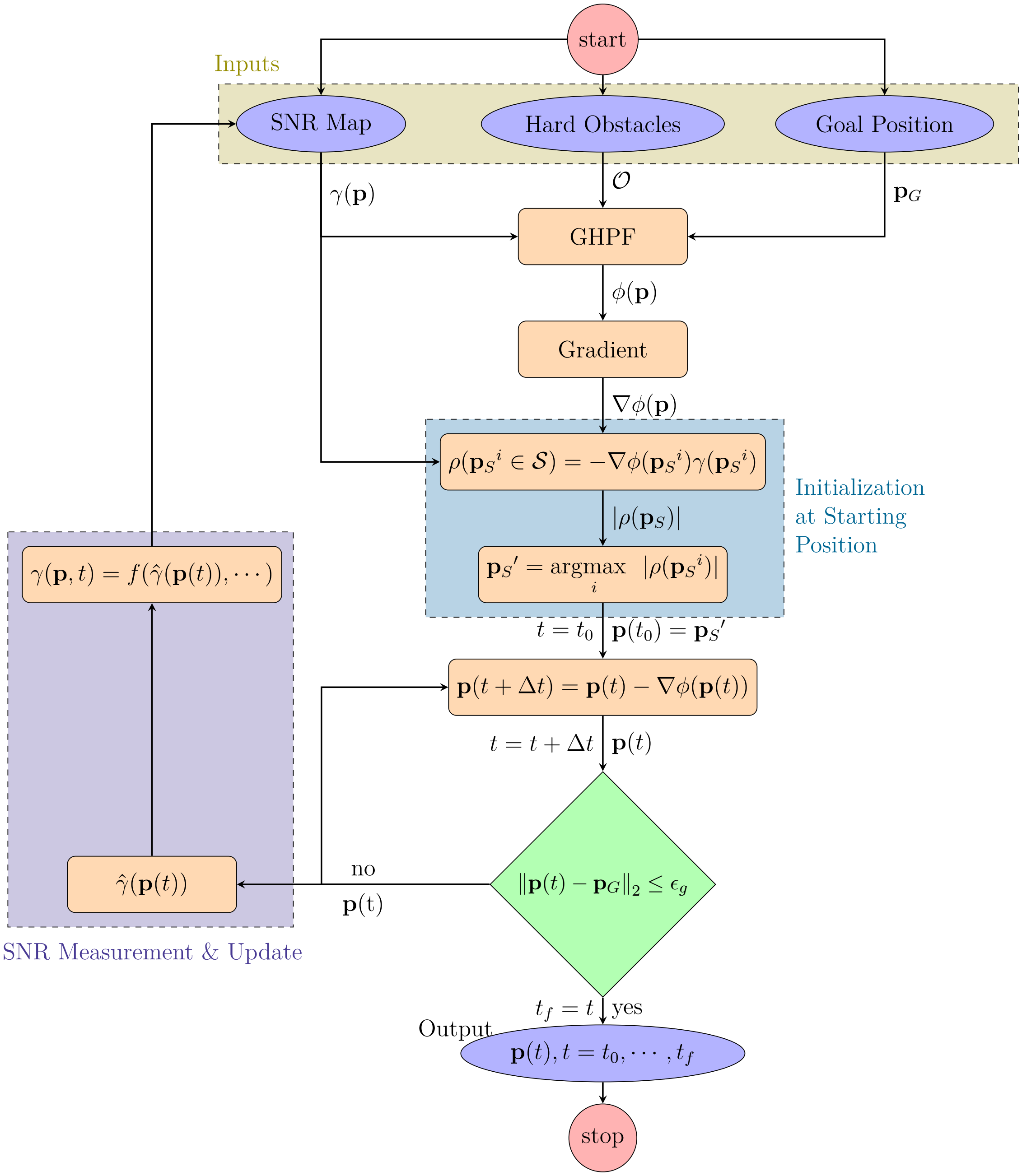

Figure 4.3: SBCAM flow graph

4.1.1 Analysis

The HPF obtained as a solution of Eq. (4.2) can change with time depending on the SNR update as the agent moves along its trajectory using the PDE-Ordinary Differential Equation (ODE) system of Eq. (3.20). This opposed to the MBCAN case where the HPF remains constant through out the agent's motion. Since the HPF is changing with time, guaranteeing convergence is important for the agent to generate trajectory in SBCAM. In the following proposition, we prove the convergence of an agent's trajectory using Eq. (4.4) where the time dependent HPF is obtained as a solution to Eq. (4.2). Throughout this section, the single integrator system of Eq. (4.5) is referred to as the agent.

PROPOSITION 4.1 *The trajectory of an agent* $\mathbf{p}(t)$ *governed by the dynamical system of Eq.* (4.4)

$$\dot{\mathbf{p}} = -\nabla\phi_t(\mathbf{p}),\ \ \mathbf{p}(0) = \mathbf{p}_S \tag{4.6}$$

will always asymptotically converge to the goal position $\mathbf{p}_G$*.*

$$\lim_{t\to\infty} \mathbf{p} \to \mathbf{p}_G,\ \ \mathbf{p}(0) = \mathbf{p}_S \in \mathcal{W}_\phi \tag{4.7}$$

if

$$\frac{\partial\phi(\mathbf{p})}{\partial\gamma}\frac{\partial\gamma(\mathbf{p})}{\partial t} \le \|\nabla\phi_t(\mathbf{p})\|^2 \tag{4.8}$$

or if the SNR-map converges, i.e.,

$$\lim_{t\to\infty} \frac{\partial\gamma}{\partial t} \to 0. \tag{4.9}$$

Proof. At time, t the HPF, ϕ_t, is obtained as a solution to the system in Eq. (4.2). Following the same methodology as in Prop. 3.8, ϕ_t at time t is a Lyapunov Function Candidate (LFC) (Prop. 3.5). Let Λ represent the LFC $\phi_t(\mathbf{p})$, where $\mathbf{p}(t), \mathbf{p}(0) = \mathbf{p}_S$, is the trajectory of the agent at time t obtained using Eq. (4.4), and using Eq. (4.3) we get

$$\Lambda = \phi(\mathbf{p}, \gamma(\mathbf{p}, t)) \tag{4.10}$$

The total derivative [83] of Eq. (4.10) can be obtained using the chain rule.

$$\frac{d\Lambda(\mathbf{p}, \dot{\mathbf{p}}, \dot{\gamma})}{dt} = \frac{\partial \phi(\mathbf{p}, \gamma)}{\partial \gamma}\dot{\gamma} + \nabla \phi(\mathbf{p}, \gamma(\mathbf{p}, t))^T \dot{\mathbf{p}} \tag{4.11}$$

substituting eq. 4.4 in eq. 4.11

$$\dot{\Lambda}(\mathbf{p}, \dot{\mathbf{p}}, \dot{\gamma}) = \frac{\partial \phi(\mathbf{p}, \gamma)}{\partial \gamma}\dot{\gamma} - \|\nabla \phi(\mathbf{p}, \gamma(\mathbf{p}, t))\|^2 \tag{4.12}$$

$\nabla \phi_t$ vanishes at the goal $\mathbf{p}_G$ and might have isolated critical points $\{\mathbf{p}_{c_i}(t)\}, i = 1, 2, 3, \cdots, n_c(t)$ ($n_c(t)$ is the time varying number of isolated critical points) in $\mathcal{W}_\phi$. It can be noted that as opposed to the MBCAN, the SBCAM can have different number of isolated critical points since the HPF is dependent on a time-dependent SNR-map. However, the goal position remains constant for all time. This leads to

$$\dot{\Lambda} - \frac{\partial \phi(\mathbf{p}, \gamma)}{\partial \gamma}\dot{\gamma} \leq 0, \forall t,\ \mathbf{p} \in \mathcal{W}_\phi \tag{4.13}$$

$$\implies \dot{\Lambda} \leq \frac{\partial \phi(\mathbf{p}, \gamma)}{\partial \gamma}\dot{\gamma}, \forall t,\ \mathbf{p} \in \mathcal{W}_\phi \tag{4.14}$$

The LaSalle principle [82] states that if $\dot{\Lambda} \leq 0$ any bounded solution of eq. 4.4 will converge to the minimum invariant set given by,

$$\mathcal{I}(t) \subset \{\mathbf{p}_G \cup \{\mathbf{p}_{c_i}(t)\}\}. \tag{4.15}$$

It can be noted that the minimum invariant set $\mathcal{I}(t)$ is changing with time as the critical points are time dependent. Finding $\mathcal{I}$ requires studying critical points of $\mathbf{p}$ at time t

$$\{\mathbf{p}_{c_i}(t)\} = \{\mathbf{p} | \nabla\phi(\mathbf{p}, \gamma(\mathbf{p}, t)) = 0\} \tag{4.16}$$

Since the HPF $\phi_t(\mathbf{p})$ is essentially a solution to a MBCAN problem at time t, proposition 3.4, can be applied to $\phi_t(\mathbf{p})$ for all time. Since the goal position $\mathbf{p}_G$ is not changing with time, $\mathbf{p}_G$ will be the only minimum (a stable equilibrium point) of $\phi_t(\mathbf{p})$ for all time instants. Similarly, $\{\mathbf{p}_{c_i}(t)\}$ are isolated critical points for all time instants and the Hessian of ϕ_t is nonsingular for all time instants. Therefore, $\{\mathbf{p}_{c_i}(t)\}$ are Morse (proposition 3.7) for all time instants. Therefore, the minimum invariant set $\mathcal{I}(t)$ will only consist of the goal position for all time instants.

$$\mathcal{I}(t) = \{\mathbf{p}_G\} \tag{4.17}$$

For the LaSalle principle to hold, the following must hold for all time

$$\dot{\Lambda} \leq 0, \forall t, \ \mathbf{p} \in \mathcal{W}_\phi \tag{4.18}$$

Thus, asymptotic convergence to the goal position is guaranteed if and only if

$$\frac{\partial\phi(\mathbf{p},\gamma)}{\partial\gamma}\dot{\gamma} - \left\|\nabla\phi_t(\mathbf{p})\right\|^2 \leq 0 \tag{4.19}$$

$$\frac{\partial\phi(\mathbf{p},\gamma)}{\partial\gamma}\dot{\gamma} \leq \left\|\nabla\phi_t(\mathbf{p})\right\|^2, \forall t \tag{4.20}$$

Eq. (4.20) gives a bound on the rate of change of γ for convergence to be guaranteed to the goal position. Since the HPF is obtained as a solution to a BVP (Eq. (4.2)), therefore, the rate of change of the SNR-map in the Right Hand Side (RHS) of Eq. (4.20) can only be designed. Therefore, it needs to be updated in such way so that the bound of Eq. (4.20) is not violated.

The bound in Eq. (4.20) requires that γ is slowly varying. Letting $\lim_{t\to\infty}\dfrac{\partial\gamma}{\partial t} \to 0$ in Eq. (4.14) will result in

$$\dot{\Lambda} \leq 0,\ t \to \infty \tag{4.21}$$

Therefore, convergence of the SNR-map guarantees asymptotic convergence of the agent's trajectory to the goal position. ∎

PROPOSITION 4.2 *The trajectory generated by the gradient dynamical system in eq. 4.4 will always avoid the HO*

$$\mathbf{p}(t)\bigcap\mathcal{O} = \varnothing,\ \forall t \tag{4.22}$$

Proof. As shown in the proof of Prop. 3.1, homogeneous Neumann boundary conditions at the boundary of the HO forces any motion component towards the HO to be zero. Thus the agent can only move tangent to the obstacle boundary or away from it. Motion always remains in $\mathcal{W}_\phi$. $\mathcal{W}_\phi$ is defined as follows

$$\mathcal{W}_\phi = \mathcal{W} - \mathcal{O} \tag{4.23}$$

where $\mathcal{W}_\phi$ is the domain (a connected open subset) in which ϕ exists. $\blacksquare$

SBCAM Optimality: An Overview

In the case of the MBCAN, it was shown in Prop. 3.10 that the MBCAN trajectory minimized the functional given in Eq. (3.84). This applied when the SNR-map was fully known and the agent choosed a starting orientation based on this knowledge.

In SBCAM, the agent starts with zero knowledge of the SNR-map (the SNR-map is initialized with the same value, uniformly over the complete workspace). The SNR-map is then updated at each time instant based on the measured RSS. This makes the SNR-map time-varying. Therefore, the definition of the flow density in Def. 3.5, is also time-varying.

$$\rho(\mathbf{p}, t) = -\nabla\phi(\mathbf{p}, t)\gamma(\mathbf{p}, t) \tag{4.24}$$

The minimization of the functional Eq. (3.84) in MBCAN (Props. 3.9 and 3.10) was dependent on choosing the starting orientation corresponding to the maximum magnitude of ρ and the fact that ρ remained constant for all time along a trajectory. These conditions are violated in the SBCAM as ρ is time-varying.

In the following, we redefine the functional to study the optimality of the SBCAM.

DEFINITION 4.1 *Using the definition of a trajectory as in Def. 3.4, let $\mathcal{T}$ be a set of all possible trajectories, an agent can take from its starting position, $\mathbf{p}_S \in \mathcal{W}_\phi$, to the goal position, $\mathbf{p}_G \in \mathcal{W}_\phi$, in its workspace. A trajectory $\mathbf{q}_i \in \mathcal{T}$ can be realized by choosing a starting position, ${\mathbf{p}_S}^i$, on a sphere $\mathcal{S}$ (3.11) and then following the gradient of ϕ at each time instant t until the agent reaches the goal position (eq. 4.4). The line integral over any trajectory $\mathbf{q}_i$ over ϕ obtained as a solution to eq. 4.2 at each time instant will be given by*

$$\boldsymbol{\Upsilon}(\mathbf{q}_i) = \int\limits_{\mathbf{p}_S=\mathbf{q}_i(0)}^{\mathbf{p}_G=\mathbf{q}_i(\infty)} -\nabla\phi(\mathbf{q}_i, \gamma(\mathbf{q}_i, t)) \cdot d\vec{\mathbf{q}}_i \tag{4.25}$$

It has to be noted that unlike the MBCAN, the HPF is updated at each time-instant. Since, a time varying gradient vector field is not conservative [95], the line integral Eq. (4.25) *cannot be computed as the difference of the potential at the goal and starting point. Using eq. 4.24, eq. 4.25 can be written as*

$$\boldsymbol{\Upsilon}(\mathbf{q}_i) = \int\limits_{\mathbf{p}_S}^{\mathbf{p}_G} \frac{\rho(\mathbf{q}_i, t)}{\gamma(\mathbf{q}_i, t)} \cdot d\vec{\mathbf{q}}_i \tag{4.26}$$

Rewriting ρ and $d\vec{\mathbf{q}}_i$ as in Eqs. (3.76) *and* (3.77) *and substituting in Eq.* (4.26) *we get*

$$\boldsymbol{\Upsilon}(\mathbf{q}_i) = \int\limits_{0}^{\infty} \frac{|\rho| \dfrac{\nabla\phi}{|\nabla\phi|}}{\gamma} \cdot |\dot{\mathbf{q}}_i| \frac{\nabla\phi}{|\nabla\phi|} dt \tag{4.27}$$

$$= \int\limits_{0}^{\infty} \frac{|\rho|\,|\dot{\mathbf{q}}_i|}{\gamma} dt \tag{4.28}$$

Notice that the substitution in Eq. (4.26) *eliminates t.*

Global optimality of the SBCAM can be ensured by choosing a trajectory $\mathbf{q}_i$ that minimizes the functional Eq. (4.28). In MBCAN, ρ was constant along a trajectory $\mathbf{q}_i$ (Prop. 3.9). Thus choosing a starting orientation with highest ρ resulted in global minimization of the functional. However, optimization of the functional in Eq. (4.28) is an advanced multi dimensional variable calculus problem.

The SBCAM updates the HPF at each time instant after locally updating the SNR-map. It was shown in Eq. (3.127), that the solution of Eq. (4.2) at a time instant results in a HPF which increases the local component of the trajectory in a local region with high SNR. Therefore, when the local SNR-map is updated, the SBCAM results in the increasing the amount of time the agent spends in a high SNR region.

4.2 SBCAM: Complexity

The complexity of MBCAN was discussed in **??**. It can be seen that the PDE setup of the SBCAM given in Eq. (4.2) actually requires solving the MBCAN problem in Eq. (3.15) at each step. Thus the computation complexity is considerably increased. More specifically the computational complexity of different algorithms used to solve the PDE in Eq. (4.2) is given in table table 4.1. It has to be noted that the storage complexity has not increased in the SBCAM trajectory generation.

HPFs based planners are known to be non-committal planners. That is, a local change in environment does not require the computation of the complete plan. Rather, the plan needs to be updated locally only. This follows from the fact that the Green's

Algorithm	Type	Time	Storage
Inversion	Direct	$\mathcal{O}\left(n^3 \cdot k\right)$	$\mathcal{O}\left(n^2\right)$
LU Decomposition	Direct	$\mathcal{O}\left(n^3 \cdot k\right)$	$\mathcal{O}\left(n^2\right)$
Jacobi	Iterative	$\mathcal{O}\left(n^2 \cdot k\right)$	$\mathcal{O}\left(n\right)$
Gauss-Seidel (GS)	Iterative	$\mathcal{O}\left(n^2 \cdot k\right)$	$\mathcal{O}\left(n\right)$
Conjugate Gradient (CG)	Iterative	$\mathcal{O}\left(n^{\frac{3}{2}} \cdot k\right)$	$\mathcal{O}\left(n\right)$
Successive Over-Relaxation (SOR)	Iterative	$\mathcal{O}\left(n^{\frac{3}{2}} \cdot k\right)$	$\mathcal{O}\left(n\right)$
Fast Fourier Transform (FFT)	Direct	$\mathcal{O}\left(n \log n \cdot k\right)$	$\mathcal{O}\left(n\right)$
Multigrid	Iterative	$\mathcal{O}\left(n \cdot k\right)$	$\mathcal{O}\left(n\right)$
Parallel Jacobi	Iterative	$\mathcal{O}\left(\frac{n^2}{p} \cdot k\right)$	$\mathcal{O}\left(n\right)$
Parallel RB GS	Iterative	$\mathcal{O}\left(\frac{n^2}{p} \cdot k\right)$	$\mathcal{O}\left(n\right)$
Parallel RB SOR	Iterative	$\mathcal{O}\left(\frac{n\sqrt{n}}{p} \cdot k\right)$	$\mathcal{O}\left(n\right)$

p = # of processors, k = # of steps

Table 4.1: Time and memory complexity of different algorithms [1], [2] for solving the PDE given in Eq. (4.2)

function for a HPF is an exponential function [16]. Thus, the effect of any local change is the environment decays as away from the position where the change happened. Exploiting the non-committal nature of the HPF leads to considerable reduction in computation time as the number of unknowns is reduced dramatically.

4.3 Investigating the Effects of Different Prediction Regions on SBCAM

The area of the predicted region holds a lot of significance in obtaining a communication-aware route to the goal. Increasing the area of prediction will lead to an increase in the computational complexity as the prediction will have to be carried out over larger set of spatial position. Also based on the received signal characteristics, the prediction quality could severely degrade in regions further away from the agent as the RSS tends to decorrelate with increasing distance. Ideally, if the SNR of the complete region can be predicted accurately, then the best trajectory to the goal can be computed. However, predicting the SNR for a complete region requires high computational complexity. Another important point to note is that for a highly volatile region with changing geometry like emergency scenarios, predicting regions far away from the agent may be useless as the spatial-map (and consequently the SNR map) in far away regions might change when the agent reaches those regions.

Fig. 4.4 shows a complex environment with a single Base-Station (BS). Let an agent be navigating in the environment of Fig. 4.4. Assume that the agent does not know the complete SNR-map of the environment. Furthermore, assume that the

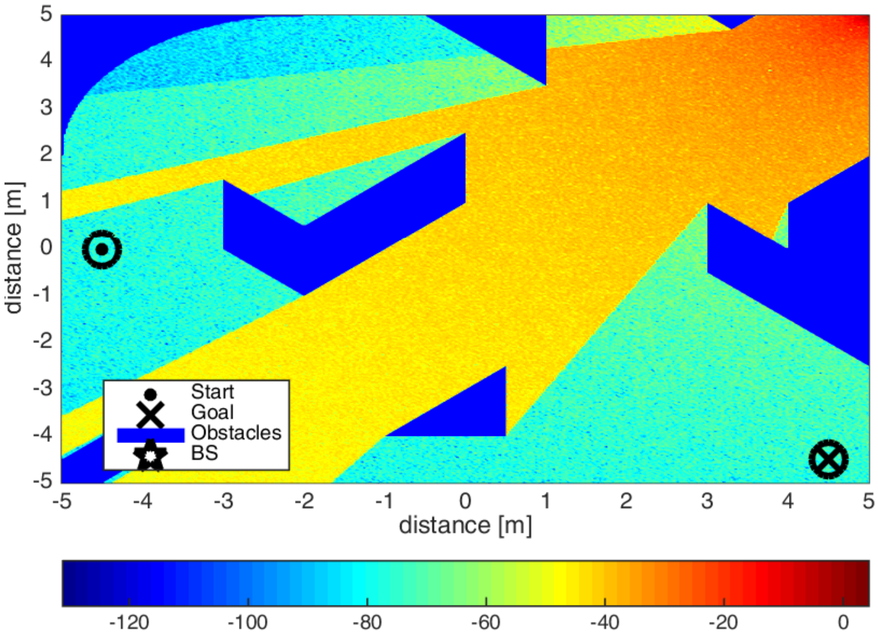

Figure 4.4: A complex environment with convex and non-convex obstacles

agent can perfectly predict the SNR within a circular region around itself as shown in Fig. 4.5 (unknown SNR shown in yellow color). The agent navigates towards its goal position and after each step along its trajectory to goal, it is able to perfectly update its SNR knowledge within a circular region. Based on the updated SNR-map, it computes its next step using the HPF obtained as a solution to eq. 3.15.

Fig. 4.6 shows the Cumulative Distribution Function (CDF)s of the instantaneous SNR of 4000 trajectories with random starting and goal positions for an agent moving in the environment shown in Fig. 4.4. The trajectories were computed for the fully known SNR-map case using MBCAN (Communication-Aware Trajectory (CAT)s) along with the completely unknown SNR-map case (Communication-Blind Trajectory (CBT)s). Further trajectories were computed using the above mentioned scenario where the agent is able to perfectly predict SNR in a circular region around itself. Trajectories were computed for four scenarios where the agent predicted SNR in circular

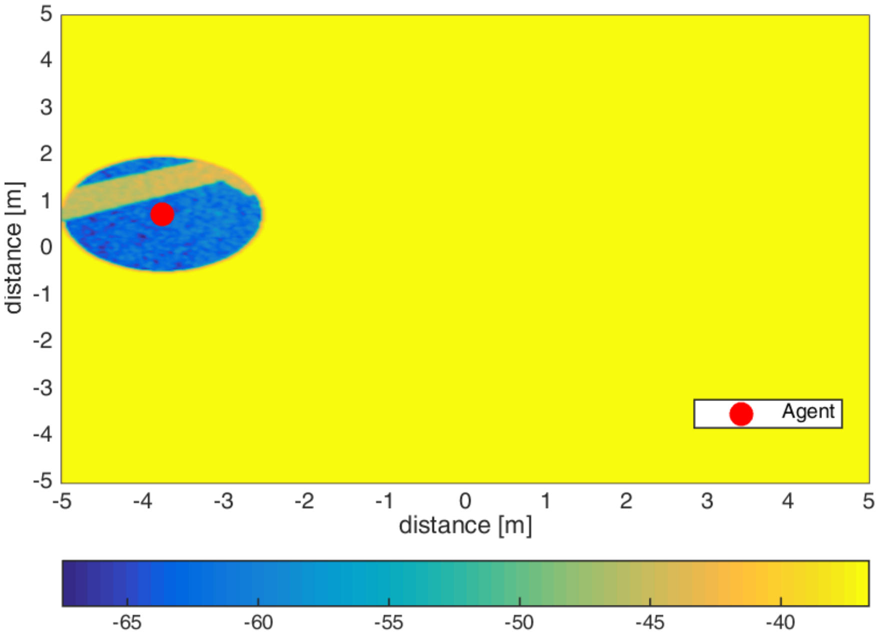

Figure 4.5: Perfect circular update around an agent.

regions having area 1%, 5%, 10% and 20% of the total environment area respectively. The CDFs of the instantaneous SNR along the trajectories were plotted as shown in Fig. 4.6 for the fully known SNR, SNR-blind and perfect updates within 1%, 5%, 10% and 20% circular region around the agent. It can be seen that with increasing area of the perfectly predicted SNR region, their CDF start to converge to the CAT CDF. Interestingly, the CDF of trajectories, which perfectly update SNR knowledge in a circular region with 10% area of the total environment area, nearly converges to the CAT CDF. The 20% region update nearly matches the fully known case CDF. Thus complete SNR-map knowledge is not needed to get near optimal performance. Even the 5% region update is further from the CBT CDF and closer to the CAT CDF. Therefore, these simulations results indicate that algorithms that only update SNR knowledge in a limited area around the agent can lead to trajectories that have SNR characteristics close to the CATs.

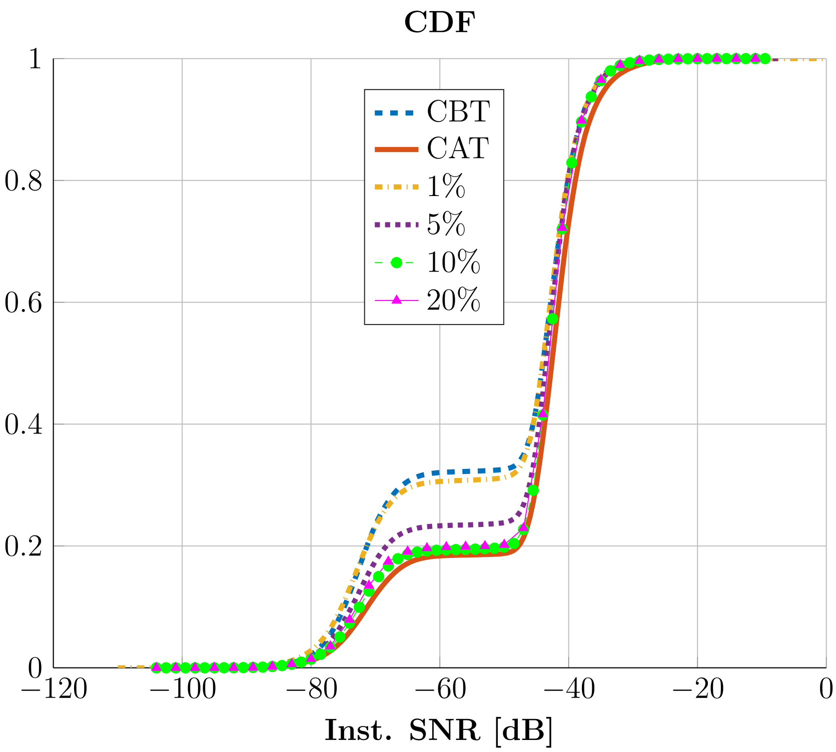

Figure 4.6: CDF of instantaneous SNR along trajectories with different random starting and goal positions for Fig. 4.4

Fig. 4.7 shows the CDF for different environments. The first row shows an environment with no obstacles and consequently, the RSS is not blocked in any region in the environment. Since the difference between the performance will be negligible, we can see that the CDFs of the CBT and all the algorithms are nearly the same.

The second row of Fig. 4.7 shows a scenario with a single obstacle blocking the RSS. The CDF plot in the second column compares the instantaneous SNR along the CAT, CBT and SBCAM trajectories with different circular update region within which the agent can update the SNR-map perfectly. It can be seen that the SBCAM with an SNR update region of around 5% around the agent can give a much better performance than the CBT. Moreover, it is closer to the CDF of the CAT which perfectly knows the complete SNR-map. Increasing the circular region area to 20%

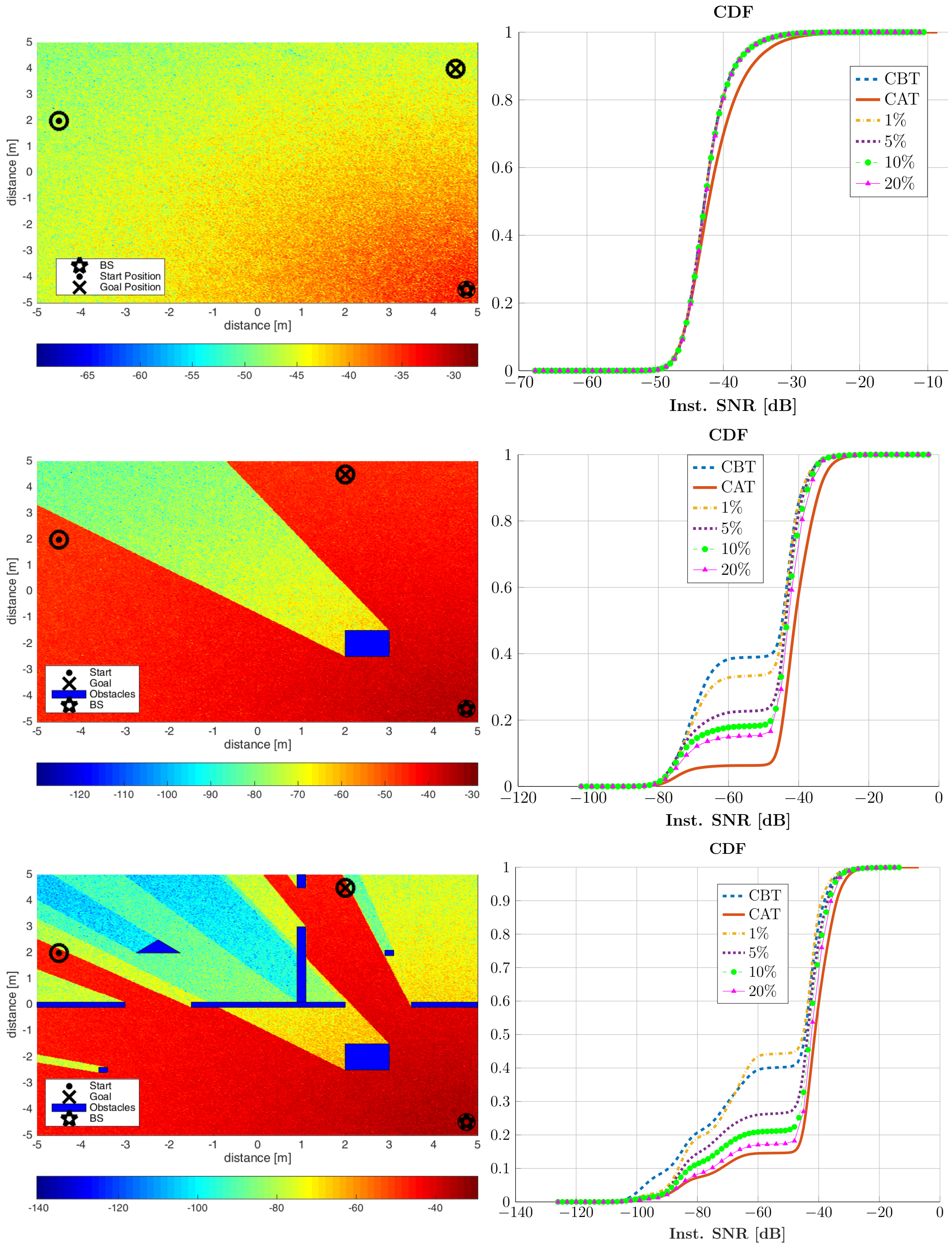

Figure 4.7: Performance of SBCAM with perfect SNR update in circular regions of different sizes

of the complete region leads to the CDF being much closer to the instantaneous SNR CDF of the CAT.

Making a general conclusion on the performance of the SBCAM as compared to the CAT is challenging as it is highly dependent on the environment (obstacles and geometry). However, if we look at environments similar to the one in the third row of Fig. 4.7 which has many obstacles of different geometries blocking the RSS then SBCAM with even a small update region gives performances very near to the CAT. The 20% update region SBCAM instantaneous SNR CDF is nearly the same as the CAT CDF for the environment in the third row of Fig. 4.7. This can also be verified for the environment in Fig. 4.4 and the CDFs of different SBCAM update in Fig. 4.6. However, in the environment of the second row in Fig. 4.7 with only a single obstacle blocking the RSS, it can be seen that 20% update region SBCAM is not as close to the CAT CDF as for the environment with more obstacles.

SBCAM with Partial SNR-Map Knowledge

In the previous section we assumed that the agent started with zero SNR knowledge and could perfectly update the SNR-map in a circular region around its position. In this section, we look at the scenario where the agent has partial information about the SNR-map initially. The agent is then able to perfectly predict the SNR in local circular area as it starts moving and sensing the RSS. Fig. 4.8 shows two scenarios where an agent is traversing in the environment shown in the third of Fig. 4.7. The agent has knowledge of the base station position and partial knowledge of the HO-map. the agent is able to construct an initial estimate of the SNR-map based on

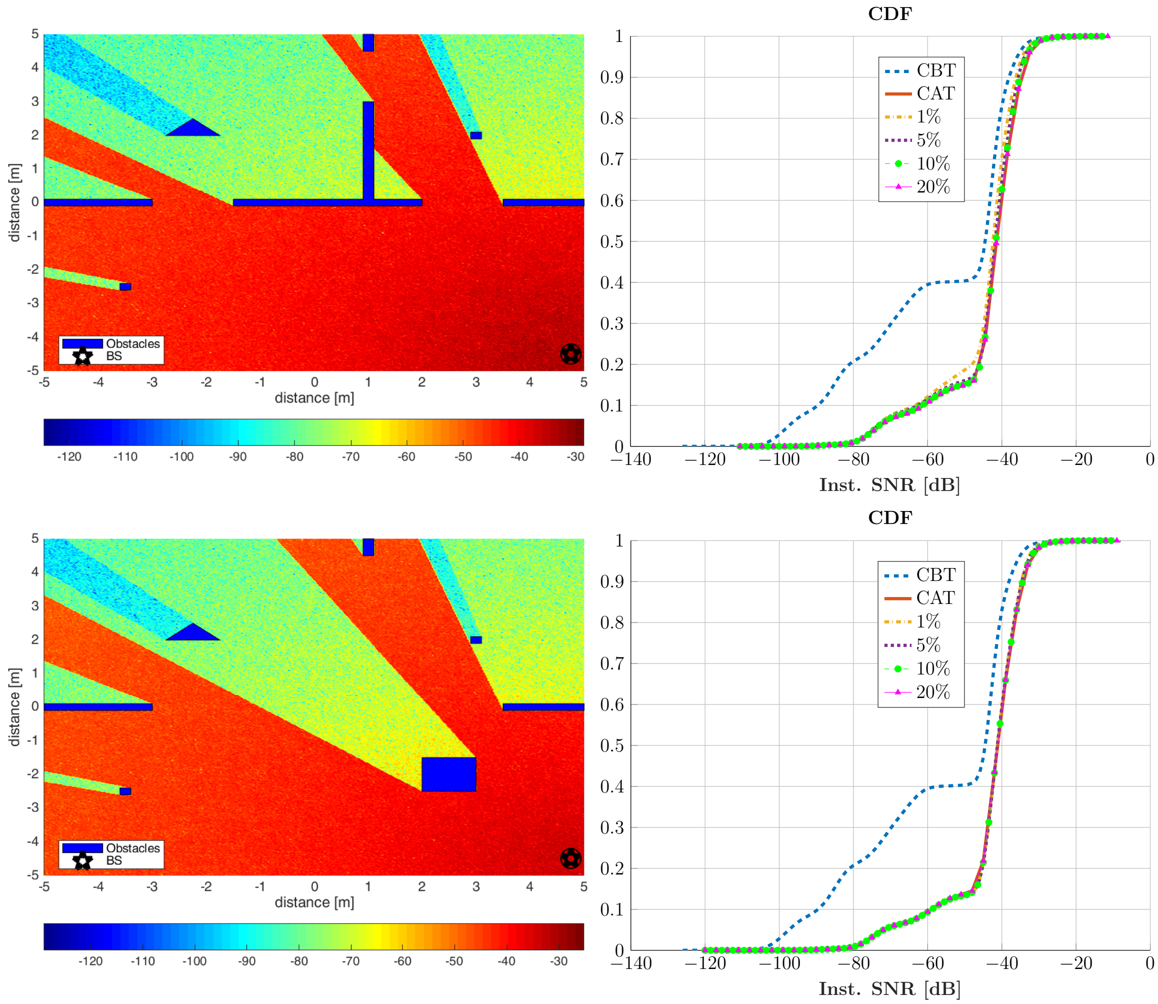

Figure 4.8: Performance of SBCAM with partial environment information and perfect SNR update.

this info. As the agent starts moving, it can perfectly predict the SNR-map using the sensed RSS. Each row in Fig. 4.8 shows the initial HO-map and reconstructed SNR-map at the agent. It can be seen in the CDF plot in the second column that for different prediction region areas the agent almost always matches the performance of the MBCAN.

4.4 Conclusions

In this chapter, we developed a HPF-based sensor-based communication-aware planner. Conditions for convergence of the SBCAM trajectory were presented. The functional that can be used to obtain the trajectory that globally optimizes the SBCAM was obtained. Simulation results were presented for the case where the agent starts with zero SNR knowledge at the beginning for different environments. Simulation results were also obtained for the case where the agent had partial initial information of the HO-maps and an estimate of the SNR-map based on the HO and base station location knowledge. Results showed that the SBCAM performance converged to the MBCAN with only local SNR updates. With partial initial information, the simulation results showed that the SBCAM was approximately the same as the MBCAN with only local updates.

CHAPTER 5

SINGLE SAMPLE GREEDY (SSG) RECONSTRUCTION

"The best preparation for tomorrow is doing your best today."

— H. Jackson Brown, Jr.

Single Sample Greedy (SSG) generates trajectory using greedy updates (agent always wants to remain in high Signal to Noise Ratio (SNR) region). It penalizes Dead Communication Zones (DCZ) highly; therefore, the agent only enters the DCZ if there is no path to goal available outside of the DCZ. In this algorithm, the planner obtains a prediction update of the SNR-map based only on the SNR measured at the current location and the location at the previous step. The planner keeps a log of the measured SNR at each position it has visited in the past up to and including its current position. Based on the slope between the current measured SNR and the SNR at the previous step, it then predicts SNR in a region in the current direction of motion. The planner then solves Eq. (4.2) to obtain the updated Harmonic Potential Field (HPF) and consequently the next step in the agent's trajectory towards the goal.

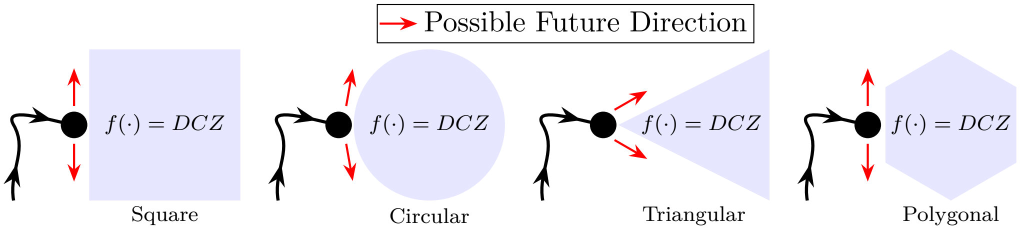

Figure 5.1: Potential trajectory if updated region is a DCZ

5.1 Update Region Geometry

The planner has no information regarding the SNR in the environment when it begins motion. Initially, it measures the SNR at its starting position and assumes that the complete SNR-map to have the same SNR, γ_S. Then it obtains its next position using eq. 3.20 based on the HPF obtained using eq. 3.15. Then it moves further by updating the SNR in a region, $\mathcal{U}$, in front of it in the current direction of motion. The update is computed in the current direction of motion of the agent since the Received Signal Strength (RSS) measurement is done by the agent as it moves. Hence, the new measurement will only be available at the current position. Thus, the validity of the prediction in other directions would be less likely.

Fig. 5.1 shows different update region with simple geometry. The SNR is updated in a triangular region in front of the agent. By controlling the width of the triangular region, any of the other update geometries can be approximated. The geometric shape of the predicted region has a strong affect on the properties of the trajectory the agent takes to the goal. If the geometry of the prediction update has long edges perpendicular the direction of motion, it could lead to the agent's trajectory having very sharp turns as shown in Fig. 5.1. Other arbitrary geometries could be used for the update region as well. However, computational cost and complexity should be

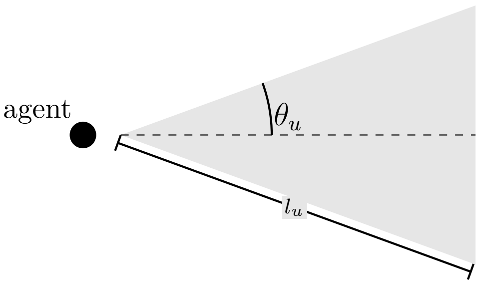

Figure 5.2: Describing a triangular update region

considered while considering any geometry.

In this algorithm, the planner aims to avoid DCZs. The SNR update algorithm updates the SNR-map so as to avoid the DCZ. It achieves this by comparing the measured SNR with ϵ_D. Where, ϵ_D is the threshold below which wireless data transmission is lost (Def. 3.3). If the measured SNR is below ϵ_D then the agent updates the region in front of it as a DCZ. Thus the recomputed gradient at that position forces motion away from that updated region. The algorithm only updates the region if it encounters a DCZ, i.e., the SNR goes below ϵ_D.

The triangular update region as shown in **??** is chosen as the update region geometry. Since a triangular region with a vertex in front of the agent will allow the agent to generate trajectory without sharp turns away from the predicted region in case the predicted region is a DCZ. The triangular region configuration with a vertex in front of the agent can be defined by (Fig. 5.2)

1. The angle associated with the vertex θ_u
2. The depth l_u (or height) of the triangular region.

The triangular region acts as the agent's 'SNR field of view' with θ_u and l_u acting as the view angle and depth respectively. θ_u and l_u together define the performance of the algorithm, i.e., avoiding DCZ. A large θ_u could lead to the agent taking sharp turns to avoid DCZs. A large l_u on the other hand could lead to the divergence of the motion of the agent and will be discussed later on in detail (section 5.5).

Assuming that the algorithm predicts a DCZ in the update region. Then the view angle control how deep an agent can go in to a DCZ before escaping the DCZ. This is illustrated in Fig. 5.3 and 5.4. Fig. 5.3 shows the path an agent takes as it reaches the edge of a DCZ. As the sequence of figures show, the agent predicts a DCZ in its triangular update region and therefore the Sensor-Based Communication-Aware Navigation (SBCAM) forces motion along the boundary of the updated region.The agent then traverses the boundary of the updated region which is inclined at θ_u from the axis along the previous direction of the agent's motion (Fig. 5.2). When the agent has traversed the computed step shown in red in Fig. 5.3 and it still senses a DCZ, it again updates the triangular region in front of it as a DCZ and takes the next step along the boundary of the updated region. This continues until the agent exits the DCZ.

Fig. 5.3 shows the behavior of an agent using triangular updates with $\theta_u = 25°$ based on SNR measurement at current and previous positions. Fig. 5.4 shows the same scenario as in Fig. 5.3 but uses $\theta_u = 60°$. The edge length l_u of the update region is the same for both the scenarios. It can be seen in the second scenario that for a greater θ_u, the agent is able to exit the DCZ much earlier than the case where $\theta_u = 25°$. It can also be noted that for $\theta_u = 25°$, the agent goes more deeper in to the DCZ before exiting and therefore spends more time in the DCZ as compared to the case where $\theta_u = 60°$.

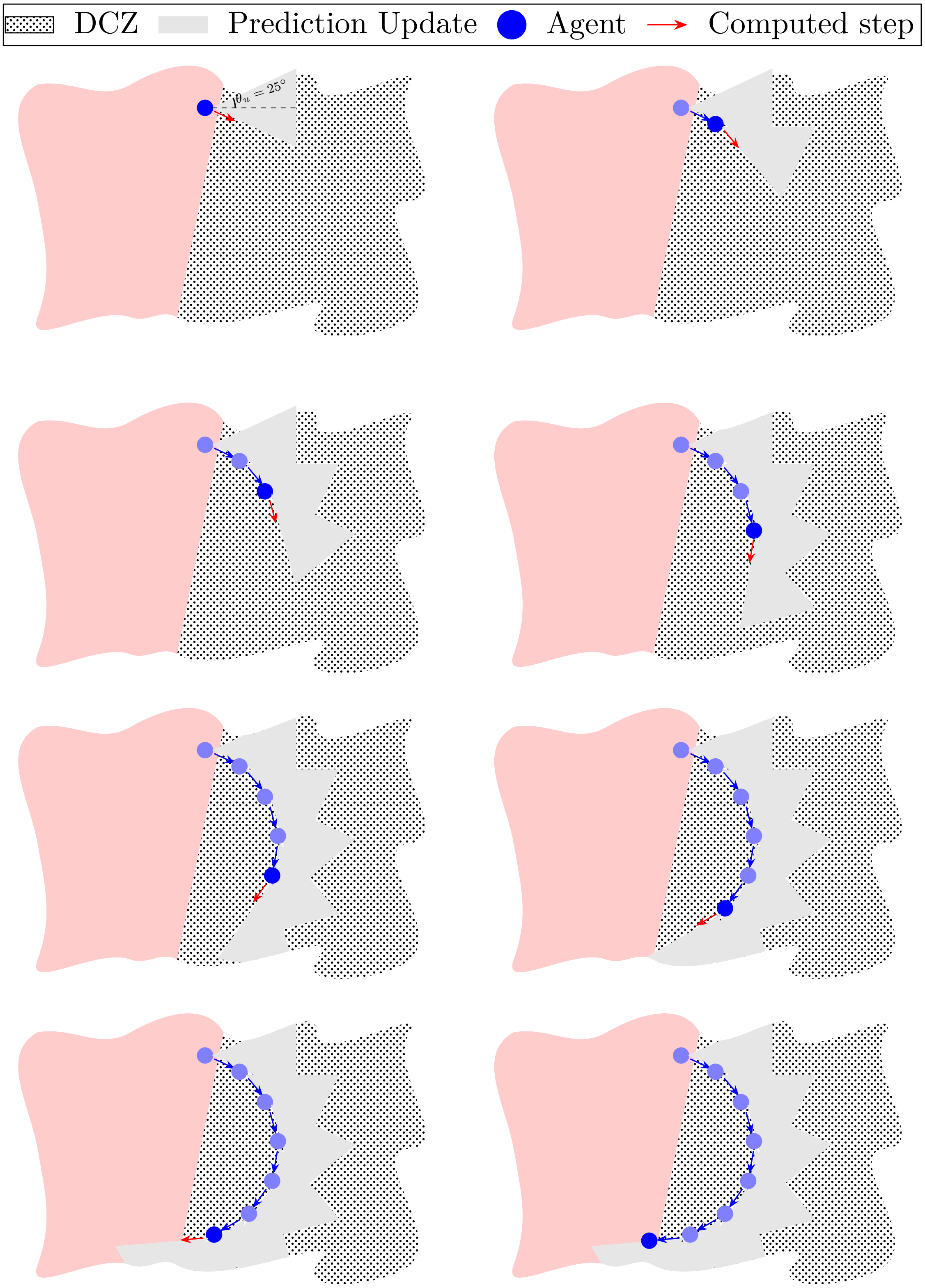

Figure 5.3: Agent avoiding DCZ for triangular region update with $\theta_u = 25^\circ$, $l_u = 2cm$

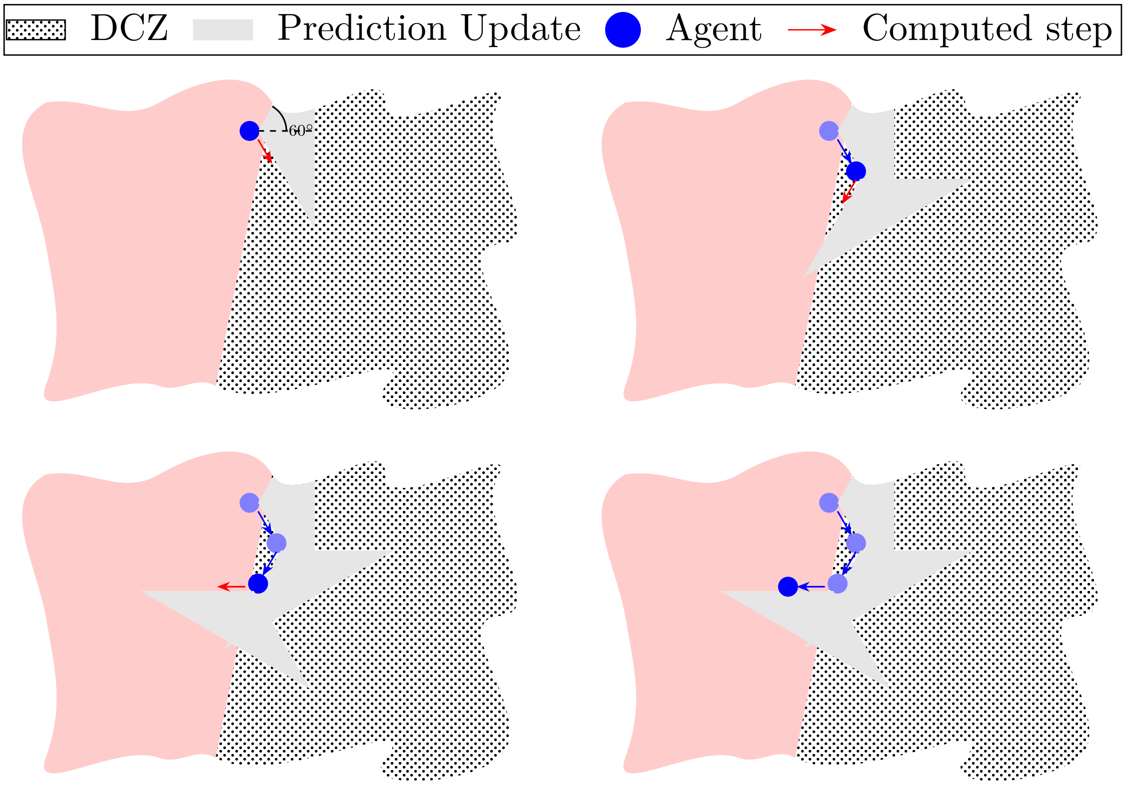

Figure 5.4: Agent avoiding DCZ for triangular region update with $\theta_u = 60°$, $l_u = 2cm$

The optimum value of θ_u is dependent on the environment. If the environment has many DCZs, then a larger value of θ_u is required. While, an environment with few DCZ would require a smaller value of θ_u. However, care has to be taken while choosing values of θ_u and l_u, as based on the number and geometry of DCZ regions, they could lead to over- or under-estimation of the DCZ. As seen in Fig. 5.4, the agent overestimates the DCZ in the last step. It updates a big region outside of the DCZ as a DCZ. Overestimation due to choosing large θ_u and l_u could also lead to the agent choosing a longer path to goal as shown in Fig. 5.5. Alternatively, underestimating the DCZ using a narrow prediction region (small θ_u) could lead to the agent entering and remaining in a DCZ. As shown in Fig. 5.6, the narrow update region results in the agent entering the DCZ and unable to exit it while moving towards the goal position.

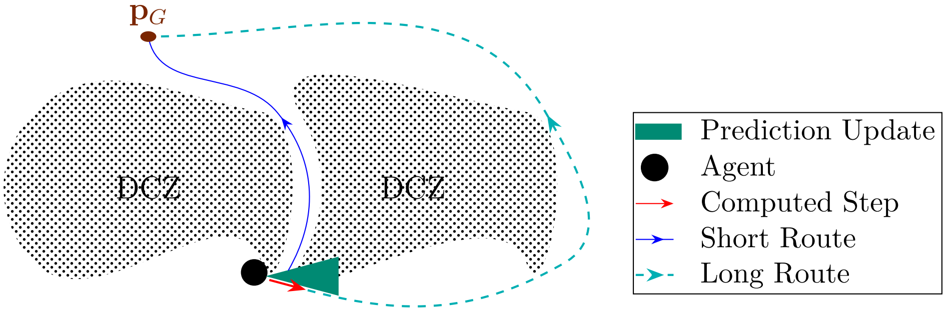

Figure 5.5: Overestimation of DCZ leading the agent to miss shorter route to goal

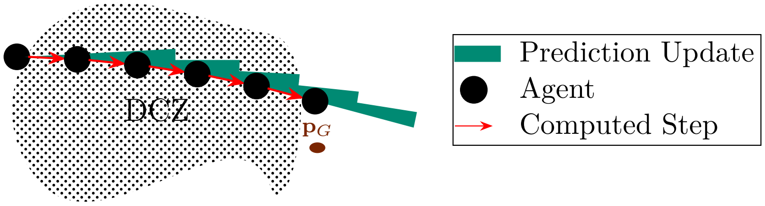

Figure 5.6: Underestimation of DCZ leads to the agent to cross the DCZ until it reaches its end.

Although the agent correctly predicts the DCZ in its updates throughout the DCZ, however, the small area of the update region leads to agent entering the DCZ and unable to exit it.

5.2 Update Function

In the previous section, we discussed the spatial properties of the SSG update and how it affects the agent's trajectory locally (Fig. 5.3 and Fig. 5.4) and globally (Fig. 5.5 and Fig. 5.6). These scenarios were discussed for the case where the spatial region was updated to be a DCZ. In this section, we discuss how the SSG algorithm predicts the SNR in the update region.

It should be noted that Small-Scale Fading (SSF) is ignored when predicting the SNR in the update region. The agent initializes its SNR field with a constant arbitrary value, γ_S greater than the DCZ threhsold ϵ_D. The SSG algorithm predicts the SNR in the update region using the current SNR measurement, $\gamma(t)$ and compares it with the DCZ threshold. If the current measurement is below the DCZ threshold, it updates the prediction region using the directional derivative [83] of the measured SNR.

$$\nabla_{\dot{\mathbf{p}}}\widehat{\gamma}(\mathbf{p}(t)) = \nabla\widehat{\gamma}(\mathbf{p}(t)) \cdot \frac{\dot{\mathbf{p}}(t)}{\left|\dot{\mathbf{p}(t)}\right|} \tag{5.1}$$

Where $\nabla_{\dot{\mathbf{p}}}\widehat{\gamma}(\mathbf{p}(t))$ is the directional derivative of $\widehat{\gamma}$ in the current direction of motion of the agent. The update function is then given as follows.

$$f(\mathbf{p}) = \gamma_S + d(\mathbf{p})\nabla_{\dot{\mathbf{p}}}\widehat{\gamma}(\mathbf{p}(t)),\ \forall \mathbf{p} \in \mathcal{U} \tag{5.2}$$

where $d(\mathbf{p})$ is given by

$$d(\mathbf{p}) = \frac{\dot{\mathbf{p}}(t)}{\|\dot{\mathbf{p}}(t)\|} \cdot (\mathbf{p} - \mathbf{p}(t)),\ \forall \mathbf{p} \in \mathcal{U} \tag{5.3}$$

Where $d(\mathbf{p})$ gives the perpendicular distance between the positions $\mathbf{p}$ in the update region from the axis normal to the current direction of motion of the agent from $\mathbf{p}(t-1)$ to $\mathbf{p}(t)$. Eq. 5.3 is a dot product of the unit vector in the current direction of the agent's motion, $\frac{\dot{\mathbf{p}}(t)}{\|\dot{\mathbf{p}}(t)\|}$ and the vector from $\mathbf{p}(t)$ to the point $\mathbf{p} \in \mathcal{U}$ in the update region. This dot product gives the component of the vector $\mathbf{p} - \mathbf{p}(t)$ along the current direction of the agent's motion, which in fact is the perpendicular distance of the point

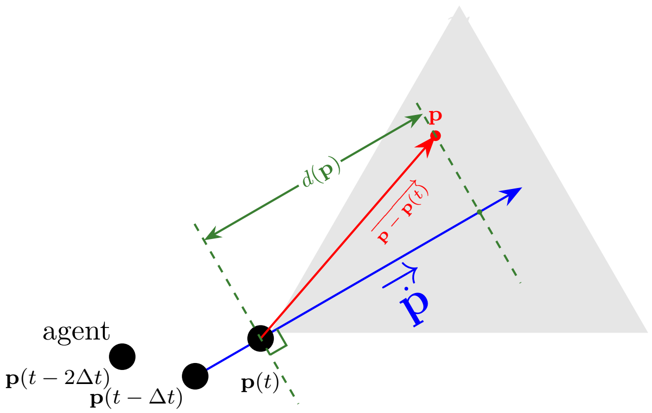

Figure 5.7: Perpendicular distance of a point to the axis normal to the agent's current direction of motion

$\mathbf{p}$ from the axis normal to the agent's current direction of motion. Fig. 5.8 shows an updated region based on eq. 5.3. It can be seen that the region has subregions in the form of bands of same SNR parallel to the axis normal to the current motion of the agent. This results in the complete update region having the same spatial gradient of the SNR at each position. This provides the basis for pushing the motion away from this region as shown in proposition 5.1. The SNR in each band is the same and is decreasing linearly (in dB) away from the agent. Also the width of the update region increases away from the agent. This acts as a 'repulsion' region to push motion as far as possible. A narrow update will only slightly change the direction of the motion of the agent and thus the agent might remain inside the DCZ as shown in Fig. 5.6.

It can be noted that the factor $d(\mathbf{p})$ in the update equation can also be taken as the more simple euclidean distance as shown in Fig. 5.9

$$d(\mathbf{p}) = \|\mathbf{p} - \mathbf{p}(t)\|_2 \tag{5.4}$$

Fig. 5.10 shows the updated region using eq. 5.4. As compared to the update in

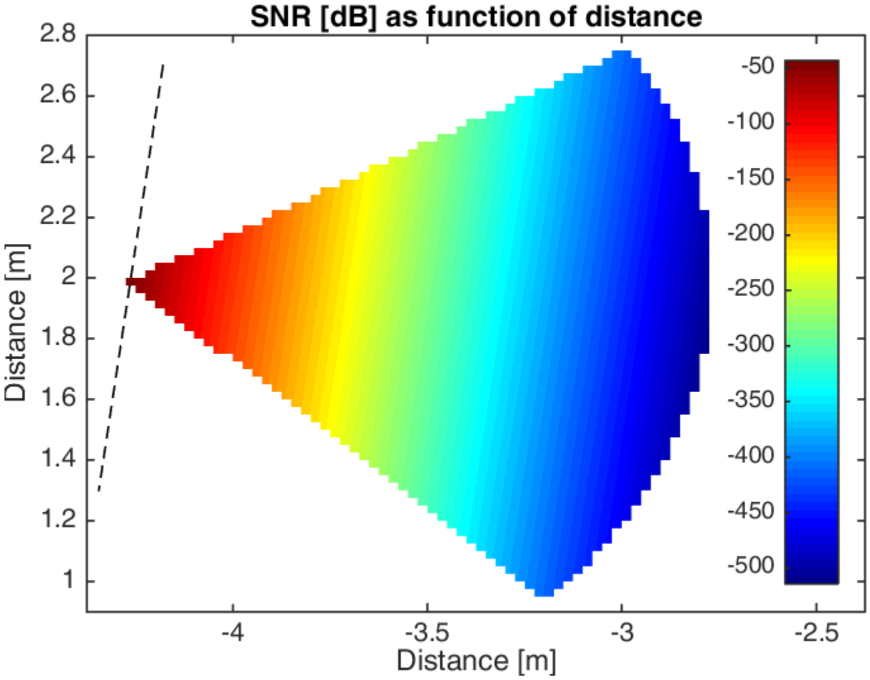

Figure 5.8: DCZ update using eq. 5.3

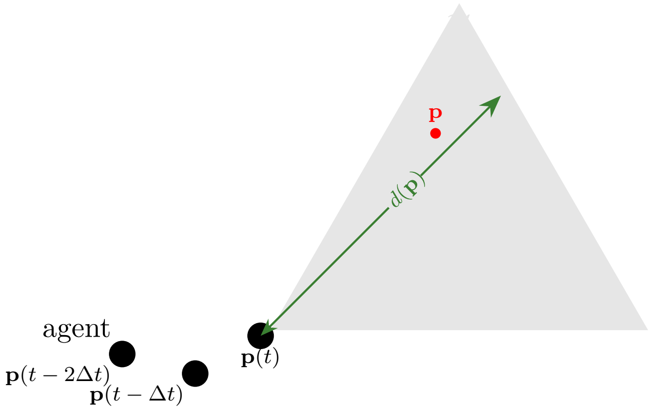

Figure 5.9: Euclidean distance of a point in the update region from $\mathbf{p}(t-1)$

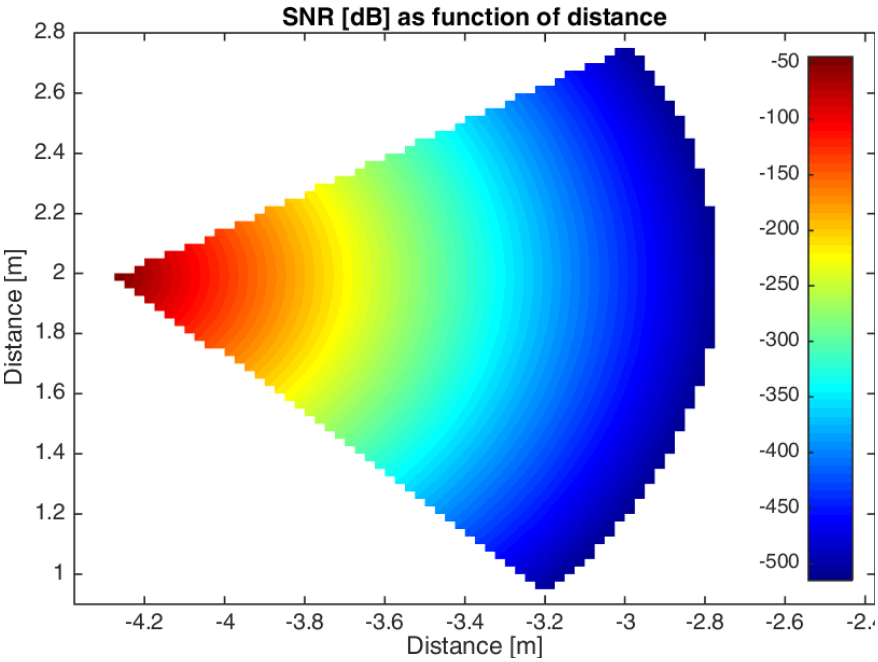

Figure 5.10: DCZ update using eq. 5.4

Fig. 5.8, it can be seen that the update regions consists of annular bands with the same SNR. The SNR is decreasing radially away from the agent's current position. The trajectory taken by an agent when the DCZ is updated using Eq. (5.3) differs from the trajectory obtained due to DCZ update using Eq. (5.4). Fig. 5.11 shows the trajectory taken by an agent in the two different DCZ region updates. It can be seen that the component along the initial direction of the agent's motion goes to zero when the DCZ is updated using Eq. (5.3) as shown in Fig. 5.11a. The agent eventually starts moving normal to its initial direction of motion. However, when the DCZ region update is based on Eq. (5.4) the agent can end up moving in a direction which has a component opposite to the agent's initial direction of motion as shown in Fig. 5.11b. This could lead to the agent moving away from the goal position resulting in the agent taking a longer trajectory to the goal. The trajectory bends when it enters from one band of SNR values to the next. This is a consequence of Eq. (3.127), where the

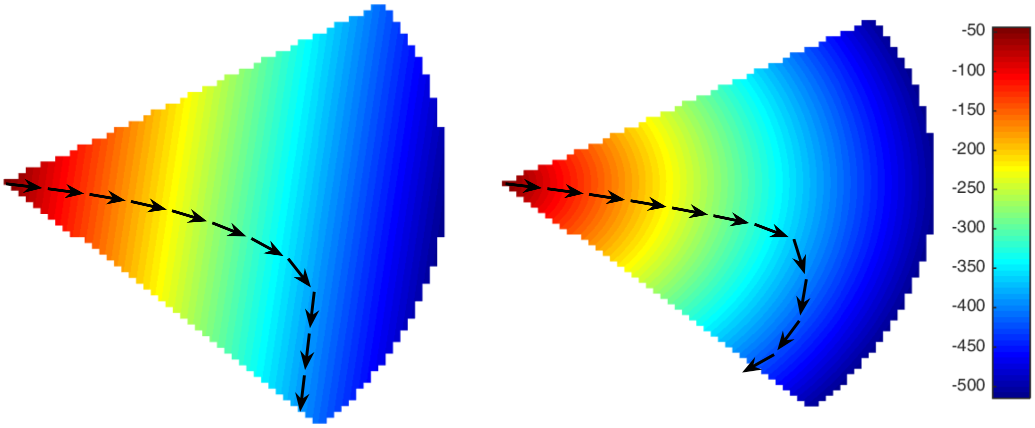

(a) Motion in DCZ update due to Eq. (5.3) **(b) Motion in DCZ update due to Eq. (5.4)**

Figure 5.11: Motion due to DCZ update using Eq. (5.3) and Eq. (5.4)

planner increases the component of the trajectory in bands with higher SNR. In this algorithm the DCZ update of Eq. (5.3) is used to avoid moving the agent away from the goal position and therefore, to avoid an increase in trajectory length. Finally, if the agent measures its current SNR to be greater than ϵ_D, then it updates the region with γ_S. The update function for SSG is, therefore, given by.

$$f(\mathbf{p}),\ \forall \mathbf{p} \in \mathcal{U} = \begin{cases} \gamma_S + d(\mathbf{p}) \cdot \delta_S, & \widehat{\gamma}(t) \leq \epsilon_D \\ \gamma_S, & \widehat{\gamma}(t) > \epsilon_D \end{cases} \tag{5.5}$$

5.3 Starting & Goal Position in DCZ

A special case of the SSG is when the agent starts in a DCZ, i.e., the starting position of the agent is in a DCZ, this would lead to the agent sensing a DCZ in any direction it measures the SNR. This could lead to the agent surrounding itself with detected

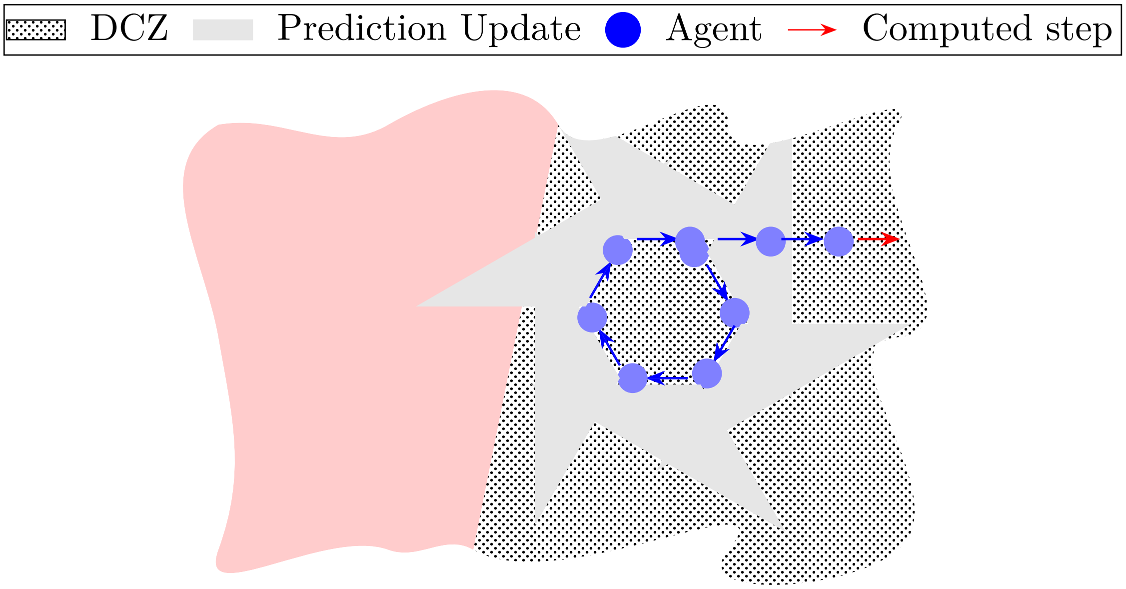

Figure 5.12: Starting position in a DCZ could lead to the agent updating region around it as DCZ

DCZs as shown in Fig. 5.12. This can be avoided by not applying the DCZ update when the agent senses a DCZ at its starting position. Thus, the agent would move without updating its SNR-map until it exits the DCZ. As soon as it exits the DCZ, it can start updating the SNR-map.

In the scenario where the start position is in a DCZ and the goal position is also in the same DCZ the agents starts moving with the DCZ updates off to avoid the situation in Fig. 5.12. This would lead to the agent reaching the goal position without exiting the DCZ. Since SSG initializes the SNR-map to the same initial value, therefore, the motion with the updates off will be governed by the normal HPF which generates trajectories that minimize motion energy.

The scenario of Fig. 5.12, where the agent trajectory might move in a loopy motion, violates the irrotational property of the HPF (i.e. $\nabla \times \nabla\phi \equiv 0$). However, the field using in Eq. (4.4) is dependent on a time-varying SNR-map and therefore, changing

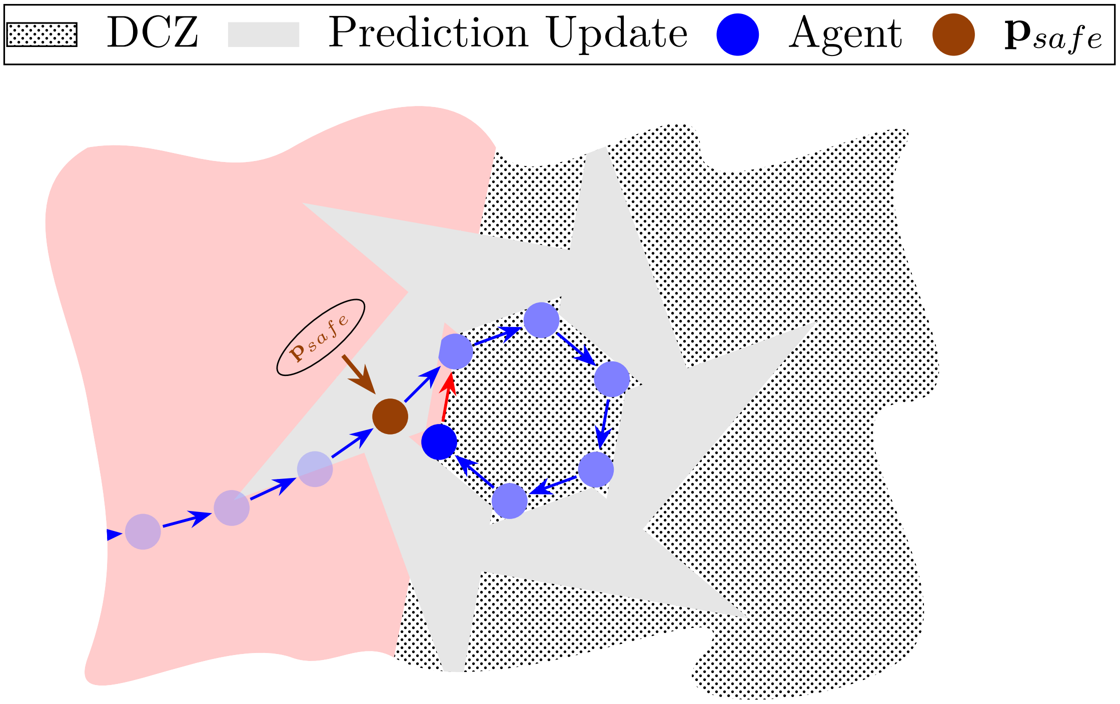

Figure 5.13: The last spatial point before an agent starts a DCZ update is saved as $\mathbf{p}_{safe}$

with time. Since time-varying fields are not conservative [95], therefore the irrotational property is also no more valid.

The scenario where an agent is encircled by DCZ updates as shown in Fig. 5.12 can also happen if the agent enters deep in to the DCZ and has a large view angle θ_u as shown in Fig. 5.12. This can be avoided by keeping memory of the agent's last spacial position, $\mathbf{p}_{safe}$ before it entered the DCZ as shown in Fig. 5.13. The agent never updates a region in the direction of $\mathbf{p}_{safe}$ as a DCZ. This allows the agent to always have a path away from the DCZ and stops the agent from being encircled by a DCZ. This is depicted in Fig. 5.14. Fig. 5.14 shows that as soon as the agent senses a DCZ, it starts the DCZ updates. However, with each DCZ update, it also updates a safety region of the same geometry but directed towards $\mathbf{p}_{safe}$. As agent progresses,

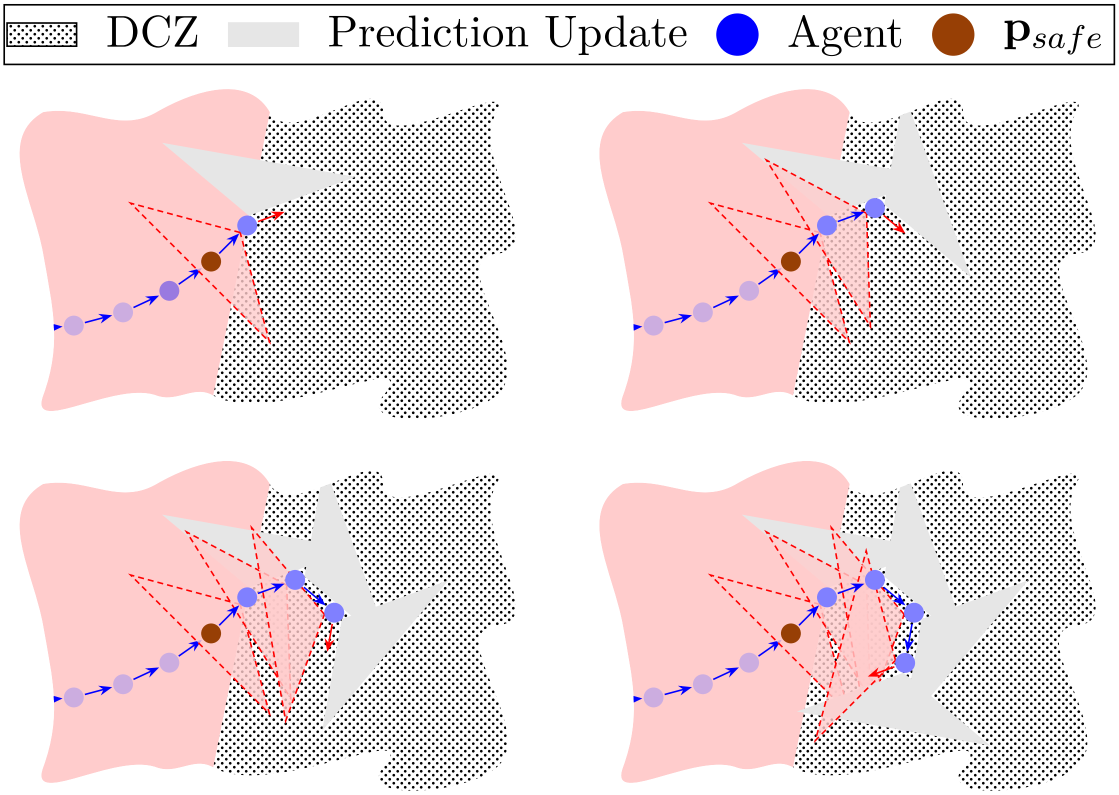

Figure 5.14: Safety region update with each DCZ update at each step.

it can be seen that the safety region updates form a region towards $\mathbf{p}_{safe}$ that is not a DCZ. This avoids the situation shown in Fig. 5.13 where the agent could surround it self with DCZ updates. However, if the goal position is in a DCZ and the starting position is in a different DCZ or not inside a DCZ, the agent cannot find a path to the goal outside of a DCZ. Consequently, the agent explores the complete boundary of the DCZ before entering it. When the agent is forced to enter the DCZ, it turns off the SNR-update. The motion in the DCZ is, therefore, governed by the HPF, with constant SNR (the SNR-map is initialized to a constant value). This results in a trajectory that minimizes motion energy.

5.4 Ocillatory Motion due to Safety Region Update

The greedy nature of the SSG could lead to situations where the agent could start oscillating between two regions. Since the next step in the trajectory is calculated by updating the HPF after each step, this could lead to the agent oscillating between two regions. This is depicted in the scenario shown in Fig. 5.15. It can be seen in Fig. 5.15a that when the agent moves away from the updated DCZ, the safe region towards $\mathbf{p}_{safe}$ makes a traversable path available through the updated DCZ. Thus in the next step, the agent moves towards this region to reach the goal faster. However, its DCZ update then blocks region again (Fig. 5.15b) which leads to the agent moving back towards the original direction. The safety region update in the next step (Fig. 5.15c) again provides a traversable region through the DCZ update. Thus, the agent will again move towards this traversable region in the next step (Fig. 5.15d). The agent could therefore potential keep moving back and forth due to a traversable region being available through a DCZ update due to the safety region update. This could lead to a zig-zag or oscillating motion.

Continuity of the Updated SNR-Map

It has to be noted that the DCZ update of Eq. (5.5) updates the region in the current direction of motion with SNR decreasing by the directional gradient Eq. (5.1) of $\widehat{\gamma}$. As a consequence, the updated SNR-map might have discontinuities at the boundary of the update region. Since, the solution to Eq. (4.2) exists only if γ is at least once differentiable (C^1). To ensure continuity at the boundary of the update region, the boundary of the udpate region is smoothed using a Gaussian kernel. The SSG

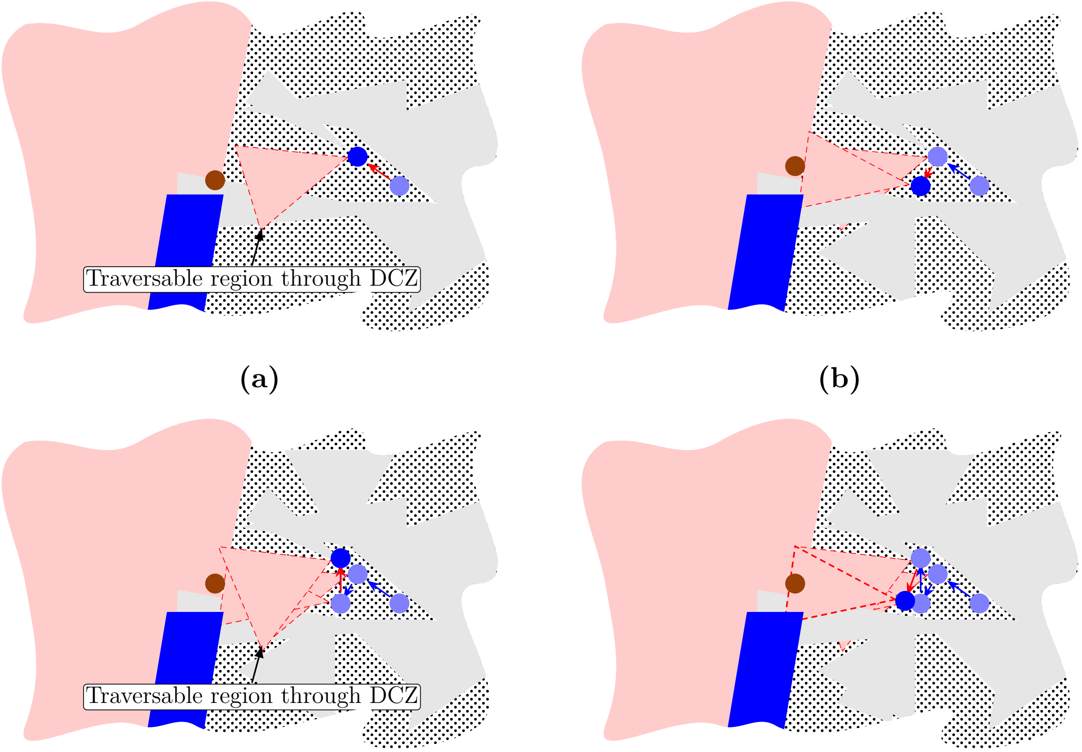

(a) **(b)**

(c) **(d)**

Figure 5.15: Possible oscillatory behavior due to the safe zone making a traversable path available through the updated DCZ

procedure is given in algorithm 3

Algorithm 3 SSG Procedure

```
Initialize SNR-map( $\gamma(\mathbf{p}) = \gamma_S, \forall \mathbf{p} \in \mathcal{W}$), $l_u$ and $\theta_u$.
if $\widehat{\gamma}(\mathbf{p}(t)) > \epsilon_D$ then
    $\mathbf{p}_{safe} = \widehat{\gamma}(\mathbf{p}(t))$.
else
    Update DCZ using Eq. (5.2).
    Update safe region.
end if
Go to operation 2
```

5.5 Analysis

The update function Eq. (5.2) produces an update with successive parallel bands of decreasing SNR perpendicular to the direction of the agent's motion as shown in Fig. 5.8. The SNR value in the bands decreases away from the agent in its direction of motion. The decrease in SNR is governed by the decrease in SNR between the current agent position (SNR in a DCZ) and it't SNR at its previous position (SNR outside of the DCZ). Therefore, at each point in the updated region, the SNR has a negative gradient in the current direction of the agent's motion. This leads us to the following proposition.

PROPOSITION 5.1 *The SNR update of Eq.* (5.2) *will always force the motion of the agent away from the updated DCZ region.*

Proof. Rewriting Eq. (3.24), we get

$$\nabla^2 \phi = -\frac{1}{\gamma}((-\nabla\gamma) \cdot (-\nabla\phi)) \tag{5.6}$$

Since, the current direction of the agent's motion $-\nabla\phi$ and the negative gradient of the SNR $-\nabla\gamma$ (direction of the greatest decrease in SNR) are aligned, this will result in a net negative factor on the right hand side. Thus, Eq. (5.6) will have a net negative divergence at the current position thus impeding motion in this direction.

On the other hand any other direction of motion which has a component antipodal or perpendicular to the direction of the highest decrease in SNR will lead to the a positive or zero net divergence respectively and motion will be encouraged in these directions. ▮

5.5.1 SSG and Convergence

As shown in section 5.1, the depth of the update region $\mathcal{U}$ is governed by the length l_u. The function in Eq. (5.2) used to update the region assigns a value decreasing by the rate of the directional derivative in Eq. (5.1). As l_u is increased, the update value would become smaller. This could lead to $\dfrac{\partial\gamma}{\partial t}$ having a large magnitude. This could result to the violation of the bound in Eq. (4.20). Therefore, a large value of l_u could lead to the divergence of the agent's trajectory.

5.6 Simulation Results

In this section, we show simulation results for the SSG SNR-map reconstruction. Fig. 5.16 shows the trajectory obtained for an environment with a single rectangular obstacle. The start and goal positions are at opposite positions outside the DCZ. It can be seen that the trajectory obtained using SSG initially follows the same trajectory

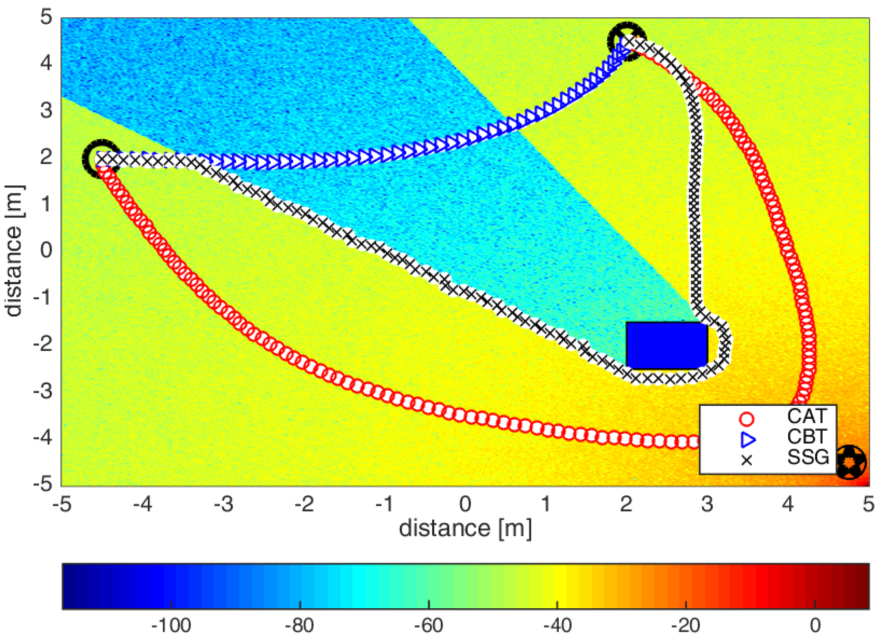

Figure 5.16: SBCAM trajectory obtained using the SSG algorithm compared with the Communication-Aware Trajectory (CAT) and CBT for an environment with a single obstacle

as the Communication-Blind Trajectory (CBT) as its motion is governed by a HPF. However, as soon as the agent senses the DCZ, it generates DCZ updates. These updates are used to generate a sequence of motion policies by solving Eq. (4.2) after each update. Motion is in turn generated using Eq. (4.4).The SBCAM-SSG trajectory thus avoids the possible DCZ before converging to the goal position.

Fig. 5.17 shows he SNR update map the agent uses to generate its trajectory. It can be seen that the agent does not need to update the complete region where the RSS is being blocked by the obstacle. The agent generates the trajectory in Fig. 5.16 using the DCZ updates shown in Fig. 5.17. It can be seen that the agent was able to avoid the DCZ without complete knowledge of the SNR-map of the environment. Fig. 5.18 shows the SNR profile along the trajectory of the agent to the goal given in Fig. 5.16. It can be seen that the SNR along the SSG based trajectory nearly matches

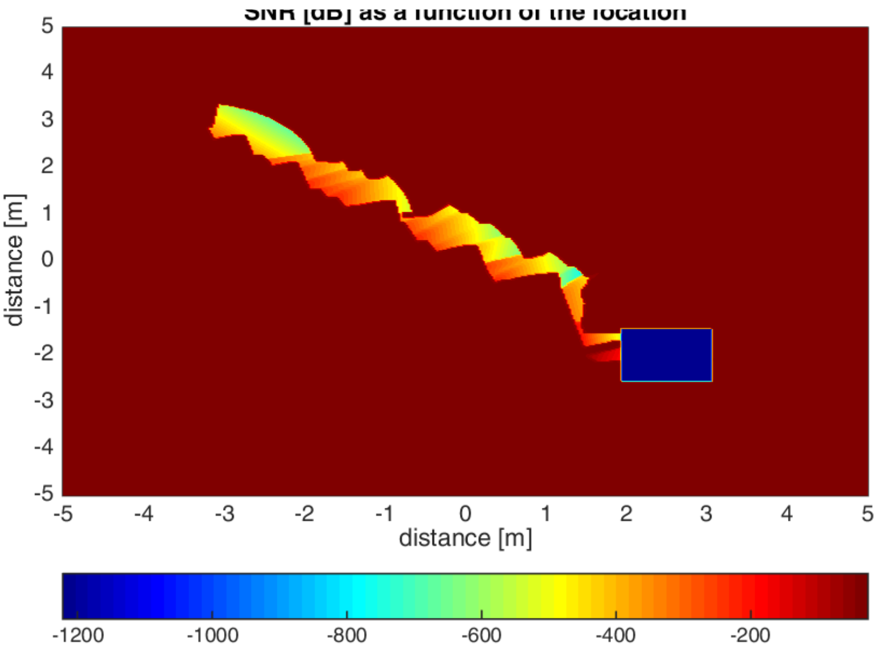

Figure 5.17: SNR-map with DCZ updates used by the agent to generate its path

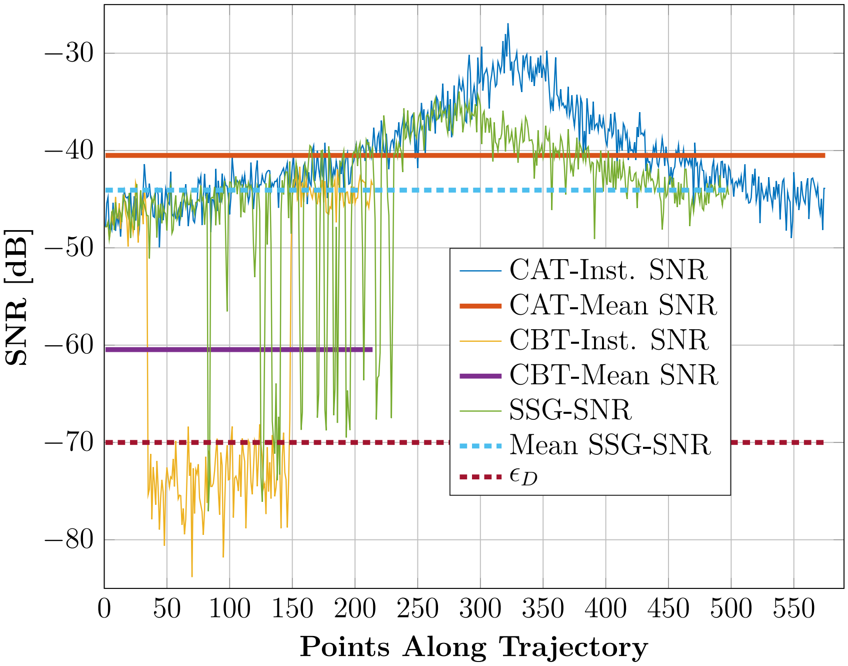

Figure 5.18: Comparison of SNR along the CAT, CBT and the SSG trajectory

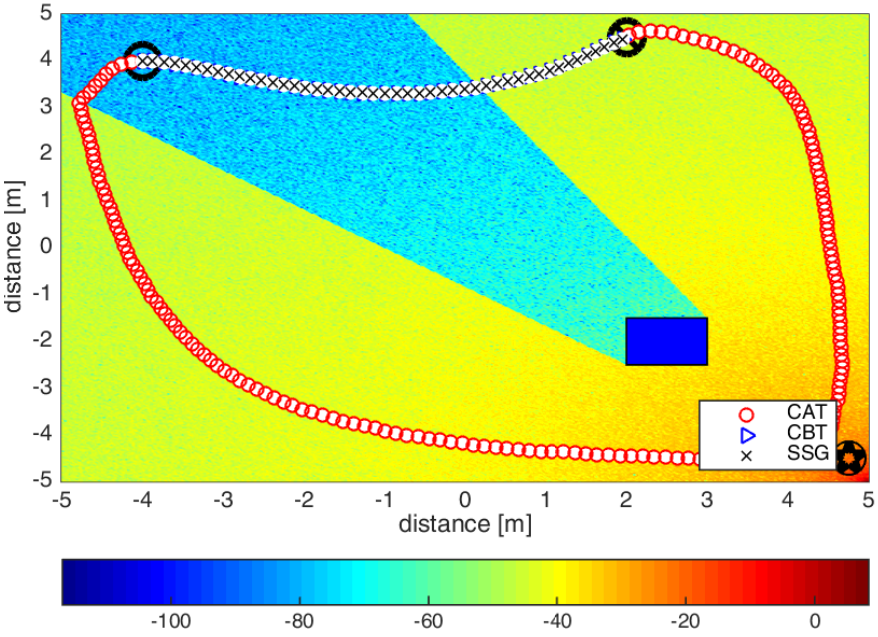

Figure 5.19: Trajectory Using SBCAM-SSG with starting position, $\mathbf{p}_S$, in a DCZ

the SNR along the CAT. However, frequent dips in SNR can be seen as the agent hit DCZs when sensing the SNR. This results in a nearly $5dB$ loss in the mean SNR along the trajectory. The lengths of the CAT, CBT and SSG trajectories (Fig. 5.16) are $20.294m$, $7.5307m$ and $17.5716m$ respectively.

5.6.1 Starting position in DCZ

For the case where the starting position of an agent is in a DCZ (section 5.3), as shown in Fig. 5.19, to avoid the situation of Fig. 5.12, the SSG algorithm doesn't update the DCZ. Therefore, the agent's motion is governed by a HPF and it moves towards the goal following the same path as the CBT as shown in Fig. 5.19. Fig. 5.19 shows the SNR-update map used by the agent when it starts in a DCZ. Since the agent doesn't know the direction where the DCZ ends, it starts moving without updating its SNR-map. After exiting the DCZ, it doesn't update the SNR-map because there

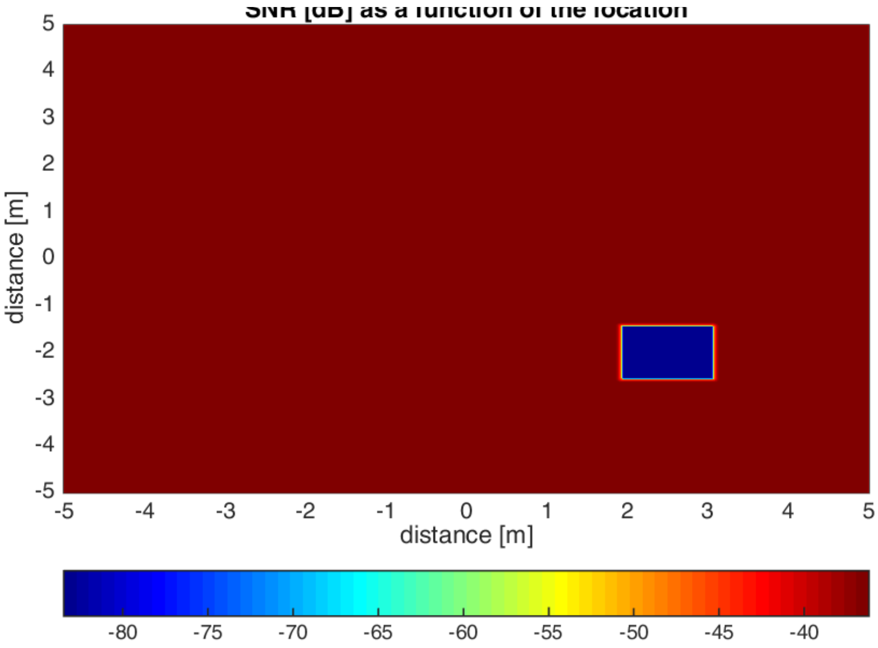

Figure 5.20: SSG-based SNR update map for the scenario in Fig. 5.19

is no other DCZ in the region. Fig. 5.21 shows the SNR along the CAT, CBT and SSG trajectories. It can be seen that since the agent doesn't update the SNR-map due to it starting in a DCZ, it exactly follows the CBT.

The length of the Model-Based Communication-Aware Navigation (MBCAN) based trajectory is $25.49m$ while both the CBT and SSG based trajectories have identical lengths equal to $6.3993m$.

5.6.2 Goal position, p_G, in DCZ

When the goal position is in a DCZ, the agent will need to stop updating its SNR-map for DCZs in order to enter a DCZ. The SSG will force the agent to search for a path outside of a DCZ to the goal. If the agent hits a dead end while moving along the boundary of the DCZ, it stops updating its SNR-map and enters the DCZ to reach its goal as shown in Fig. 5.22. The length of the MBCAN based trajectory for the

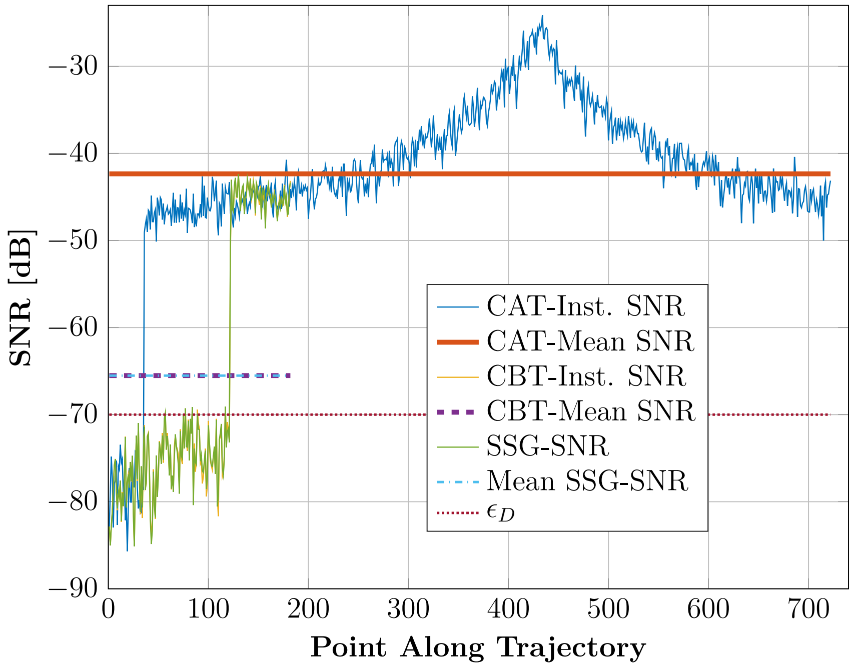

Figure 5.21: SNR comparison of the CAT, CBT and SBCAM-SSG trajectories with starting position in DCZ

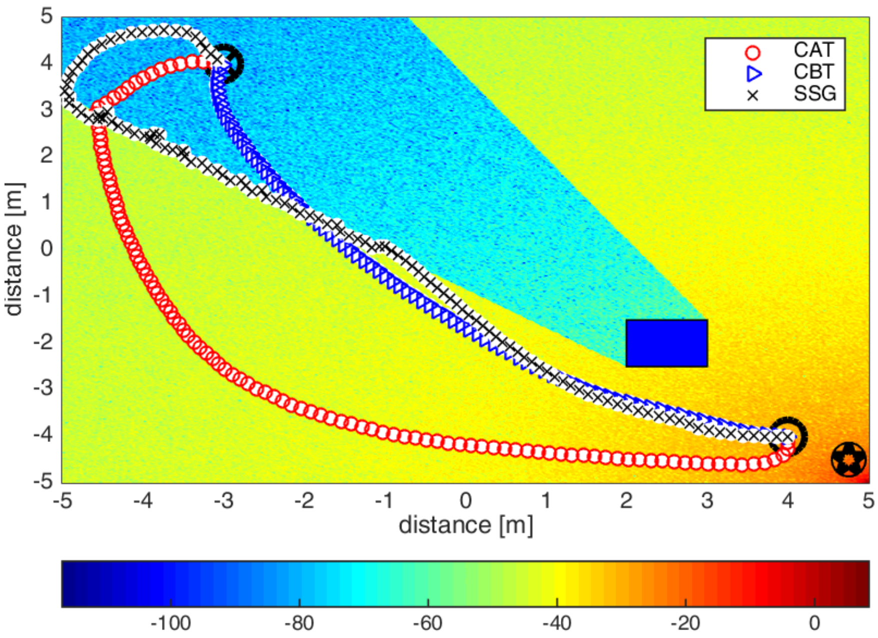

Figure 5.22: Trajectory Using SSG with the goal position, $\mathbf{p}_G$, in a DCZ

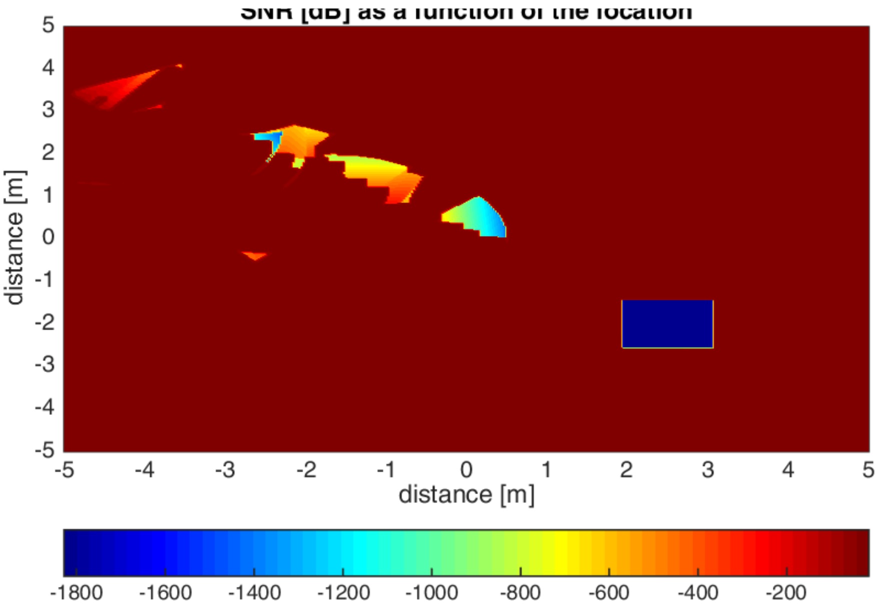

Figure 5.23: DCZ update map for the scenario of Fig. 5.22.

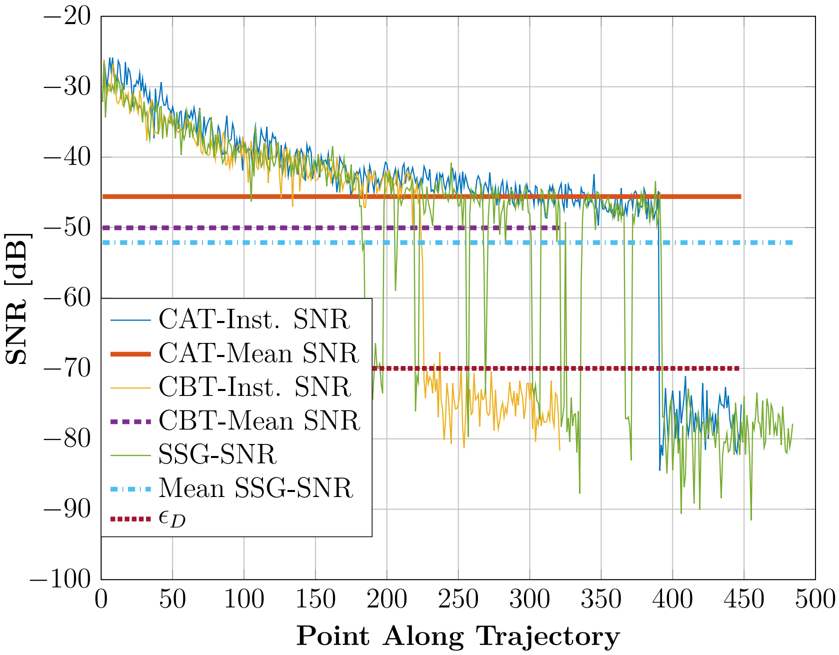

Figure 5.24: Comparison of SNR along a trajectory for the scenario of Fig. 5.22.

scenario in Fig. 5.22 is 15.8038m, the length of the CBT trajectory is 11.3137m and the SSG based trajectory is 17.0766m. It can be noted here that the increase in length of the CAT as compared to the CBT results in a higher mean SNR but the increase in length of the SSG trajectory doesn't provide any significant improvement in the SNR performance.

5.6.3 Complex environments

In the previous section, we looked at the detailed results for the performance of the SSG algorithm in an environment with a single obstacle. In the following, more complex environments with both convex and non-convex obstacles are considered. Fig. 5.25 shows such an environment where multiple obstacles create low SNR regions. It can be seen the SBCAM-SSG trajectory avoids the DCZ. However, it does enter low SNR regions while moving towards the goal as it needs to measure the SNR outside of its predicted DCZ update. Fig. 5.26 shows the DCZ updates to the SNR map by agent based on its SNR measurements. Its interesting to note that the agent does not need to map the complete DCZ in order to avoid it. The agent uses minimal DCZ updates at the boundary of the possible DCZs before reaching the goal.

The SNR performance of the SSG along its trajectory is compared to that of the CAT and CBT in Fig. 5.27. It can be seen that, since the agent is dependent on SNR measurement for its 'greedy' DCZ updates, there are multiple dips in the SNR along the SSG trajectory. This leads to a drop in the mean-SNR of the SSG trajectory compared to the CAT. The mean-SNR of the SSG trajectory is approximately 5dB less than that of the CAT. However, its performance is significantly better than that

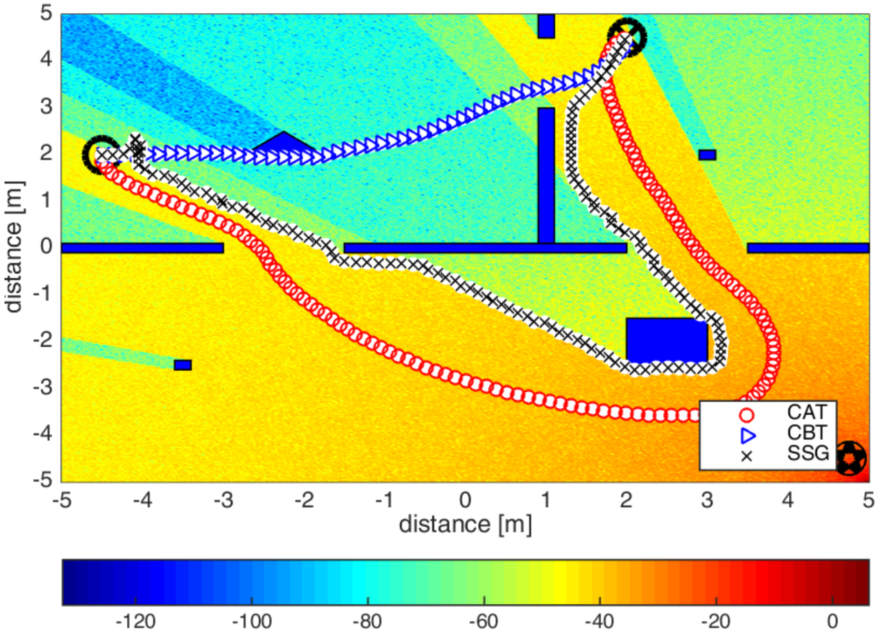

Figure 5.25: SBCAM-SSG trajectory in a complex environment with multiple obstacles.

of the CBT. The length of the CAT, CBT and SSG trajectories for the scenario in Fig. 5.25 are 18.8090m, 7.4600m and 18.9858m respectively. The SSG trajectory is the longest, however, its mean-SNR is lower than that of the CAT.

Another interesting scenario is shown in Fig. 5.28. This scenario has both convex and non-convex obstacles with irregular geometry. Also, both the starting and goal points are in DCZs. The SSG based trajectory initially follows the CBT trajectory. This is due to the fact that the DCZ is not updated due to the starting point being in a DCZ as discussed in section 5.3. However, when the agent exits the DCZ, it then starts the DCZ update when moving towards the goal. Thus, the SSG trajectory moves away from the CBT and starts moving along the border of the DCZ in which the goal position is located. When the agent is not able to find a path outside of the DCZ to the goal position, it then enters the DCZ to move towards the goal. This

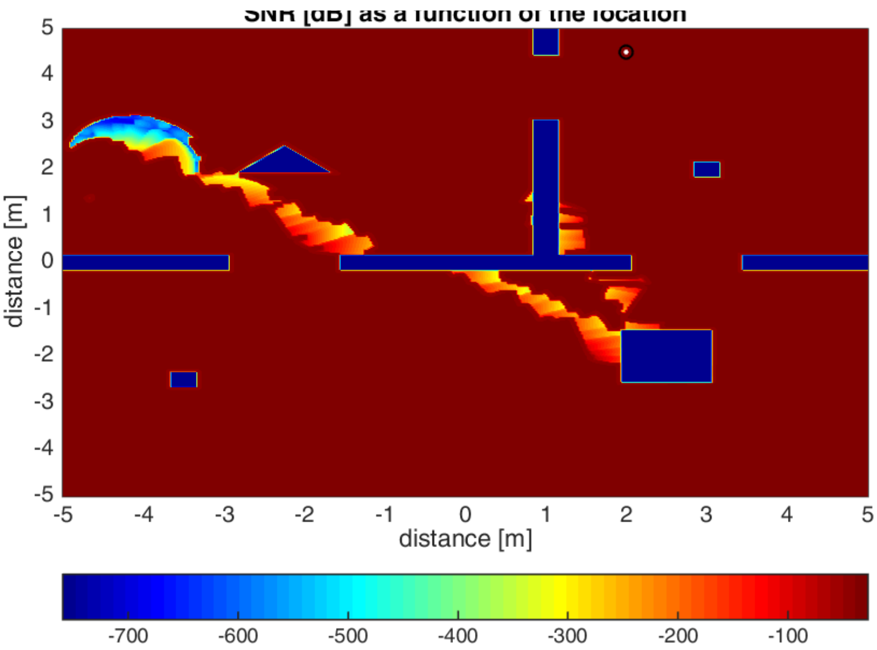

Figure 5.26: SSG reconstruction of the SNR-map of environment in Fig. 5.25.

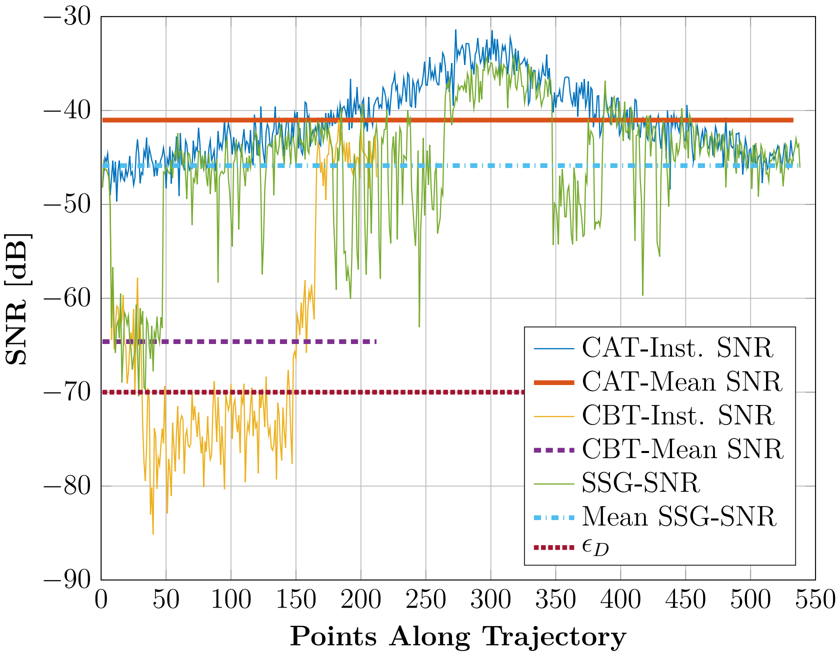

Figure 5.27: SNR updates and SNR comparison of MBCAN, CBT and SBCAM-SSG trajectories (Fig. 5.25)

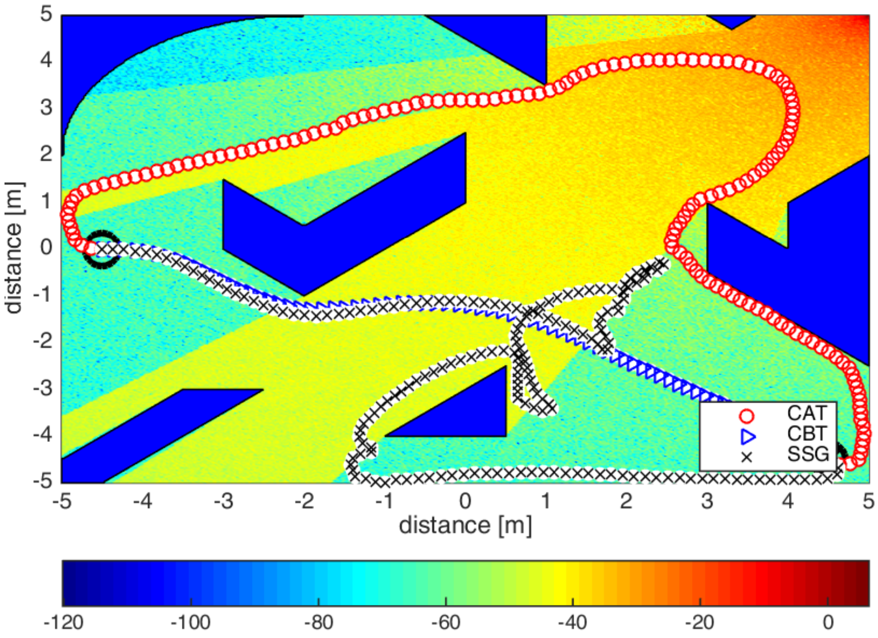

Figure 5.28: SBCAM-SSG trajectory in a complex environment with multiple convex and non-convex obstacles of irregular geometry.

results in the trajectory shown in Fig. 5.28. Although, this trajectory is a result of the greedy nature of the SSG algorithm which aggressively tries to remain in the region with high SNR.

Fig. 5.29 shows the DCZ updates of the agent using the SSG algorithm for the environment in Fig. 5.28. Fig. 5.30 compares the SNR along the CAT, CBT and the SSG trajectory. It can be seen that the mean SNR along the SSG trajectory is much lower that of the mean SNR along the CAT. However, it is still greater than the mean SNR along the CBT.

Finally, the length of the CAT is $20.9304m$, the length of the CBT is $10.5359m$ and that of the SSG trajectory is $25.2791m$. The SSG trajectory length is greater than that of the CAT, however, it does not result in any gain in mean SNR. The increase in length is mainly due to the agent trying to find a path to goal outside of the DCZ.

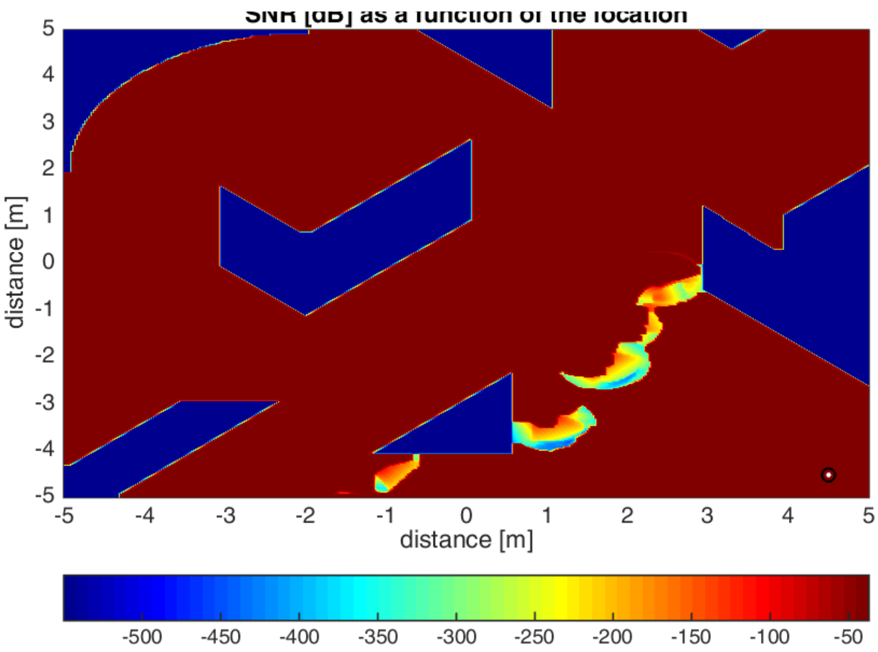

Figure 5.29: SSG SNR-map reconstruction for the environment in Fig. 5.28

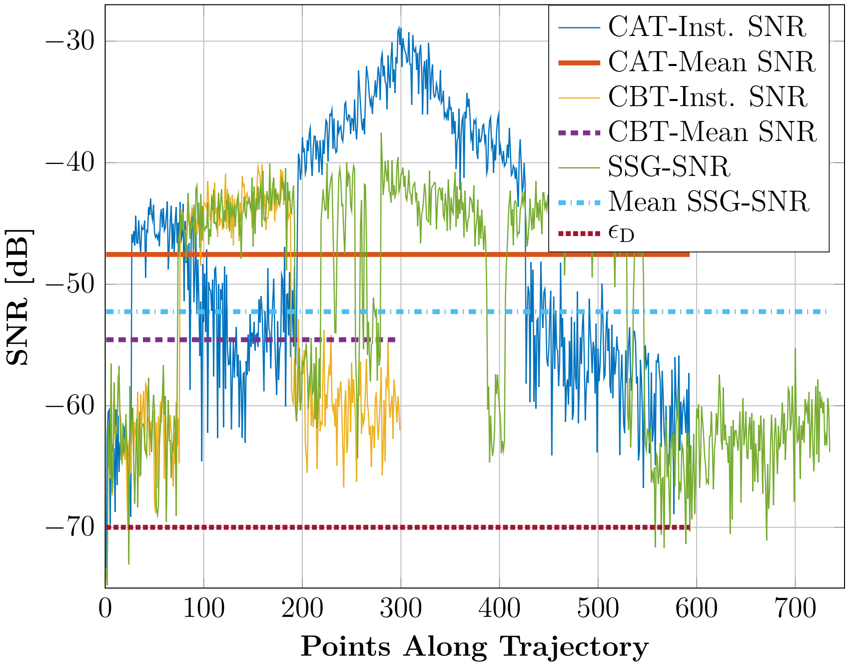

Figure 5.30: SNR comparison of MBCAN, CBT and SBCAM-SSG trajectories for the environment in Fig. 5.28

5.7 Conclusions

The SSG guarantees avoidance of DCZ if the agent starts outside of a DCZ and the goal position is also outside of a DCZ. However, if the starting position is inside a DCZ it could generate trajectories similar to CBTs. Goal positions in a DCZ lead to the SSG generating a longer trajectory than the CAT but could result in a low mean SNR. When the goal position is in a DCZ, the greedy nature of the SSG algorithm leads to the agent spending a significant amount of time to find a path to the goal without entering the DCZ. Thus if the start or goal position is in a DCZ, the performance of SSG degrades. However if both the starting and goal points are outside of a DCZ and the region with high SNR is connected, the SSG algorithm guarantees a path outside of the DCZ and its SNR performance is nearer to the performance of MBCAN.

CHAPTER 6

MULTIPLE-SENSOR-ARRAY CIRCULAR REGION (MSACR) UPDATE

> *”We are what we repeatedly do. Excellence, then, is not an act, but a habit.”*
>
> —Aristotle.

The Single Sample Greedy (SSG) update of the Signal to Noise Ratio (SNR)-map allows the agent to remain wirelessly connected to the Base-Station (BS) when it starts outside of a Dead Communication Zones (DCZ). However, its performance degraded severely when the start or goal position was inside a DCZ. Also, the agent is forced to enter a DCZ in order to detect a communication blackout. In this section we introduce another SNR update procedure where we assume a circular update region around the agent. We assume the agent to have multiple equi-distant passive antennas in a circular ring that measure the Received Signal Strength (RSS). Based on these measurements, the SNR in the circular region around the agent can be updated. The transceiver antenna is located on the agent at the center of the circular region. The path-plan of the agent is computed at the center of the agent at the transceiver antenna. The sensing antennas are off-center and therefore if one of the sensing antennas detects a DCZ, the Sensor-Based Communication-Aware Navigation (SBCAM) is able to guide the agent and consequently, the transceiver antenna away from the DCZ.

6.1 Antenna Configuration & SNR-Map Reconstruction

Fig. 6.1 shows the configuration of the sensing and transceiver antenna used in this update algorithm. d_{sen} is the distance between two adjacent sensing antennas and r_{sen} is the radius of the circle on which the sensing antennas are located around the transceiver antenna. Multiple-Sensor-Array Circular Region (MSACR) initializes the complete SNR-map to a constant value γ_S. The value γ_S is the SNR sensed at the transceiver antenna. Since the transceiver is located at the center of the agent and the path plan is computed at the center of the agent as well, therefore, at each time instant the position of the transceiver antenna is the same as the position of the agent

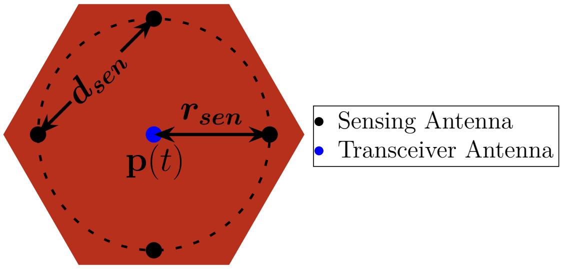

Figure 6.1: Antenna configuration on agent

given by Eq. (3.20). Hence, γ_S at each time instant t is given by,

$$\gamma_S = \widehat{\gamma}(\mathbf{p}(t)) \tag{6.1}$$

Where $\widehat{\gamma}(\mathbf{p}(t))$ is the SNR sensed at the transceiver antenna.

The SNR sensed at each sensing antenna is used to reconstruct the SNR-map locally in a circular region around the agent. The reconstruction is done by using a Gaussian kernel centered at the antenna location and normalized to have unit magnitude at its center. The Gaussian kernel's variance is set so that its value tapers to zero at the center of the nearest antenna. The Gaussian Update Function (UF) is given as follows

$$f_i(\mathbf{p}) = \exp\left(-\frac{1}{2}(\mathbf{p}-\mathbf{p}_{a_i})^T\sigma^{-2}\mathrm{I}(\mathbf{p}-\mathbf{p}_{a_i})\right), i = 1, 2, \ldots, N_{ant} \tag{6.2}$$

Where $\mathbf{p}_{a_i}$ is the location of the i^{th} antenna and σ governs that width of the Gaussian function such that the measurement at an antenna will not affect the RSS measurement at other antenna. N_{sen} is the number of sensing antenna around the transceiver antenna. The Gaussian Update Function (UF) is weighted by the SNR measurement at the antenna. The center of the Gaussian UF is normalized to one and therefore represents the measured SNR. Away from the center, the reconstructed map is a weighted sum of the SNR sensed at different antennas. If the sum of the Gaussian UFs is less than one at a position $\mathbf{p}$, then the remaining factor is weighted by γ_s. On the other hand, if the Gaussian UFs add to greater than one at a position $\mathbf{p}$, then

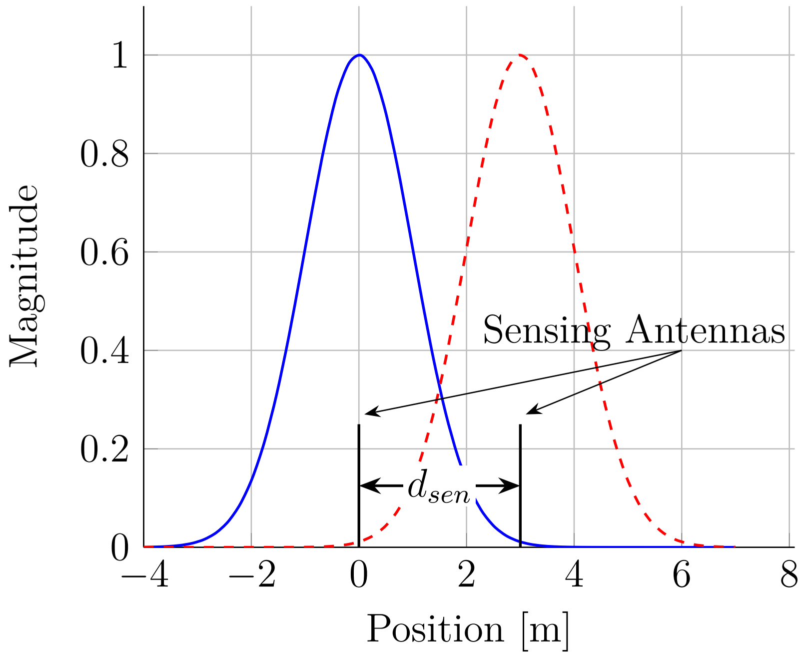

Figure 6.2: Gaussian UF with $\sigma = 1$ used to reconstruct SNR-map based on the sensed SNR at the sensing antennas.

they are normalized by the their sum. The update rule is given as follows

$$\gamma(\mathbf{p}) = \begin{cases} \sum_{i=1}^{N_{ant}} \widehat{\gamma}_i \cdot f_i(\mathbf{p}) + \gamma_s \cdot \left(1 - \sum_{i=1}^{N_{ant}} f_i(\mathbf{p})\right), & \sum_{i=1}^{N_{ant}} f_i(\mathbf{p}) < 1 \\ \sum_{i=1}^{N_{ant}} \widehat{\gamma}_i \cdot f_i(\mathbf{p}), & \sum_{i=1}^{N_{ant}} f_i(\mathbf{p}) = 1 \\ \sum_{i=1}^{N_{ant}} \widehat{\gamma}_i \cdot \frac{f_i(\mathbf{p})}{\sum_{i=1}^{N_{ant}} f_i(\mathbf{p})}, & \sum_{i=1}^{N_{ant}} f_i(\mathbf{p}) > 1 \end{cases} \tag{6.3}$$

Where, N_{ant} is the number of antennas on the agent including the transceiver antenna and $\widehat{\gamma}_i$ is the SNR sensed at the i^{th} antenna. Away from the center a weighted version of the measurements will add up to form the SNR update. This is demonstrated for one dimensional Gaussian functions in Fig. 6.2. It shows the UF which will be weighted by the measured SNR at a sensing antenna. The center of the Gaussian UF is unity and therefore, will represent the measurement and away from the center it falls off. The factor, σ of the Gaussian UF governs the rate at which the function tapers off.

It has to be noted that γ_S is changing with time (Eq. (6.1)). Since away from the update region, the Gaussian UF tapers to zero, therefore, the MSACR update always assumes that away from the reconstructed region, the SNR-map will be equal to γ_S.

6.2 Analysis

The aim of using a circular band of equi-distant antennas is to reconstruct the SNR-map locally. The updated SNR-map is then used to update the Harmonic Potential Field (HPF) and consequently help the agent decide on its future motion course. Gaussian update functions are used because the wireless signals are band-limited [78].

It is desired that the SNR update at one sensing antenna doesn't affect or has minimal effect at other sensing antennas. This results in constraints on the width of the gaussian function. The width of Gaussian functions depends on its variance (or standard deviation) (Eq. (6.2)). The standard deviation can be chosen based on how much overlap is acceptable between two consecutive sensing antenna updates. Since the gaussian updates tapers off exponentially away from its center, antennas further away from the adjacent sensing antennas will have less overlap than the adjacent sensing antennas as shown in Fig. 6.3. It can be seen that the gaussian function with $\sigma = 1$ corresponding to the antenna at location $(3, 0)$ overlaps with the function at location $(0, 0)$ but the function at location $(6, 0)$ has negligible overlap with the one

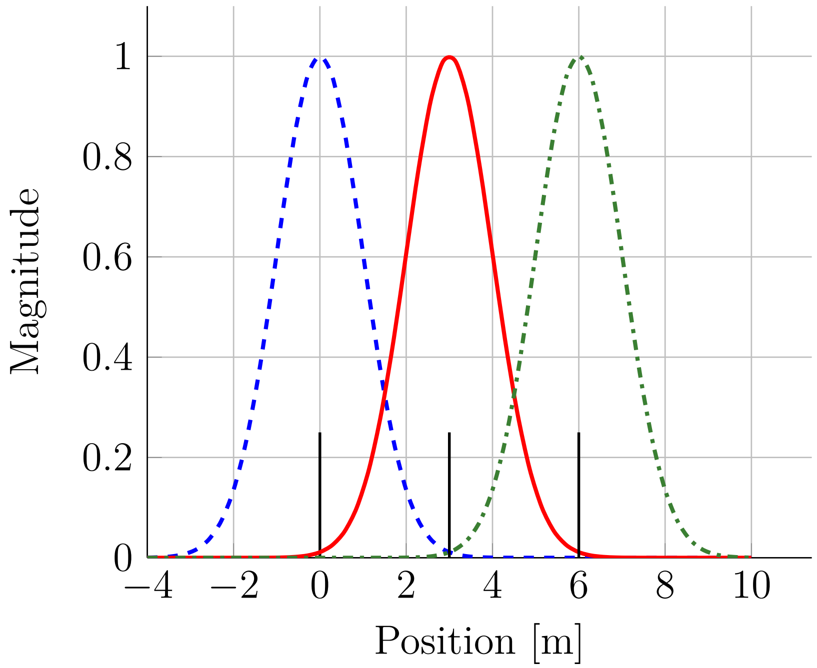

Figure 6.3: Overlap between Gaussian update functions with $\sigma = 1$

at location $(0, 0)$. Therefore, it can be safely assumed the sensing antennas further away will not have any overlap. Changing σ can result in overlap with functions at antennas further away as shown in Fig. 6.4. It can be seen that the update function in the middle will have large contributions from its adjacent update functions. On the other hand choosing a very narrow σ can result in the update functions not covering the regions between the sensing antennas as shown in Fig. 6.5. Therefore, the width of the update function governs how much the SNR measured at an antenna is propagated away from the antenna in the SNR-map reconstruction. Thus the update functions should have a sufficient width such that the region between the antennas is also updated but the update should have minimal effect at other sensing antenna locations. This leads us to the following definition.

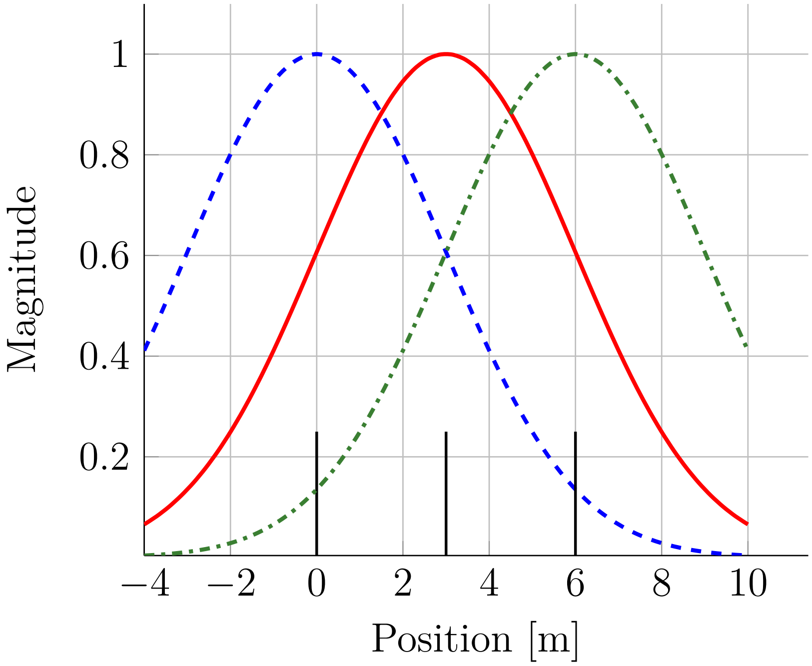

Figure 6.4: Overlap between Gaussian update functions with $\sigma = 3$

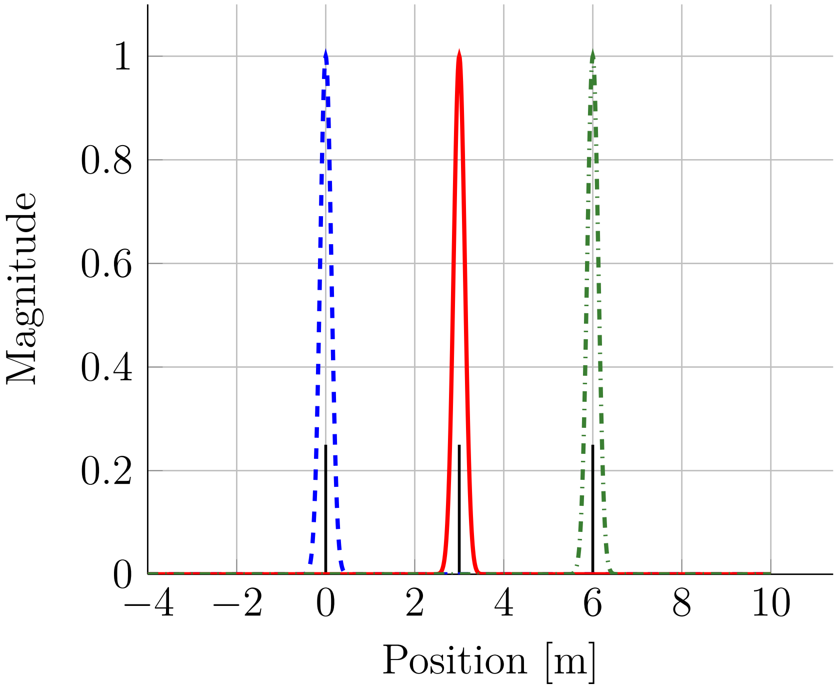

Figure 6.5: Overlap between Gaussian update functions with $\sigma = 0.125$

DEFINITION 6.1 *The overlap* $\epsilon_{OL}^{i,j}$ *between two update functions given by Eq.* (6.2) *is defined as follows.*

$$\epsilon_{OL}^{i,j} = \int_{-\infty}^{+\infty} f_i(\mathbf{p}) \cdot f_j(\mathbf{p}) d\mathbf{p} \tag{6.4}$$

Def. 6.1 leads us to the following proposition.

PROPOSITION 6.1 *Using Def. 6.1, we get the following condition on the width of the Gaussian update functions of Eq.* (6.2) *governed by* σ.

$$\sigma(\epsilon_{OL}^{i,j}) \approx \frac{d_{sen}}{\ln\left(\epsilon_{OL}^{i,j}{}^{-4}\right)}, 0 < \epsilon_{OL}^{i,j} \ll 1 \tag{6.5}$$

Eq. (6.5) *obtains* σ *as a function of the overlap between the UFs of two adjacent sensing antennas.*

Proof. Using the 1-D version of Eq. (6.2) in Eq. (6.4) we get the overlap between two UFs of adjacent sensing antennas as follows.

$$\begin{aligned}
\epsilon_{OL}^{i,j} &= \int_{-\infty}^{+\infty} f_i(\mathbf{p}) \cdot f_j(\mathbf{p}) dx,\ \forall\{i,j\} = 1, \cdots, N_{sen}, i \neq j, |i-j| = 1 && (6.6)\\
&= \int_{-\infty}^{+\infty} e^{-\dfrac{(\mathbf{p}-\mathbf{p}_{a_i})^2}{2\sigma^2}} \cdot e^{-\dfrac{\left(\mathbf{p}-\mathbf{p}_{a_j}\right)^2}{2\sigma^2}} dx && (6.7)\\
&= \int_{-\infty}^{+\infty} e^{-\dfrac{(\mathbf{p}-\mathbf{p}_{a_i})^2 + \left(\mathbf{p}-\mathbf{p}_{a_j}\right)^2}{2\sigma^2}} dx && (6.8)\\
&= \int_{-\infty}^{+\infty} e^{-\dfrac{\left[2\mathbf{p}^2 - 2\mathbf{p}\left(\mathbf{p}_{a_i}+\mathbf{p}_{a_j}\right) + \mathbf{p}_{a_i}^2 + \mathbf{p}_{a_j}^2\right]}{2\sigma^2}} dx && (6.9)\\
&= \int_{-\infty}^{+\infty} e^{-\dfrac{M}{2\sigma^2}} dx && (6.10)
\end{aligned}$$

Where,

$$M = \left[2\mathbf{p}^2 - 2\mathbf{p}\left(\mathbf{p}_{a_i} + \mathbf{p}_{a_j}\right) + \mathbf{p}_{a_i}^2 + \mathbf{p}_{a_j}^2\right] \tag{6.11}$$

Completing squares in Eq. (6.11)

$$\begin{aligned}
M &= 2\mathbf{p}^2 - 2\mathbf{p}\left(\mathbf{p}_{a_i} + \mathbf{p}_{a_j}\right) + \mathbf{p}_{a_i}^2 + \mathbf{p}_{a_j}^2 && (6.12)\\
&= 2\left[\mathbf{p}^2 - \mathbf{p}\left(\mathbf{p}_{a_i} + \mathbf{p}_{a_j}\right)\right] + \mathbf{p}_{a_i}^2 + \mathbf{p}_{a_j}^2 && (6.13)\\
&= 2\left[\mathbf{p}^2 - \mathbf{p}\left(\mathbf{p}_{a_i} + \mathbf{p}_{a_j}\right) + \frac{\left(\mathbf{p}_{a_i} + \mathbf{p}_{a_j}\right)^2}{4} - \frac{\left(\mathbf{p}_{a_i} + \mathbf{p}_{a_j}\right)^2}{4}\right] + \mathbf{p}_{a_i}^2 + \mathbf{p}_{a_j}^2 && (6.14)\\
&= 2\left[\mathbf{p} - \frac{\left(\mathbf{p}_{a_i} + \mathbf{p}_{a_j}\right)}{2}\right]^2 - \frac{\left(\mathbf{p}_{a_i} + \mathbf{p}_{a_j}\right)^2}{2} + \mathbf{p}_{a_i}^2 + \mathbf{p}_{a_j}^2 && (6.15)\\
&= 2\left[\mathbf{p} - \frac{\left(\mathbf{p}_{a_i} + \mathbf{p}_{a_j}\right)}{2}\right]^2 - \frac{\left(\mathbf{p}_{a_i} + \mathbf{p}_{a_j}\right)^2}{2} + \mathbf{p}_{a_i}^2 + \mathbf{p}_{a_j}^2 && (6.16)\\
&= 2\left[\mathbf{p} - \frac{\left(\mathbf{p}_{a_i} + \mathbf{p}_{a_j}\right)}{2}\right]^2 \frac{-\mathbf{p}_{a_i}^2 - 2\mathbf{p}_{a_i}\mathbf{p}_{a_j} - \mathbf{p}_{a_j}^2 + 2\mathbf{p}_{a_i}^2 + 2\mathbf{p}_{a_j}^2}{2} && (6.17)\\
&= 2\left[\mathbf{p} - \frac{\left(\mathbf{p}_{a_i} + \mathbf{p}_{a_j}\right)}{2}\right]^2 \frac{+\mathbf{p}_{a_i}^2 - 2\mathbf{p}_{a_i}\mathbf{p}_{a_j} + \mathbf{p}_{a_j}^2}{2} && (6.18)\\
&= \frac{4\left[\mathbf{p} - \frac{\left(\mathbf{p}_{a_i} + \mathbf{p}_{a_j}\right)}{2}\right]^2 + \left(\mathbf{p}_{a_i} - \mathbf{p}_{a_j}\right)^2}{2} && (6.19)
\end{aligned}$$

Substituting Eq. (6.19) in Eq. (6.10),

$$\begin{aligned}
\epsilon_{OL}^{i,j} &= \int_{-\infty}^{+\infty} e^{-\frac{4\left[\mathbf{p} - \frac{\left(\mathbf{p}_{a_i} + \mathbf{p}_{a_j}\right)}{2}\right]^2 + \left(\mathbf{p}_{a_i} - \mathbf{p}_{a_j}\right)^2}{4\sigma^2}} dx && (6.20)\\
&= \int_{-\infty}^{+\infty} e^{-\frac{4\left[\mathbf{p} - \frac{\left(\mathbf{p}_{a_i} + \mathbf{p}_{a_j}\right)}{2}\right]^2}{4\sigma^2}} e^{-\frac{\left(\mathbf{p}_{a_i} - \mathbf{p}_{a_j}\right)^2}{4\sigma^2}} dx && (6.21)\\
&= e^{-\frac{\left(\mathbf{p}_{a_i} - \mathbf{p}_{a_j}\right)^2}{4\sigma^2}} \int_{-\infty}^{+\infty} e^{-\frac{\left[\mathbf{p} - \frac{\left(\mathbf{p}_{a_i} + \mathbf{p}_{a_j}\right)}{2}\right]^2}{\sigma^2}} dx && (6.22)
\end{aligned}$$

In Eq. (6.22) the integrand is also a Gaussian function with mean

$$\mu_{\epsilon_{OL}^{i,j}} = \frac{\left(\mathbf{p}_{a_i} + \mathbf{p}_{a_j}\right)}{2} \tag{6.23}$$

and standard deviation

$$\sigma_{\epsilon_{OL}^{i,j}} = \frac{\sigma}{\sqrt{2}} \tag{6.24}$$

It was shown by Nicholas and Yates in [96] that

$$\int_{-\infty}^{+\infty} e^{-\frac{[\mathbf{p}-\mu]^2}{2\sigma^2}} dx = \sqrt{2\pi}\sigma \tag{6.25}$$

Using Eq. (6.25) in Eq. (6.22), we get

$$\epsilon_{OL}^{i,j} = e^{-\frac{\left(\mathbf{p}_{a_i} - \mathbf{p}_{a_j}\right)^2}{4\sigma^2}} \cdot \sqrt{2\pi}\sigma_{\epsilon_{OL}^{i,j}} \tag{6.26}$$

using Eq. (6.24) in Eq. (6.26),

$$\epsilon_{OL}^{i,j} = e^{-\frac{\left(\mathbf{p}_{a_i} - \mathbf{p}_{a_j}\right)^2}{4\sigma^2}} \cdot \sqrt{2\pi}\frac{\sigma}{\sqrt{2}} \tag{6.27}$$

$$\frac{\epsilon_{OL}^{i,j}}{\sqrt{\pi}\sigma} = e^{-\frac{\left(\mathbf{p}_{a_i} - \mathbf{p}_{a_j}\right)^2}{4\sigma^2}} \tag{6.28}$$

$$\epsilon_{OL}^{i,j} \approx e^{-\frac{\left(\mathbf{p}_{a_i} - \mathbf{p}_{a_j}\right)^2}{4\sigma^2}}, \text{ for } 0 < \epsilon_{OL}^{i,j} \ll 1 \tag{6.29}$$

$$-4\sigma^2 \ln\left(\epsilon_{OL}^{i,j}\right) \approx \left(\mathbf{p}_{a_i} - \mathbf{p}_{a_j}\right)^2 \tag{6.30}$$

$$\sigma^2 \ln\left(\frac{1}{{\epsilon_{OL}^{i,j}}^4}\right) \approx \left(\mathbf{p}_{a_i} - \mathbf{p}_{a_j}\right)^2 \tag{6.31}$$

$$\sigma^2 \ln\left(\frac{1}{{\epsilon_{OL}^{i,j}}^{4}}\right) \approx \left(\mathbf{p}_{a_i} - \mathbf{p}_{a_j}\right)^2 \tag{6.32}$$

$$\sigma\sqrt{\ln\left(\frac{1}{{\epsilon_{OL}^{i,j}}^{4}}\right)} \approx \left|\mathbf{p}_{a_i} - \mathbf{p}_{a_j}\right| \tag{6.33}$$

$$\sigma \approx \frac{\left|\mathbf{p}_{a_i} - \mathbf{p}_{a_j}\right|}{\sqrt{\ln\left({\epsilon_{OL}^{i,j}}^{-4}\right)}} \tag{6.34}$$

$$\forall\{i,j\} = 1,\cdots,N_{sen}, i \neq j, |i-j| = 1$$

The numerator of Eq. (6.34) is the distance between the positions of two adjacent sensing antennas. Since the sensing antennas are equidistant, therefore

$$\left|\mathbf{p}_{a_i} - \mathbf{p}_{a_j}\right| = d_{sen},\ \forall\{i,j\} = 1,\cdots,N_{sen}, i \neq j, |i-j| = 1 \tag{6.35}$$

Using Eq. (6.35) in Eq. (6.34), we get

$$\boxed{\sigma \approx \frac{d_{sen}}{\sqrt{\ln\left({\epsilon_{OL}^{i,j}}^{-4}\right)}},\ 0 < \epsilon_{OL}^{i,j} \ll 1} \tag{6.36}$$

Eq. (6.36) holds for multi-dimensional UFs as its spatially independent. ∎

The transceiver antenna also updates the SNR-map with its RSS measurements. It uses the same UF as the sensing antennas therefore, in order for the SNR-map reconstruction to be consistent, the transceiver antenna should have the same distance to the sensing antennas as d_{sen}, i.e.

$$r_{sen} = d_{sen} \tag{6.37}$$

This can be achieved using a hexagonal configuration ($N_{sen} = 6$) of the sensing an-

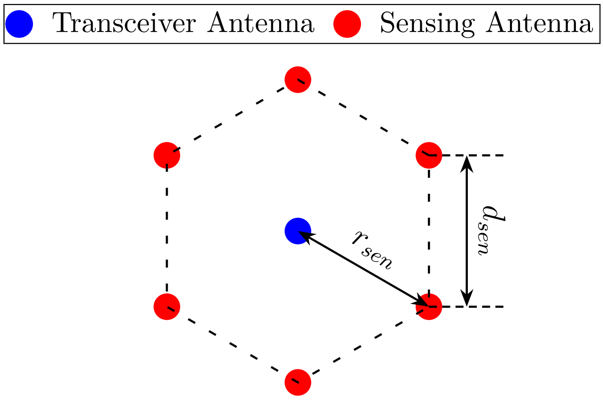

Figure 6.6: Hexagonal sensing antenna configuration.

tennas with the transceiver at the center of the hexagon as shown in Fig. 6.6.

Increasing the number of sensing antennas will increase the accuracy of the SNR-map reconstruction. However, a large N_{sen} can affect the convergence of the SBCAM as shown in the following proposition.

PROPOSITION 6.2 *A large number of sensing antennas, $N_{sen} \to \infty$, could lead to the divergence of the SBCAM-MSACR trajectory.*

Proof. The approximate distance between two adjacent sensing antennas is given by,

$$d_{sen} \approx \frac{2 \cdot \pi \cdot r_{sen}}{N_{sen}} \tag{6.38}$$

Applying the limit $N_{sen} \to \infty$ to Eq. (6.38), we get,

$$d_{sen} = \lim_{N_{sen} \to \infty} \frac{2 \cdot \pi \cdot r_{sen}}{N_{sen}} \tag{6.39}$$

$$\implies d_{sen} \to 0 \tag{6.40}$$

From Eq. (6.5), $\sigma \to 0$ if $d_{sen} \to 0$. Thus the UFs would reduce to a series of impulses weighted by the sensed SNR at the location of the sensing antennas on a circle around the transceiver antenna. From Prop. 4.1, $\frac{\partial \gamma}{\partial t}$ should be low for guaranteed convergence. However, narrow UF due to small d_{sen} can lead to high values of $\frac{\partial \gamma}{\partial t}$, potentially violating the bound of Eq. (4.20) ▌

Using a large number of antennas would also lead to the SNR-map not being updated away from the sensing antenna location. The reconstructed SNR-map would be updated locally as a circle of impulses around the transceiver antenna.

A corollary of Prop. 6.2 is given as follows

COROLLARY 6.1 *Reducing the radius of the sensing antenna circle could lead to the divergence of the SBCAM-MSACR trajectory.*

Proof. This can be seen by setting the limit $r_{sen} \to 0$ in Eq. (6.38).

$$d_{sen} = \lim_{r_{sen} \to 0} \frac{2 \cdot \pi \cdot r_{sen}}{N_{sen}} \implies d_{sen} \to 0, \sigma \to 0 \tag{6.41}$$

In other words the MSACR update will collapse in to a point update and the UF will converge to an impulse ($d_{sen} \to 0 \implies \sigma \to 0$ from Eq. (6.5)). An impulse UF could lead to $\frac{\partial \gamma}{\partial t}$ have a large value and therefore possibly violate the bound of Eq. (4.20) and lead to the SBCAM diverging. The SNR-map reconstruction would also be just a point update at the location of the transceiver. ▌

6.2.1 DCZ Avoidance

The transceiver antenna is surrounded by the sensing antennas which are at a distance of r_{sen} from it. Therefore, if the agent is outside of a DCZ, then the sensing antennas in the direction of the DCZ would enter the DCZ before the transceiver antenna. Therefore, the reconstructed region will have a DCZ in a small region around the location of the sensing antenna.

Since, the SBCAM solves a Model-Based Communication-Aware Navigation (MB-CAN) problem at each time step, therefore, the agent is guided away from the DCZ. However if r_{sen} is small, then as a shown in Corollary 6.1, the update around the sensed antenna will be small as σ will be small. The solver is limited by resolution of the grid used when solving for ϕ. Hence the smaller the footprint of the reconstructed region in the SNR-map, the more dense (higher resolution) the grid needs to be. The density of the solver grid on the other hand is limited by the memory available. Moreover, denser grids require more computation time.

This limitation of the solver can lead to the agent not being able to avoid DCZs as the solver is not able to incorporate changes outside the resolution of the grid. On the other hand, larger r_{sen} leads to a larger reconstructed region which can be handled by grids with lower resolutions.

Moreover, looking at Eq. (3.24)

$$\nabla^2 \phi = -\frac{1}{\gamma}((-\nabla \gamma) \cdot (-\nabla \phi)) \tag{6.42}$$

in the DCZ in the reconstructed region will result in a net negative divergence and therefore impeding motion in that direction. However, the if r_{sen} is small then the reconstructed DCZ will cover a small region and the region surrounding it will result in a net positive or zero divergence. Thus motion will be encouraged in regions

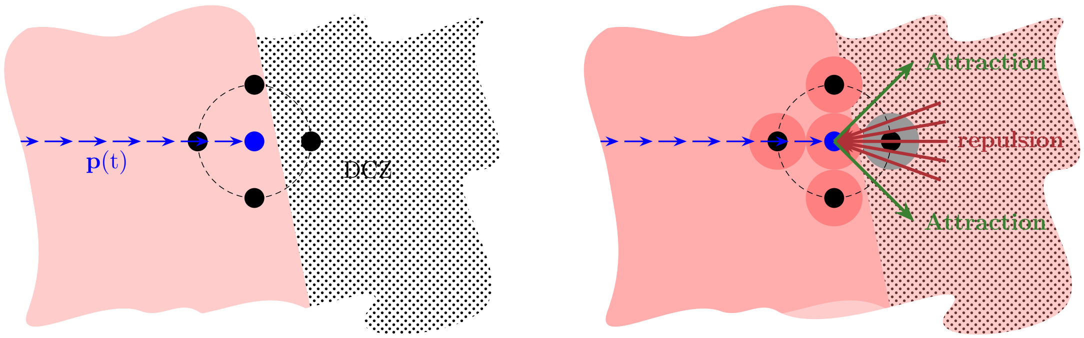

(a) Antenna positions as agent approaches DCZ **(b)** MSACR update as agent approaches DCZ

Figure 6.7: MSACR reconstruction with small r_{sen}

immediately surrounding the DCZ.

This attraction of motion to regions in close vicinity of the DCZ could lead to the agent entering the DCZ as demonstrated in Fig. 6.7. The agent is equipped with four equidistant sensing antennas. When it approaches the DCZ, the antenna in the direction of motion first enters the DCZ and reconstructs the SNR-map. It is represented as a gray circle in Fig. 6.7b. The region outside of the reconstructed SNR map is given the same SNR as the one sensed at the transceiver antenna (Eq. (6.1)). Thus it can be seen in the figure that small reconstruction regions could lead to the the agent to move in to a DCZ.

A large r_{sen} on the other hand will have a large reconstructed region. Also, since r_{sen} is large, when a sensing antenna enters the DCZ, the transceiver antenna will be much further away from the DCZ, and therefore, it can change its direction of motion much before it approaches a DCZ.

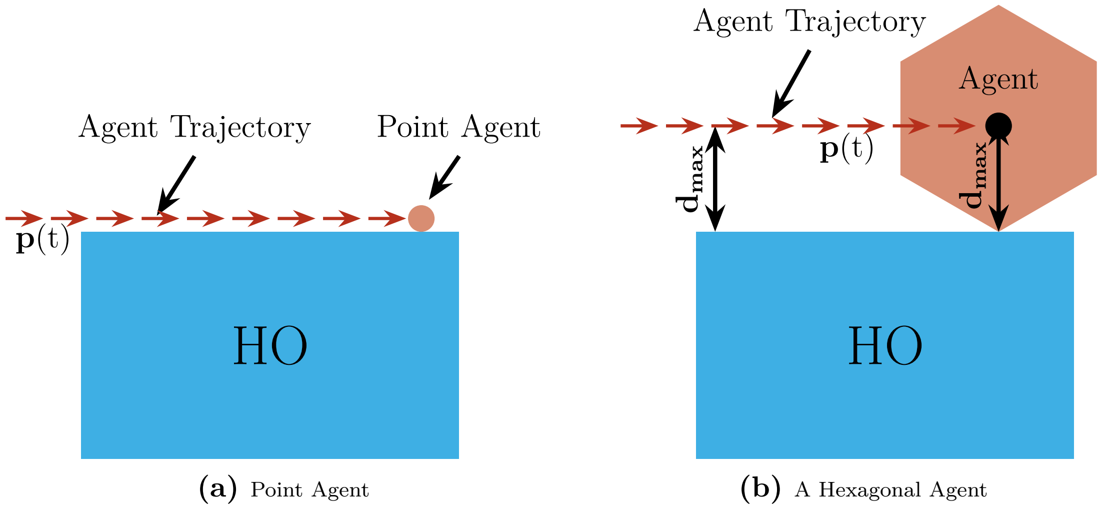

(a) Point Agent **(b)** A Hexagonal Agent

Figure 6.8: HO and obstacle avoidance.

6.3 Hard Obstacle or Hazardous Region (HO) Extension & Agent Size

In chapter 3 and in the SSG algorithm a point agent is assumed. However, in the MSACR point agents are not assumed and the agent is required to have, at the least, the same size as the circle on which the sensing antennas are placed. Therefore, the agent will have a finite area and the the point agent assumption could lead to the agent hitting the Hard Obstacle or Hazardous Region (HO). Fig. 6.8 shows the trajectory of a point agent and a hexagonal agent while navigating a rectangular obstacle. The trajectory of the agents is computed at their center position as shown in Fig. 6.8b. In order to ensure safe navigation of HO, the dimensions of the regular agents have to be taken in to account. If a regular agent follows the same trajectory as a point agent, it will crash in to the obstacle.

In order to safely navigate HO, the computed path plan has to take in to account

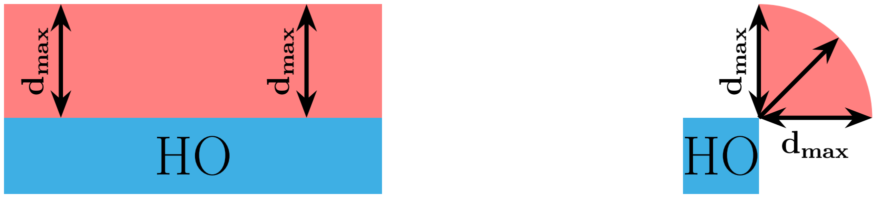

(a) Extending edges **(b)** Extending corners

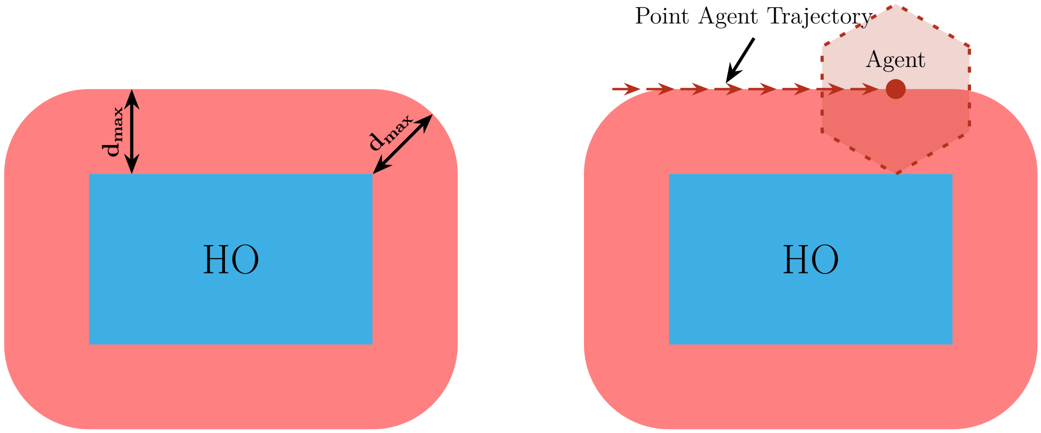

(c) An extended obstacle **(d)** Regular agent as point agent.

Figure 6.9: Extending obstacles to accommodate the dimensions of regular agents

the dimensions of the agent. This can be ensured by reshaping the HO based on the largest dimension of the agent, d_{max}. This is done by extending the HO size at its edges by the maximum dimension and extending the corners using arcs with radii equal to the maximum dimension of the agent. This is demonstrated in Fig. 6.9 The path-planner can then use extended obstacle and treat the agent as a point agent. The obstacle extension will account for the size of the agent as shown in Fig. 6.9d. The extension of any obstacle with any geometry can be done by decomposing it in to edges and corners and using line and arc extensions correspondingly.

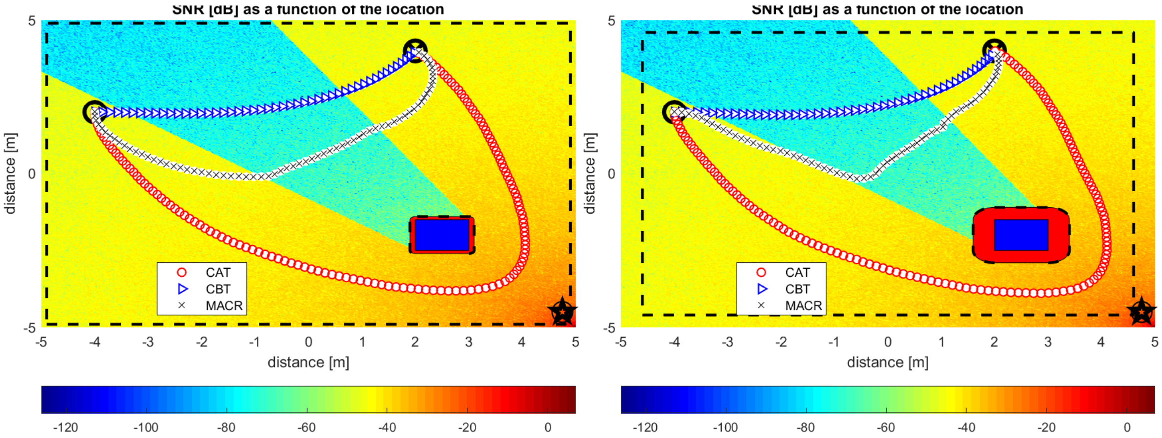

(a) $r_{sen} = 10$ cm **(b)** $r_{sen} = 40$ cm

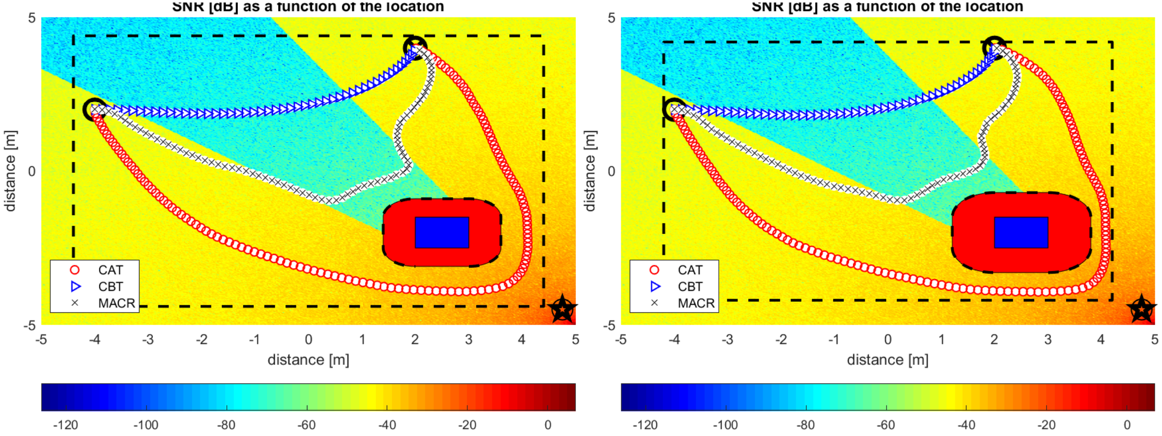

(c) $r_{sen} = 60$ cm **(d)** $r_{sen} = 80$ cm

Figure 6.10: SBCAM-trajectory with MSACR update for different sensing regions

6.4 Results

We present simulation results obtained for the SBCAM with MSACR update. We generated trajectories for values r_{sen} ranging from 10 cm to 90 cm. The number of sensing antennas is taken to be 8.

6.4.1 Single Obstacle Environment

Fig. 6.10 shows the trajectory of an agent with four different radii for the the sensing region. It can be seen that the agent's trajectory improves as compared to the communication blind case. The improvement increases with increasing r_{sen}. However, the trajectories are not able to match the MBCAN trajectory. This is due to the fact that the agent's trajectory is dependent on the starting orientation it chooses. since, at the beginning the agent is completely blind to the SNR-map, it chooses are trajectory different from the MBCAN.

In Fig. 6.11 the reconstructed SNR-map corresponding to the trajectories in Fig. 6.10. It can be seen that a larger r_{sen} results in a better reconstruction of the SNR-map. Another interesting observation is the extension of the obstacle. It can be seen that the obstacles get extended with the increase in r_{sen}. This is to due to the fact that the size of the agent increases with r_{sen} and therefore, the obstacle gets extended to compensate for the size. Fig. 6.12 shows the SNR along the trajectory of the agent with different r_{sen}. It can be seen that the mean-SNR has improved with increasing r_{sen}.

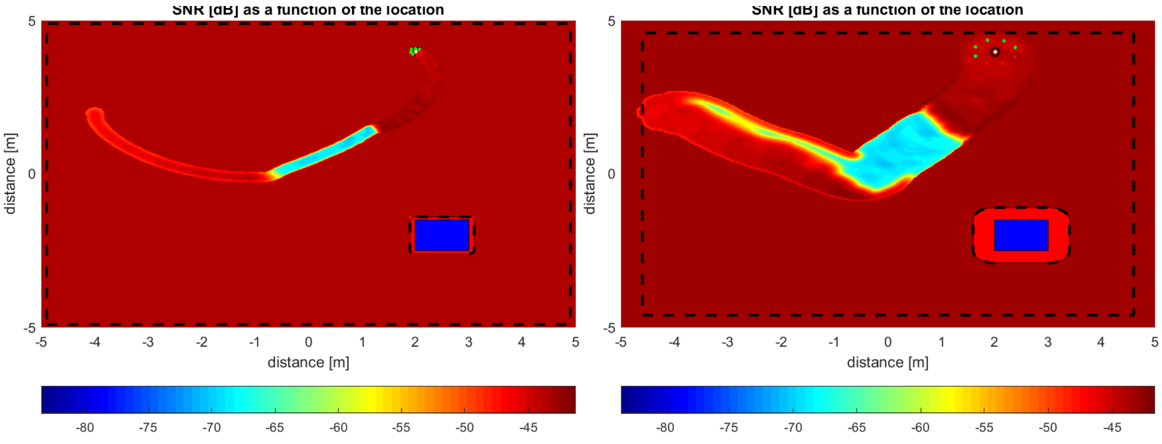

(a) $r_{sen} = 10$ cm **(b)** $r_{sen} = 40$ cm

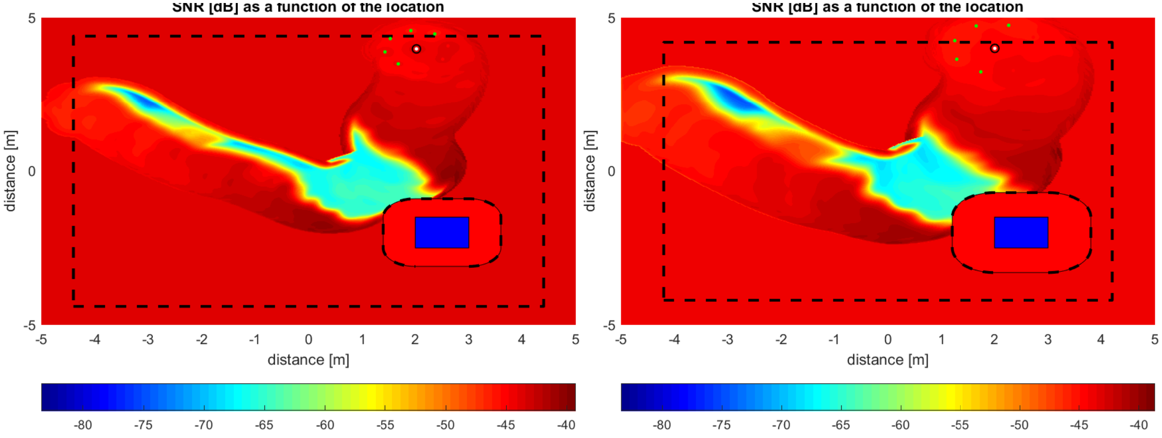

(c) $r_{sen} = 60$ cm **(d)** $r_{sen} = 80$ cm

Figure 6.11: SNR & HO maps

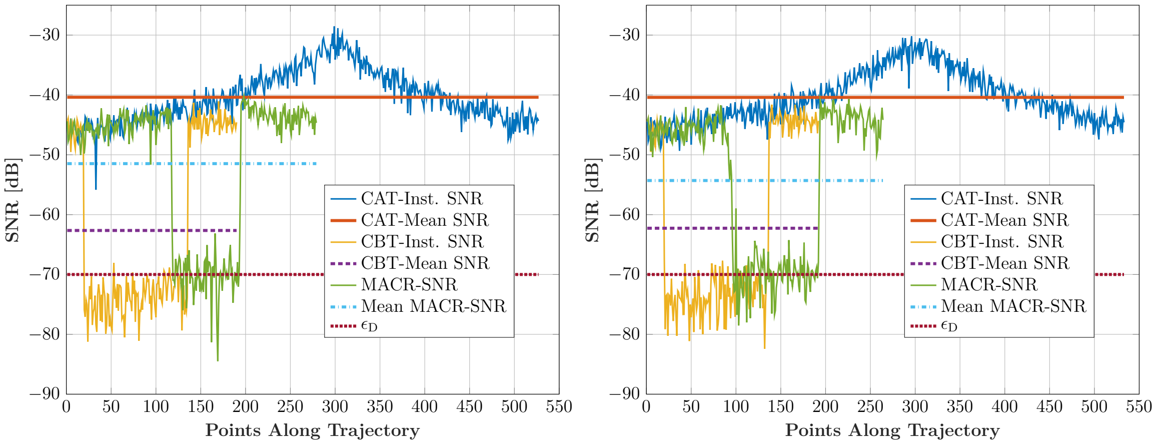

(a) $r_{sen} = 10$ cm **(b)** $r_{sen} = 40$ cm

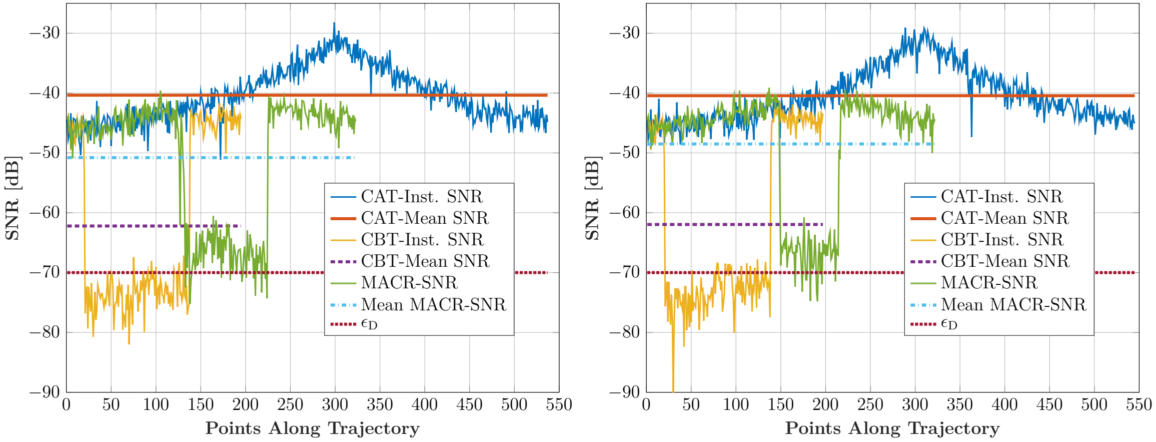

(c) $r_{sen} = 60$ cm **(d)** $r_{sen} = 80$ cm

Figure 6.12: SNR Comparison

6.4.2 Environment Containing Obstacles of Regular Geometry

In this section we look at the trajectory of the agent using SBCAM with MSACR updates for different r_{sen} where the environment consists of multiple obstacles (convex and non convex) of regular geometry. Fig. 6.13 shows the trajectory of agent using MSACR based SNR-map reconstruction with different r_{sen}. In this scenario we see that MSACR with $r_{sen} = 10$ cm improves on the CBT but its worse than the CAT. The trajectories improve with increasing r_{sen} and nearly converges to the CAT at $r_{sen} = 8$.

In Fig. 6.14 the reconstructed SNR-map corresponding to the trajectories in Fig. 6.13 are shown. It can be seen that a larger r_{sen} results in a better reconstruction of the SNR-map. Interestingly it can be seen that the agent avoids regions with low SNR by just reconstructing the boundary of the low SNR region and without reconstructing the complete SNR-map. Another interesting observation is the extension of the obstacle to accommodate the agent. This is to due to the fact that the size of the agent increases with r_{sen} and therefore, the obstacle gets extended to compensate for the size of the agent with increasing r_{sen}. However, at large r_{sen}, the extended obstacles cover nearly the complete workspace. This places large constraints on the motion of the agent as most of the workspace becomes inaccessible to the agent. Fig. 6.15 shows the SNR along the trajectory of the agent with different r_{sen}. It should be noted the there is not a large improvement in the mean-SNR between $r_{sen} = 40$ cm

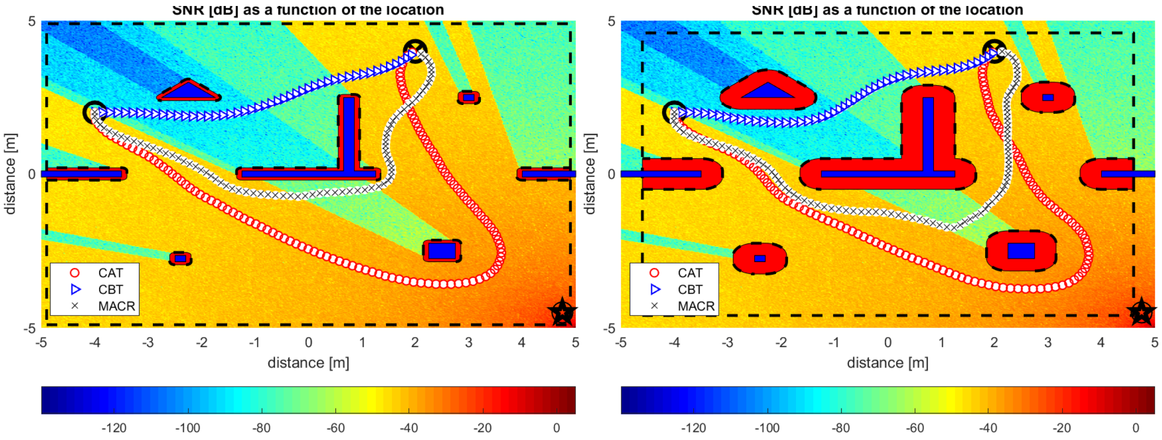

(a) $r_{sen} = 10$ cm **(b)** $r_{sen} = 40$ cm

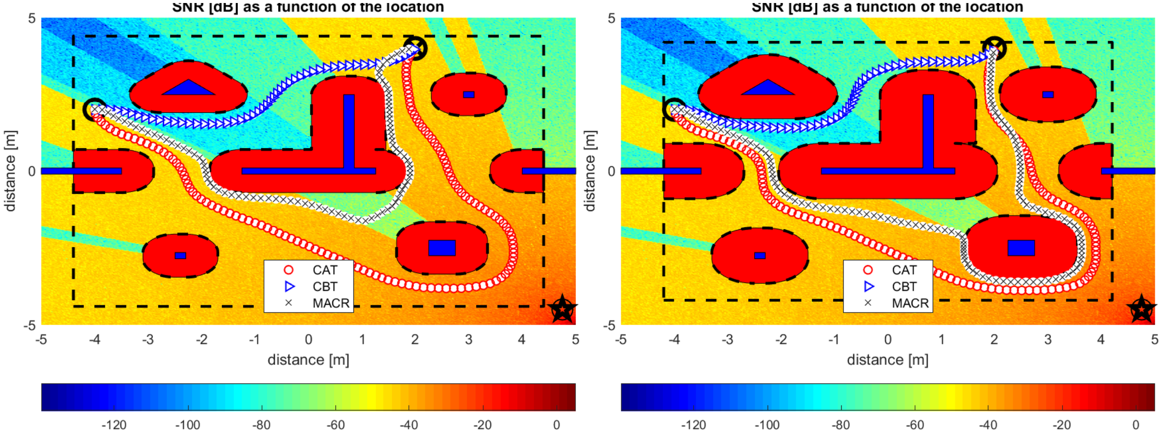

(c) $r_{sen} = 60$ cm **(d)** $r_{sen} = 80$ cm

Figure 6.13: Trajectory with MSACR update for different sensing regions

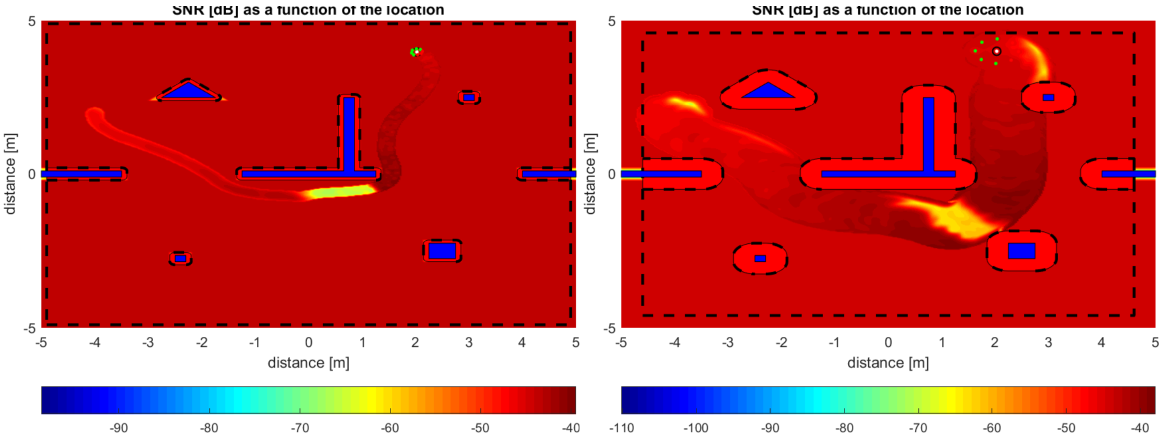

(a) $r_{sen} = 10$ cm **(b)** $r_{sen} = 40$ cm

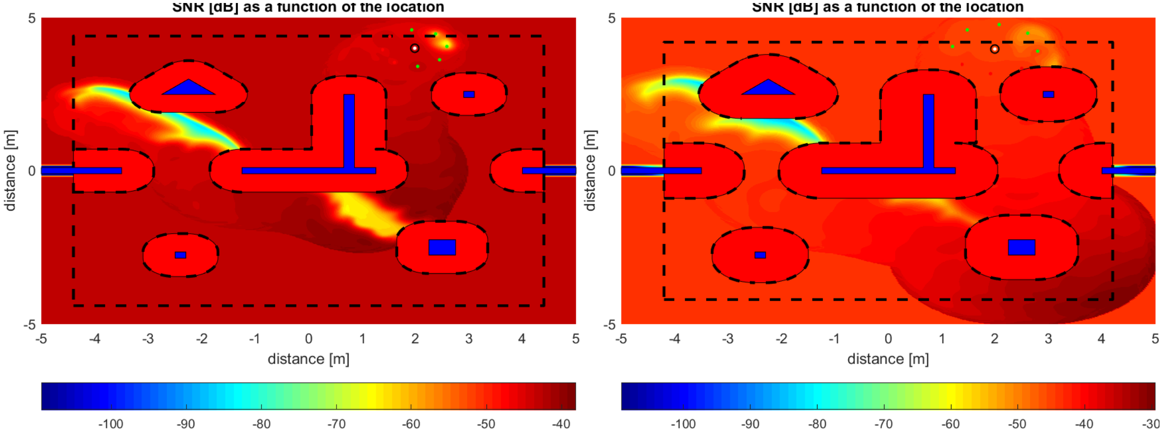

(c) $r_{sen} = 60$ cm **(d)** $r_{sen} = 80$ cm

Figure 6.14: SNR & HO maps

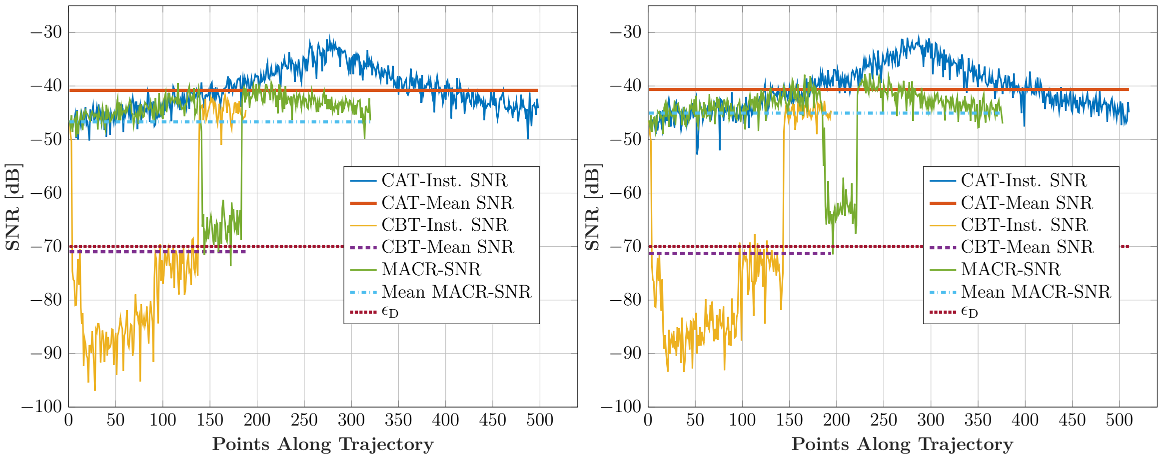

(a) $r_{sen} = 10$ cm **(b)** $r_{sen} = 40$ cm

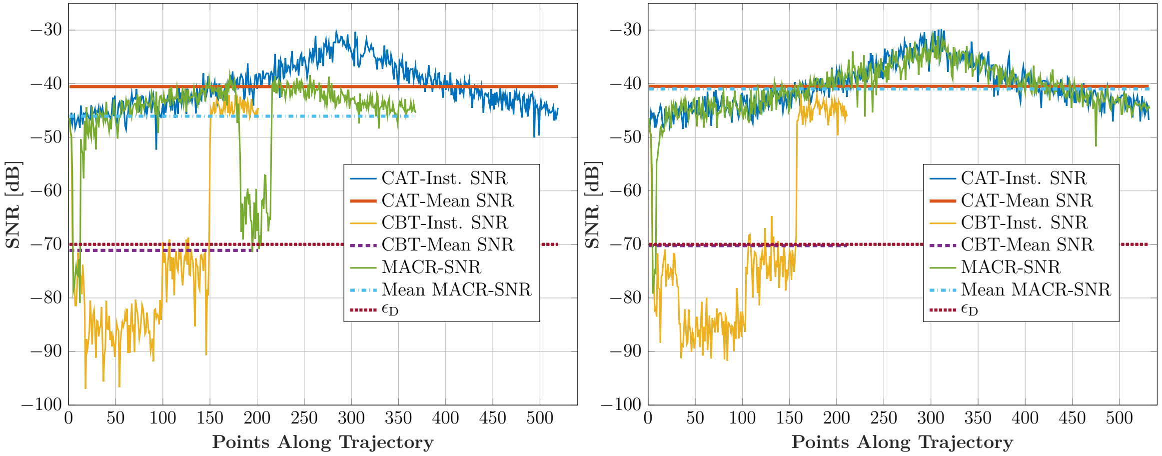

(c) $r_{sen} = 60$ cm **(d)** $r_{sen} = 80$ cm

Figure 6.15: SNR Comparison

and $r_{sen} = 60$ cm. However, the mean SNR for the MSACR reconstruction with $r_{sen} = 80$ cm nearly matches the CAT's performance.

6.4.3 Complex Environment With Obstacles of Irregular Geometry

In this section we look at the trajectory of the agent using SBCAM with MSACR updates for different r_{sen} in a complex environment with multiple obstacles (convex and non convex) of irregular geometry. This is a particularly chanllenging scenario as the start and goal positions of the agent lie in a low SNR region (possible DCZ). Fig. 6.16 shows the trajectory of an agent using MSACR based SNR-map reconstruction with different r_{sen}. In this scenario we see that MSACR is not able to improve on the CBT at all except at very high r_{sen}. At $r_{sen} = 80$ cm the SBCAM with MSACR SNR-Map reconstruction is able to approximately match the CAT. The reason that the trajectories could not be improved is the starting position being in a low SNR region. When the sensing region size increases, the agent is able to reconstruct the SNR-Map that consists of the upper region of high SNR. This information helps the agent choose the starting orientation close to the starting orientation of the CAT. However, this requires a large sensing radius. This can be seen in the reconstructed SNR-map (Fig. 6.17) corresponding to the trajectories in Fig. 6.16. It can be observed that sub-Fig. 6.17d corresponding to $r_{sen} = 80$ cm shows the most accurate SNR-Map reconstruction. The others could not reconstruct the upper region of high SNR. As in the previous environment, the extension of the obstacles leads to most of the environment becoming inaccessible to the agent. Fig. 6.18 shows the SNR along the trajectory of the agent with different r_{sen}. The agent shows poor mean-SNR performance which

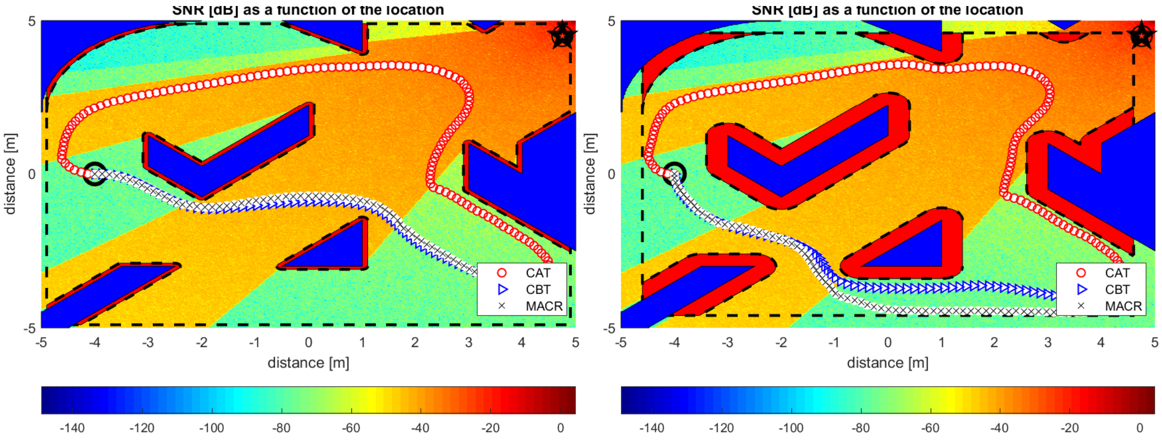

(a) $r_{sen} = 10$ cm **(b)** $r_{sen} = 40$ cm

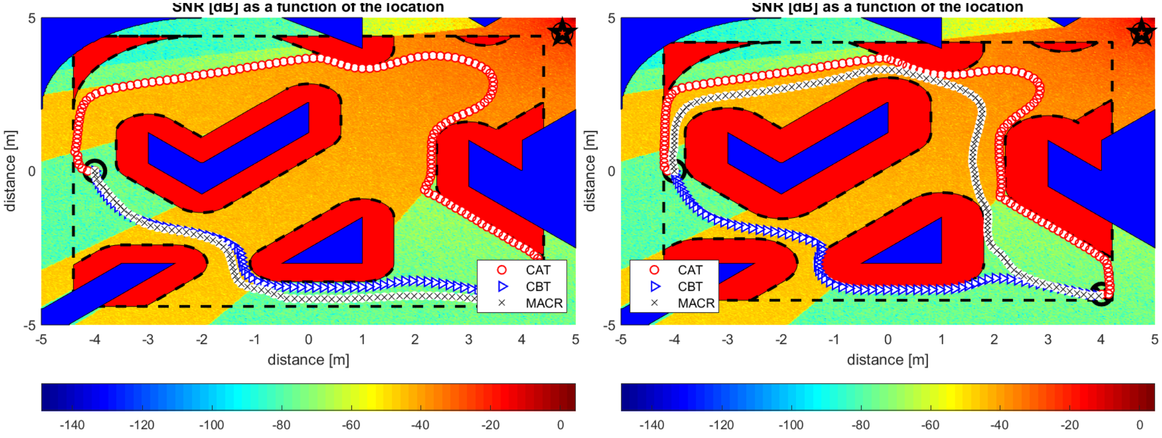

(c) $r_{sen} = 60$ cm **(d)** $r_{sen} = 80$ cm

Figure 6.16: Trajectory with MSACR update for different sensing regions

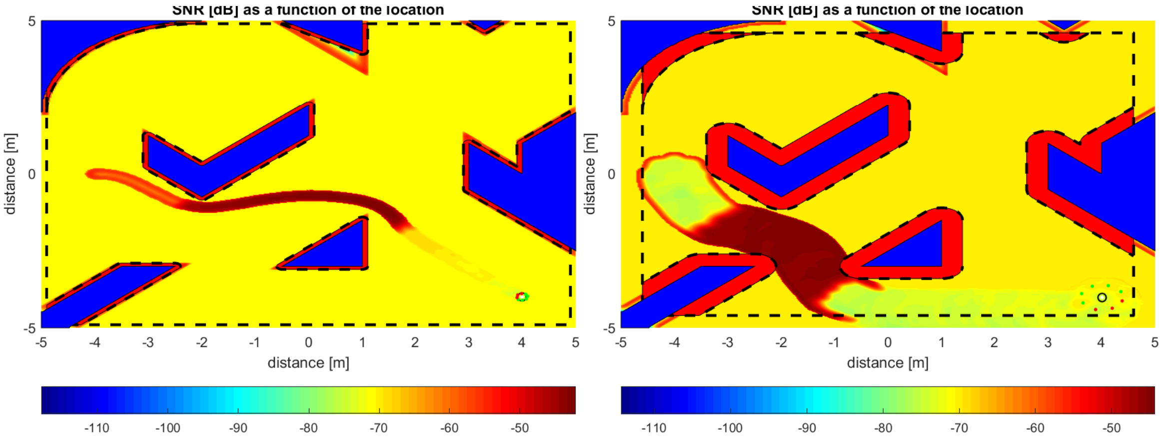

(a) $r_{sen} = 10$ cm **(b)** $r_{sen} = 40$ cm

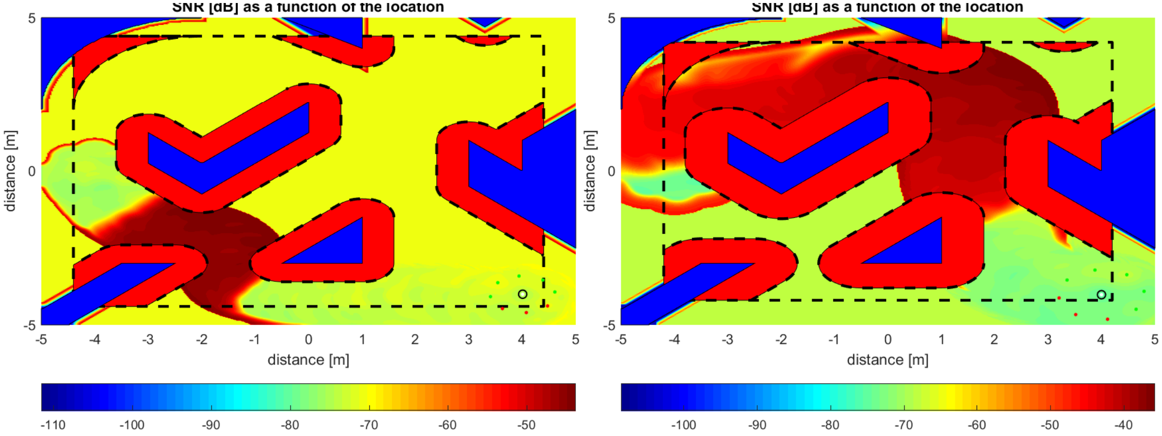

(c) $r_{sen} = 60$ cm **(d)** $r_{sen} = 80$ cm

Figure 6.17: SNR & HO maps

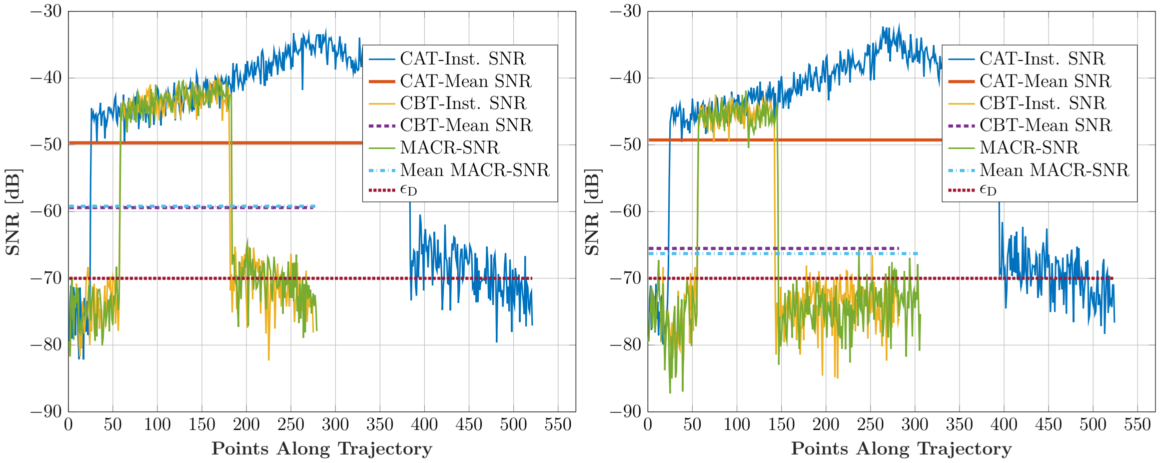

(a) $r_{sen} = 10$ cm **(b)** $r_{sen} = 40$ cm

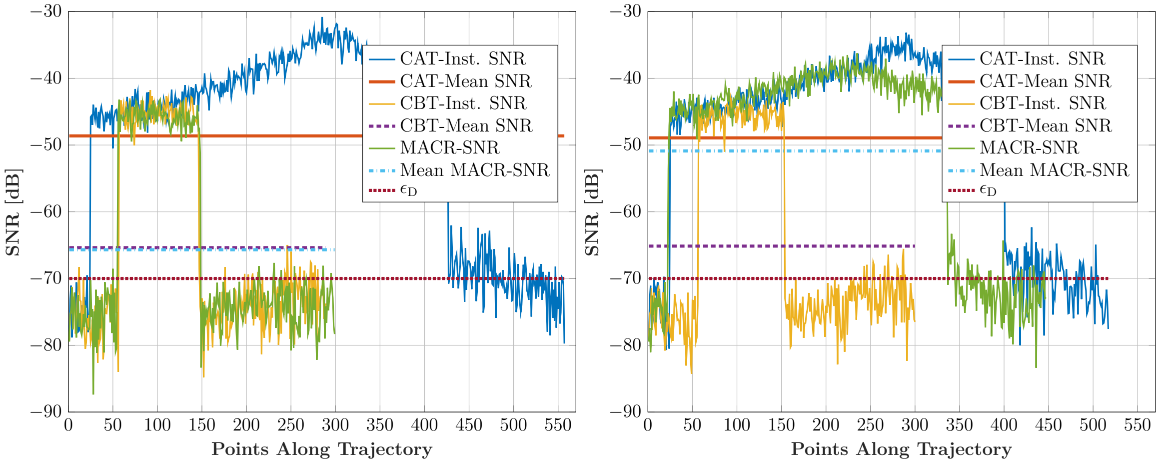

(c) $r_{sen} = 60$ cm **(d)** $r_{sen} = 80$ cm

Figure 6.18: SNR Comparison

is similar to the CBT performance (or worse in the case of $r_{sen} = 40$ cm. However, at $r_{sen} = 80$ cm it nearly matches the performance of the CAT.

6.5 Greedy Multiple-Sensor-Array Circular Region (GMSACR)

It was seen in the previous section that although the MSACR udpate was able to reconstruct an approximate SNR-map, it was not able to avoid possible DCZs for low r_{sen} values. Larger r_{sen} values on the other hand require a large (some times impractically large) agent size.

In this section, we propose a greedy version of the MSACR update. The greedy-MSACR SNR-map reconstruction is an 'optimistic' reconstruction where the agent assumes that it has high SNR at each position in the environment.Thus the default SNR update of Eq. (6.1) γ_S

$$\gamma_S = \gamma_m \tag{6.43}$$

Where γ_m is the maximum possible value of the SNR in the workspace.

If one of its antenna senses a DCZ (as defined in Def. 3.3), it reconstructs that region with a very low weight ϵ_{gr}, $0 < \epsilon_{gr} \lll 1$. It detects a DCZ by comparing the sensed SNR with the DCZ threshold ϵ_D (Def. 3.3). However, if the sensed SNR is above ϵ_D, it reconstructs that region by letting the sensed SNR at that antenna equal to γ_m. The UF weighting given in Eq. (6.3) is modified as follows

$$\gamma(\mathbf{p}) = \begin{cases} \sum_{i=1}^{N_{ant}} \gamma_{gi} \cdot f_i(\mathbf{p}) + \gamma_s \cdot \left(1 - \sum_{i=1}^{N_{ant}} f_i(\mathbf{p})\right), & \sum_{i=1}^{N_{ant}} f_i(\mathbf{p}) < 1 \\ \sum_{i=1}^{N_{ant}} \gamma_{gi} \cdot f_i(\mathbf{p}), & \sum_{i=1}^{N_{ant}} f_i(\mathbf{p}) = 1 \\ \sum_{i=1}^{N_{ant}} \gamma_{gi} \cdot \frac{f_i(\mathbf{p})}{\sum_{i=1}^{N_{ant}} f_i(\mathbf{p})}, & \sum_{i=1}^{N_{ant}} f_i(\mathbf{p}) > 1 \end{cases} \tag{6.44}$$

Where γ_g is given as follows,

$$\gamma_{gi} = \begin{cases} \epsilon_G, & \widehat{\gamma}_i < \epsilon_D \\ \gamma_m, & \text{otherwise} \end{cases} \tag{6.45}$$

6.5.1 Analysis

Using the equation Eq. (3.24),

$$\nabla^2 \phi = -\frac{1}{\gamma}((-\nabla\gamma) \cdot (-\nabla\phi)) \tag{6.46}$$

if the agent approaches a DCZ, the reconstructed DCZ will have a very low value. Therefore, the SNR gradient, $-\nabla\gamma$ will have a very large value at the boundary of the DCZ. This is due to that fact that the UFs are weighted with a very low value in the DCZ and a very high value outside it. The dot product on the Right Hand Side (RHS) will have a vary large negative value resulting a strong repulsive region. Thus even a small reconstructed DCZ region will force motion away from the DCZ.

Although a large SNR gradient at the boundary of the DCZ would force the motion of the agent away from the DCZ, however, this could lead to the divergence of the SBCAM as shown in the following proposition.

PROPOSITION 6.3 *The greedy SNR-map reconstuction using Eq.* (6.44) *could lead the SBCAM to diverge.*

Proof. The proof follows from Prop. 4.1 and **??**. A large change in the SNR at a position in the workspace could lead to a large value of $\frac{\partial \gamma}{\partial t}$ and consequently a large value of $\frac{\partial \phi}{\partial t}$. This could lead to the violation of the bound in Eq. (4.20) and therefore lead to the SBCAM diverging. ▮

6.5.2 GMSACR Results

Here we apply the GMSACR to the same environments as in section 6.4 using the same range of r_{sen} (10 cm to 80 cm) and $N_{sen} = 8$.

Single Obstacle

Fig. 6.19 shows the trajectory of an agent with four different radii for the the sensing region. As compared to the MSACR reconstruction, the GMSACR reconstruction improves the performance of the agent. It can be seen that with $r_{sen} = 60$ cm the agent nearly converges to the CAT. In Fig. 6.20 the reconstructed SNR-map corresponding to the trajectories in Fig. 6.19. As compared to the MSACR it can be seen that he GMSACR reconstruction reconstructs the SNR regions below the threshold $\epsilon_D = -47dB$ as a DCZ and assigns it a very low value and the rest of the region is assigned

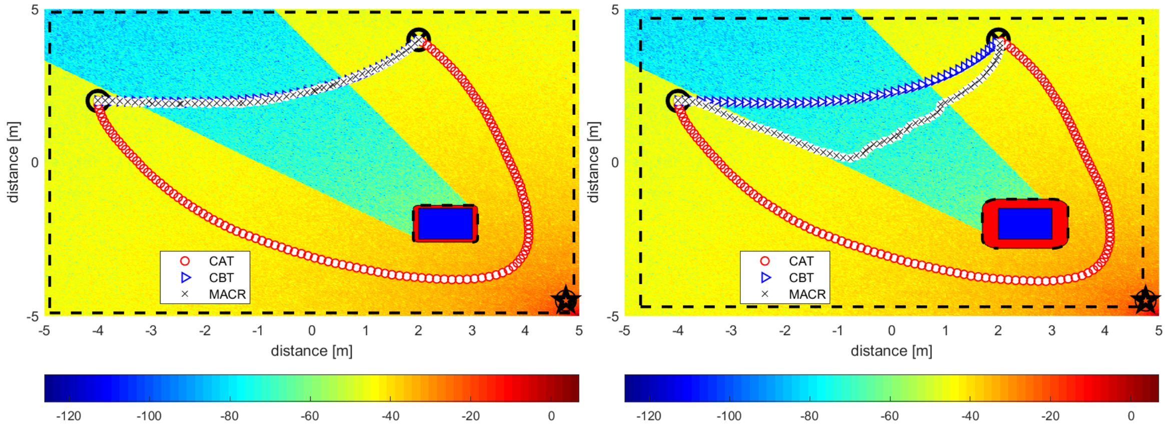

(a) $r_{sen} = 10$ cm **(b)** $r_{sen} = 30$ cm

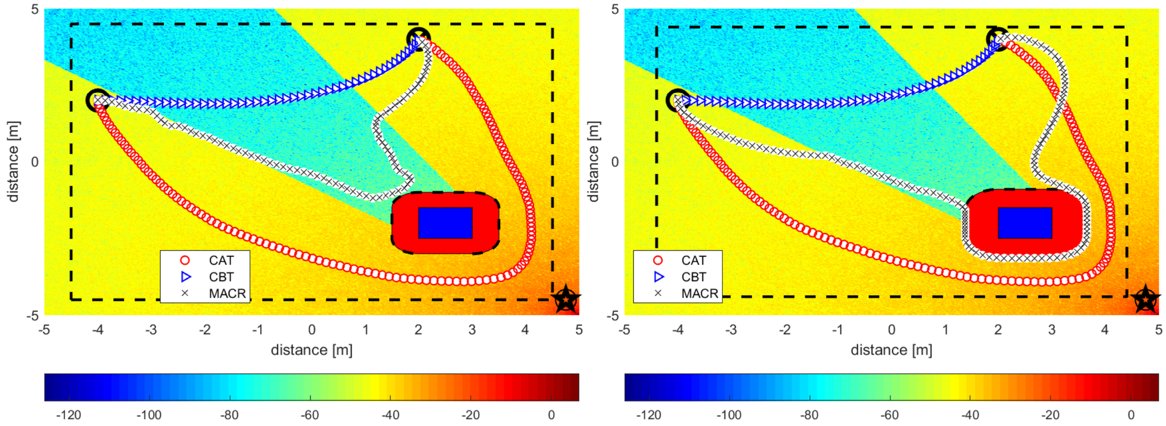

(c) $r_{sen} = 50$ cm **(d)** $r_{sen} = 60$ cm

Figure 6.19: Trajectory with GMSACR update for different sensing regions

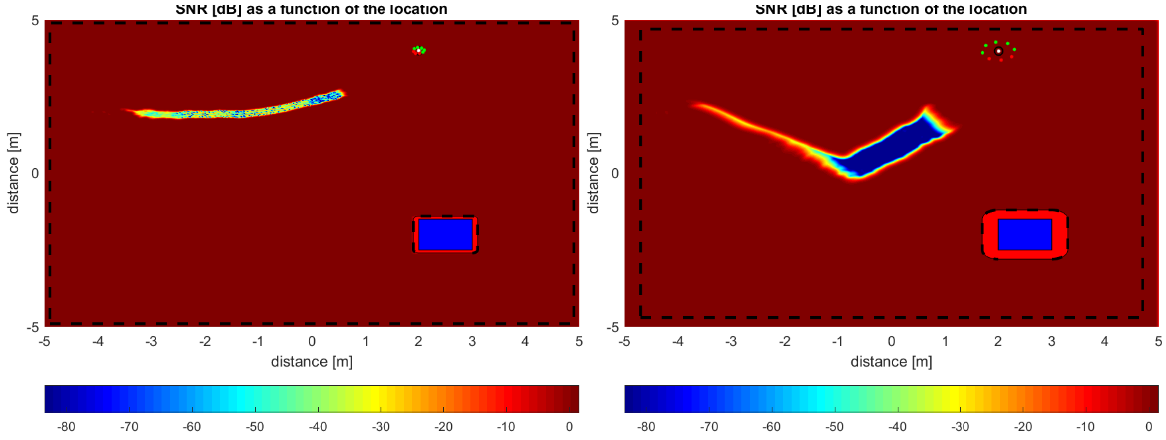

(a) $r_{sen} = 10$ cm **(b)** $r_{sen} = 30$ cm

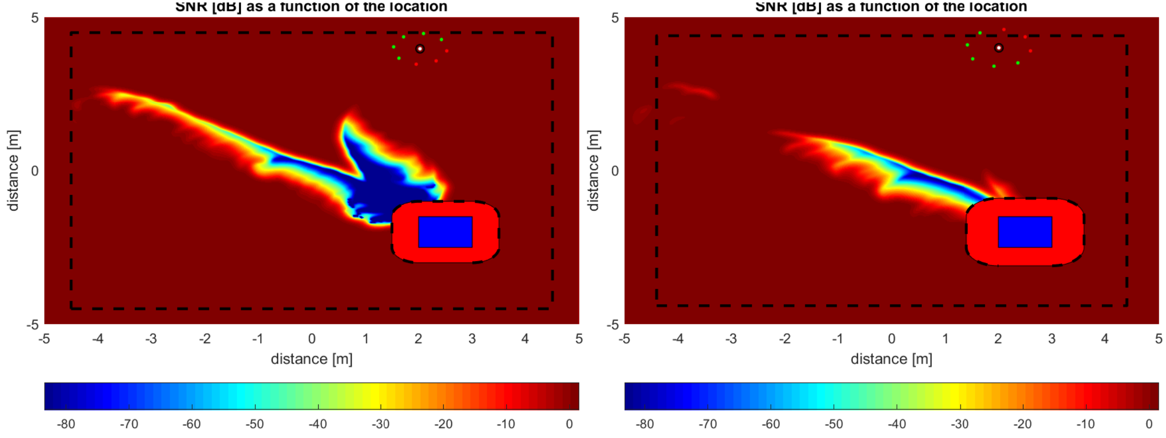

(c) $r_{sen} = 50$ cm **(d)** $r_{sen} = 60$ cm

Figure 6.20: SNR & HO maps

a very high value. Also, it can be seen again in sub-Fig. 6.20d that only the edge of the low SNR region is reconstructed. Therefore, the agent doesn't need to know the complete low SNR region to avoid it. Fig. 6.21 shows the SNR along the trajectory of the agent with different r_{sen}. It can be seen that the SNR improves with increasing r_{sen}. It nearly converges to the CAT performance at $r_{sen} = 60$ cm. Its performance starts to converge to the performance of the CAT as r_{sen} is increased further.

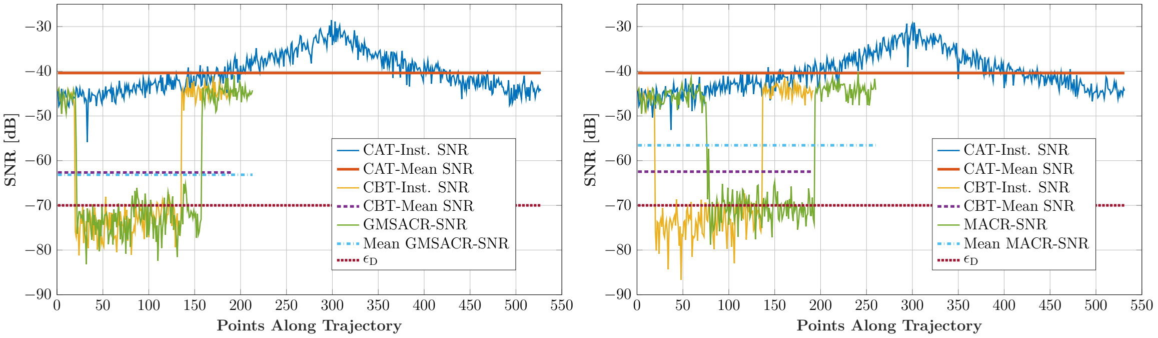

(a) $r_{sen} = 10$ cm **(b)** $r_{sen} = 30$ cm

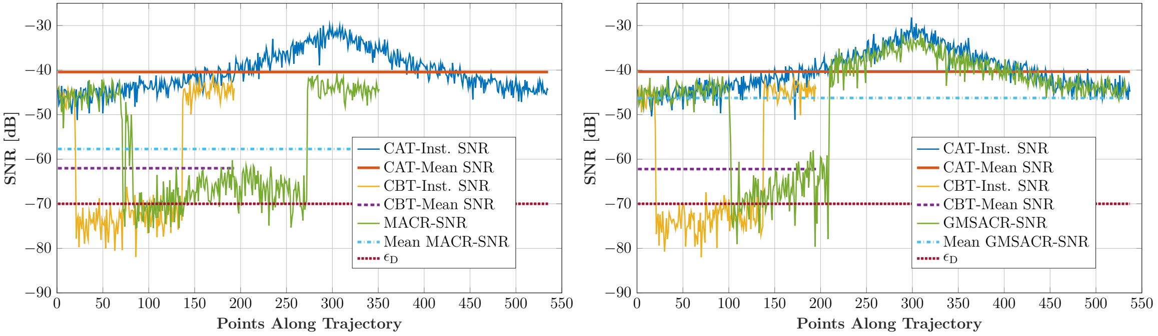

(c) $r_{sen} = 50$ cm **(d)** $r_{sen} = 60$ cm

Figure 6.21: SNR Comparison

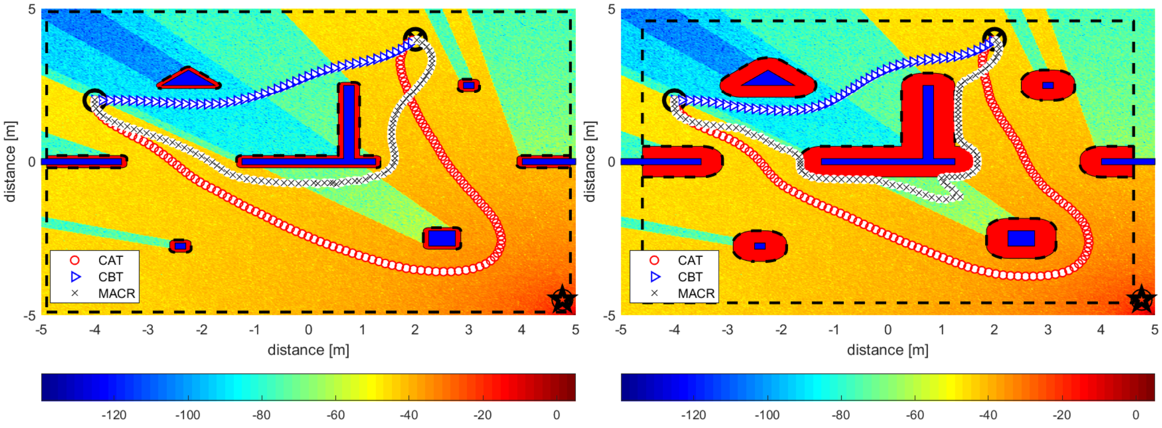

(a) $r_{sen} = 10$ cm **(b)** $r_{sen} = 40$ cm

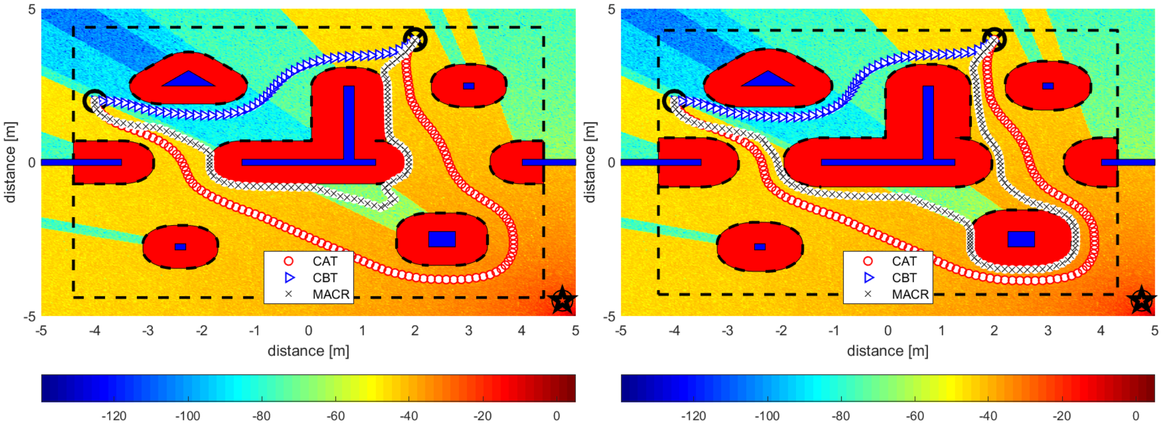

(c) $r_{sen} = 60$ cm **(d)** $r_{sen} = 70$ cm

Figure 6.22: Trajectory with GMSACR update for different sensing regions

Environment Containing Obstacles of Regular Geometry

In this section we look at the trajectory of the agent using SBCAM with GMSACR updates for different r_{sen} where the environment consists of multiple obstacles (convex and non convex) of regular geometry. Fig. 6.22 shows the trajectory of agent using GMSACR based SNR-map reconstruction with different r_{sen}. We can see that the trajectory of the GMSACR approximately converges to the CAT at smaller sensing radius than the MSACR reconstruction as shown in Figs. 6.22 to 6.24 Fig. 6.24

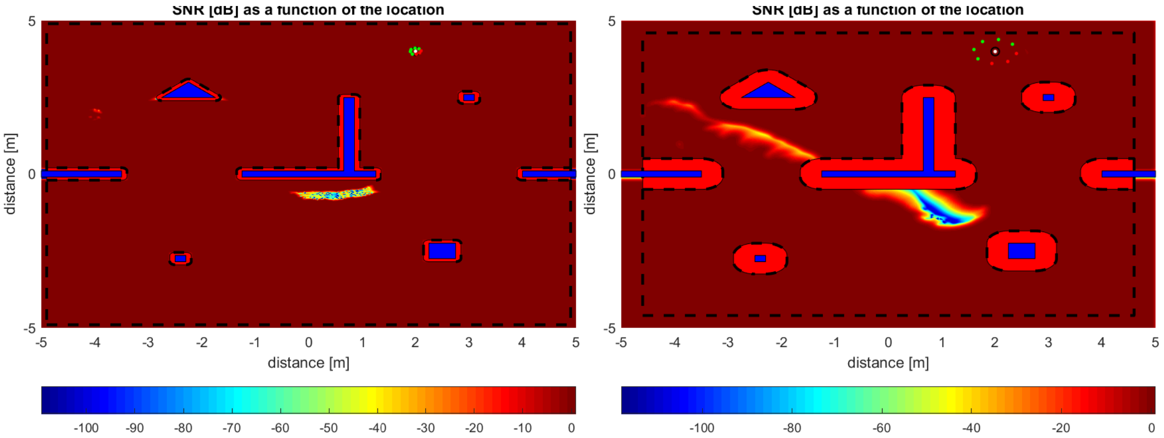

(a) $r_{sen} = 10$ cm **(b)** $r_{sen} = 40$ cm

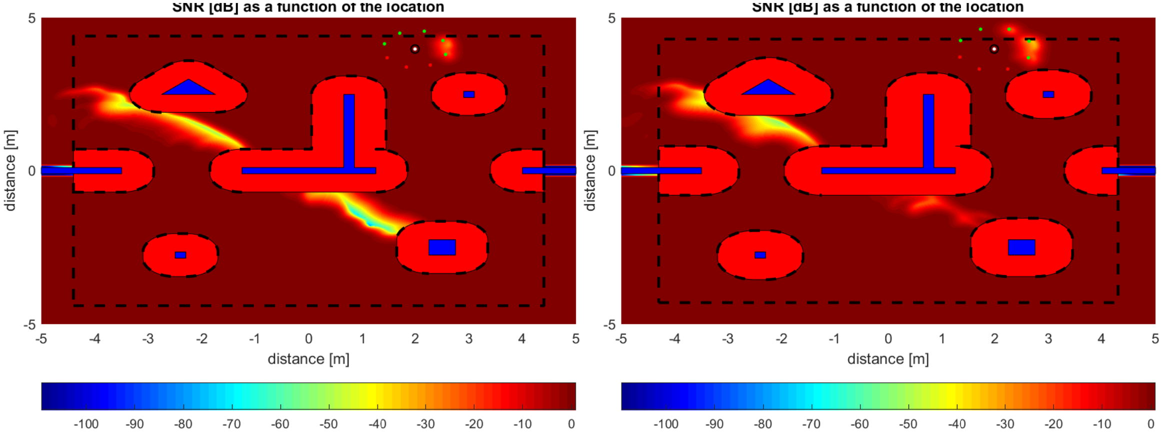

(c) $r_{sen} = 60$ cm **(d)** $r_{sen} = 70$ cm

Figure 6.23: SNR & HO maps

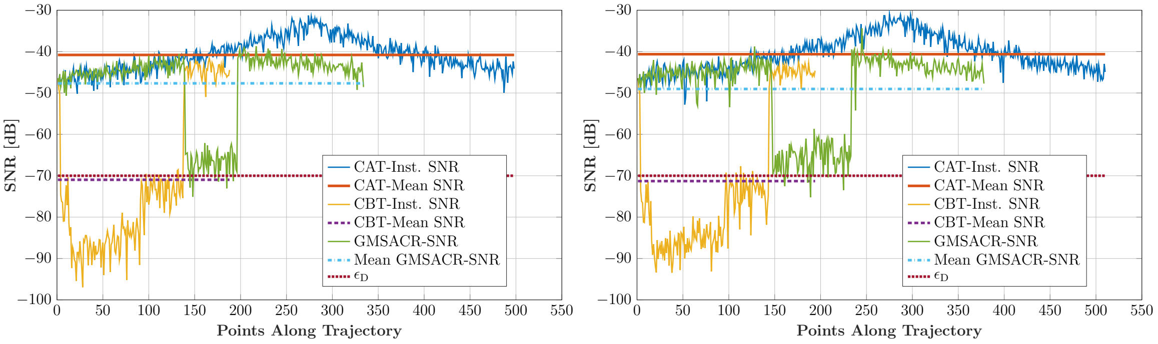

(a) $r_{sen} = 10$ cm

(b) $r_{sen} = 40$ cm

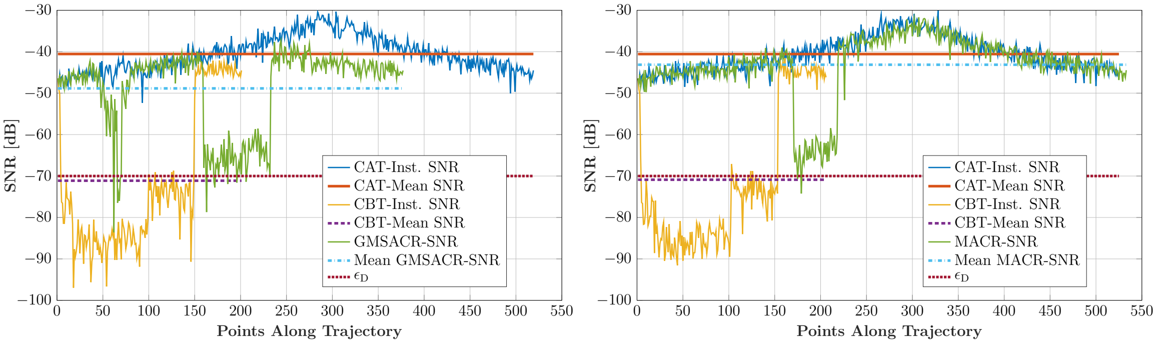

(c) $r_{sen} = 60$ cm

(d) $r_{sen} = 70$ cm

Figure 6.24: SNR Comparison

shows the SNR along the trajectory of the agent with different r_{sen}. It should be noted the there is not a large improvement in the mean-SNR between $r_{sen} = 40$ cm and $r_{sen} = 60$ cm. However, the mean SNR for the GMSACR reconstruction with $r_{sen} = 80$ cm nearly matches the CAT's performance.

Complex Environment With Obstacles of Irregular Geometry

In this section we look at the trajectory of the agent using SBCAM with GMSACR updates for different r_{sen} in a complex environment with multiple obstacles (convex and non convex) of irregular geometry. As mentioned earlier this is a particularly challenging scenario as the start and goal positions of the agent lie in a low SNR region (possible DCZ). Figs. 6.25 to 6.27 show the trajectory of an agent using GMSACR based SNR-map reconstruction with different r_{sen}, their corresponding reconstructed SNR-Maps and SNR along the trajectories. Similar to before the performance approximately converges to the CAT at sensing region radius of 80 cm. This is due the fact the at lesser radii the sensing antenna at the start position cannot detect the high SNR region in the upper half of the environment. The agent chooses the wrong starting orientation and consequently the trajectory. Another thing that can be noted is the divergent behavior of the trajectory in Figs. 6.25b and 6.25c. This is due to the large difference the GMSACR reconstruction assigns to regions with SNR below ϵ_D as dicussed in section 6.5.1

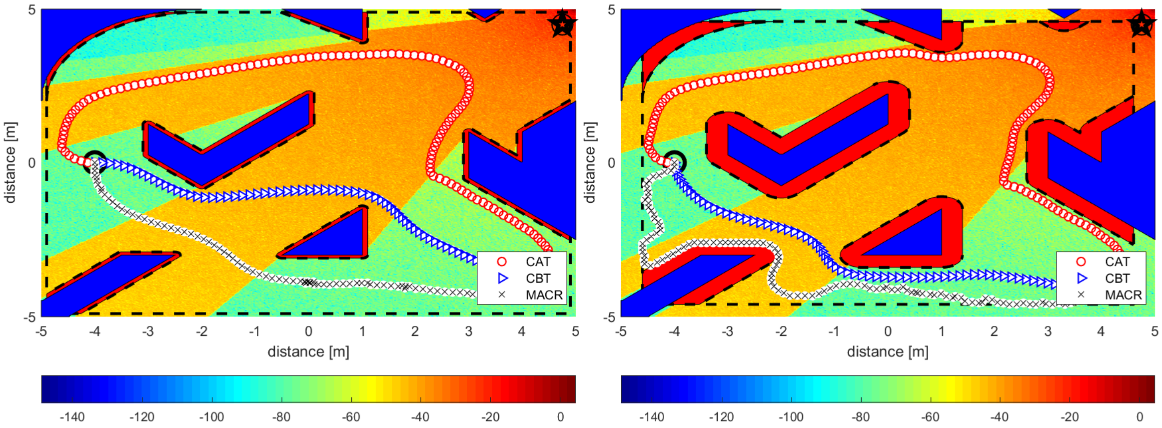

(a) $r_{sen} = 10$ cm **(b)** $r_{sen} = 40$ cm

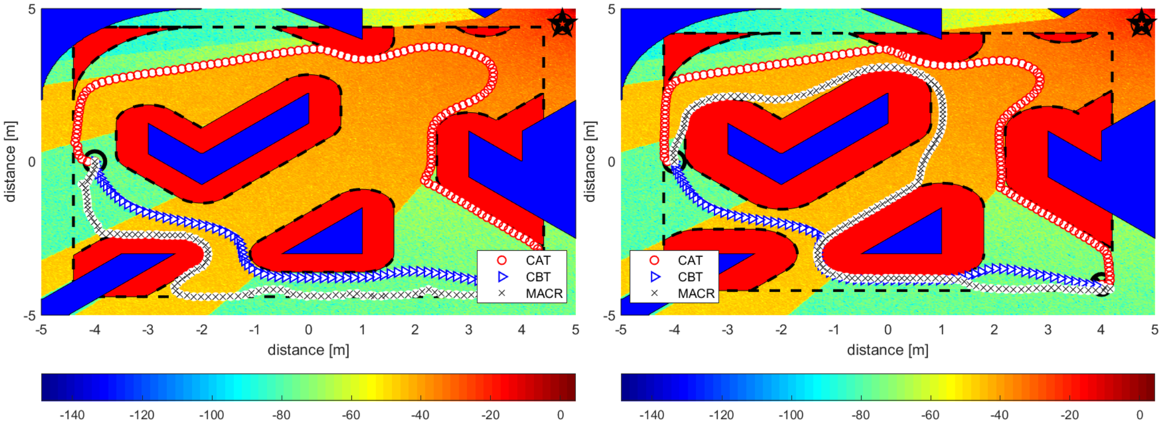

(c) $r_{sen} = 60$ cm **(d)** $r_{sen} = 80$ cm

Figure 6.25: Trajectory with GMSACR update for different sensing regions

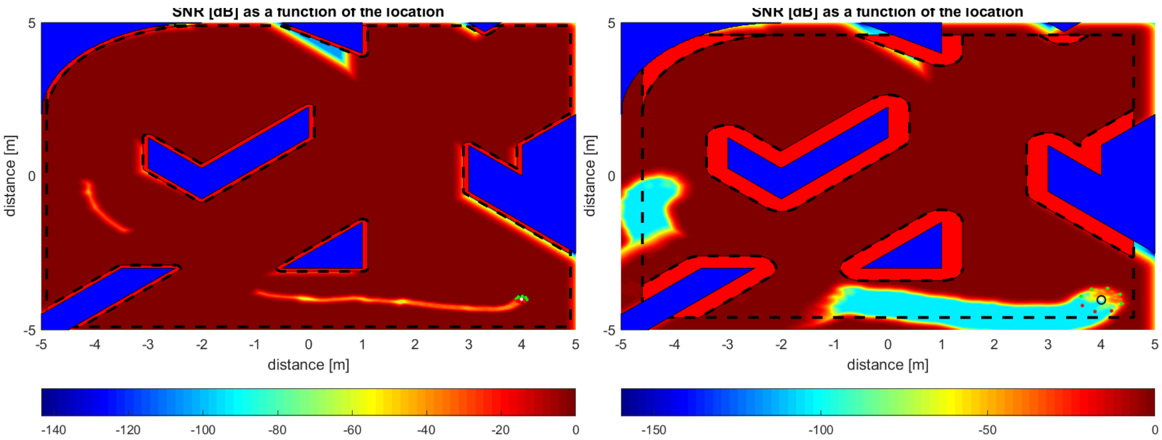

(a) $r_{sen} = 10$ cm **(b)** $r_{sen} = 40$ cm

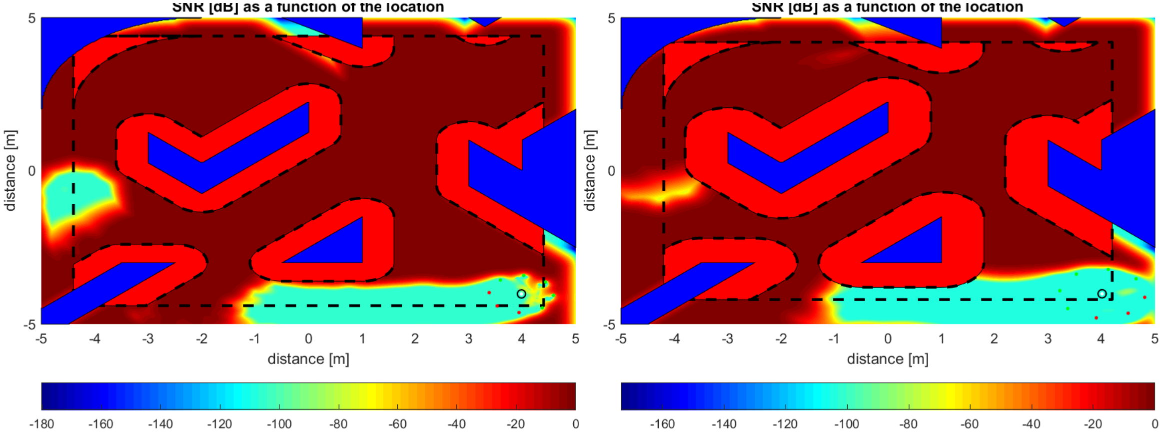

(c) $r_{sen} = 60$ cm **(d)** $r_{sen} = 80$ cm

Figure 6.26: SNR & HO maps

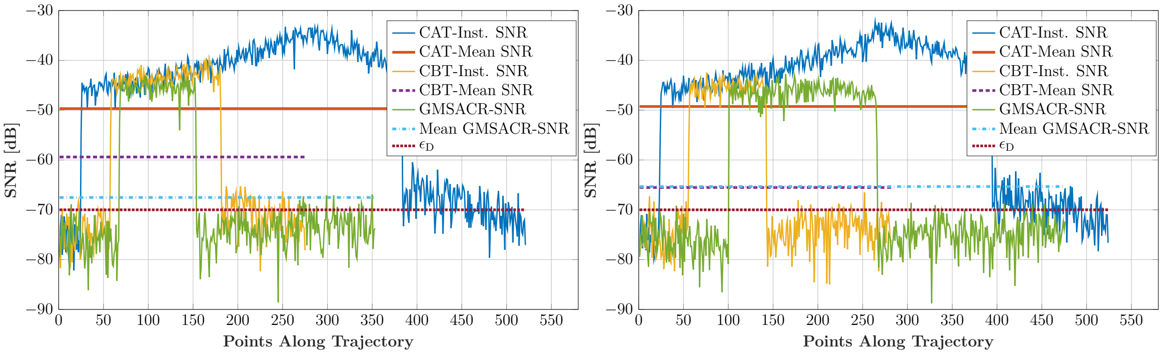

(a) $r_{sen} = 10$ cm

(b) $r_{sen} = 40$ cm

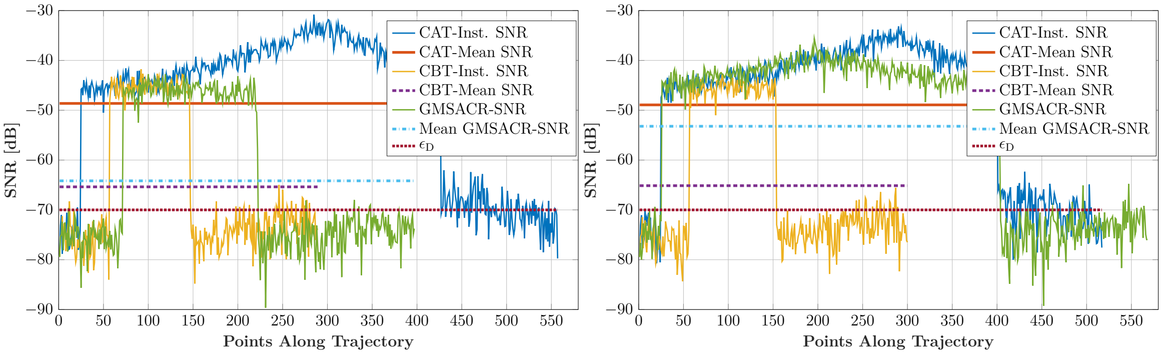

(c) $r_{sen} = 60$ cm

(d) $r_{sen} = 80$ cm

Figure 6.27: SNR Comparison

6.5.3 Conclusions

We presented a SNR-Map reconstruction technique using multiple sensors placed on a circle around the agent. The SBCAM trajectory obtained using MSACR reconstruction resulted in improvement in the performance at large sensing radii. The greedy SNR-map reconstruction resulted in better performance at smaller sensing radii. It was seen that when the starting position was in a low SNR region, the performance only improved only if the sensing radii was large as the agent needed high SNR knowledge to choose the correct starting orientation.

CHAPTER 7

PREDICTION-BASED SNR-MAP RECONSTRUCTION (PBSMR)

"And that there is not for man except that [good] for which he strives"

—The Glorious Qur'ān, an-Najm (The Star) 53:39.

We have seen that Multiple-Sensor-Array Circular Region (MSACR) gave a much better performance than Single Sample Greedy (SSG). However, MSACR required a large r_{sen} to match the performance of the Model-Based Communication-Aware Navigation (MBCAN) trajectory for all scenarios. The greedy-MSACR version was able to improve on MSACR but it could make the Sensor-Based Communication-Aware Navigation (SBCAM) diverge. It was shown in section 4.3 that increasing the area of the reconstructed Signal to Noise Ratio (SNR)-map region led to the performance of the SBCAM converging to the performance of the MBCAN. However, large radii of the circle of the sensing antennas leads to agent having an impractically large size for confined spaces. Therefore, it is desired to have a sufficiently large region of the reconstructed SNR-map while keeping r_{sen} to a minimum.

In this section, we propose a SNR-map reconstruction mechanism that uses prediction based reconstruction of the SNR-map. The proposed mechanism makes use of the MSACR update and then uses the Laplacian of Gaussian (LoG) edge detection filter [97] to detect the Dead Communication Zones (DCZ). Once a DCZ is detected, Prediction-Based SNR-Map Reconstruction (PBSMR) updates a region in the direction of the detected DCZ outside of the sensing antenna circle.

The LoG filter along with the Gradient of Gaussian (GoG) filter is known to robustly detect edges in images [98]. In an image, an edge is a sharp change in the pixel values of the image. Similarly, a DCZ occurs when the SNR value dips in any region of the workspace.

The LoG filter for a 2-D filter is given as follows [97]

$$LG(x,y) = 4\frac{x^2+y^2-c^2}{c^4}e^{-\left(\frac{x^2+y^2}{c^2}\right)} \tag{7.1}$$

where c governs the width of the Gaussian function.

The LoG filter has the following properties

- It is zero far away from an edge (step change in magnitude)
- It is positive after decline in magnitude.
- It is negative before decline in magnitude.
- It is zero at some point in between on the edge itself.

The GoG filter for a 2-D is given as follows

$$\nabla G = -\frac{2}{c^2}\begin{bmatrix} x \\ \\ y \end{bmatrix} e^{-\left(\dfrac{x^2+y^2}{c^2}\right)} \tag{7.2}$$

The GoG filter gives a non-zero value at an edge and is zero otherwise.

Assuming the SNR map given in Fig. 7.1a, when the LoG filter is applied to it, it detects the DCZ boundaries which can be seen in Fig. 7.1b. Fig. 7.1c shows the SNR horizontally across the SNR map. It can be seen that when the SNR declines the log filters gives a negative value before the decline and a positive value after the decline. The middle figure shows the magnitude $\|\nabla G\|$ of the GoG filter. It can be noted that GoG filter gives peaks at points where the SNR declines or increases.

By detecting the transition of the LoG from negative to positive along with comparing the peaks of the GoG to a threshold, we can detect the presence of a DCZ. The transitions of the LoG can be detected by using a *sgn* function.

$$sgn(LG) = \begin{cases} 1, & LG > 0 \\ 0, & LG = 0 \\ -1, & LG < 0 \end{cases} \tag{7.3}$$

We employ the LoG and GoG filter with the MSACR update. After the local reconstruction of the SNR-map, LoG and GoG fitlers are applied to detect DCZs. Once a DCZ is detected, then a prediction region in the direction of the detected DCZ is updated as a DCZ.

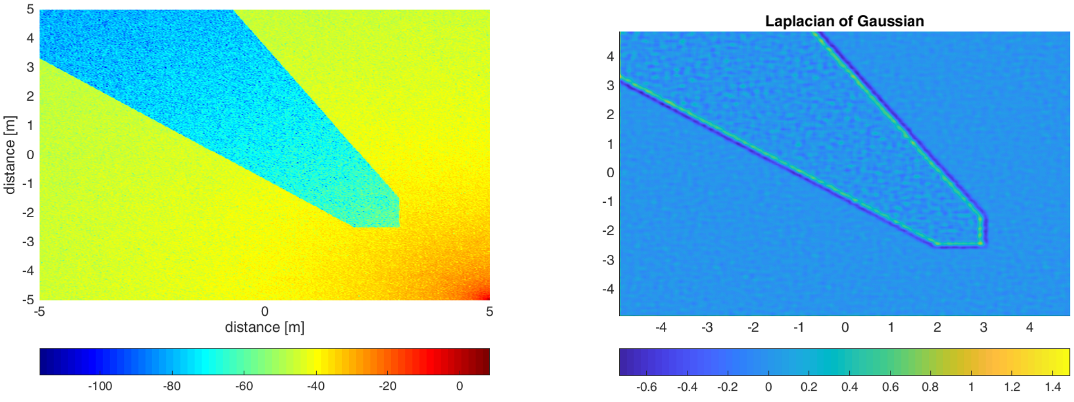

(a) SNR Map **(b)** LoG filtering

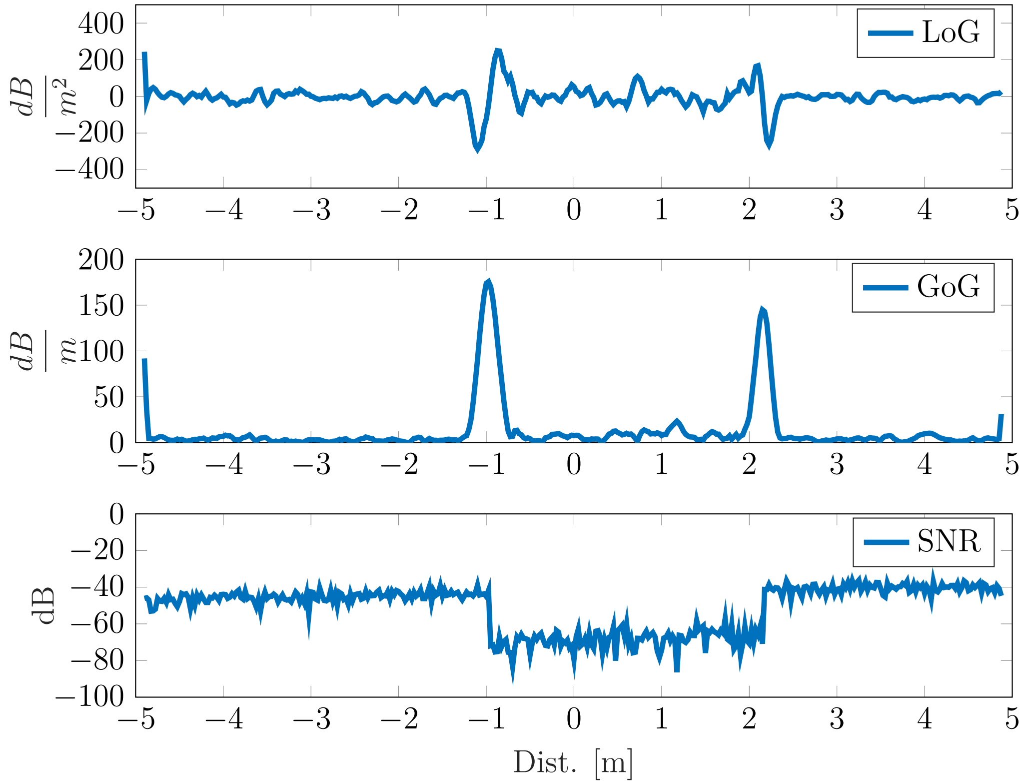

(c) 1D cross section of the SNR map

Figure 7.1: DCZ detection using LoG & GoG filters

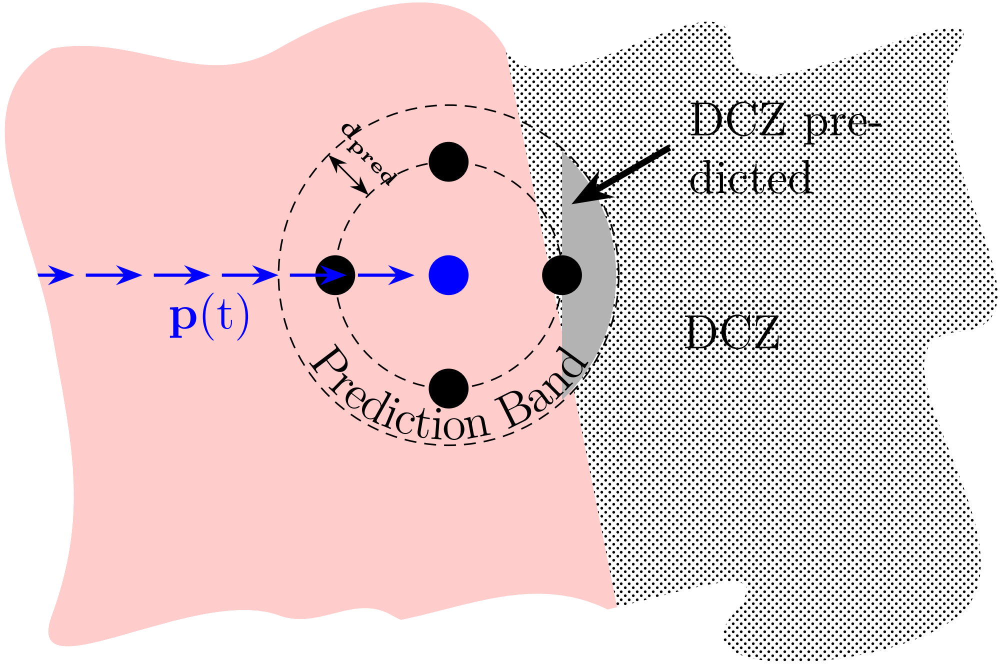

Figure 7.2: DCZ prediction using LoG & GoG

7.1 Prediction

For the prediction we assume a circular band of width d_{pred} surrounding the agent. If a DCZ is detected, the prediction band in front of that antenna is updated as a DCZ. The prediction region is assigned the same SNR that was sensed at the antenna that detected the DCZ. This is demonstrated in Fig. 7.2. The PBSMR algorithm is given in algorithm 4

Algorithm 4 PBSMR Algorithm

```
Update SNR-Map using MSACR.
Apply LoG filter to SNR-Map.
Apply GoG filter to SNR-Map.
if Negative to Positive Transition in LoG Detected then
    if Magnitude of GoG is above threshold $\epsilon_{gog}$ then
        Update prediction region in the direction of detected DCZ.
    end if
end if
```

7.2 Sensor-Based Obstacle Map Reconstruction (SBOMR)

In this dissertation it has been assumed so far that the agent completely knows the Hard Obstacle or Hazardous Region (HO)-map in the environment. The planner can then accommodate for the obstacle and agent size while navigating towards the goal. In this section, we consider the more realistic scenario where the the Hard Obstacle or Hazardous Region (HO) are unknown to the agent. The agent has to detect the obstacles in real-time and incorporate the detected HO in its path-plan to successfully navigate the obstacle.

This is a challenging task as the HO has to be detected before the agent could crash in to it. Typically, agents are equipped with range sensors, like ultrasonic sensors, radars, sonars or lidars, to detect the HO. The range sensors can detect obstacles with their maximum range. They detect HO by transmitting energy in the form of sound, light or electromagnetic energy and detect reflections from the HO.

We assume that the agent is equipped with a range sensor with a maximum range of d_r. As soon the sensor detects an obstacle it updates the obstacle map $\mathcal{O}$ which is initially empty. Since the sensors obtain the range to the sensor, the HO is updated as a point at the range detected using the sensor. The agent then updates the HO map by updating the point as a circle with radius equal to d_{max}. This is shown in Fig. 7.3 The agent incorporates the detected position in the path-planner by adding the detected point on the obstacle to $\mathcal{O}$ in Eq. (4.2). The detected position is added

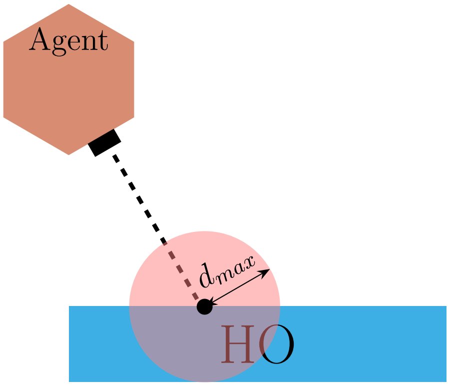

Figure 7.3: Obstacle detected using range sensor

as circle with radius d_{max} to the HO map as follows

$$\mathcal{O} = \mathcal{O} \bigcup \{\mathbf{p} | \, \|\mathbf{p} - \mathbf{p}_{sen}\| \leq d_{max}\} \tag{7.4}$$

The agent is able to reconstruct obstacles of any size and geometry by adding circular extensions of the points detected on the HO. The HO-map update is then used by the SBCAM to compute the updated path plan.

7.2.1 Results

In this section, we will present the simulation results for PBSMR with Sensor-Based Obstacle Map Reconstruction (SBOMR). The agent uses PBSMR and SBOMR jointly to update both the SNR-map and HO-map simultaneously. The agent initially has no knowledge of the SNR- and HO-map. The prediction band width d_{pred} is taked as 50 cm and the threshold for the GoG filter to detect a dip in the SNR ϵ_{gog} is taken to be $-6dB$. The range d_r of range sensors is taken as $1m$.

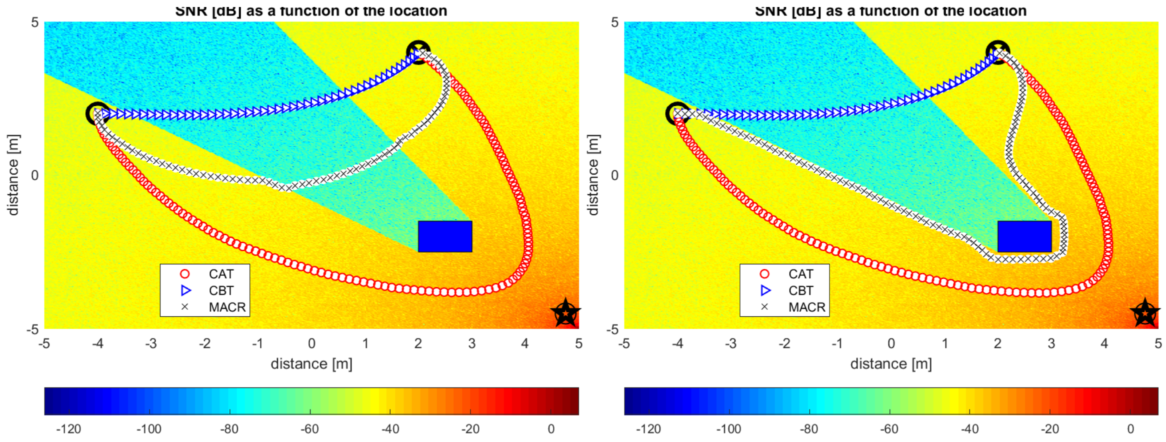

(a) $r_{sen} = 10$ cm **(b)** $r_{sen} = 20$ cm

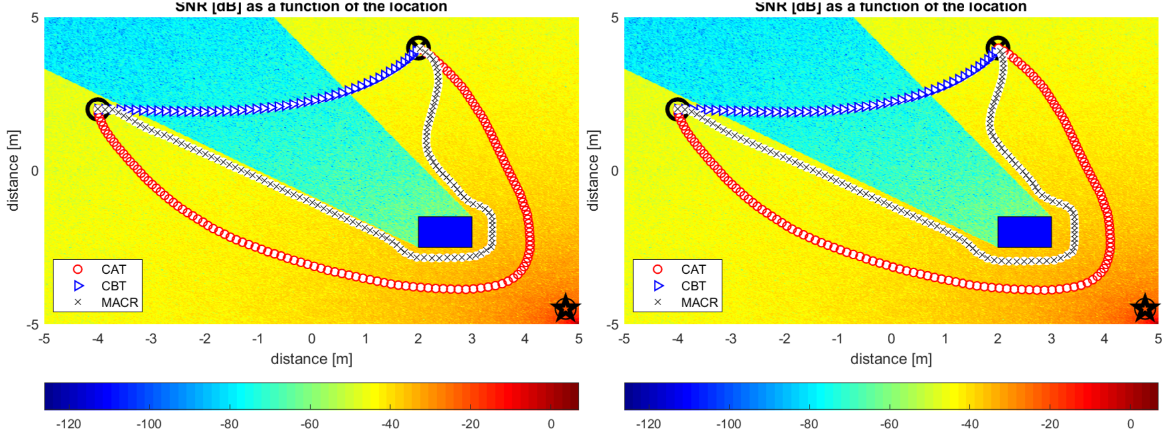

(c) $r_{sen} = 30$ cm **(d)** $r_{sen} = 40$ cm

Figure 7.4: Trajectory with PBSMR update for different sensing regions

Environment With Single Obstacle

Fig. 7.4 shows the trajectory of an agent with four different radii for the sensing region. It can be seen that the agent's trajectory approximately converges to the Communication-Aware Trajectory (CAT) at very low sensing radii. The improvement is very large as compared to MSACR reconstruction. For the same environment, the SBCAM with MSACR reconstruction could not converge to the CAT even at $r_{sen} = 80$ cm, however with PBSMR reconstruction, the SBCAM is able to converge to the CAT at $r_{sen} = 20$ cm.

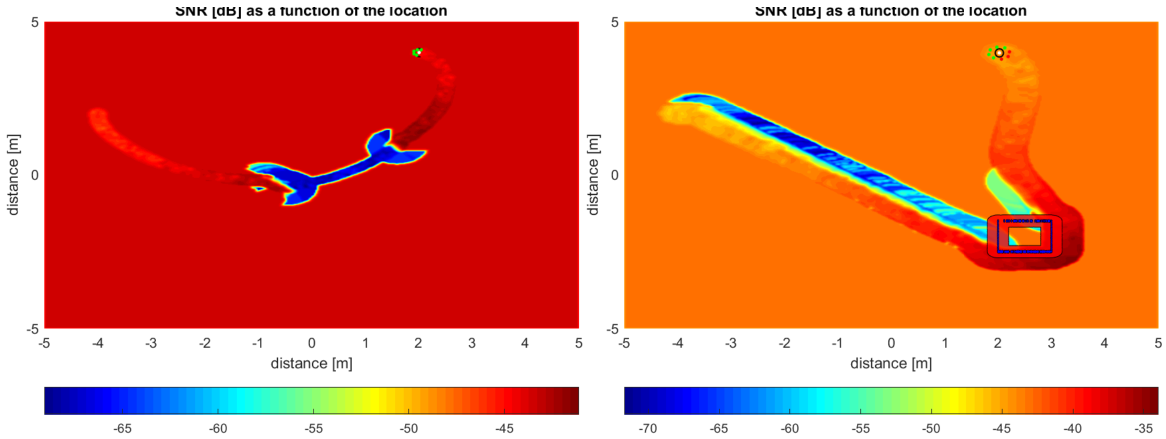

(a) $r_{sen} = 10$ cm **(b)** $r_{sen} = 20$ cm

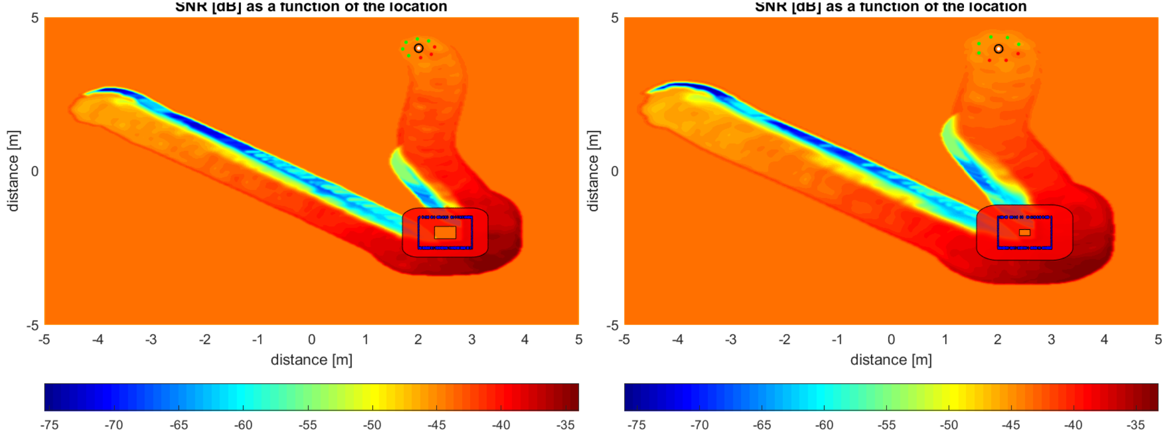

(c) $r_{sen} = 30$ cm **(d)** $r_{sen} = 40$ cm

Figure 7.5: SNR & HO maps

In Fig. 7.5 the reconstructed SNR-map corresponding to the trajectories in Fig. 7.4. As before, it can be seen that the agent needs to reconstruct only the boundary of the low SNR region to avoid it. Also, the HO-map reconstruction using SBOMR can be observed in Fig. 7.4. The agent is able to reconstruct the complete obstacle by combining the circular representation of the points detected on the obstacle. Fig. 7.6 shows the SNR along the trajectory of the agent with different r_{sen}. Since, the SBCAM with PBSMR converges to the CAT at very low r_{sen}, the SNR performance of the trajectories is nearly the same to that of the CAT except at $r_{sen} = 10$ cm.

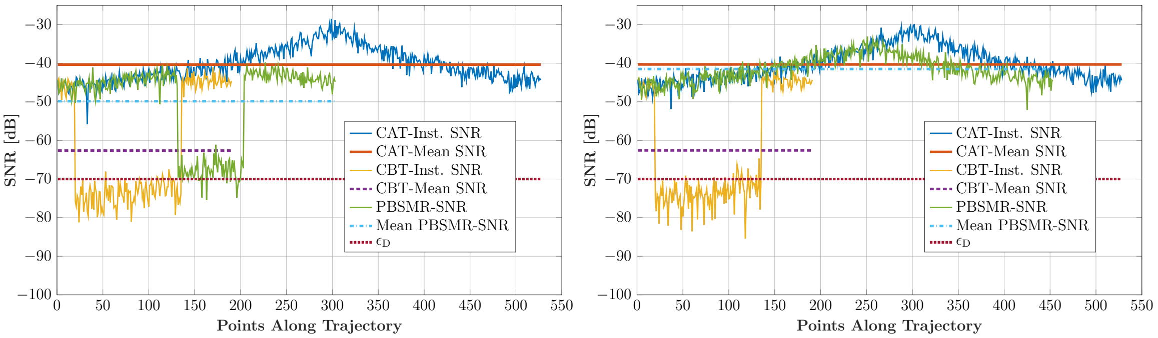

(a) $r_{sen} = 10$ cm **(b)** $r_{sen} = 20$ cm

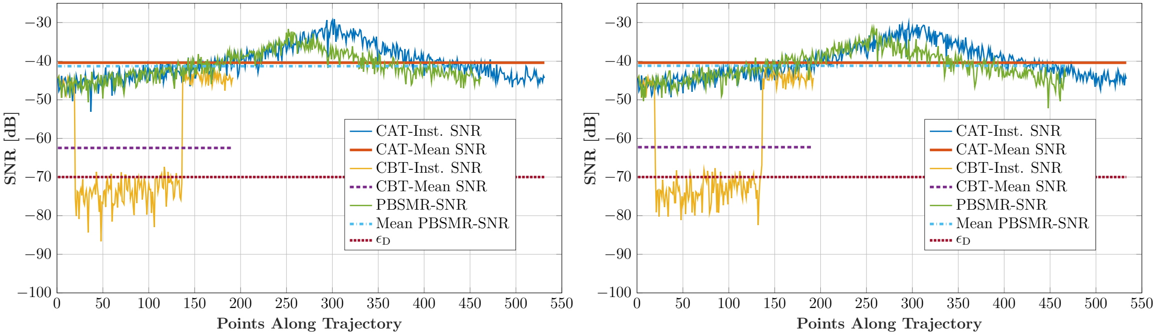

(c) $r_{sen} = 30$ cm **(d)** $r_{sen} = 40$ cm

Figure 7.6: SNR Comparison

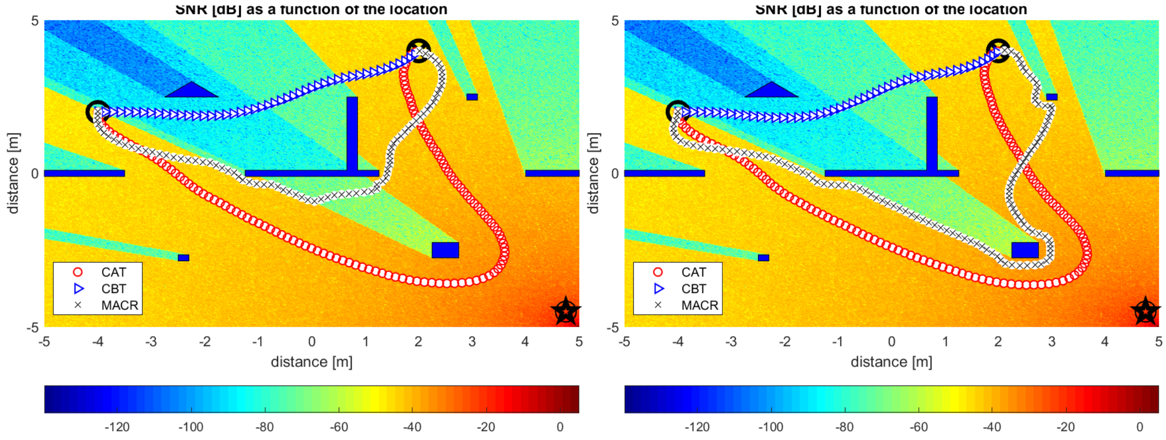

(a) $r_{sen} = 10$ cm **(b)** $r_{sen} = 20$ cm

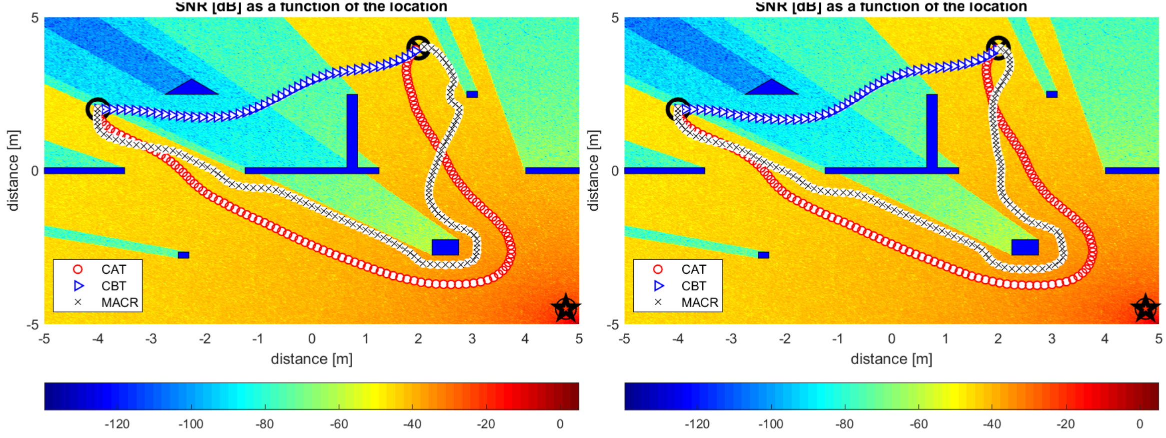

(c) $r_{sen} = 30$ cm **(d)** $r_{sen} = 40$ cm

Figure 7.7: Trajectory with PBSMR update for different sensing regions

Environment Containing Obstacles of Regular Geometry

In this section we look at the trajectory of the agent using SBCAM with PBSMR updates for different r_{sen} where the environment consists of multiple obstacles (convex and non convex) of regular geometry. Again, it can be seen that the trajectory using SBCAM with PBSMR reconstruction converges to the CAT at $r_{sen} = 20$ cm as compared to $r_{sen} = 80$ cm for the MSACR reconstruction.

In Fig. 7.8 the reconstructed SNR-map and HO-map corresponding to the trajec-

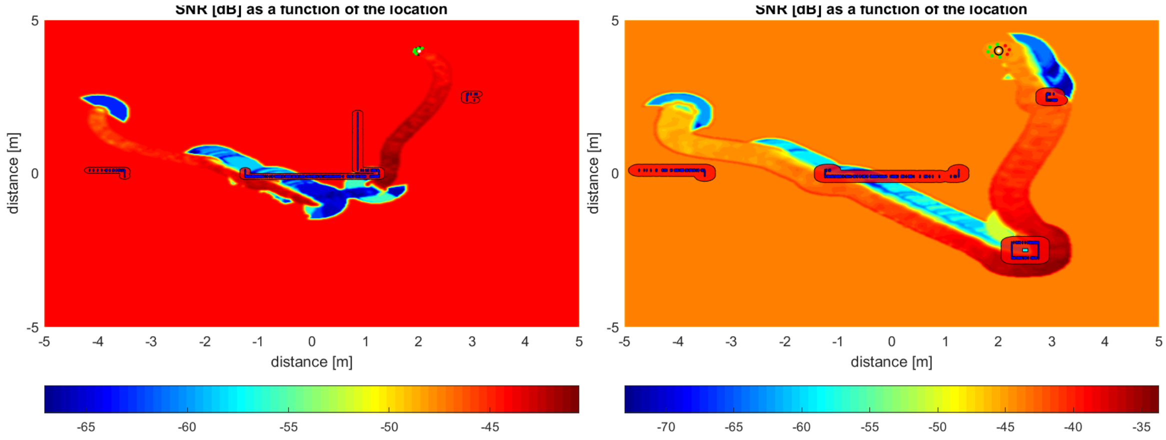

(a) $r_{sen} = 10$ cm **(b)** $r_{sen} = 20$ cm

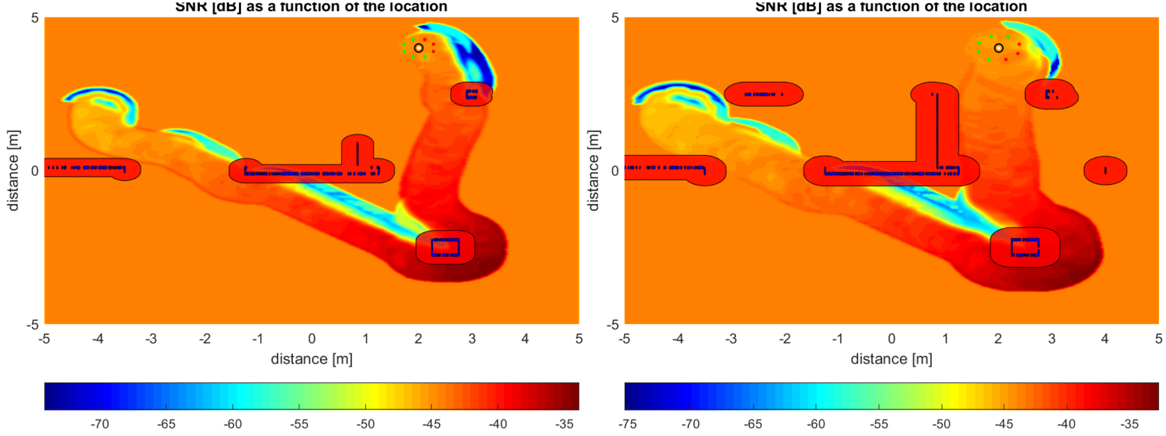

(c) $r_{sen} = 30$ cm **(d)** $r_{sen} = 40$ cm

Figure 7.8: SNR & HO maps

tories in Fig. 7.7 are shown. Interestingly, it can be seen that the agent does not need to reconstruct the compelete HO-map in order to converge to the CAT. The agent is able to converge to the goal with a partial representation of the HO-map in the case of $r_{sen} = 20$ cm. Fig. 7.9 shows the SNR along the trajectory of the agent with different r_{sen}. As in the previous section for the radii at which the trajectories approximately converge to the CAT, the SBCAM is able to match the performance of the MBCAN.

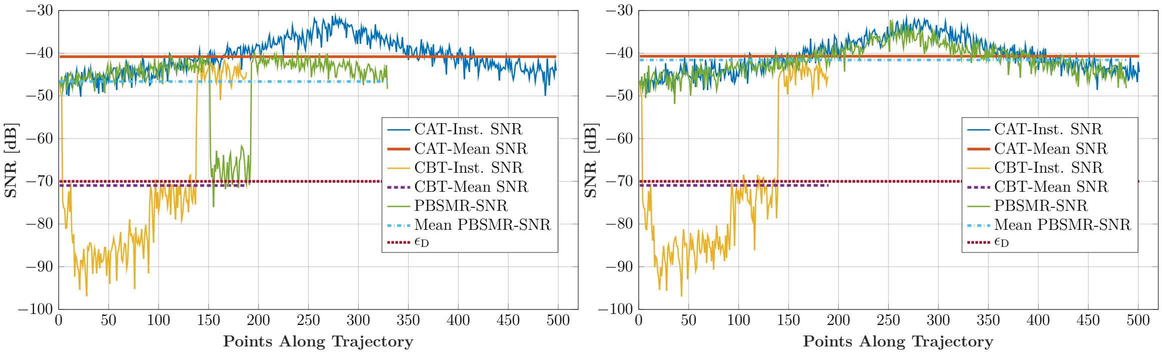

(a) $r_{sen} = 10$ cm **(b)** $r_{sen} = 20$ cm

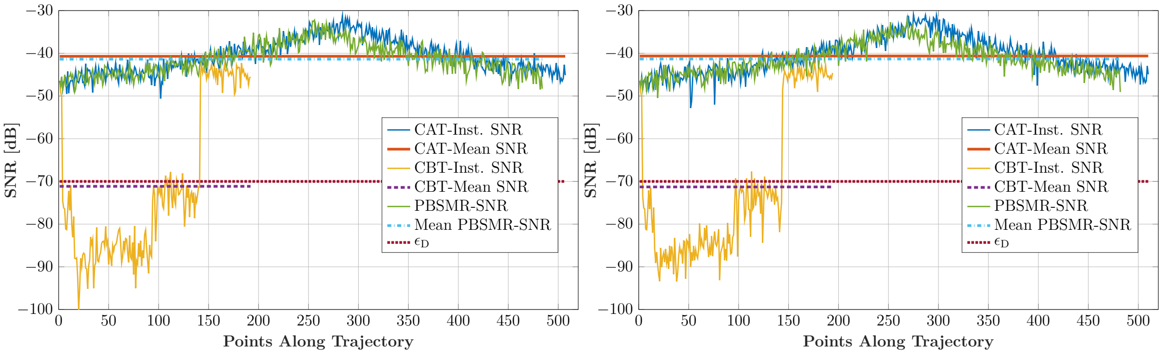

(c) $r_{sen} = 30$ cm **(d)** $r_{sen} = 40$ cm

Figure 7.9: SNR Comparison

Complex Environment With Obstacles of Irregular Geometry

In this section we look at the trajectory of the agent using SBCAM with PBSMR updates for different r_{sen} in a complex environment with multiple obstacles (convex and non convex) of irregular geometry. Since, both the start and goal positions are inside a low SNR region, this presents the planner with a challenging situation as it is completely blind to both the SNR and HO maps at the start. The SBCAM is not able to converge to the CAT. It approaches the CAT at $r_{sen} = 70$ cm as at lower radii the agent is not able to update the region with high SNR above it. Even at high r_{sen}, the agent avoids entering the low SNR region towards the goal unlike the CAT which enters the DCZ much earlier to approach the goal position. The SBCAM with PBSMR and SBOMR only enters the DCZ when it reconstructs the complete boundary of the low SNR within which the goal position exists. The SNR and HO map reconstruction corresponding to the trajectories in Fig. 7.10 are shown in Fig. 7.11. It can be observed that sub-figure 7.11d that the PBSMR completely reconstructed the boundary of the low SNR region within which the goal exits. Also, it can be observed that the agent does not need to reconstruct the complete HO map to navigate towards the goal for different sensing radii. Also, the agent was able to reconstruct the complex irregular obstacles by using the circular representation of the points detected on those obstacles. Fig. 7.12 shows the SNR along the trajectory of the agent with different r_{sen}. Below $r_{sen} = 70$ cm, the performance of the SBCAM with joint PBSMR and SBOMR is poor. However, it nearly matches the performance

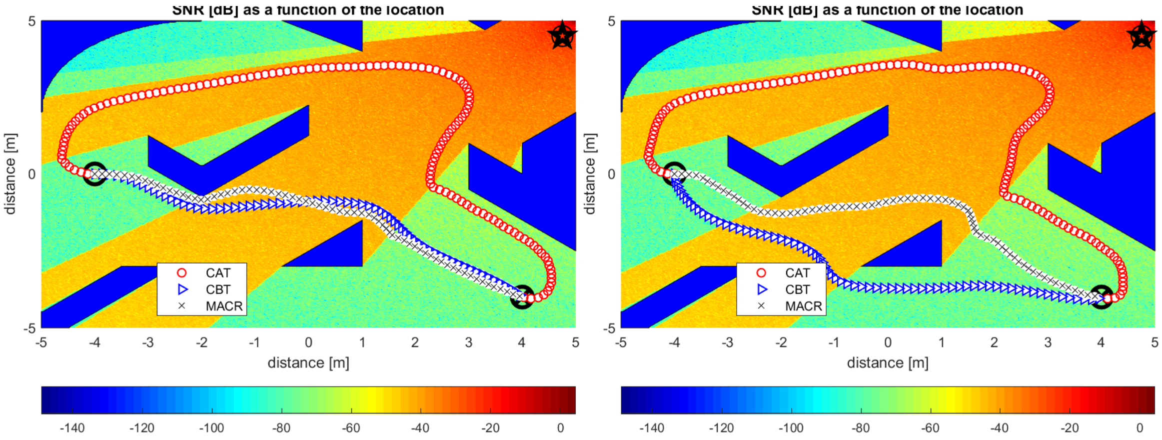

(a) $r_{sen} = 10$ cm **(b)** $r_{sen} = 40$ cm

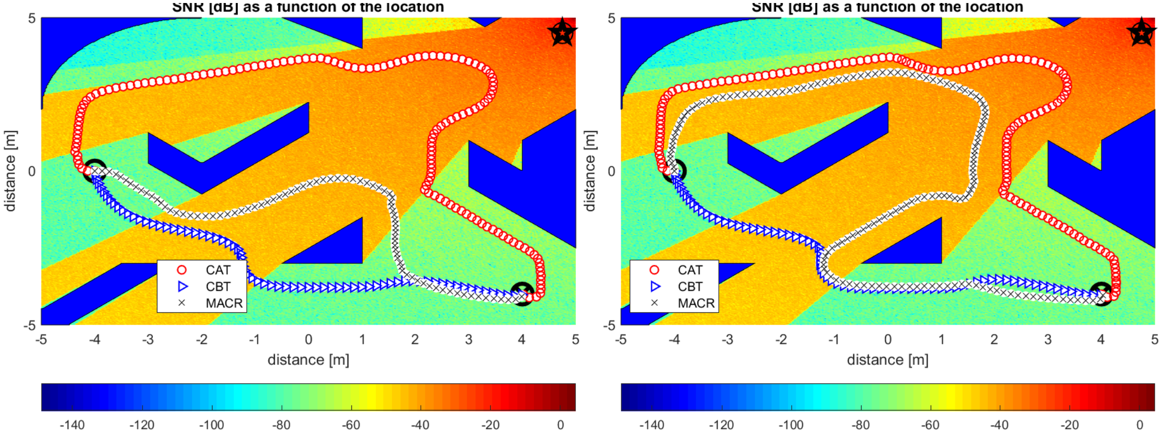

(c) $r_{sen} = 60$ cm **(d)** $r_{sen} = 70$ cm

Figure 7.10: Trajectory with PBSMR update for different sensing regions

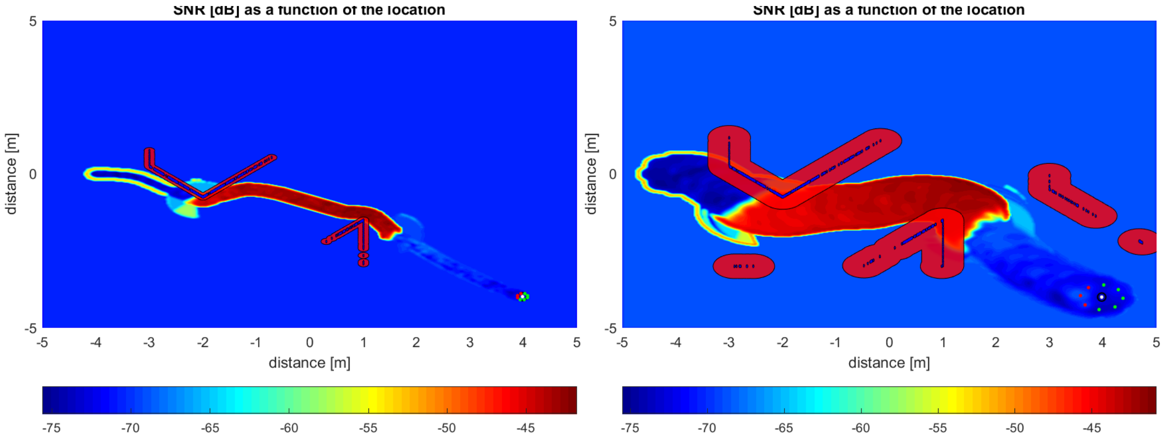

(a) $r_{sen} = 10$ cm

(b) $r_{sen} = 40$ cm

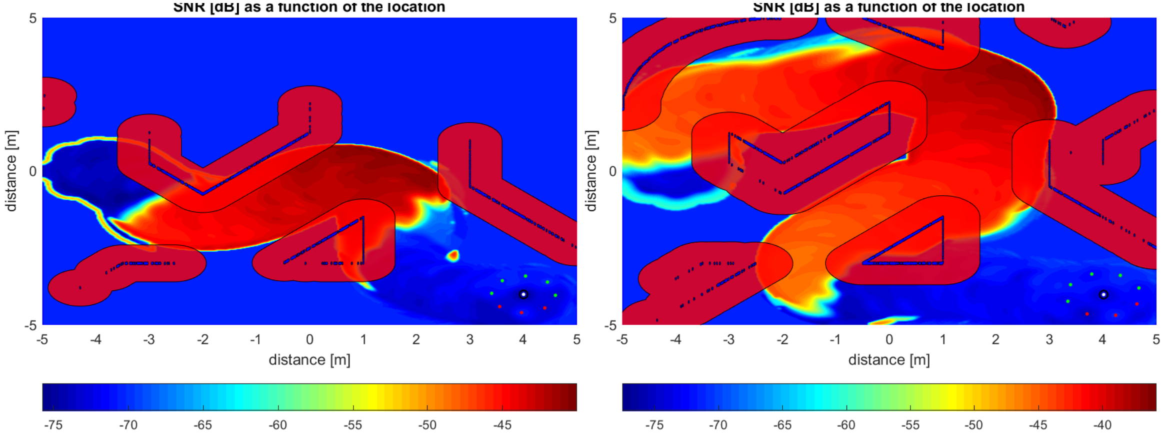

(c) $r_{sen} = 60$ cm

(d) $r_{sen} = 70$ cm

Figure 7.11: SNR & HO maps

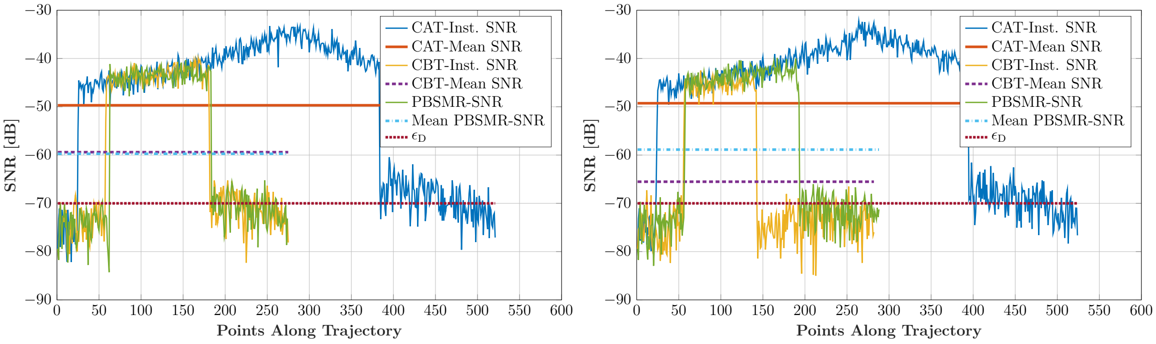

(a) $r_{sen} = 10$ cm **(b)** $r_{sen} = 40$ cm

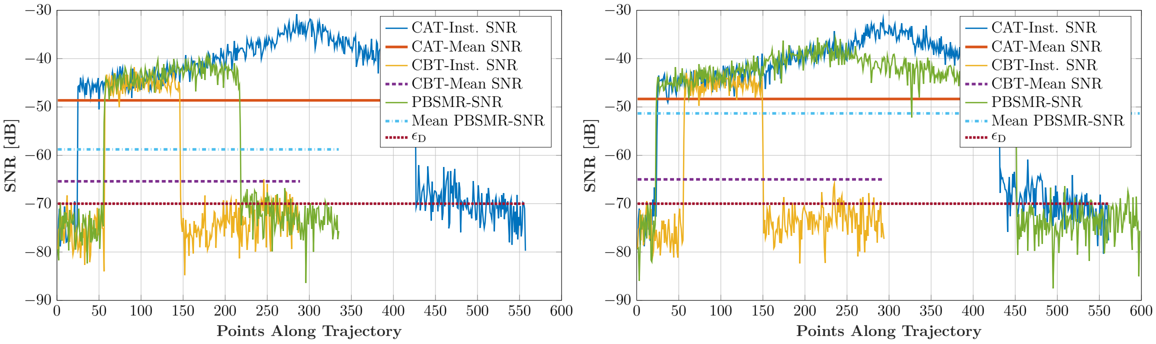

(c) $r_{sen} = 60$ cm **(d)** $r_{sen} = 70$ cm

Figure 7.12: SNR Comparison

of the MBCAN at $r_{sen} = 70$ cm and above. However, the trajectory length of the SBCAM is larger.

7.2.2 Greedy-Prediction-Based SNR Map Reconstruction (GPBSMR) Results

In this section, we present simulation results for the greedy version of PBSMR. Similar to Greedy Multiple-Sensor-Array Circular Region (GMSACR), Greedy-Prediction-Based SNR Map Reconstruction (GPBSMR) assigns the prediction region with a very low value ϵ_{gr}.

Environment With Single Obstacle

Fig. 7.13 shows the trajectory of an agent with four different radii for the the sensing region. It can be seen that the trajectories generated by SBCAM with joint GPBSMR and SBOMR are able to converge to all the CAT for all r_{sen}. This improves on the PBSMR reconstruction which converged to the CAT at r_{sen} larger than 20 cm. Figs. 7.14 and 7.15 show the reconstructed SNR-map and SNR along the corresponding trajectories in Fig. 7.13. The SNR performance of the GPBSMR reconstruction nearly matches the CAT performance for all sensing radii r_{sen}.

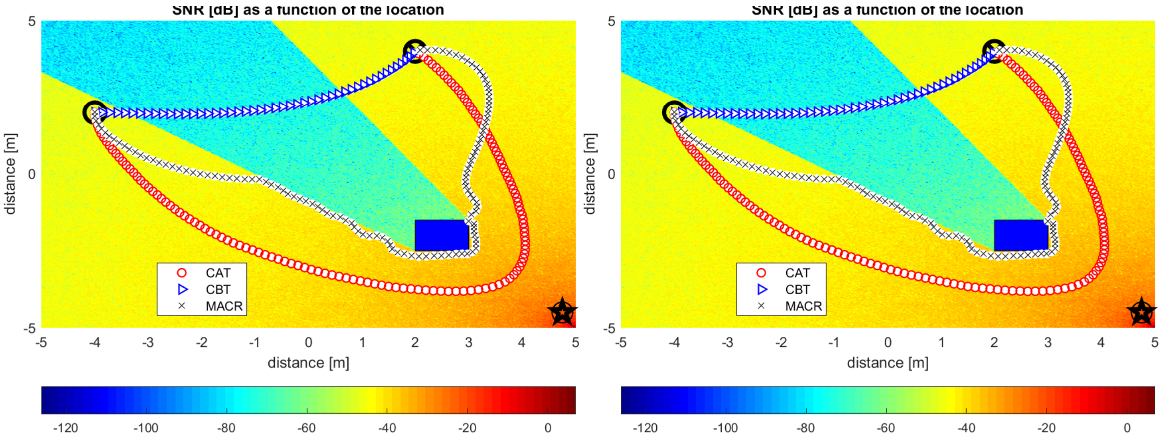

(a) $r_{sen} = 10$ cm **(b)** $r_{sen} = 20$ cm

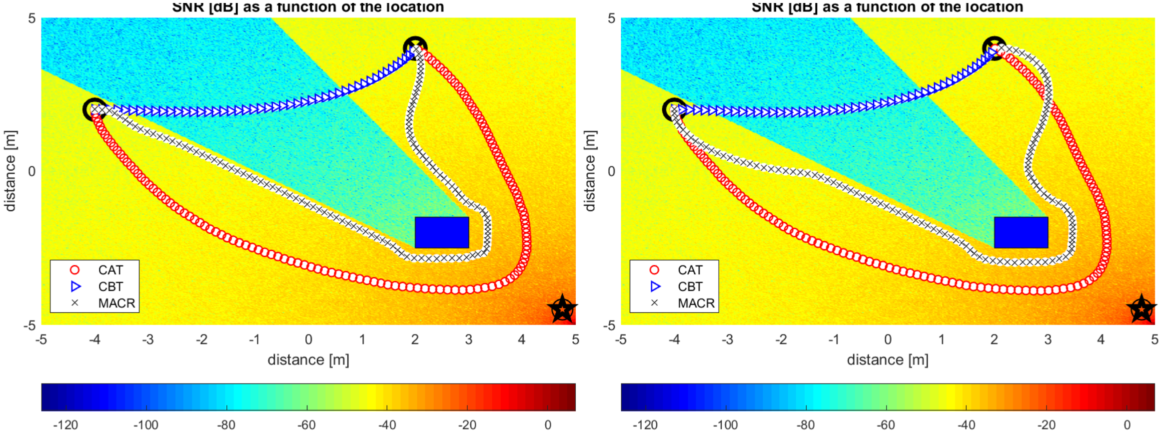

(c) $r_{sen} = 30$ cm **(d)** $r_{sen} = 40$ cm

Figure 7.13: Trajectory with GPBSMR update for different sensing regions

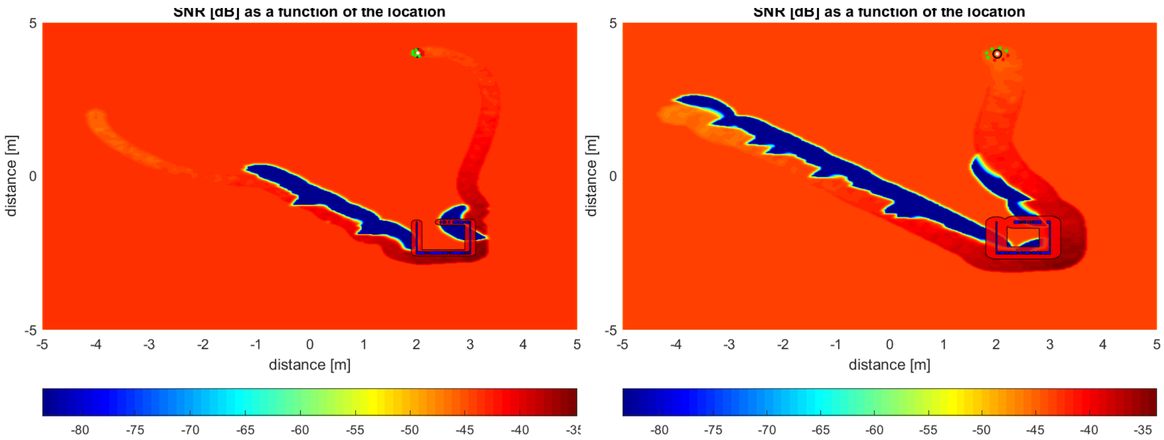

(a) $r_{sen} = 10$ cm **(b)** $r_{sen} = 20$ cm

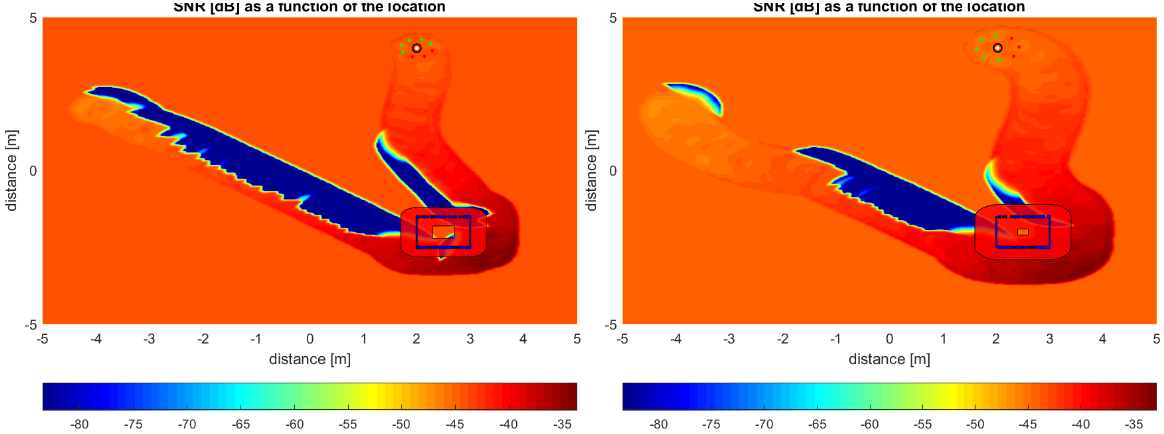

(c) $r_{sen} = 30$ cm **(d)** $r_{sen} = 40$ cm

Figure 7.14: SNR & HO maps

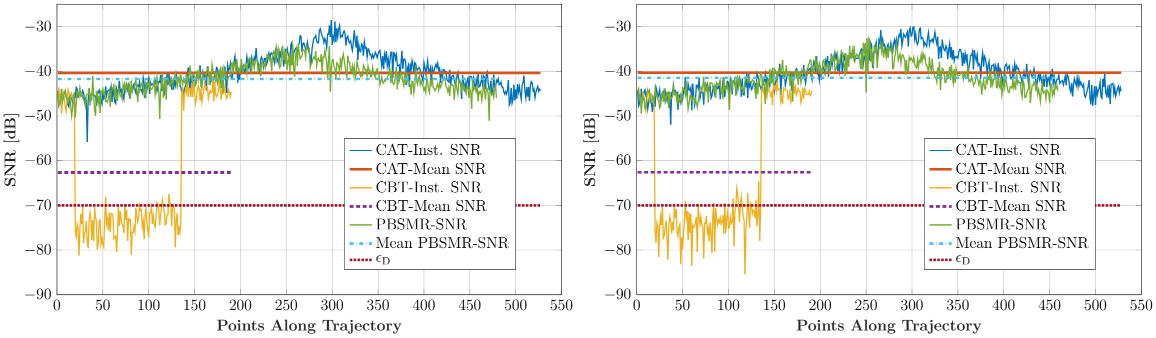

(a) $r_{sen} = 10$ cm **(b)** $r_{sen} = 20$ cm

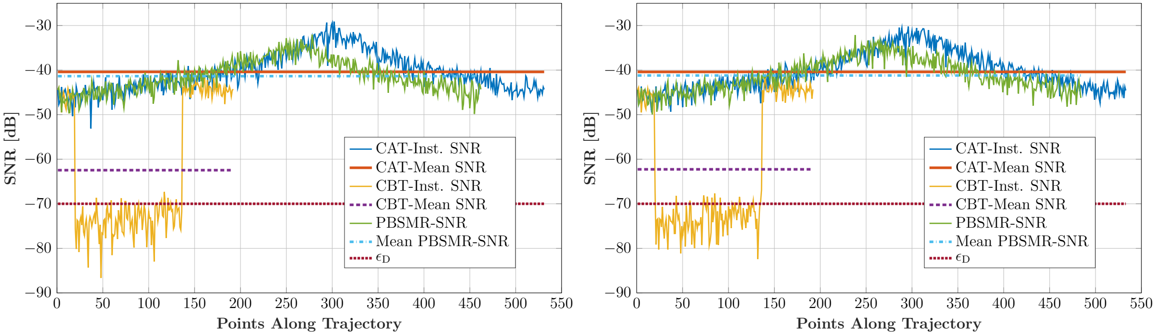

(c) $r_{sen} = 30$ cm **(d)** $r_{sen} = 40$ cm

Figure 7.15: SNR Comparison

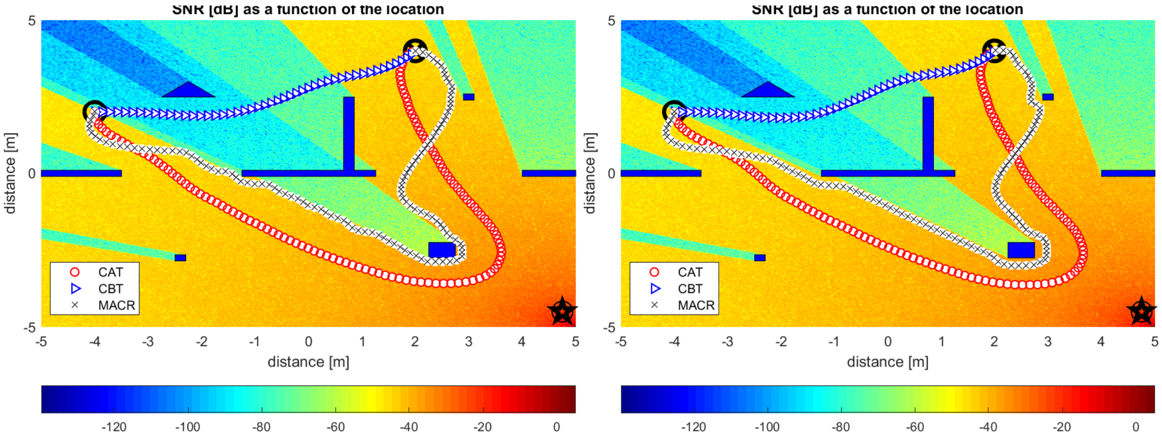

(a) $r_{sen} = 10$ cm **(b)** $r_{sen} = 20$ cm

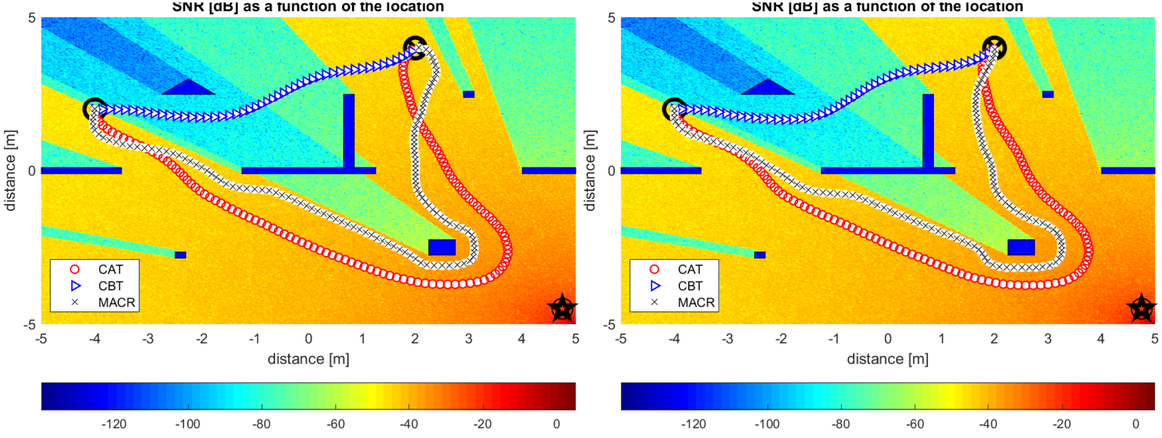

(c) $r_{sen} = 30$ cm **(d)** $r_{sen} = 40$ cm

Figure 7.16: Trajectory with GPBSMR update for different sensing regions

Environment Containing Obstacles of Regular Geometry

Figs. 7.16 to 7.18 show the trajectories, reconstructed SNR and HO maps and the SNR performance of trajectories for different sensing radii respectively. As in the previous section, the trajectories obtained using SBCAM with joint GPBSMR and SBOMR approximately converge to the CAT for all sensing radii. Fig. 7.18 confirms this as the SNR of trajectories for all sensing radii nearly matches the SNR along the CAT.

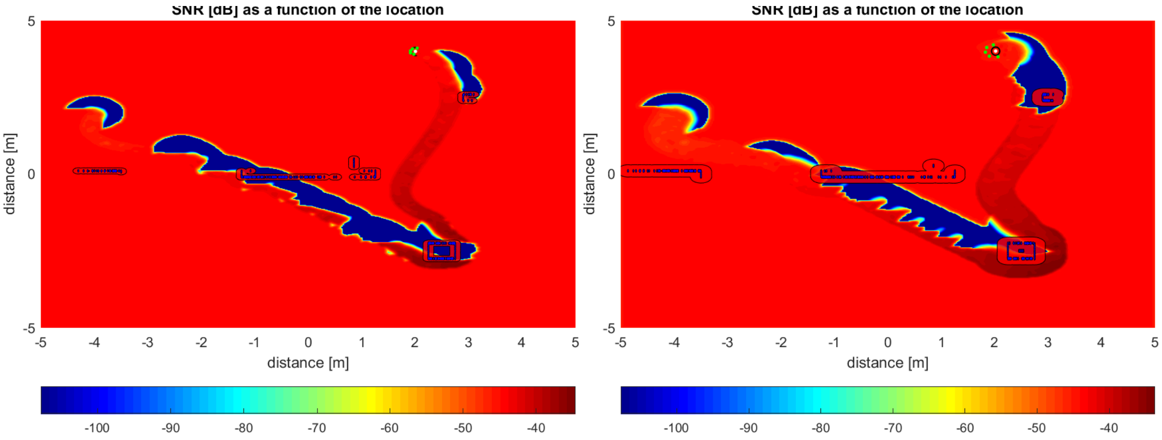

(a) $r_{sen} = 10$ cm **(b)** $r_{sen} = 20$ cm

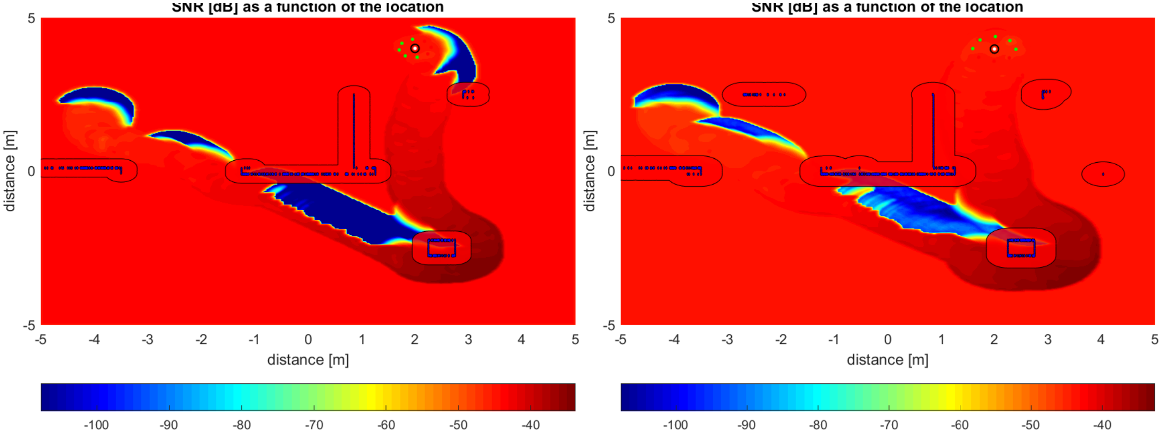

(c) $r_{sen} = 30$ cm **(d)** $r_{sen} = 40$ cm

Figure 7.17: SNR & HO maps

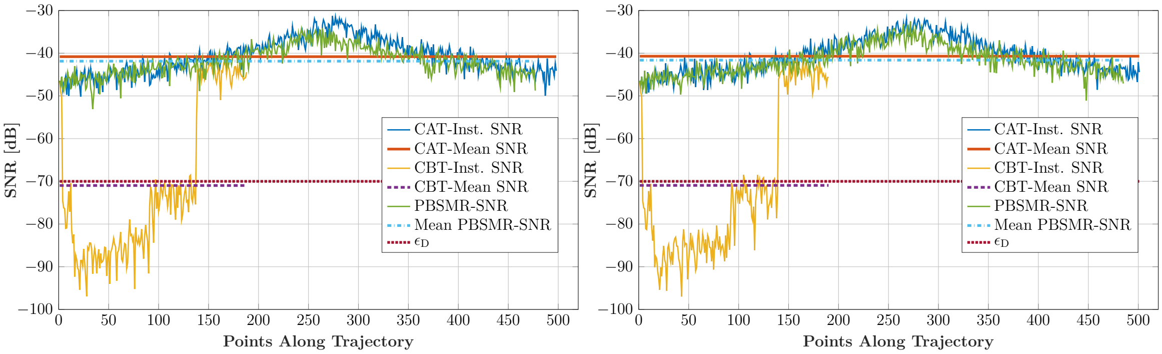

(a) r_{sen} = 10 cm **(b)** r_{sen} = 20 cm

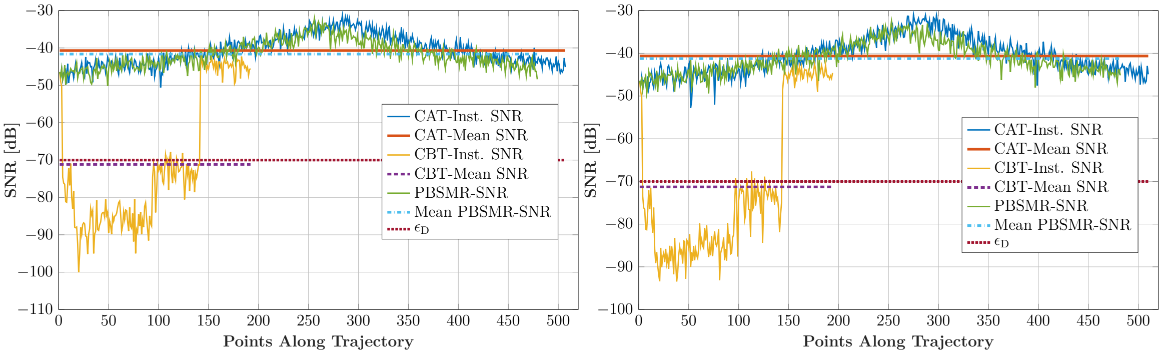

(c) r_{sen} = 30 cm **(d)** r_{sen} = 40 cm

Figure 7.18: SNR Comparison

Complex Environment With Obstacles of Irregular Geometry

In this section we look at the trajectory of the agent using SBCAM with joint GPBSMR and SBOMR updates for different r_{sen} in a complex environment with multiple obstacles (convex and non convex) of irregular geometry. Fig. 7.19 shows the trajectories obtained using SBCAM with joint GPBSMR and SBOMR. As in the previous cases the agent is not able to converge to the CAT at low sensing radii. At higher sensing radii, it parly converges to the MBCAN. However, at lower sensing radii, the trajectory of the agent is not very smooth. This is due to the divergent nature of the greedy algorithms. Assigning low values to updated regions could lead to $\frac{\partial \gamma}{\partial t}$ to have a large value which could lead to the SBCAM diverging as discussed section 6.5.1. Fig. 7.20 shows the SNR and HO map reconstruction. As seen before in section 7.2.1 the GPBSMR has to reconstruct the complete boundary of the low SNR region within which the goal point is present before converging towards the goal. Fig. 7.21 shows the SNR along the trajectory of the agent with different r_{sen}. As in section 7.2.1 the performance of the SBCAM with joint GPBSMR and SBOMR approximately matches the performance of the CAT at higher radii only.

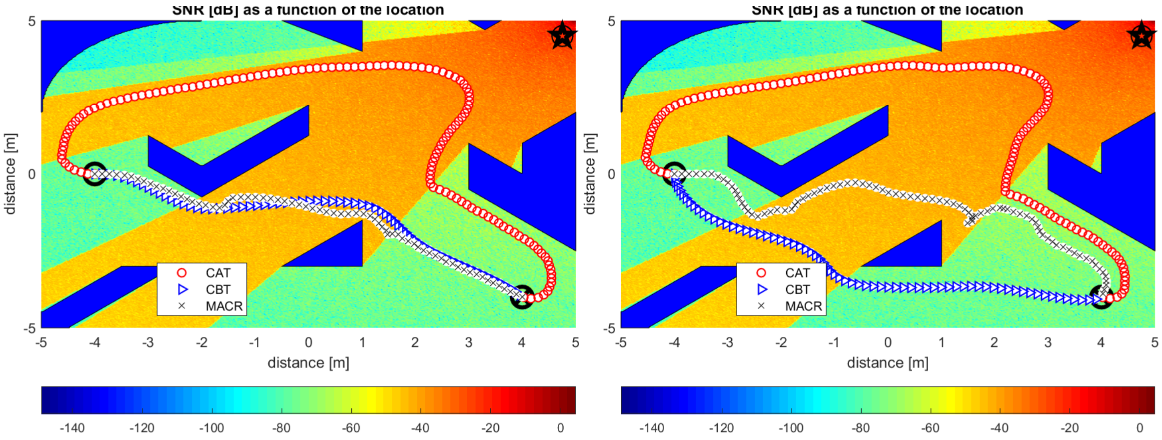

(a) $r_{sen} = 10$ cm **(b)** $r_{sen} = 30$ cm

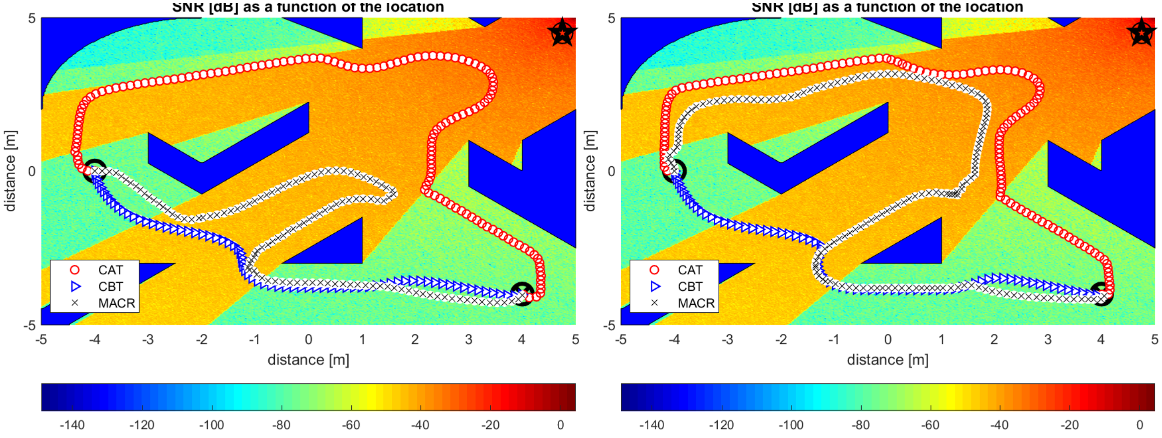

(c) $r_{sen} = 60$ cm **(d)** $r_{sen} = 80$ cm

Figure 7.19: Trajectory with GPBSMR update for different sensing regions

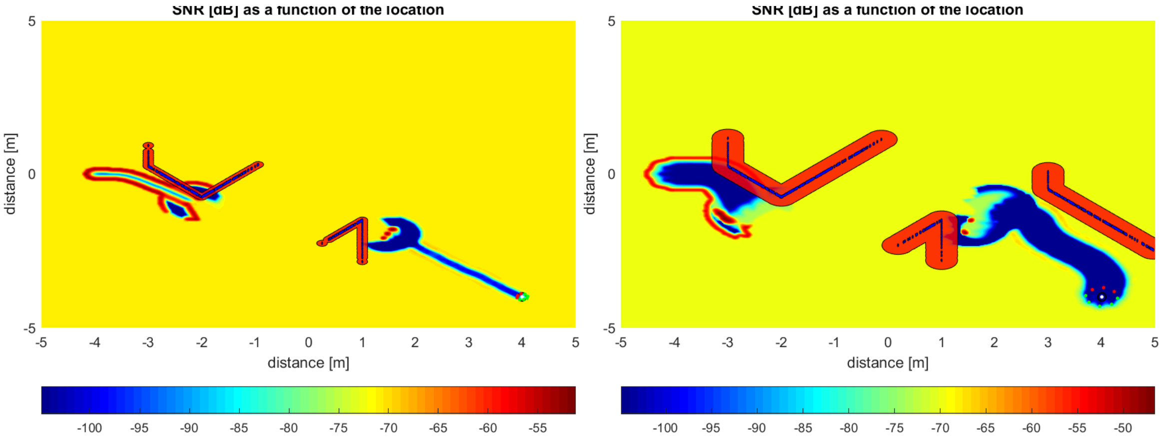

(a) $r_{sen} = 10$ cm **(b)** $r_{sen} = 30$ cm

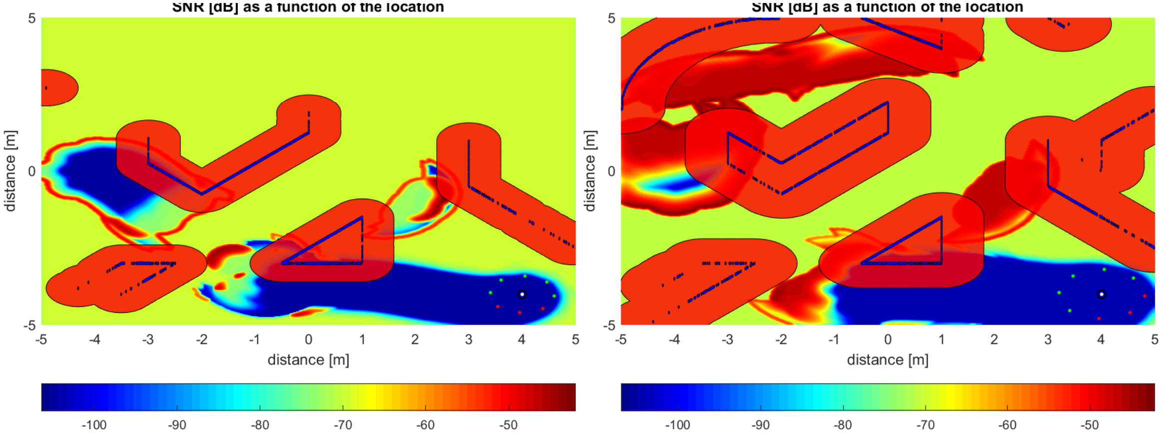

(c) $r_{sen} = 60$ cm **(d)** $r_{sen} = 80$ cm

Figure 7.20: SNR & HO maps

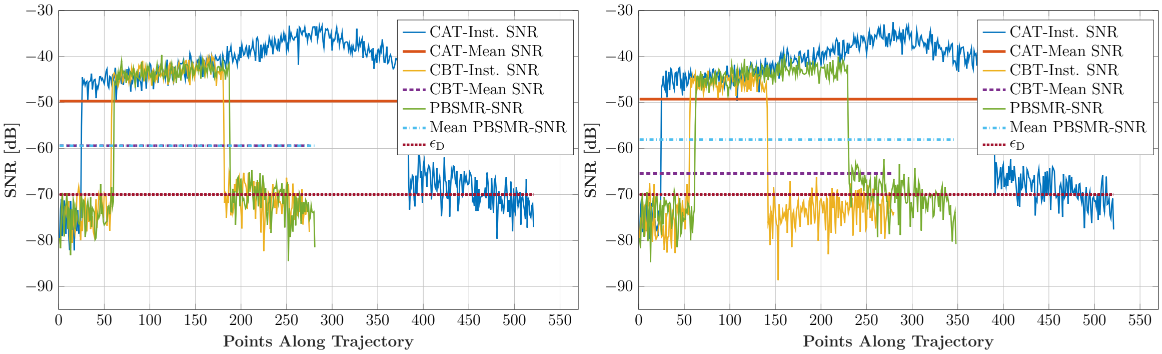

(a) $r_{sen} = 10$ cm

(b) $r_{sen} = 30$ cm

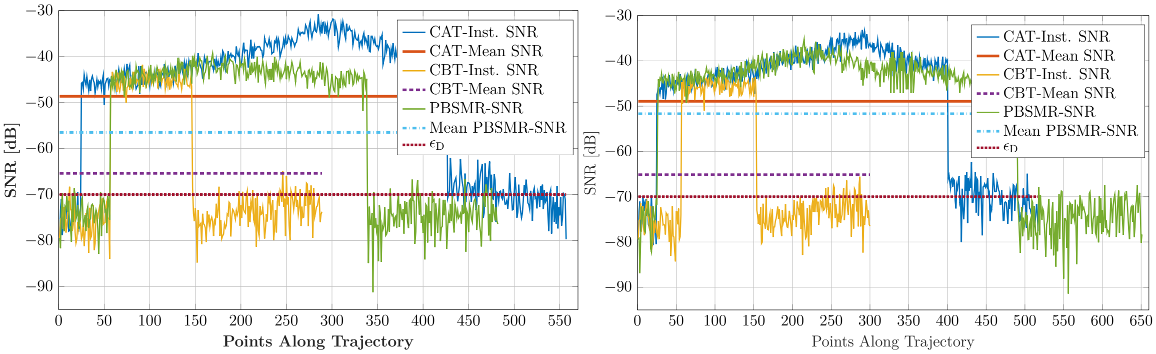

(c) $r_{sen} = 60$ cm

(d) $r_{sen} = 80$ cm

Figure 7.21: SNR Comparison

7.2.3 Discussion & Conclusions

For the case where the start and goal positions were outside of low SNR regions, the SBCAM with joint PBSMR and SBOMR was able to match the performance of the MBCAN at lower sensing radii. However, especially, if the goal position is in a low SNR region, the SBCAM with joint PBSMR and SBOMR did not perform very well at low sensing radii. At higher sensing radii it partially converged to the CAT but it only converged to the goal after completely reconstructing the boundary of the low SNR region within which the goal position is present.

The greedy PBSMR improved on the PBSMR and was able to converge to the CAT at all sensing radii when the start and goal positions were outside of low SNR regions. However, the trajectories obtained using SBCAM with GPBSMR were not smooth when the start and goal positions were inside a low SNR regions. The PBSMR which gives smoother trajectories outperforms the GPBSMR in this case.

The MSACR SNR reconstruction required large sensing radii to converge to the CAT. The greedy MSACR improved on the MSACR but still required large sensing radii. The greedy versions of both MSACR and PBSMR suffered convergence problems.

HO extension was incorporated to accommodate agent size. Due to obstacle extension, large parts of the workspace became inaccessible for agents with large sizes due to larger sensing radii. The SBOMR was able to reconstruct HO using range sensors. Obstacles of any shape and size were reconstructed by using circular representation of the points detected on the obstacles using the range sensors. Agents of any sensing radii were able to converge to the goal with partial reconstruction of the HO map using SBOMR.

CHAPTER 8

CONCLUSIONS AND FUTURE WORKS

> *”The only thing I know is that I know nothing.”*
>
> —SOCRATES.

In this dissertation, we presented a provably correct joint communication and hard-obstacle aware navigation technique. Wireless communication and Hard Obstacle or Hazardous Region (HO) avoidance constraints were integrated with a Harmonic Potential Field (HPF)-based planner. The wireless communication performance was represented as a Signal to Noise Ratio (SNR)-map. The Hard Obstacle or Hazardous Region (HO) were represented using binary maps with regions consisting of HO assigned a high value and empty regions were assigned a low value.

Full SNR and HO information was assumed in Model-Based Communication-Aware Navigation (MBCAN). Detailed analysis was done. Convergence to the goal position was proven. Avoidance of low SNR regions was also proven. It was also shown that Dead Communication Zones (DCZ)s are always avoided for the case when both the start and goal positions are outside of DCZs. Optimality was proven by obtaining the functional being minimized by the Model-Based Communication-Aware Navigation (MBCAN). Extensive simulations were performed explore the MBCAN technique. Different scenarios ranging from no obstacles to multiple convex and non convex obstacles with both regular and irregular geometries were used for the simulations. Performance results were obtained for different starting and goal positions both inside and outside DCZ. The results correlated with the analytical findings. The trajectories always converged to the goal while avoiding the HO and maintaining high SNR performance for all scenarios. The trajectories obtained had no loops and were always goal oriented. The lengths of the trajectories were short in DCZs and were not very lengthy in high SNR regions. Complexity analysis was provided for the MBCAN. Comparison of the motion and communication energy consumption was done for the Communication-Aware Trajectory (CAT) and Communication-Blind Trajectory (CBT). It was seen that in the presence of DCZs there was a huge improvement in the motion and energy consumption for CATs as compared to the CBTs for the same communication performance. Comparison of the MBCAN with the state of the art techniques showed that the MBCAN outperformed the start-of the-art, especially, in the presence of obstacles and multiple shadowed regions.

It was shown using simulation results that trajectories could be obtained with limited SNR knowledge comparable in performance to the MBCAN. A sensor based frame work, Sensor-Based Communication-Aware Navigation (SBCAM), was developed that obtained trajectories to the goal with zero SNR and HO knowledge at the start. Conditional convergence to goal was proven.

A purely sensor based planner, Sensor-Based Communication-Aware Navigation (SBCAM), with zero SNR and HO information at the start was presented. Important convergence results were provided. Multiple SNR reconstruction techniques were presented.

A greedy heuristic, Single Sample Greedy (SSG), was presented that used single SNR measurement to reconstruct the SNR-map locally so as to avoid low SNR regions. It was seen that the agent had to enter a low SNR region to detect it using SSG. SBCAM with SSG reconstruction was able to avoid low SNR regions only if start and goal positions were outside of the low SNR region. However, it resulted in long trajectories when the goal position was inside a low SNR region. The performance was verified with simulations for the same environments as the MBCAN.

Multiple-Sensor-Array Circular Region (MSACR) reconstruction using multiple passive antennas was obtained using a circular ring of antennas. Analysis was done for different radii for the sensing antennas. Gaussian kernels were used at the antennas to reconstruct the SNR in a local region. Width of the Gaussian kernel was obtained as a function of sensing antenna distance and overlap between kernels of adjacent sensing antennas. Extension of HO was shown for non-point agents. Simulation results showed the SNR performance converged to the CAT as the sensing radii increases for all the environments. However, very large radii were required for sufficiently good performance. Greedy version of the reconstruction results in a better performance at lower sensing radii.

Joint sensor based HO map reconstruction and SNR prediction using Laplacian of Gaussian (LoG) and Gradient of Gaussian (GoG) filter was shown using multiple antennas in a circular ring. HO reconstruction was done using range sensors. HO-map was updated as a circle at the point detected on a HO by the range sensor. Obstacles of any shape or size could be updated using this technique. Low SNR regions were predicted by detecting the negative to positive transition in the LoG filter and comparing the GoG with a threshold. Trajectories obtained using SBCAM with joint prediction and HO reconstruction converged to the MBCAN at very low sensing radii. Greedy prediction resulted in convergence to the MBCAN for all sensing radii.

This work paves the way for significant future research possibilities. Both the MBCAN and SBCAM algorithms only make use of the normalized gradient of the Harmonic Potential Field (HPF) to obtain trajectories. Utilization of the gradient magnitude to modulate the velocity along the trajectory could be used to further improve the communication performance of the system. This is especially beneficial to exploit multi-path fading which depends on the speed of the agent when the physical environment around the agent is static.

Another important open problem is communication-aware path planning for multiple agents sharing the same workspace using Harmonic Potential Fields. Formulation, performance and convergence analysis are all open problems. Studying the analyticity of the SBCAM trajectory is also another important open problem.

Optimization of depth and width of the SSG heuristic for different scenarios is another open problem. Optimization of different parameters like antenna number, orientation, sensing radii, prediction region, overlap and kernel to be used are all open problems for the multiple antenna reconstruction. An interesting problem would be finding adaptive parameters for different environments.

Lastly considerable time was spent on the developing the solver and simulator. Open problems in solver design include adaptive meshing for environments of different geometry. Adapting meshing to different SNR maps like using a higher resolution in regions with fast changing SNR and low mesh resolution in slowly varying SNR regions.

This dissertation presented and solved the communication-aware motion planning problem using Harmonic Potential Fields for different scenarios. It provided convergence analysis for the full information and information blind cases and provided multiple SNR and HO reconstruction. Simulation results comparing the performance of different reconstruction techniques with the fully known case were done to illustrate their performance for different scenarios.

REFERENCES

[1] A. Grama, G. Karypis, V. Kumar, and A. Gupta, *Introduction to Parallel Computing.* Pearson, 2nd ed., 2003.

[2] L. N. Trefethen and D. B. III, *Numerical Linear Algebra.* SIAM: Society for Industrial and Applied Mathematics, 1st ed., 1997.

[3] B. Sklar, “Rayleigh fading channels in mobile digital communication systems. i. characterization,” *IEEE Commun. Mag.*, vol. 35, no. 9, pp. 136–146, 1997.

[4] J. Walter, “World disasters report 2005,” tech. rep., (International Federation of Red Cross and Red Crescent Societies, Kumarian Press, Bloomfield, 2005.

[5] NFPA, “Standard on operations and training for technical rescue incidents,” 2014.

[6] R. R. Murphy, S. Tadokoro, D. Nardi, A. Jacoff, P. Fiorini, H. Choset, and A. M. Erkmen, “Search and rescue robotics,” in *Springer Handb. Robot.* (O. Siciliano, Bruno and Khatib, ed.), pp. 1151–1173, Springer Berlin Heidelberg, 2008.

[7] S. M. LaValle, *Planning Algorithms.* Cambridge: Cambridge University Press, 2006.

[8] S. A. M. Coenen, *Motion Planning for Mobile Robots - A Guide.* PhD thesis, Eindhoven University of Technology, 2012.

[9] A. A. Masoud, "Motion planning with gamma-harmonic potential fields," *IEEE Trans. Aerosp. Electron. Syst.*, vol. 48, no. October 2012, pp. 2786–2801, 2012.

[10] C. Goerzen, Z. Kong, and B. Mettler, "A survey of motion planning algorithms from the perspective of autonomous uav guidance," *J. Intell. Robot. Syst.*, vol. 57, pp. 65–100, Nov. 2009.

[11] Y. K. Hwang and N. Ahuja, "Gross motion planning—a survey," *ACM Comput. Surv.*, vol. 24, pp. 219–291, Sept. 1992.

[12] O. Khatib, "Real-time obstacle avoidance for manipulators and mobile robots," *Int. J. Rob. Res.*, vol. 5, pp. 90–98, Mar. 1986.

[13] C. Connolly, J. Burns, and R. Weiss, "Path planning using laplace's equation," in *Proceedings., IEEE Int. Conf. Robot. Autom.*, (Cincinnati), pp. 2102–2106, IEEE Comput. Soc. Press, 1990.

[14] C. I. Connolly and R. A. Grupen, "The applications of harmonic functions to robotics," *J. Robot. Syst.*, vol. 10, pp. 931–946, Oct. 1993.

[15] K. Sato, "Deadlock-free motion planning using the laplace potential field," *Adv. Robot.*, vol. 7, pp. 449–461, Jan. 1992.

[16] O. D. Kellogg, *Foundations of Potential Theory.* Berlin, Heidelberg: Springer Berlin Heidelberg, 1967.

[17] A. A. Masoud, “Motion planning with gamma-harmonic potential fields,” in *2010 IEEE/ASME Int. Conf. Adv. Intell. Mechatronics*, pp. 297–302, IEEE, July 2010.

[18] H. Choset, W. Burgard, S. Hutchinson, G. Kantor, L. E. Kavraki, K. Lynch, and S. Thrun, *Principles of Robot Motion: Theory, Algorithms, and Implementation.* MIT Press, June 2005.

[19] J.-C. Latombe, *Robot Motion Planning.* Norwell: Kluwer Academic Publishers, 1991.

[20] G. Campion, G. Bastin, and B. Dandrea-Novel, “Structural properties and classification of kinematic and dynamic models of wheeled mobile robots,” *IEEE Trans. Robot. Autom.*, vol. 12, no. 1, pp. 47–62, 1996.

[21] A. A. Masoud, “A harmonic potential field approach for navigating a rigid, nonholonomic robot in a cluttered environment,” in *2009 IEEE Int. Conf. Robot. Autom.*, (Kobe, Japan), pp. 3993–3999, IEEE, May 2009.

[22] A. A. Masoud, “A harmonic potential field approach for joint planning and control of a rigid, separable nonholonomic, mobile robot,” *Rob. Auton. Syst.*, vol. 61, pp. 593–615, June 2013.

[23] A. A. Masoud, “A harmonic potential approach for simultaneous planning and control of a generic uav platform,” *J. Intell. Robot. Syst.*, vol. 65, pp. 153–173, Aug. 2011.

[24] A. A. Masoud, "A virtual velocity attractor, harmonic potential approach for joint planning and control of a uav," in *Proc. 2011 Am. Control Conf.*, (San Francisco, CA), pp. 432–437, IEEE, June 2011.

[25] C. Shannon, "Communication in the presence of noise," *Proc. IRE*, vol. 37, pp. 10–21, Jan. 1949.

[26] Z. Sun and I. Akyildiz, "Channel modeling and analysis for wireless networks in underground mines and road tunnels," *IEEE Trans. Commun.*, vol. 58, pp. 1758–1768, June 2010.

[27] K. A. Remley, G. Koepke, E. Messina, A. Jacoff, and G. Hough, "Standards development for wireless communicati ons for urban search and rescue robots," tech. rep., National Institute of Standards and Technology, 2007.

[28] K. A. Remley, G. Koepke, D. G. Camell, C. Grosvenor, G. Hough, and R. T. Johnk, "Wireless communications in tunnels for urban search and rescue robots," *Proc. 8th Work. Perform. Metrics Intell. Syst. - Permis '08*, p. 236, 2008.

[29] D. Popa, H. Stephanou, C. Helm, and A. Sanderson, "Robotic deployment of sensor networks using potential fields," in *IEEE Int. Conf. Robot. Autom. 2004. Proceedings. ICRA '04. 2004*, pp. 642–647 Vol.1, IEEE, 2004.

[30] T. Chung, J. Burdick, and R. Murray, "A decentralized motion coordination strategy for dynamic target tracking," in *Proc. 2006 IEEE Int. Conf. Robot. Autom. 2006. ICRA 2006.*, (Orlando, FL), pp. 2416–2422, IEEE, 2006.

[31] T. Chung, V. Gupta, J. Burdick, and R. Murray, “On a decentralized active sensing strategy using mobile sensor platforms in a network,” in *2004 43rd IEEE Conf. Decis. Control (IEEE Cat. No.04CH37601)*, pp. 1914–1919 Vol.2, IEEE, 2004.

[32] P. Yang, R. A. Freeman, and K. M. Lynch, “Distributed cooperative active sensing using consensus filters,” in *Proc. 2007 IEEE Int. Conf. Robot. Autom.*, pp. 405–410, IEEE, Apr. 2007.

[33] L. Mihaylova, T. Lefebvre, H. Bruyninckx, K. Gadeyne, and J. D. Schutter, “Active sensing for robotics - a survey,” in *Proc. 5 th Int’l Conf. Numer. Methods Appl.*, pp. 316—-324, 2002.

[34] G. A. Bekey and D.-Y. Yeung, “A decentralized approach to the motion planning problem for multiple mobile robots,” in *Proceedings. 1987 IEEE Int. Conf. Robot. Autom.*, vol. 4, pp. 1779–1784, Institute of Electrical and Electronics Engineers, 1987.

[35] L. Parker, “A distributed and optimal motion planning approach for multiple mobile robots,” in *Proc. 2002 IEEE Int. Conf. Robot. Autom. (Cat. No.02CH37292)*, vol. 3, (Washington, DC), pp. 2612–2619, IEEE, 2002.

[36] J. Esposito and T. Dunbar, “Maintaining wireless connectivity constraints for swarms in the presence of obstacles,” in *Proc. 2006 IEEE Int. Conf. Robot. Autom. 2006. ICRA 2006.*, (Orlando, FL), pp. 946–951, IEEE, 2006.

[37] R. Arkin and J. Diaz, "Line-of-sight constrained exploration for reactive multiagent robotic teams," in *7th Int. Work. Adv. Motion Control. Proc. (Cat. No.02TH8623)*, pp. 455–461, IEEE, 2002.

[38] A. Cowley, V. Kumar, and C. Taylor, "Towards the deployment of a mobile robot network with end-to-end performance guarantees," in *Proc. 2006 IEEE Int. Conf. Robot. Autom. 2006. ICRA 2006.*, (Orlando, FL), pp. 2085–2090, IEEE, 2006.

[39] A. Wagner and R. Arkin, "Multi-robot communication-sensitive reconnaissance," in *IEEE Int. Conf. Robot. Autom. 2004. Proceedings. ICRA '04. 2004*, pp. 4674–4681 Vol.5, IEEE, 2004.

[40] J. D. Sweeney, R. Grupen, and P. Shenoy, "Active qos flow maintenance in controlled mobile networks," in *Proc. Fourth Int. Symp. Robot. Autom. (ISRA). Queretaro*, 2004.

[41] H. G. Nguyen, N. Farrington, and N. Pezeshkian, "Maintaining communication link for tactical ground robots," in *AUVSI Unmanned Syst. North Am. 2004*, pp. 3–5, 2004.

[42] K.-E. Årzén, A. Bicchi, G. Dini, S. Hailes, K. H. Johansson, J. Lygeros, and A. Tzes, "A component-based approach to the design of networked control systems," *Eur. J. Control*, vol. 13, pp. 261–279, Jan. 2007.

[43] Z. Butler and D. Rus, "Event-based motion control for mobile-sensor networks," *IEEE Pervasive Comput.*, vol. 2, pp. 34–42, Oct. 2003.

[44] D. Puccinelli and M. Haenggi, “Multipath fading in wireless sensor networks,” in *Proceeding 2006 Int. Conf. Commun. Mob. Comput. - IWCMC ’06*, (New York, New York, USA), p. 1039, ACM Press, 2006.

[45] M. Lindhé, K. Johansson, and A. Bicchi, “An experimental study of exploiting multipath fading for robot communications,” in *Proc. Robot. Sci. Syst.*, (Atlanta, GA, USA), 2007.

[46] M. Lindhe and K. H. Johansson, “Communication-aware trajectory tracking,” in *2008 IEEE Int. Conf. Robot. Autom.*, (Pasadena, CA), pp. 1519–1524, IEEE, May 2008.

[47] M. Lindhe and K. Johansson, “Using robot mobility to exploit multipath fading,” *IEEE Wirel. Commun.*, vol. 16, pp. 30–37, Feb. 2009.

[48] M. Lindhé and K. H. Johansson, “Adaptive exploitation of multipath fading for mobile sensors,” in *2010 IEEE Int. Conf. Robot. Autom.*, (Anchorage, AK), pp. 1934–1939, IEEE, May 2010.

[49] M. Lindhe, T. Keviczky, and K. H. Johansson, “Multi-robot path following with visual connectivity,” in *2011 Conf. Rec. Forty Fifth Asilomar Conf. Signals, Syst. Comput.*, (Pacific Grove, CA), pp. 1466–1471, IEEE, Nov. 2011.

[50] Y. Mostofi, “Decentralized communication-aware motion planning in mobile networks: An information-gain approach,” *J. Intell. Robot. Syst.*, vol. 56, pp. 233–256, May 2009.

[51] Y. Mostofi, “Communication-aware motion planning in fading environments,” *2008 IEEE Int. Conf. Robot. Autom.*, pp. 3169–3174, May 2008.

[52] Y. Mostofi and P. Sen, “Compressed mapping of communication signal strength,” in *MILCOM 2008 - 2008 IEEE Mil. Commun. Conf.*, pp. 1–7, IEEE, Nov. 2008.

[53] Y. Mostofi, M. Malmirchegini, and A. Ghaffarkhah, “Estimation of communication signal strength in robotic networks,” in *2010 IEEE Int. Conf. Robot. Autom.*, (Anchorage, AK), pp. 1946–1951, IEEE, May 2010.

[54] A. Ghaffarkhah and Y. Mostofi, “Communication-aware surveillance in mobile sensor networks,” in *Proc. 2011 Am. Control Conf.*, (San Francisco, CA), pp. 4032–4038, IEEE, June 2011.

[55] A. Ghaffarkhah, Y. Yan, and Y. Mostofi, “Dynamic coverage of time-varying environments using a mobile robot — a communication-aware perspective,” in *2011 IEEE GLOBECOM Work. (GC Wkshps)*, (Houston, TX), pp. 1297–1302, IEEE, Dec. 2011.

[56] A. Ghaffarkhah and Y. Mostofi, “Dynamic networked coverage of time-varying environments in the presence of fading communication channels,” *ACM Trans. Sens. Networks*, vol. 10, pp. 1–38, Apr. 2014.

[57] A. Ghaffarkhah and Y. Mostofi, “Communication-aware target tracking using navigation functions – centralized case,” in *Proc. 2nd Int. Conf. Robot. Commun. Coord.*, (Odense), IEEE, 2009.

[58] E. Rimon and D. Koditschek, “Exact robot navigation using artificial potential functions,” *IEEE Trans. Robot. Autom.*, vol. 8, no. 5, pp. 501–518, 1992.

[59] A. Ghaffarkhah and Y. Mostofi, “Communication-aware navigation functions for cooperative target tracking,” in *2009 Am. Control Conf.*, no. 1, (St. Louis, MO), pp. 1316–1322, IEEE, 2009.

[60] A. Ghaffarkhah and Y. Mostofi, “Channel learning and communication-aware motion planning in mobile networks,” in *Proc. 2010 Am. Control Conf.*, (Baltimore, MD), pp. 5413–5420, IEEE, June 2010.

[61] A. Ghaffarkhah and Y. Mostofi, “A communication-aware framework for robotic field estimation,” in *IEEE Conf. Decis. Control Eur. Control Conf.*, (Orlando, FL), pp. 3553–3558, IEEE, Dec. 2011.

[62] A. Ghaffarkhah and Y. Mostofi, “Communication-aware motion planning in mobile networks,” *IEEE Trans. Automat. Contr.*, vol. 56, pp. 2478–2485, Oct. 2011.

[63] A. Ghaffarkhah and Y. Mostofi, “Optimal motion and communication for persistent information collection using a mobile robot,” in *2012 IEEE Globecom Work.*, (Anaheim, CA), pp. 1532–1537, IEEE, Dec. 2012.

[64] A. Ghaffarkhah and Y. Mostofi, “Path planning for networked robotic surveillance,” *IEEE Trans. Signal Process.*, vol. 60, pp. 3560–3575, July 2012.

[65] Y. Yan and Y. Mostofi, “Co-optimization of communication and motion planning of a robotic operation in fading environments,” in *2011 Conf. Rec. Forty*

Fifth Asilomar Conf. Signals, Syst. Comput., (Pacific Grove, CA), pp. 1455–1460, IEEE, Nov. 2011.

[66] Y. Yan and Y. Mostofi, “Co-optimization of communication and motion planning of a robotic operation under resource constraints and in fading environments,” *IEEE Trans. Wirel. Commun.*, vol. 12, pp. 1562–1572, Apr. 2013.

[67] Y. Yan and Y. Mostofi, “Robotic router formation in realistic communication environments,” *IEEE Trans. Robot.*, vol. 28, pp. 810–827, Aug. 2012.

[68] Yuan Yan and Y. Mostofi, “Communication and path planning strategies of a robotic coverage operation,” in *2013 Am. Control Conf.*, (Washington DC), pp. 860–866, IEEE, June 2013.

[69] Y. Yan and Y. Mostofi, “To go or not to go: On energy-aware and communication-aware robotic operation,” *IEEE Trans. Control Netw. Syst.*, vol. 1, pp. 218–231, Sept. 2014.

[70] U. Ali, Y. Yan, Y. Mostofi, and Y. Wardi, “An optimal control approach for communication and motion co-optimization in realistic fading environments,” in *2015 Am. Control Conf.*, pp. 2930–2935, IEEE, July 2015.

[71] S. Gil, S. Kumar, D. Katabi, and D. Rus, “Adaptive communication in multi-robot systems using directionality of signal strength,” *Int. J. Rob. Res.*, vol. 34, pp. 946–968, June 2015.

[72] U. Ali, Hong Cai, Y. Mostofi, and Y. Wardi, “Motion and communication co-optimization with path planning and online channel prediction,” in *2016 Am. Control Conf.*, pp. 7079–7084, IEEE, July 2016.

[73] A. Muralidharan and Y. Mostofi, “First passage distance to connectivity for mobile robots,” in *2017 Am. Control Conf.*, pp. 1517–1523, IEEE, May 2017.

[74] A. Muralidharan and Y. Mostofi, “Energy optimal distributed beamforming using unmanned vehicles,” *IEEE Trans. Control Netw. Syst.*, pp. 1–1, 2017.

[75] A. Muralidharan and Y. Mostofi, “Path planning for a connectivity seeking robot,” in *2017 IEEE Globecom Work. (GC Wkshps)*, pp. 1–6, IEEE, Dec. 2017.

[76] A. F. Molisch, *WIRELESS COMMUNICATIONS.* Wiley, 2nd editio ed., 2010.

[77] A. Goldsmith, *Wireless Communications.* Cambridge: Cambridge University Press, 2005.

[78] D. Tse and P. Viswanath, *Fundamentals of Wireless Communication.* Cambridge: Cambridge University Press, 2005.

[79] J. A. Stratton, *Electromagnetic Theory.* Hoboken, NJ, USA: John Wiley & Sons, Inc., Oct. 2015.

[80] J. Milnor, *Morse Theory.* Princeton University Press, 1963.

[81] D. Koditschek, “Exact robot navigation by means of potential functions: Some topological considerations,” in *Proceedings. 1987 IEEE Int. Conf. Robot. Autom.*, vol. 4, pp. 1–6, Institute of Electrical and Electronics Engineers, 1987.

[82] J. LaSalle, “Some extensions of liapunov’s second method,” *IRE Trans. Circuit Theory*, vol. 7, no. 4, pp. 520–527, 1960.

[83] J. Stewart, *Multivariable Calculus.* Brooks Cole, 7 ed., 2011.

[84] J. L. W. V. Jensen, “Sur les fonctions convexes et les inégalités entre les valeurs moyennes,” *Acta Math.*, vol. 30, pp. 175–193, Dec. 1906.

[85] S. Bergman and M. Schiffer, *Kernel Functions and Elliptic Differential Equations in Mathematical Physics.* Dover Publications, 1st ed., 2005.

[86] M. Giaquinta and S. Hildebrandt, *Calculus of Variations I*, vol. 310 of *Grundlehren der mathematischen Wissenschaften.* Berlin, Heidelberg: Springer Berlin Heidelberg, 2004.

[87] S. Larsson and V. Thomee, *Partial Differential Equations with Numerical Methods.* Springer, 2008.

[88] S. Xiao, A. Postula, and N. Bergmann, “Hardware design of a fast, parallel random tree path planner,” in *2015 Int. Conf. F. Program. Technol.*, pp. 204–207, IEEE, Dec. 2015.

[89] S. M. A. Zeinolabedin, N. Karimi, and S. Samavi, “Low computational complexity hardware implementation of laplacian pyramid,” in *2010 18th Iran. Conf. Electr. Eng.*, pp. 465–470, IEEE, May 2010.

[90] L. Hentilä, P. Kyösti, M. Käske, M. Narandzic, and M. Alatossava., “Matlab implementation of the winner phase ii channel model,” 2007.

[91] Yongguo Mei, Yung-Hsiang Lu, Y. Hu, and C. Lee, “Deployment of mobile robots with energy and timing constraints,” *IEEE Trans. Robot.*, vol. 22, pp. 507–522, June 2006.

[92] M. Malmirchegini and Y. Mostofi, “On the spatial predictability of communication channels,” *IEEE Trans. Wirel. Commun.*, vol. 11, pp. 964–978, Mar. 2012.

[93] G. Dartmann, W. Afzal, X. Gong, and G. Ascheid, “Low complexity cooperative downlink beamforming in multiuser multicell networks,” in *2010 IEEE 12th Int. Conf. Commun. Technol.*, vol. 49, pp. 717–721, IEEE, Nov. 2010.

[94] G. Foschini and M. Gans, “On limits of wireless communications in a fading environment when using multiple antennas,” *Wirel. Pers. Commun.*, vol. 6, no. 3, pp. 311–335, 1998.

[95] S. Nedić, “Non-conservativeness of natural orbital systems,” in *Proc. 2016 Chapel Nat. Philos. Soc.*, (College Park, MD), 2016.

[96] C. P. Nichola and R. C. Yates, “The probability integral,” *Am. Math. Mon.*, vol. 57, pp. 412–413, 1950.

[97] R. C. Gonzalez and R. E. Woods, *Digital Image Processing.* Pearson, 4th ed., 2017.

[98] R. Szeliski, *Computer Vision.* Texts in Computer Science, London: Springer London, 2011.

VITAE

- Name: Waqas Afzal
- Nationality: Pakistani
- Date of Birth: 13 October 1984
- Email: *waqas4.afzal@gmail.com*
- Permanent Address: H. 417, St. 1, Sec. I-8/4, Islamabad 44000, Pakistan
- Postal Address: House 78-A Street 5-Major Colony, Al Madina Estate Khanna East, Islamabad 44000, Pakistan.
- **Ph.D. ELECTRICAL ENGINEERING (ROBOTICS & CONTROL), King Fahd University of Petroleum & Minerals (KFUPM)**, Dhahran, Saudi Arabia, Feb 2018.
- **M.SC COMMUNICATIONS ENGINEERING, Rheinisch-Westfälische Technische Hochschule (RWTH) Aachen University**, Aachen, Germany, May 2010.
- **B.S COMMUNICATION SYSTEMS ENGINEERING, Institute of Space Technology (IST)**, Islamabad, Pakistan, Jun 2007.

LIST OF PUBLICATIONS

Conferences

C1 **W. Afzal** and A. A. Masoud, “Harmonic potential based communication-aware navigation and beamforming in cluttered spaces with full channel-state information,” in 2017 IEEE Int. Conf. Robot. Autom. Singapore: IEEE, May 2017, pp. 6198–6203

C2 **W. Afzal** and A. A. Masoud, “Harmonic potential-based communication-aware navigation of mobile agents in cluttered spaces,” in 2016 IEEE 55th Conf. Decis. Control. Las Vegas, Nevada, USA: IEEE, Dec. 2016, pp. 5146–5151

C3 G. Dartmann, **W. Afzal**, X. Gong, and G. Ascheid, “Joint optimization of beamforming, user scheduling, and multiple base station assignment in a multicell network,” in 2011 IEEE Wirel. Commun. Netw. Conf. IEEE, Mar. 2011, pp. 209–214

C4 G. Dartmann, **W. Afzal**, X. Gong, and G. Ascheid, “Low complexity cooperative downlink beamforming in multiuser multicell networks,” in 2010 IEEE 12th Int. Conf. Commun. Technol., vol. 49, no. 241. IEEE, Nov. 2010, pp. 717–721

C5 **W. Afzal** and A. Mahmood, “Design review of satellite telemetry based on ccsds standards and proposed hardware implementation of cansat,” in Int. MultiConference Eng. Comput. Sci. IAENG, 2008

Journals

J1 **W. Afzal** and A. A. Masoud, “Real-time multiple sensor antenna array based communication-aware motion using harmonic potential fields,” Prep. to submit to IEEE Trans. Control Networked Syst.

J2 **W. Afzal** and A. A. Masoud, “Sensor-based communication-aware motion in unknown environments,” Prep. to submit to IEEE Trans. Autom. Control

J3 **W. Afzal** and A. A. Masoud, “On the mobility of agents in communication starved cluttered environments using harmonic potential fields,” Prep. to submit to IEEE Trans. Autom. Control

J4 **W. Afzal** and A. A. Masoud, “Real-time greedy single measurement based communication-aware motion using harmonic potential fields,” Prep. to submit to IEEE Trans. Mob. Comput.

J5 **W. Afzal** and A. A. Masoud, “Real-time transmitter-tracking in cluttered environments using harmonic potential fields,” Prep. to submit to IEEE Trans. Autom. Control

J6 G. Dartmann, X. Gong, **W. Afzal**, and G. Ascheid, “On the duality of the max–min beamforming problem with per-antenna and per-antenna-array power constraints,” IEEE Trans. Veh. Technol., vol. 62, no. 2, pp. 606–619, Feb. 2013

Patents

P1 **W. Afzal** and A. A. Masoud, “A wireless communication-aware mobility method for navigating robots in unstructured confines.” US patent pending

P2 **W. Afzal**, “Parkme application,” US patent pending